

## Crystal Engineering of Metal-Organic Frameworks for Molecular Recognition

Pustovarenko, Alexey

**DOI**

[10.4233/uuid:4384094a-a8ab-4ddc-87e1-078118280711](https://doi.org/10.4233/uuid:4384094a-a8ab-4ddc-87e1-078118280711)

**Publication date**

2021

**Document Version**

Final published version

**Citation (APA)**

Pustovarenko, A. (2021). *Crystal Engineering of Metal-Organic Frameworks for Molecular Recognition*. [Dissertation (TU Delft), Delft University of Technology]. <https://doi.org/10.4233/uuid:4384094a-a8ab-4ddc-87e1-078118280711>

**Important note**

To cite this publication, please use the final published version (if applicable).  
Please check the document version above.

**Copyright**

Other than for strictly personal use, it is not permitted to download, forward or distribute the text or part of it, without the consent of the author(s) and/or copyright holder(s), unless the work is under an open content license such as Creative Commons.

**Takedown policy**

Please contact us and provide details if you believe this document breaches copyrights.  
We will remove access to the work immediately and investigate your claim.

# **CRYSTAL ENGINEERING OF METAL-ORGANIC FRAMEWORKS FOR MOLECULAR RECOGNITION**

**Oleksii PUSTOVARENKO**





# **Crystal Engineering of Metal-Organic Frameworks for Molecular Recognition**

Dissertation

for the purpose of obtaining the degree of doctor  
at Delft University of Technology  
by the authority of the Rector Magnificus Prof.dr.ir. T.H.J.J. van der Hagen,  
Chair of the Board for Doctorates  
to be defended publicly on  
Monday, 11 January 2021 at 15:00 o'clock

by

Oleksii PUSTOVARENKO  
Master of Science in Chemistry, Taras Shevchenko National University of Kyiv, Ukraine  
born in Vinnytsia, USSR

**This dissertation has been approved by the promotors:**

Prof.dr. F. Kapteijn and Prof.dr. J. Gascon Sabate

**Composition of the doctoral committee:**

Rector Magnificus	chairperson
Prof.dr. J. Gascon Sabate	King Abdullah University of Science and Technology and Delft University of Technology, promotor
Prof.dr. F. Kapteijn	Delft University of Technology, promotor

**Independent members:**

Prof.dr. M. Dinca	Massachusetts Institute of Technology, USA
Prof.dr. M. Tsapatsis	John Hopkins University, USA
Prof.dr. R. Ameloot	KU Leuven, Belgium
Prof.dr. S. Furukawa	Kyoto University, Japan
Prof.dr. E. J. R. Sudhölter	Delft University of Technology
Prof.dr. J. H. van Esch	Delft University of Technology, reserve member

The research reported in this thesis was conducted at the Catalysis Engineering group of the Chemical Engineering department, Faculty of Applied Sciences (TNW) of the Delft University of Technology and at the Advanced Catalytic Materials group, KAUST Catalysis Center, King Abdullah University of Science and Technology

This research received funding from the ERC Grant Agreement № 335746, CrystEng-MOF-MMM and King Abdullah University of Science and Technology.

ISBN/EAN: 978-94-6421-153-5  
Copyright © 2021 Oleksii Pustovarenko  
All rights reserved

Cover designed by Oleksii Pustovarenko

Printed by Ipskamp Printing, Enschede  
An electronic version of this dissertation is available at <http://repository.tudelft.nl/>

## TABLE OF CONTENTS

<b>Chapter 1. INTRODUCTION</b>	<b>1</b>
1.1 Introduction	1
1.2 MOFs crystal engineering at molecular level	4
1.2.1 Engineering catenation and interpenetration in MOF structures	4
1.2.2 MOF functionalization <i>via</i> post-synthetic modification (PSM)	6
1.3 MOF crystal engineering beyond the molecular scale: size and morphology	7
1.3.1 MOF crystal shape and size control in synthesis with surfactants	8
1.3.2 MOF crystal shape and size control by chemical modulation	9
1.4 Thesis outline	12
<b>Chapter 2. CONTROL OF INTERPENETRATION OF COPPER-BASED MOFs ON SUPPORTED SURFACES BY ELECTROCHEMICAL SYNTHESIS</b>	<b>17</b>
2.1 Introduction	19
2.2 Experimental section	20
2.2.1 Materials	20
2.2.2 Electrochemical synthesis of copper MOFs	20
2.2.2.1 Synthesis of MOFs as bulk powder	20
2.2.2.2 Synthesis of MOFs as surface supported films	20
2.2.2.3 Optimization procedure for surface growth	20
2.2.3 Characterization methods	21
2.3 Results and discussion	21
2.4 Conclusions	27
Appendix A	31
<b>Chapter 3. RAPID FABRICATION OF MOF-BASED MIXED MATRIX MEMBRANES THROUGH A 3D PRINTING BY DIGITAL LIGHT PROCESSING</b>	<b>39</b>
3.1 Introduction	41
3.2 Experimental section	42
3.2.1 Materials	42
3.2.2 Syntheses and protocols	42
3.2.2.1 Synthesis of MIL-53(Al)-NH <sub>2</sub> nanoparticles	42
3.2.2.2 Post-synthetic modification of MIL-53(Al)-NH <sub>2</sub> with methacrylate functionality	43
3.2.2.3 Photocurable ink formulation for DLP process	43
3.2.2.4 3D printing of polyacrylate membranes	43
3.2.3 Characterization methods	44
3.2.3.1 Determination of crosslinking degree and methacrylic group conversion	44
3.2.3.2 General characterization	44
3.2.4 Gas permeation measurements	47
3.3 Results and discussion	48
3.4 Conclusions	57
Appendix B	61

<b>Chapter 4. NANOSHEETS OF NON-LAYERED ALUMINIUM METAL-ORGANIC FRAMEWORKS THROUGH A SURFACTANT-ASSISTED METHOD</b>	<b>87</b>
4.1 Introduction	89
4.2 Experimental section	90
4.2.1 Materials	90
4.2.2 Syntheses and protocols	90
4.2.2.1 Synthesis of MIL-53(Al)-NH <sub>2</sub> nanoparticles	90
4.2.2.2 Synthesis of MIL-53(Al)-NH <sub>2</sub> MOF nanosheets and optimization procedures	90
4.2.2.3 Generalization of the surfactant-assisted synthesis approach to other MOFs	91
4.2.2.4 Synthesis of MOF-polymer composite materials and membrane casting	92
4.2.2.5 Fabrication of MOF-coated devices	92
4.2.3 Characterization methods	93
4.2.3.1 General characterizations	93
4.2.3.2 Powder X-ray diffraction (PXRD)	94
4.2.3.3 Gas sorption isotherms	96
4.2.4 Gas permeation experiments	96
4.2.5 Sensing studies	97
4.3 Results and discussion	98
4.4 Conclusions	105
Appendix C	109
<b>Chapter 5. METAL-ORGANIC FRAMEWORK DERIVED SYNTHESIS OF COBALT INDIUM CATALYSTS FOR CO<sub>2</sub> HYDROGENATION TO METHANOL</b>	<b>125</b>
5.1 Introduction	127
5.2 Experimental section	129
5.2.1 Materials	129
5.2.2 Synthetic procedures	129
5.2.2.1 Synthesis of 300 nm ZIF-67(Co) material	129
5.2.2.2 Synthesis of 22 nm ZIF-67(Co) material	129
5.2.2.3 Synthesis of MOF-derived In@Co catalysts by <i>IWI</i>	129
5.2.3 Characterization methods	130
5.2.4 Catalytic testing in CO <sub>2</sub> hydrogenation to methanol	132
5.3 Results and discussion	133
5.4 Conclusions	147
Appendix D	151
<b>Summary and outlook</b>	<b>189</b>
<b>Samenvatting en vooruitzichten</b>	<b>195</b>
<b>Acknowledgements</b>	<b>201</b>
<b>List of publications</b>	<b>203</b>
<b>Curriculum vitae</b>	<b>207</b>

## INTRODUCTION

# Chapter 1



"What would the properties of materials be if we could really  
arrange the atoms the way we want them?"

Richard Feynman



## 1.1 INTRODUCTION

Crystal engineering is a research field that emerged at the boundary between chemistry and crystallography. Crystal engineering studies interactions in solid crystalline matter and utilizes acquired knowledge in design of materials with desired physical and chemical properties.<sup>1</sup> Unsurprisingly, structures with modular composition do not only fall in the category of crystal engineering but are certainly prioritized. Among them, metal-organic frameworks stand out for their pronounced structure-property relations and wealth of diversity.<sup>2</sup>

Metal–Organic Frameworks (MOFs) are considered as a relatively new generation of coordination polymers possessing permanent porosity<sup>3–4</sup> derived from channels and/or interconnected cages that can reach diameters up to 2 nm.<sup>5</sup> These crystalline, ordered materials are constructed from metal ions or clusters bridged by organic ligands (linkers), giving rise to network structures of diverse dimensionality (1D, 2D or 3D dimensional).<sup>6–8</sup> The term “MOF” firstly was introduced by Omar Yaghi in 1995<sup>9</sup> along with the report of a 2D pyridine-templated [Co(btc)(py)<sub>2</sub>]<sub>n</sub> framework (btc = 1,3,5-benzenetricarboxylic acid, py = pyridine). Not long after, in 1997 Kitagawa *et al.*<sup>10</sup> presented 3D MOFs based on 4,4'-bipy ligand (4,4'-bipy = 4,4'-bipyridine) and several transition metals (Co, Ni, Zn) with accessible porous structure. In the following years, MOF chemistry evolved on the edge of coordination chemistry and material science into a new area of research that continues to grow exponentially until now.<sup>5</sup>

Such tremendous interest in MOF materials is caused by chemical diversity of their well-defined structures and high specific surface (BET) areas, reaching a record level ( $\sim 7100 \text{ m}^2\cdot\text{g}^{-1}$  for NU-110E) among porous materials and according to predictions could be improved to  $14600 \text{ m}^2\cdot\text{g}^{-1}$ .<sup>11</sup> Owing to the structural versatility of these advanced materials, MOFs have been adapted for a wide range of applications, including gas separation<sup>12</sup> and storage,<sup>13</sup> drug delivery<sup>14</sup> and biomedical integration,<sup>15</sup> catalysis,<sup>16</sup> sensing,<sup>17</sup> energy storage,<sup>18</sup> to mention a few. The well-defined structure-property relations in MOF chemistry allow researchers to seek certain framework architectures for given applications. The judicious combination of structural units (linkers and metal nodes/clusters) under specific conditions of coordination-driven self-assembly (synthetic conditions) allows construction of crystalline frameworks with desired functionalities. The approach of building MOF structures of deliberated topological features starting from predesigned building blocks with certain geometries, was firstly proposed by Yaghi and co-workers,<sup>19</sup> laying the foundation of the *isorecticular design* principle. Even complicated 3D frameworks with desired properties and porosity can be obtained with help of a reverse predictive approach, narrowing the task to the appropriate choice of building blocks, as the net topology is usually determined by their geometry (metal coordination or cluster geometry, linker length)<sup>20</sup> and connectivity (bi-, tri-, tetra-dentate, etc.).<sup>5,21</sup> It is worth to mention



that other parameters (synthesis conditions) might play a role in changing probabilities of different topological occurrences. An analysis of Cambridge Structural Database revealed a domination of high symmetry topologies in experimental results, whereas theoretical speculations were more open to low symmetry outcomes.<sup>22</sup> Nevertheless, the isorecticular principle is not applicable in particular cases hence, alternative synthetic routes should be considered. Moreover, the set of crystal engineering tools cannot be limited by methods acting on molecular level only. The macroscopic properties (size, morphology of crystals and their aggregates) deserve to be brought to attention as another parameters in MOF crystal engineering for their ability to influence integrability, performance and applicability.<sup>23-24</sup>

In the following paragraphs, some relevant crystal engineering tools at different levels will be discussed.

## **1.2 MOFs CRYSTAL ENGINEERING AT THE MOLECULAR LEVEL**

Although the rationalized combination of metal ions and predesigned organic ligands usually determines the underlying framework topology, the arrangement of MOF nets (isomerism) in some cases may deviate from expected under influential factors such as synthetic conditions or reagent concentration. Moreover, functional design of MOF structures also implies alternative routes of crystal engineering that can be applied to the framework that cannot be achieved through the direct synthetic route. The following paragraphs will address several relevant approaches dedicated to tune MOF structures according to desired functions. Among others, the factors governing interpenetration of MOF networks and post-synthetic modification methods will be discussed more in detail.

### **1.2.1 Engineering catenation and interpenetration in MOF structures**

Since the applicability of a given MOF is strongly structure dependent, great attention is paid to their ability to create polymorphs.<sup>25</sup> As a subtype of MOF polymorphism that substantially influences the pore size, structure and accessibility, an interpenetration is proven to be one of effective tools of crystal design and play a remarkable role in the functional applications.<sup>26-27</sup> The interpenetration, also referred as catenation, is defined as a phenomenon of a net self-entanglement in which the voids associated with one framework are occupied by one or more independent frameworks (topologically identical or distinctive).<sup>28</sup> Despite the fact that there are no chemical bonds between interpenetrated networks, the obtained structures cannot be separated in components without breaking it on a deep level. Formation of interpenetrated networks is difficult to predict and can be associated with a tendency of the system to minimize its energy through effective void utilization.<sup>27</sup> One of the limitations is the

accessible pore volume, since one net should possess enough space to accommodate another. Noteworthy, the minimization of unfilled voids through interpenetration considerably improves MOF stability as a result of repulsive forces that prevent the structure from collapse.<sup>29</sup> Undoubtedly, interpenetration can be interesting from perspectives of better understanding of mechanisms lying behind self-assembly processes and beneficial for practical use.<sup>30</sup>

Considering approaches for control over interpenetration in MOF structures, synthesis parameters (such as temperature,<sup>31-32</sup> time,<sup>33</sup> concentration of reactants,<sup>34</sup> solvent system,<sup>35</sup> etc.), strategy of the synthesis (surface growth,<sup>36</sup> ultrasonic assistance,<sup>37</sup> etc.) as well as rational design of SBUs (flexibility,<sup>38</sup> bulkiness<sup>39</sup> and length of linker,<sup>40-41</sup> SBU continuity,<sup>42</sup> etc.) are perhaps more influential in this sense. As a rule, the use of longer linkers often affords interpenetrated MOF structures. Contrary to that the short linkers do not favor catenation and can effectively restrict net interpenetration. From the process prospective, it was shown that high synthesis temperatures generally support faster kinetics and crystal growth which together reinforce the probability for interpenetration to occur. Likewise, higher reagent concentrations lead to higher chances to obtain a catenated structure. Following this strategy, Zhang *et al.*<sup>34</sup> reported pair of  $[\text{Cd}(\text{bipy})(\text{bdc})]_n$  (bipy = 4,4'-bipyridine, bdc = 1,4-benzenedicarboxylic acid) frameworks with and without interpenetration. The authors managed to control the level of the interpenetration by varying concentration and temperature revealing that both parameters have strong positive correlation with the catenation level. Interestingly, the desired level of interpenetration and occupancy of the second subnet can be achieved by varying the reaction time and solvent composition.<sup>33</sup> In addition, the guest molecules (such as solvents, counterions, template molecules) also contribute in determining whatever interpenetration is conceivable or not. The tendency dictates that the larger/bulkier template molecules are the lower degree of interpenetration and the higher the chances for a non-interpenetrated MOF structure.<sup>35,43</sup>

Noteworthy, MOF interpenetration suppression can also be achieved by choosing the appropriate synthesis protocol. Shekhah *et al.*<sup>36</sup> reported a layer-by-layer growth of MOF-508 ( $[\text{Zn}(\text{bdc})(\text{bipy})_{0.5}]_n$ , bipy = 4,4'-bipyridine, bdc = 1,4-benzenedicarboxylic acid) and experimentally proved that an effective suppression of the second, interpenetrating lattice in SURMOF (a surface-mounted metal-organic frameworks) can be achieved by epitaxial growth on substrate. The authors proposed that the lack of nucleation sites of the second sublattice at the surface is responsible for the suppression of interpenetrated lattice during liquid epitaxy synthesis. Nevertheless, the question of whether the surface growth is a general approach to suppress interpenetration in MOFs remains open.

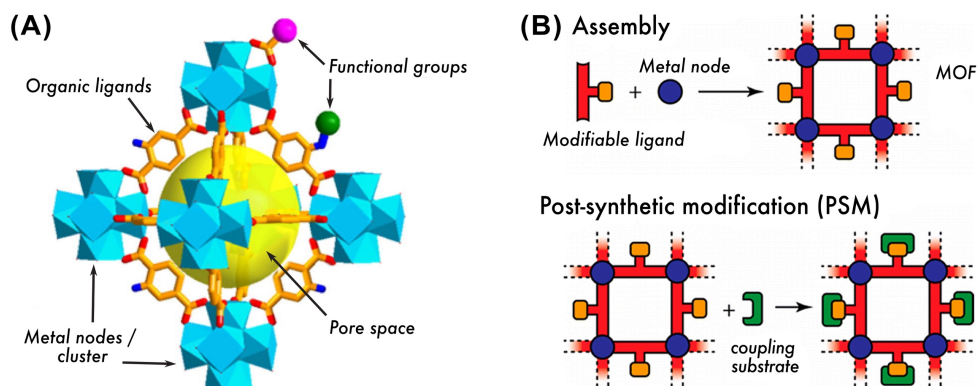


**Figure 1.1.** (A) Representation of constructive elements of functional MOF structure.<sup>5</sup> (B) Schematic illustrations of MOF self-assembly from metal node and modifiable linkers and post-synthetic modification (PSM) on the ligand possessing reactive sites.<sup>44</sup>

### 1.2.2 MOF functionalization *via* post-synthetic modification (PSM)

Not every functionality can be integrated in a MOF structure with structural building units (SBUs) prior to or during the synthesis because of limitations associated with interference (functional, steric-hindrance of bulky moieties) of precursor features,<sup>45</sup> dominance of kinetically favored syntones,<sup>46–47</sup> or incompatibility with synthetic conditions (thermal stability, solubility, etc.).<sup>45</sup> Thus, post-synthetic modification (PSM) turns out to be a unique and most efficient way to generate MOFs with certain functionalities when the above mentioned restrictions are in place. Since the pioneering work of Wang and Cohen on the direct PSM of a MOF ligand,<sup>48</sup> the PSM approach has become an essential tool for functionalization of MOF structures with diverse chemical moieties while preserving topological analogy.<sup>49–50</sup> The PSM can be defined as the chemical modification of the framework after its self-assembly in heterogeneous manner. The targets for such functional insertions could be either metal nodes/clusters, pore space or pre-functionalized moieties in the bridging linkers (Fig. 1.1A).<sup>5</sup>

The major PSM strategies for MOF functionalization include transformations that might be classified into three main groups: non-covalent (host-guest) interactions, coordination or covalent coupling.<sup>45</sup> Non-covalent or host-guest modification commonly implies the removal or exchange of guest molecules from the of MOF pores to load the vacancies with functional molecules or nanoparticles retaining the structural integrity.<sup>51</sup> The PSM through formation of coordinative bonds generally exploits the chemistry of unsaturated metal sites and coordination sites of organic linkers. Additionally, the variation of coordination PSM has emerged lately including exchange/insertion approaches known as post-synthetic metal ion exchange (PSE) (transmetalation, post-synthetic metalation) / insertion (PSI) or solvent-

assisted linker exchange (SALE) / incorporation (SALI) or even sequential linker elimination and installation (SLE&I).<sup>52-53</sup>

In turn, covalent coupling PSMs entail formation of covalent bonds utilizing suitable chemical groups (amino, formyl, azide, alkyne and others).<sup>45,53</sup> A schematic illustration of covalent PSM reaction involving the modifiable group of the linker component and modifying reagent (or functional group) is shown in Figure 1.1B.<sup>44</sup> The covalent anchoring of a functional group to a modifiable element of the linker can be accomplished by applying classical organic transformations such as acetylation and “click” reactions, imine condensation, etc.<sup>45,52</sup> Generally, covalent PSM offers effective and firm incorporation of desired functionality into MOF structure or on its surface given a stronger character of covalent bonds compared to non-covalent and coordinative interactions. Thus, covalent PSM becomes an optimal alteration remedy when the anchored functionality must form a continuous conjugated system within the MOF or secure a firm integration of a given MOF component within a composite. For instance, Zhang *et al.*<sup>54</sup> have explored a covalent PSM of NH<sub>2</sub>-UiO-66 with polymerizable methyl methacrylic moieties to generate MOF nanocrystals able to participate in UV-induced cross-linking with butyl methacrylate component. Such wise, a stand-alone elastic membrane with well distributed and covalently linked MOF particles without significant pore obstruction can be obtained. Another interesting example of a successful stitching MOF and polymeric components together by PSM means has been delivered by Matzger’s group.<sup>55</sup> A hybrid polymer-MOF composite featuring core-shell architecture was prepared by growing a shell of IRMOF-3 over MOF-5 core followed by clipping an ATRP (atom transfer radical polymerization) initiator fragment on NH<sub>2</sub>-sites of IRMOF-3 outer shell via acylation PSM. Further polymerization with methyl methacrylate occurred selectively on the grafted initiator sites resulting in propagation of high molecular weight PMMA chains from the crystal surface, yet, allowing the internal structure of the MOF to remain intact.

### 1.3 MOF CRYSTAL ENGINEERING BEYOND THE MOLECULAR SCALE: SIZE AND MORPHOLOGY

Although the most relevant MOF properties can be controlled at the stage of their self-assembly relying on geometrical features of SBUs and their packing modes, the crystal engineering cannot overlook the influence of crystal morphologies and particle sizes onto their applicability. The approaches allowing to engineer MOF particles consider a great number of parameters, which include components variations (solvents, reactant ratios and their chemical nature), synthetic conditions (temperature; microwave, ultrasonic and electrochemical

assistance, pH, heating- and diffusion-controlled methods) and additive usage (ionic liquids, initiators, capping and stabilizing agents, modulators and surfactants).<sup>23,56</sup>

In the following paragraphs, some of the methods applied in this Thesis will be overviewed in greater details.

### 1.3.1 MOF crystal shape and size control in synthesis with surfactants

Surfactant-assisted strategies for controlling crystal sizes and morphologies have been manifested in the bibliography for many years and applied for a variety of different materials.<sup>57,58</sup> Among them, the metal-organic frameworks are not of the least importance in this comprehensive list.<sup>59</sup> Relying on molecular structure, that commonly comprises the hydrophobic and hydrophilic fragments, surfactants own the ability to undergo a self-organization into several ordered substructures (micelles) depending on property of the media (solvent polarity, pH, ionic power, etc.).<sup>60</sup> Therefore, the systems bearing the surfactant component are frequently used in order to downsize MOFs particles significantly narrowing the size distribution profile.<sup>23,61</sup> For example, Zhao *et al.*<sup>62</sup> used surfactant/ionic liquid/water emulsion system to limit the size of the Zn(bdc)-type (bdc = 1,4-benzenedicarboxylic acid) MOF particles to roughly 80 nm in diameter with a uniform size distribution. Additionally, surface active additives also known to be acting as shape directing agents and crystal form modulators.<sup>63-66</sup> Pan *et al.*<sup>67</sup> synthesized ZIF-8 crystals with different shapes by controlling the amount of the cationic surfactant CTAB in the reaction media. It was demonstrated that the crystal shape changes from rhombic dodecahedron to truncated rhombic dodecahedron and to truncated cube as a function of CTAB concentration suggestive to a selective attachment of the surfactant to some crystal facets and slowing down crystal growth rate in certain directions.

Remarkably, pre-organized surfactant systems have also been applied for morphology controlled and/or shape-replicated growth of MOF crystals.<sup>59</sup> Lin's group<sup>68</sup> developed a strategy to synthesize Gd(btc) MOF (bdc = 1,4-benzenedicarboxylic acid) nanoplates from a microemulsion composed of CTAB (cetyltrimethylammonium bromide) surfactant, isooctane, 1-hexanol and water. Further, the approach was extended to other MOFs. As evidenced by Junggeburth *et al.*<sup>69</sup> and Flügel *et al.*,<sup>70</sup> thin nanolamellae of Zn-bim, Zn-im or Zn-mim (bim = benzimidazole, im = imidazole, mim = 2-methylimidazole) can be formed from lamellar reverse microemulsions prepared with CTAB, heptane, 1-hexanol and water. The key idea was to use the lamellar structure of CTAB micelles in reverse microemulsion to create confined spaces for crystals growth. Being limited in certain directions, MOF crystals with big aspect ratios were formed, grouped in stacks of nanosheets separated by CTAB layers. Moreover, the stacks

were exfoliated in solvents like tetrahydrofuran and chloroform to render free-standing MOF nanosheets with thicknesses around 10 nm and lateral dimensions exceeding it in order of magnitude. Recently, Zhang *et al.*<sup>71</sup> confirmed the efficiency of a self-organized surfactant media in a synthesis of ultrathin (3–4 nm) 2D Zr-MOF nanosheets simultaneously exploring a pseudo-assembly process to exfoliate 3D MOFs to 2D nanolamellae. Notably, the authors claimed that the thickness of the nanosheets can be controlled by varying the hydrophobic chain length of the surfactant.

### 1.3.2 MOF crystal shape and size control by chemical modulation

Modulated synthesis has emerged as another alternative approach to extend the control over MOFs' self-assembly regulating the size, defectivity and morphological features (crystal habits) of MOF crystals along with surface functionalization.<sup>23,72-74</sup> The modulating strategy implies an involvement in reaction modulating agents or modulators – compounds of different chemical nature, which able to alter acid-base equilibria of either precursor materials or an intermediate SBU units formed at germinal stages of MOF formation.<sup>72</sup> Thus, a modulator initiates a self-assembly of the framework in a certain fashion driving a coordinative net expansion in a particular way and determining nucleation and/or growing rate of MOF crystals. Depending on the type of interaction between modulator and MOF, the modulating process can be classified into two categories – coordinative and non-coordinative modulation.<sup>23</sup> The term “coordination modulation” was firstly introduced by Kitagawa *et al.*<sup>75</sup> while investigating formation of pillar-layered  $[\text{Cu}_2(\text{ndc})_2(\text{dabco})]_n$  (dabco = 1,4-diazabicyclo[2.2.2]octane, ndc = 1,4-naphthalene dicarboxylate). It was observed that the addition of either acetic acid or pyridine promotes anisotropic growth of the MOF crystal, suppressing certain crystal faces and developing other at fastest rate, relying upon a chemical termination of each of the surfaces (Fig. 1.2A). Later on, the same group has evidenced a plausibility of modulator approach in the derivation HKUST-1 ( $[\text{Cu}_3(\text{btc})_2]_n$ , btc = benzene-1,3,5-tricarboxylate) crystal forms from octahedron, cuboctahedron, truncated cube to cube using lauric acid (LA) at different molar proportions relative to btc linker.<sup>76</sup> In agreement with Monte-Carlo simulations, it was concluded that different amounts of LA on the facets endow the primary SBU with distinct attachment energy creating anisotropy in growing rates along different directions, thus generating a diversity in crystal geometries (Fig. 1.2B). Alternatively, the modulator might be viewed as a component that competes with the organic linker for coordination to a metal site throughout MOF formation, and therefore introduces some reversibility and kinetic control over the crystallization process. Hence, the additive component can either inhibit crystal growth

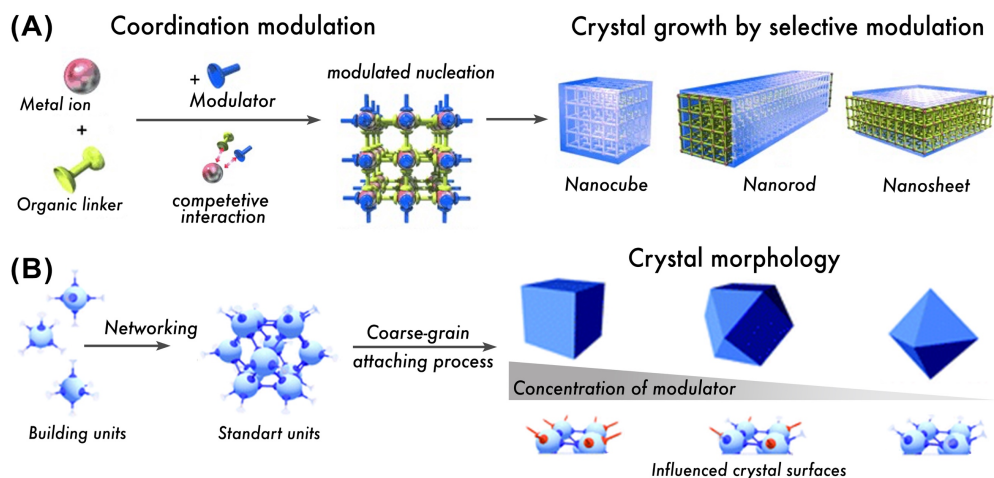


**Figure 1.2.** (A) Schematic illustration of coordination modulation method for fabricating MOF with different crystal features induced by the addition of modulators with the same functionality as bridging linkers.<sup>75</sup> (B) Coarse-grain model of the process corresponding to evolvement of crystal habits as function of coordinated modulator concentration.<sup>76</sup>

down to the nanometric scale or to promote crystal growth to render large single crystals.<sup>73</sup> The latter scenario is known to be the option for growing high quality crystals of UiO-66, UiO-67<sup>77</sup> and UiO-68,<sup>78</sup> involving benzoic acid as modulating agent (Fig. 1.3A). However, the modulator also might act as a capping agent that allows the crystal to develop until a certain size and hereafter arresting further growth of the particles by coordination, securing its surfaces.<sup>23</sup> Thereby, Hermes *et al.*<sup>79</sup> in 2007 communicated that stable size-selected colloids can be obtained by modulated synthesis of MOF-5 with *p*-perfluoro-methylbenzene, that being added at the initiation step of MOF assembly inhibits crystal growth and affords controllable nanoparticle formation. Similarly, the addition of only one equivalent of sodium formate with respect to btc (benzene-1,3,5-tricarboxylate) in hydrothermal synthesis of HKUST-1 was able to lower down the crystal size from 20  $\mu\text{m}$  down to 300 nm.<sup>80</sup> Remarkable that the parent MOF linker itself can behave as a capping agent. Lim *et al.*<sup>81</sup> described a systematic approach to synthesize size-specific ZIF-8 at different rates of nucleation by adjusting Zn:mim (mim = 2-methylimidazole) molar ratios. It was found that the increase of mim content undoubtedly decreases ZIF-8 crystal size from 1  $\mu\text{m}$  to 50 nm (Fig. 1.3B). These results experimentally support the fact that excess of linker equivalents shifts metal-ligand equilibria towards fast local depletion of the metal ion, whereas the excess of the linker concentrates on the surface of formed MOF particles.

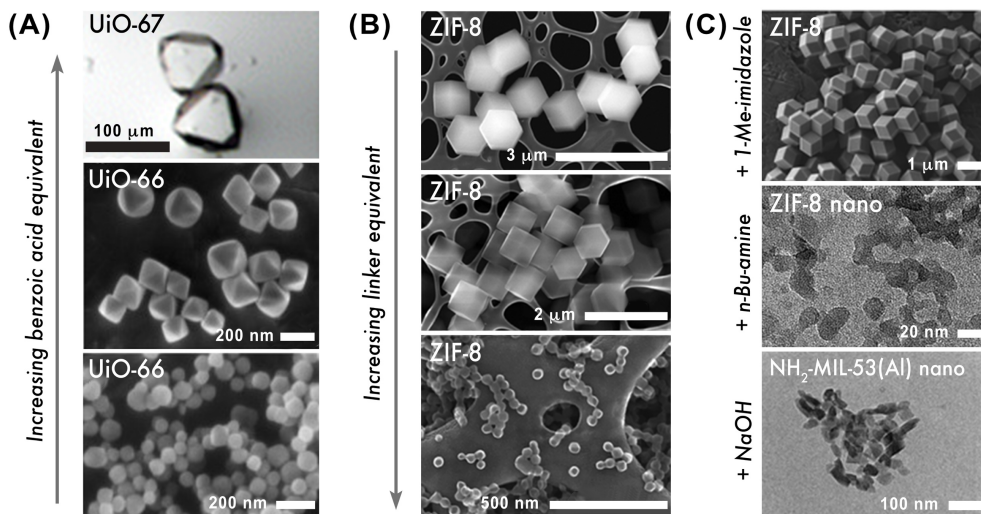


**Figure 1.3.** (A) UiO-67 and UiO-66 crystals obtained by modulated synthesis with benzoic acid.<sup>77-78</sup> (B) SEM images of ZIF-8 crystals formed at different Zn:mim ratios (top to bottom: 2:1, 1:1 and 1:4).<sup>81</sup> (C) ZIF-8 materials precipitated with 1-methylimidazole coordinative modulator and *n*-butylamine base (from top to down),<sup>82</sup> MIL-53(Al)-NH<sub>2</sub> nanoparticles isolated with NaOH additive.<sup>83</sup>

In turn, non-coordinative modulation relies on the ability of a modulating agent to modify pH of the reaction media and, therefore, affect linker deprotonation rather than being involved directly into coordinative interactions. Although the modulators of acidic nature, which compete for bases during the self-assembly and introduce additional protons to inhibit linker deprotonation, stimulate the nucleation to slow down producing larger particles, the modulators of basic character tend to manifest with opposite effect. For instance, Cravillon *et al.*<sup>82</sup> while exploring a modulated synthesis of ZIF-8 showed that even weak alkylamine bases like *n*-butylamine can trigger rapid nucleation leading to formation of uniform particles sizing of about 20 nm, that is five times smaller than that offered by coordinative modulation with 1-methylimidazole (Fig. 1.3C). In this line, Chin *et al.*<sup>83</sup> also observed that the addition of NaOH to the reaction mixture of MIL-53(Al)-NH<sub>2</sub> facilitate the formation of nanoparticles with remarkably narrow size distribution (Fig. 1.3C). As a matter of fact, the linker deprotonation occurs more swiftly at higher pH inducing faster nucleation and sharply terminating crystal growth to yield monodisperse fine particles. Thus, the approaches based on aforementioned mechanism conveniently serve for the effective particle size reduction and fabrication of size-selective MOF materials.<sup>74</sup>



### 1.4 THESIS OUTLINE

The thesis consists of three main parts. Part 1, comprising this Chapter 1, depicts the current state of crystal engineering of metal-organic frameworks and discusses available tools dedicated to MOF design at different scales: from molecular to crystal size and shape. It can serve as a brief guide through the methods applied and structural levels involved in the following chapters.

Part 2 (Chapter 2 and Chapter 3) focuses on tuning MOF functionality at the molecular level. Chapter 2 provides an example of controlled network interpenetration by means of electrochemical growth on a sacrificial copper surface. The degree of interpenetration of MOF synthesized as bulk powder and on supported copper surfaces was investigated for CuTATB ( $H_3TATB = 4,4',4''$ -s-triazine-2,4,6-triyl-tribenzoic acid) system. In Chapter 3 the post-synthetic modification of MIL-53(Al)-NH<sub>2</sub> with MMA (methyl methacrylate) groups was performed to improve integrability of the MOF filler into 3D printed mixed matrix membranes using DLP (Digital Light Processing) technology and further used for H<sub>2</sub>/CO<sub>2</sub> separation.

Part 3 (Chapter 4 and Chapter 5) brings the focus to the micro level. A new bottom-up surfactant-assisted synthetic approach for the fabrication of nanosheets of various nonlayered MOFs is reported in Chapter 4 accounting nonlayered Al-containing MOF structures (MIL-53(Al)-NH<sub>2</sub>, CAU-10(Al)-NH<sub>2</sub>, CAU-10(Al))-H. Nanosheets obtained with this method were evaluated in chemical sensing of alcohols and CH<sub>4</sub>/CO<sub>2</sub> gas separation. In Chapter 5, ZIF-67(Co) nanoparticles of different sizes were synthesized with help of chemical modulators and subsequently used as sacrificial matrix for preparation of Co-supported indium oxide catalysts for selective CO<sub>2</sub> hydrogenation to methanol.

The chapters of the thesis have been written as individual publications, can be read independently and some overlap is unavoidable.

## REFERENCES

- [1] G. R. Desiraju, *J. Am. Chem. Soc.* **2013**, 135, 9952-9967.
- [2] S. Mukherjee, M. J. Zaworotko, *Trends Chem.* **2020**, DOI: 10.1016/j.trechm.2020.02.013.
- [3] S. R. Batten, N. R. Champness, X.-M. Chen, J. Garcia-Martinez, S. Kitagawa, L. Öhrström, M. O'Keeffe, M. P. Suh, J. Reedijk, *CrystEngComm* **2012**, 14, 3001-3004.
- [4] S. R. Batten, N. R. Champness, X.-M. Chen, J. Garcia-Martinez, S. Kitagawa, L. Öhrström, M. O'Keeffe, M. P. Suh, J. Reedijk, *Pure Appl. Chem.* **2013**, 85, 1715.
- [5] L. Jiao, J. Y. R. Seow, W. S. Skinner, Z. U. Wang, H.-L. Jiang, *Mater. Today* **2019**, 27, 43-68.
- [6] M. D. Allendorf, V. Stavila, *CrystEngComm* **2015**, 17, 229-246.
- [7] H. Furukawa, K. E. Cordova, M. O'Keeffe, O. M. Yaghi, *Science* **2013**, 341, 1230444.
- [8] S. L. James, *Chem. Soc. Rev.* **2003**, 32, 276-288.
- [9] O. M. Yaghi, G. Li, H. Li, *Nature* **1995**, 378, 703-706.
- [10] M. Kondo, T. Yoshitomi, H. Matsuzaka, S. Kitagawa, K. Seki, *Angew. Chem., Int. Ed.* **1997**, 36, 1725-1727.
- [11] O. K. Farha, I. Eryazici, N. C. Jeong, B. G. Hauser, C. E. Wilmer, A. A. Sarjeant, R. Q. Snurr, S. T. Nguyen, A. Ö. Yazaydin, J. T. Hupp, *J. Am. Chem. Soc.* **2012**, 134, 15016-15021.
- [12] J.-R. Li, R. J. Kuppler, H.-C. Zhou, *Chem. Soc. Rev.* **2009**, 38, 1477-1504.
- [13] L. J. Murray, M. Dinca, J. R. Long, *Chem. Soc. Rev.* **2009**, 38, 1294-1314.
- [14] P. Horcajada, T. Chalati, C. Serre, B. Gillet, C. Sebrie, T. Baati, J. F. Eubank, D. Heurtaux, P. Clayette, C. Kreuz, J.-S. Chang, Y. K. Hwang, V. Marsaud, P.-N. Bories, L. Cynober, S. Gil, G. Ferey, P. Couvreur, R. Gref, *Nat. Mater.* **2010**, 9, 172-178.
- [15] J. Yang, Y.-W. Yang, *Small* **2020**, 16, 1906846.
- [16] J. Gascon, A. Corma, F. Kapteijn, F. X. Llabrés i Xamena, *ACS Catal.* **2014**, 4, 361-378.
- [17] A. Amini, S. Kazemi, V. Safarifard, *Polyhedron* **2020**, 177, 114260.
- [18] T. Mehtab, G. Yasin, M. Arif, M. Shakeel, R. M. Korai, M. Nadeem, N. Muhammad, X. Lu, *J. Energy Storage* **2019**, 21, 632-646.
- [19] B. Chen, M. Eddaoudi, S. T. Hyde, M. O'Keeffe, O. M. Yaghi, *Science* **2001**, 291, 1021-1023.
- [20] H. Deng, S. Grunder, K. E. Cordova, C. Valente, H. Furukawa, M. Hmadeh, F. Gándara, A. C. Whalley, Z. Liu, S. Asahina, H. Kazumori, M. O'Keeffe, O. Terasaki, J. F. Stoddart, O. M. Yaghi, *Science* **2012**, 336, 1018-1023.
- [21] M. Eddaoudi, D. B. Moler, H. Li, B. Chen, T. M. Reineke, M. O'Keeffe, O. M. Yaghi, *Acc. Chem. Res.* **2001**, 34, 319-330.
- [22] N. W. Ockwig, O. Delgado-Friedrichs, M. O'Keeffe, O. M. Yaghi, *Acc. Chem. Res.* **2005**, 38, 176-182.
- [23] B. Seoane, S. Castellanos, A. Dikhtiarenko, F. Kapteijn, J. Gascon, *Coord. Chem. Rev.* **2016**, 307, 147-187.
- [24] S. Furukawa, J. Reboul, S. Diring, K. Sumida, S. Kitagawa, *Chem. Soc. Rev.* **2014**, 43, 5700-5734.
- [25] R. Haldar, N. Sikdar, T. K. Maji, *Mater. Today* **2015**, 18, 97-116.
- [26] G. Verma, S. Butikofer, S. Kumar, S. Ma, *Top. Curr. Chem.* **2019**, 378, 4.
- [27] H.-L. Jiang, T. A. Makal, H.-C. Zhou, *Coord. Chem. Rev.* **2013**, 257, 2232-2249.
- [28] R. Zhu, J. Ding, L. Jin, H. Pang, *Coord. Chem. Rev.* **2019**, 389, 119-140.

- [29] N. C. Burtch, J. Heinen, T. D. Bennett, D. Dubbeldam, M. D. Allendorf, *Adv. Mater.* **2018**, 30, 1704124.
- [30] V. Bon, I. Senkovska, S. Kaskel, in *Nanoporous Materials for Gas Storage*, DOI: 10.1007/978-981-13-3504-4\_6 (Eds: K. Kaneko, F. Rodríguez-Reinoso), Springer Singapore, Singapore **2019**, 137-172.
- [31] Y. Wang, L. Cheng, K.-J. Wang, Z. Perry, W. Jia, R. Chen, Z.-L. Wang, J. Pang, *Inorg. Chem.* **2019**, 58, 18-21.
- [32] A. Dikhtiarenko, P. Serra-Crespo, S. Castellanos, A. Pustovarenko, R. Mendoza-Meroño, S. García-Granda, J. Gascon, *Cryst. Growth Des.* **2016**, 16, 5636-5645.
- [33] A. Ferguson, L. Liu, S. J. Tapperwijn, D. Perl, F.-X. Coudert, S. Van Cleuvenbergen, T. Verbiest, M. A. van der Veen, S. G. Telfer, *Nat. Chem.* **2016**, 8, 250-257.
- [34] J. Zhang, L. Wojtas, R. W. Larsen, M. Eddaoudi, M. J. Zaworotko, *J. Am. Chem. Soc.* **2009**, 131, 17040-17041.
- [35] S. K. Elsaidi, M. H. Mohamed, L. Wojtas, A. Chanthapally, T. Pham, B. Space, J. J. Vittal, M. J. Zaworotko, *J. Am. Chem. Soc.* **2014**, 136, 5072-5077.
- [36] O. Shekhah, H. Wang, M. Paradinas, C. Ocal, B. Schüpbach, A. Terfort, D. Zacher, R. A. Fischer, C. Wöll, *Nat. Mater.* **2009**, 8, 481-484.
- [37] J. Kim, S.-T. Yang, S. B. Choi, J. Sim, J. Kim, W.-S. Ahn, *J. Mater. Chem.* **2011**, 21, 3070-3076.
- [38] T. K. Prasad, M. P. Suh, *Chem. Eur. J.* **2012**, 18, 8673-8680.
- [39] X.-F. Wang, Y.-B. Zhang, W. Xue, *Cryst. Growth Des.* **2012**, 12, 1626-1631.
- [40] D. Feng, K. Wang, Z. Wei, Y.-P. Chen, C. M. Simon, R. K. Arvapally, R. L. Martin, M. Bosch, T.-F. Liu, S. Fordham, D. Yuan, M. A. Omary, M. Haranczyk, B. Smit, H.-C. Zhou, *Nat. Commun.* **2014**, 5, 5723.
- [41] J. Lippke, B. Brosent, T. von Zons, E. Virmani, S. Lilienthal, T. Preuße, M. Hülsmann, A. M. Schneider, S. Wuttke, P. Behrens, A. Godt, *Inorg. Chem.* **2017**, 56, 748-761.
- [42] N. L. Rosi, M. Eddaoudi, J. Kim, M. O'Keeffe, O. M. Yaghi, *Angew. Chem., Int. Ed.* **2002**, 41, 284-287.
- [43] D. Rankine, A. Avellaneda, M. R. Hill, C. J. Doonan, C. J. Sumby, *Chem. Commun.* **2012**, 48, 10328-10330.
- [44] T. R. Cook, Y.-R. Zheng, P. J. Stang, *Chem. Rev.* **2013**, 113, 734-777.
- [45] D. Farrusseng, J. Canivet, A. Quadrelli, in *Metal-Organic Frameworks: Applications from Catalysis to Gas Storage* **2011**, Ch. 2, 23-48.
- [46] G. R. Desiraju, *Angew. Chem., Int. Ed.* **2007**, 46, 8342-8356.
- [47] A. K. Nangia, G. R. Desiraju, *Angew. Chem., Int. Ed.* **2019**, 58, 4100-4107.
- [48] Z. Wang, S. M. Cohen, *J. Am. Chem. Soc.* **2007**, 129, 12368-12369.
- [49] K. K. Tanabe, S. M. Cohen, *Chem. Soc. Rev.* **2011**, 40, 498-519.
- [50] J. Jiang, Y. Zhao, O. M. Yaghi, *J. Am. Chem. Soc.* **2016**, 138, 3255-3265.
- [51] L. Chen, R. Luque, Y. Li, *Chem. Soc. Rev.* **2017**, 46, 4614-4630.
- [52] S. M. Cohen, *J. Am. Chem. Soc.* **2017**, 139, 2855-2863.
- [53] Z. Yin, S. Wan, J. Yang, M. Kurmoo, M.-H. Zeng, *Coord. Chem. Rev.* **2019**, 378, 500-512.
- [54] Y. Zhang, X. Feng, H. Li, Y. Chen, J. Zhao, S. Wang, L. Wang, B. Wang, *Angew. Chem., Int. Ed.* **2015**, 54, 4259-4263.
- [55] K. A. McDonald, J. I. Feldblyum, K. Koh, A. G. Wong-Foy, A. J. Matzger, *Chem. Commun.* **2015**, 51, 11994-11996.

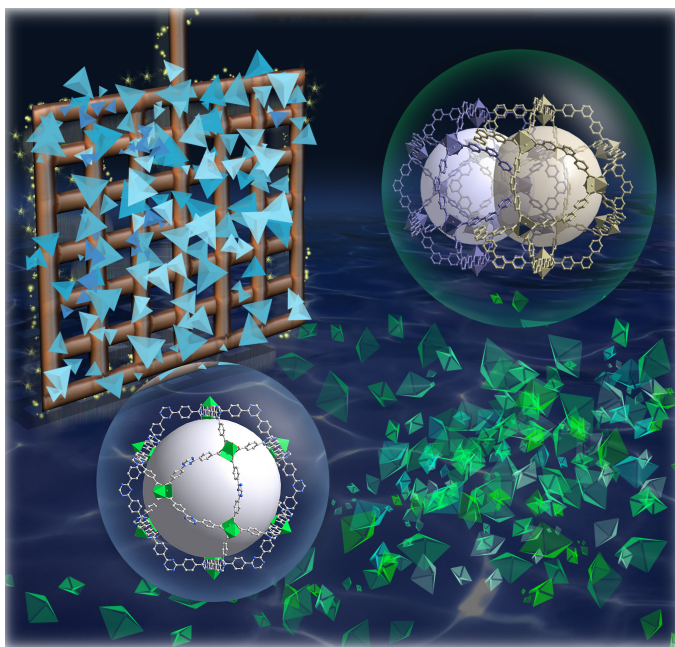
- [56] M. Y. Masoomi, A. Morsali, *RSC Adv.* **2013**, 3, 19191-19218.
- [57] W.-W. Xiong, Q. Zhang, *Angew. Chem., Int. Ed.* **2015**, 54, 11616-11623.
- [58] V. T. John, B. Simmons, G. L. McPherson, A. Bose, *Curr. Opin. Colloid Interface Sci.* **2002**, 7, 288-295.
- [59] J. Zhao, X. Liu, Y. Wu, D.-S. Li, Q. Zhang, *Coord. Chem. Rev.* **2019**, 391, 30-43.
- [60] K. Shinoda, B. Lindman, *Langmuir* **1987**, 3, 135-149.
- [61] E. A. Flügel, A. Ranft, F. Haase, B. V. Lotsch, *J. Mater. Chem.* **2012**, 22, 10119-10133.
- [62] Y. Zhao, J. Zhang, B. Han, J. Song, J. Li, Q. Wang, *Angew. Chem., Int. Ed.* **2011**, 50, 636-639.
- [63] D. Li, H. Wang, X. Zhang, H. Sun, X. Dai, Y. Yang, L. Ran, X. Li, X. Ma, D. Gao, *Cryst. Growth Des.* **2014**, 14, 5856-5864.
- [64] M. Pang, A. J. Cairns, Y. Liu, Y. Belmabkhout, H. C. Zeng, M. Eddaoudi, *J. Am. Chem. Soc.* **2012**, 134, 13176-13179.
- [65] X.-Y. Liu, W.-S. Lo, C. Wu, B. P. Williams, L. Luo, Y. Li, L.-Y. Chou, Y. Lee, C.-K. Tsung, *Nano Lett.* **2020**, 20, 1774-1780.
- [66] Q. Zuo, T. Liu, C. Chen, Y. Ji, X. Gong, Y. Mai, Y. Zhou, *Angew. Chem., Int. Ed.* **2019**, 58, 10198-10203.
- [67] Y. Pan, D. Heryadi, F. Zhou, L. Zhao, G. Lestari, H. Su, Z. Lai, *CrystEngComm* **2011**, 13, 6937-6940.
- [68] W. J. Rieter, K. M. L. Taylor, H. An, W. Lin, W. Lin, *J. Am. Chem. Soc.* **2006**, 128, 9024-9025.
- [69] S. C. Junggeburth, L. Diehl, S. Werner, V. Duppel, W. Sigle, B. V. Lotsch, *J. Am. Chem. Soc.* **2013**, 135, 6157-6164.
- [70] E. A. Flügel, M. T. Aronson, S. C. Junggeburth, B. F. Chmelka, B. V. Lotsch, *CrystEngComm* **2015**, 17, 463-470.
- [71] X. Zhang, P. Zhang, C. Chen, J. Zhang, G. Yang, L. Zheng, J. Zhang, B. Han, *Green Chem.* **2019**, 21, 54-58.
- [72] R. S. Forgan, *Chem. Sci.* **2020**, DOI: 10.1039/D0SC01356K.
- [73] C. V. McGuire, R. S. Forgan, *Chem. Commun.* **2015**, 51, 5199-5217.
- [74] C. R. Marshall, S. A. Staudhammer, C. K. Brozek, *Chem. Sci.* **2019**, 10, 9396-9408.
- [75] T. Tsuruoka, S. Furukawa, Y. Takashima, K. Yoshida, S. Isoda, S. Kitagawa, *Angew. Chem., Int. Ed.* **2009**, 48, 4739-4743.
- [76] A. Umemura, S. Diring, S. Furukawa, H. Uehara, T. Tsuruoka, S. Kitagawa, *J. Am. Chem. Soc.* **2011**, 133, 15506-15513.
- [77] S. Øien, D. Wragg, H. Reinsch, S. Svelle, S. Bordiga, C. Lamberti, K. P. Lillerud, *Cryst. Growth Des.* **2014**, 14, 5370-5372.
- [78] A. Schaate, P. Roy, A. Godt, J. Lippke, F. Waltz, M. Wiebcke, P. Behrens, *Chem. Eur. J.* **2011**, 17, 6643-6651.
- [79] S. Hermes, T. Witte, T. Hikov, D. Zacher, S. Bahn Müller, G. Langstein, K. Huber, R. A. Fischer, *J. Am. Chem. Soc.* **2007**, 129, 5324-5325.
- [80] F. Wang, H. Guo, Y. Chai, Y. Li, C. Liu, *Micropor. Mesopor. Mat.* **2013**, 173, 181-188.
- [81] I. H. Lim, W. Schrader, F. Schüth, *Chem. Mater.* **2015**, 27, 3088-3095.
- [82] J. Cravillon, R. Nayuk, S. Springer, A. Feldhoff, K. Huber, M. Wiebcke, *Chem. Mater.* **2011**, 23, 2130-2141.
- [83] J. M. Chin, E. Y. Chen, A. G. Menon, H. Y. Tan, A. T. S. Hor, M. K. Schreyer, J. Xu, *CrystEngComm* **2013**, 15, 654-657.



# Chapter

# 2

## CONTROL OF INTERPENETRATION OF COPPER-BASED MOFs ON SUPPORTED SURFACES BY ELECTROCHEMICAL SYNTHESIS



This chapter is based on the following publication:

S. Sachdeva, A. Pustovarenko, E. J. R. Sudhölter, F. Kapteijn,  
L. C. P. M. de Smet, J. Gascon

*CrystEngComm*, **2016**, 18, 4018–4022

---

### Abstract

A study of a copper-based metal–organic framework (MOF) synthesized by an electrochemical route is presented. Morphological and adsorption properties of the MOF synthesized as bulk powder and on supported copper surfaces were investigated. Differences in these properties and structural refinement studies indicate that when 4,4',4''-s-triazine-2,4,6-triyl-tribenzoic acid ( $H_3TATB$ ) is used as level of linker interpenetration can be prevented when the structure is grown on a surface.

---

## 2.1 INTRODUCTION

Metal–Organic Frameworks (MOFs) are porous, crystalline materials comprised of metal ions coordinatively linked with organic ligands.<sup>1–3</sup> The high porosity and structural versatility of these materials have attracted research towards many potential applications, including gas separation,<sup>4</sup> gas storage,<sup>5</sup> drug delivery,<sup>6</sup> catalysis<sup>7</sup> and sensing.<sup>8</sup> Some of these applications require MOFs to be grown as thin films<sup>9</sup> with a maximum pore volume available for selective gas interactions.

Another interesting aspect about MOF chemistry lays in the principle of *isorecticular design*, which was introduced by Yaghi.<sup>10</sup> Typically, the first step within this concept involves figuring out the reaction conditions that lead to the formation of a particular tecton with corresponding connectivity. Then control over the formation of similar MOFs becomes possible by simply changing the size of the organic linker while keeping the same connectivity.<sup>11</sup> This can further allow systematic control over pore size and functionality of MOFs. Such a powerful approach has however a number of limitations, the most important being the fact that the use of longer organic linkers may lead to network interpenetration, with the corresponding loss in porosity.<sup>2, 12–13</sup>

In spite of the importance of interpenetration for the final application opportunities of MOFs, only a few studies have been reported on the control of this phenomenon.<sup>13</sup> The general approach in most cases relies on changing reaction conditions,<sup>14</sup> solvent removal<sup>15</sup> or by using a template,<sup>16</sup> while, to the best of our knowledge, only one study deals with the control of interpenetration during surface growth.<sup>17</sup> In this case, interpenetration is suppressed by using liquid-phase epitaxy on an organic template, resulting in a controlled layer-by-layer growth preventing interpenetration.

Over the last few decades, several approaches have been developed for the positioning of MOFs on different surfaces.<sup>18</sup> Pioneered by BASF for the continuous production of MOF crystals,<sup>19</sup> electrochemical synthesis allows the metal salt-free synthesis of MOFs. The principle relies on supplying the metal ion by anodic dissolution to a synthesis solution of the organic linker in an electrolyte. The production of MOF coatings on electrodes is another attractive feature of electrochemistry.<sup>20–23</sup> In previous years we, among others, have demonstrated that it is possible to synthesize high-quality coatings of MOF structures such as HKUST-1 on the surface of Cu electrodes. In short, the high concentration of Cu ions near the surface of the electrode upon application of voltage favors formation of the MOF on the electrode. Recently, we optimized the process in terms of MOF growth over the electrode surface by using a pulsed current for a limited number of cycles.<sup>20</sup>



Building on our previous works on electrochemical synthesis of Cu-based MOFs, we report a simple, fast and controlled way of limiting framework interpenetration in a framework isorecticular with the well-known HKUST-1.

## **2.2 EXPERIMENTAL SECTION**

### **2.2.1 Materials**

All chemicals were purchased from Sigma Aldrich as used as received. The electrode used were made from 99.9% pure copper.

### **2.2.2 Electrochemical synthesis of copper MOFs**

The electrodes were inserted between 2 PTFE plates, which only allowed a small square opening (6.26 mm × 6.26 mm) to be in contact with the synthesis solution. The potentiostat used was an AUTOLAB PGSTAT302N.

#### **2.2.2.1 Synthesis of MOFs as bulk powder**

200 mg of linker ( $\text{H}_3\text{BTC}$  or  $\text{H}_3\text{TATB}$ ) and 25 mg of methyltributylammonium methylsulfate (MTBS) electrolyte were dissolved in 8 mL of 96% ethanol. The solution was mixed in a home-built, Teflon electrochemical cell (~10 mL, see literature<sup>20</sup> for details of larger version of this cell) at either room temperature or 70 °C for high-temperature synthesis with two copper electrodes spaced 2.4 mm apart. Constant current of 1 mA was applied for 10 h to obtain the material in solution. The material was then filtered and washed with ethanol overnight at 75 °C. The material was then filtered again and dried at 100 °C for 2 h.

#### **2.2.2.2 Synthesis of MOFs as surface supported films**

The 100 mg of linker ( $\text{H}_3\text{BTC}$  or  $\text{H}_3\text{TATB}$ ) and 25 mg of electrolyte (MTBS) were dissolved in 8 mL of 96% ethanol. The solution was mixed in the electrochemical cell at room temperature with two electrodes, copper mesh as anode and copper electrode as cathode, which were spaced 2.4 mm apart. Cyclic pulses of 2 mA for 5 s and 0 mA for 5 s (or 1 mA / 5 s and 0 mA / 5 s) were applied for 12 cycles (60 s of current). The meshes were washed with ethanol at room temperature overnight and dried at 100 °C for 2 h.

#### **2.2.2.3 Optimization procedure for surface growth**

3.15 g of  $\text{H}_3\text{BTC}$  and different concentrations of MTBS (155-623 mg, *i.e.* 0.5-2 mmol) were dissolved in 100 mL of 96% ethanol. The solution was mixed in the electrochemical cell at room temperature with two copper electrodes spaced 3 cm apart with a circular opening of 25

mm in contact with solution (area 4.9 cm<sup>2</sup>). Cyclic pulses of 50 mA / 5 s and 0 mA / 5 s were applied to keep the current density constant with other experiments. Different pulse cycles were applied to obtain the crack-free uniform layer. The meshes were washed with ethanol overnight and dried at 100 °C for 2 h.

### 2.2.3 Characterization methods

Scanning Electron Microscopy (SEM) images were obtained with a JEOL JSM 6010LA setup. N<sub>2</sub> and CO<sub>2</sub> sorption analysis were carried out in a Micromeritics instrument Tristar II. The samples were pre-treated before measurement by outgassing under vacuum at a temperature of 393 K for 16 h. The powder X-ray diffraction measurements were performed on a Bruker D8-Advance diffractometer operated in Bragg-Brentano geometry, equipped with a Co-K $\alpha$  source ( $\lambda = 1.78897 \text{ \AA}$ ). The diffraction data for MOFs found in bulk were collected over an angle range from 5° to 62° and for MOFs samples obtained on the electrode surface from 2° to 80° with a step width of 0.02° and scan speed of 0.2°/s.

Rietveld refinement of CuTATB obtained in bulk has been performed with EXPO2014,<sup>24</sup> by which zero offset, scale factor, eight background terms and profile parameters as a PearsonVII function were refined.

## 2.3 RESULTS AND DISCUSSION

In order to investigate the interpenetration process, we performed the electrochemical synthesis of Cu paddlewheel MOFs using benzene-1,3,5-tricarboxylic acid (H<sub>3</sub>BTC) and 4,4',4''-s-triazine-2,4,6-triyl-tribenzoic acid (H<sub>3</sub>TATB) as organic linkers (Fig. A1, Appendix A). The MOFs were synthesized under optimized synthesis conditions by an electrochemical route. Hereafter, these MOFs will be referred as CuBTC and CuTATB respectively. CuBTC is a well-characterized MOF<sup>25</sup> and it has been chosen as reference material as there should be no interpenetration due to the small size of the linker.

The syntheses of CuBTC and CuTATB were carried out in an electrochemical cell in a 96% ethanol solution. Conditions were tuned in such a way that all of these MOFs could be synthesized both as bulk powder and as surface-supported films on copper electrodes. After synthesis, these materials were filtered and washed with ethanol to remove the excess unreacted linker and electrolyte before being dried at 100 °C. In a second step, the electrolyte concentration and the number of current cycles were modified to obtain uniform, crack-free layers on the surface.

The crystalline nature of CuBTC and CuTATB was determined by powder X-ray diffraction with cobalt as X-ray source. The diffraction pattern of synthesized CuBTC was similar to

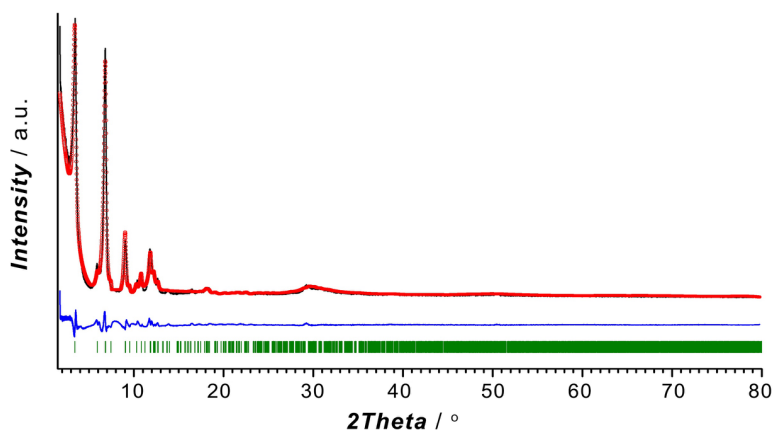


**Figure 2.1.** Rietveld refinement plot for the CuTATB MOF obtained in bulk. The experimental data are presented as black line, the calculated data by red circles and difference as blue line. The Bragg positions of the peaks are represented as green sticks.

patterns simulated from the crystal structure and as reported from the literature (Fig. A2).<sup>20</sup> Known MOF structures built of copper metal centers and  $H_3TATB$  as a linker did not show resemblance with the synthesized CuTATB,<sup>26-27</sup> but resembled a highly interpenetrated polymeric structure based on copper and 4,4',4'',-benzene-1,3,5-triyl-tris(benzoic acid) ( $H_3BTB$ ), reported by Walton *et al.*<sup>28</sup> Furthermore, based on this known CuBTB structure, the isostructurality of CuTATB was confirmed by Rietveld refinement showing only slight differences in the unit cell dimensions (Fig. 2.1 and Table A1).

Thus, the CuTATB framework consists of a 2D polymeric network built from copper paddlewheel units, linked in an alternated manner by the two carboxylate groups of the TATB ligand (Fig. 2.2). One of them is protonated and points out of the 2D polymeric layer, being involved in hydrogen bonding with the parallel-laid network, forming a 3D architecture (Fig. 2.2C). By using simplified building units for this 3D structure (as illustrated in Fig. A4) shows that the network can be described as a 3,4-connected binodal net of **sur** topological type and expressed by a  $(6^2 \cdot 8^2 \cdot 10^2)(6^2 \cdot 8)_2$  Schläfli symbol.<sup>29</sup> Furthermore, the network structure of CuTATB consists of four highly interpenetrated simple nets where each net is symmetry-equivalent and related to other by translations [100] and by inversion (Fig. A5). All the interpenetration nets have the topology of **sur** net and the interpenetration type belongs to a rare class IIIa (for details see Appendix A).<sup>30</sup>

MOF films were synthesized on copper electrode surfaces including copper meshes. Powder XRD patterns for CuTATB coated electrodes exhibits a single detectable reflection at  $2\theta = 6.42^\circ$  that does not match with the sample obtained in bulk (Fig. A6). Additionally, similar

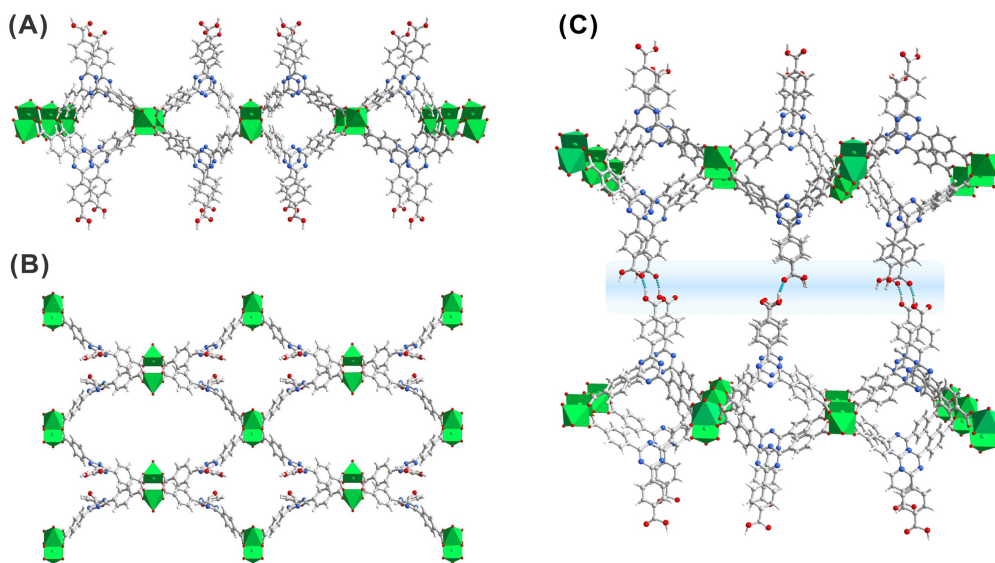


**Figure 2.2.** Two-dimensional framework structure of bulk CuTATB MOF obtained by Rietveld refinement: (A) view along *b*-crystallographic direction and (B) along *a*-axis, and (C) three-dimensional arrangement of 2D-layers expanded via hydrogen bonding (blue region).

patterns were obtained even when the synthesis was carried out with a higher number of cycles. It was observed that during the electrochemical synthesis of CuTATB, a thin layer of MOF was formed on the copper mesh in the first seconds of the synthesis. This further resulted in the formation of islands at various nucleation sites, as reported recently.<sup>31</sup> As the intergrowth of the deposited MOF layer takes place, these islands can detach from the surface. This detachment can also have self-limiting effect on thickness of the deposited layer. Thus, these processes result in layers of similar thickness of MOFs even when the synthesis was carried out with higher number of cycles (up to 200 cycles). In order to identify the structure of the MOF directly grown on the Cu surface, this surface was scratched off and analyzed by PXRD (Fig. A6). A comparison of experimental XRD patterns with simulated ones for CuBTC and CuTATB (here compared to the previously reported PCN-6 MOF)<sup>26</sup> was performed. The reflection at  $2\theta = 6.42^\circ$  corresponds well with the most intense (202) diffraction of the PCN-6 structure (Fig. A6). Correspondingly, the crystal structure of CuTATB consists of a 3D network of the cage-type architecture and possesses large accessible voids (Fig. 2.3A and B).

However, compared to the non-interpenetrated (PCN-6') framework, the free accessible volumes of the cages of the low-interpenetrated form of the PCN-6 structure reduces by a factor of about 1.5,<sup>27</sup> as a result of the interpenetration of two equivalent frameworks (Fig. 2.3C). Following a previously used consideration for the bulk framework simplification (Fig. A4A

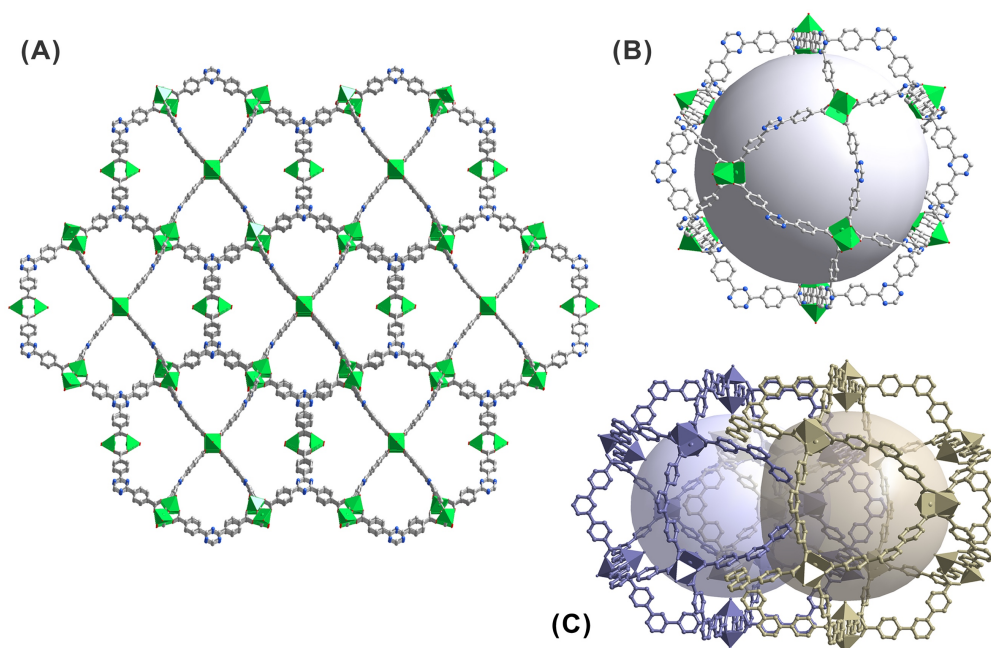


**Figure 2.3.** (A) The 3D framework structure of CuTATB MOF grown on the electrode surface, (B) visualization of the cage of non-interpenetrated CuTATB MOF (PCN-6'), and (C) arrangement of voids within the interpenetrated structure of PCN-6. All structures were obtained based on reported studies.<sup>26-27</sup>

and B), the network of CuTATB grown on the electrode surface (PCN-6) is a 3,4-connected binodal net of twisted boracite topological type (*tbo*) and expressed by a  $(6^2 \cdot 8^2 \cdot 10^2)_3(6^3)_4$  Schläfli symbol.<sup>29</sup> Moreover, the network structure consists of two equivalent symmetry nets, which are interpenetrated (Fig. A8).<sup>30</sup>

Further characterization of these materials was carried out using scanning electron microscopy (SEM). Synthesized powder samples of CuTATB with constant current synthesis showed needle-like structures (Fig. 2.4A and B). The obtained material also showed a wide particle size distribution where the length varied from nanometers to a few micrometers. When the material was synthesized on the supported surfaces, a different morphology of the material was observed. By using a square-wave electrical current for the electrochemical growth of copper-based MOFs, concentration polarization near the surface of the metal electrode can be controlled. This leads to a good MOF coverage on the electrode surface (Fig. 2.4C) due to a fast nucleation process.

To further investigate the differences in the bulk powder MOFs and surface grown MOFs in terms of porosity, gas adsorption studies were performed. The reference CuBTC MOF displayed a similar isotherm and BET area ( $\sim 1300 \text{ m}^2 \cdot \text{g}^{-1}$ ) as reported in the

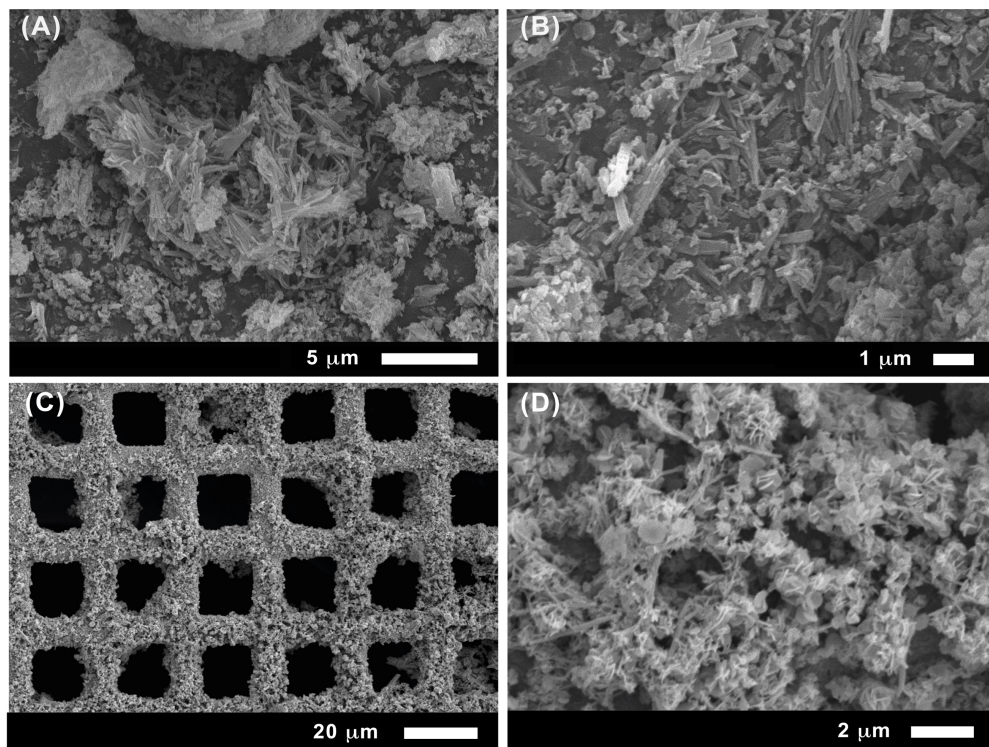


**Figure 2.4.** Scanning electron microscope pictures of CuTATB synthesized as bulk powder (A and B), and grown on a copper mesh (C and D).

literature (Fig. A9).<sup>16</sup> Fig. 2.5A and B shows the  $N_2$  adsorption isotherms at 77 K of CuTATB measured as bulk powder and as a deposited layer on several copper meshes. The isotherm indicates a microporous nature of CuTATB (Fig. 2.5A). The BET area and Langmuir area of CuTATB, calculated from  $N_2$  adsorption isotherm, were found to be approximately  $570 \text{ m}^2\cdot\text{g}^{-1}$  and  $740 \text{ m}^2\cdot\text{g}^{-1}$ , respectively. The porosity of the material was also observed to be close to the reported material with  $H_3\text{BTB}$  synthesized solvothermally.<sup>28</sup> Further, in case of CuTATB, the amount of  $N_2$  adsorbed per mol of copper in the MOF was similar to that of CuBTC (Fig. A9).

In contrast, the  $N_2$  adsorption isotherm of CuTATB deposited on a copper mesh shows a completely different shape (Fig. 2.5B). Even though the exact mass of the deposited material could not be calculated (although roughly estimated by measuring the mass change of electrode), the  $N_2$  adsorption isotherm shows a two-step shape (Fig. 2.5B), indicating a clear difference in the structure of CuTATB synthesized on the surface. This is also supported by the XRD pattern of the MOF on the mesh as discussed earlier (Fig. A6). Further, the cage structure in the molecular network, which arises from controlling interpenetration in the structure, supports the two-step adsorption.

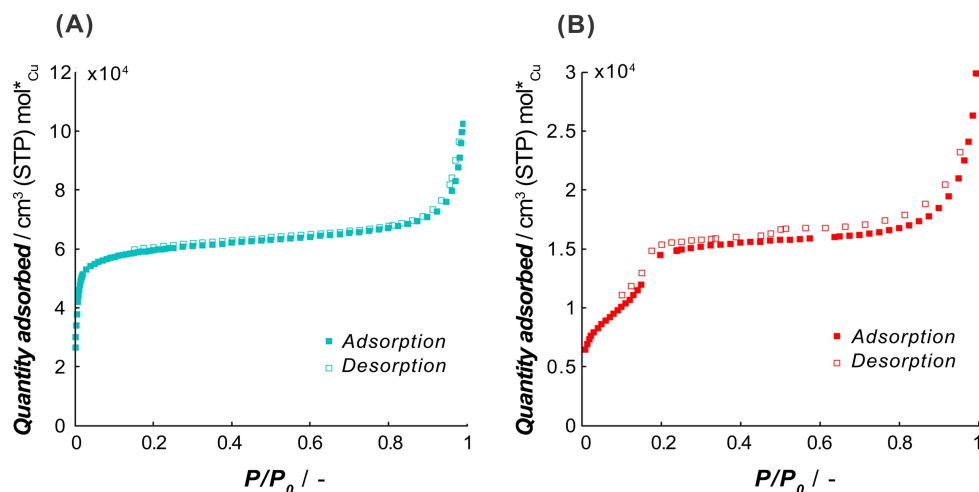


**Figure 2.5.**  $N_2$  sorption isotherms of CuTATB (@ 77 K), synthesized as bulk powder (A) and obtained from multiple electrochemically modified copper meshes (B). \* Quantity adsorbed per mol of Cu in MOF (A) or per mol of Cu in MOF at mesh surface.

The results obtained so far indicate that there are differences in properties of CuTATB on surface growth with respect to the powder samples. This can be attributed to interpenetration in these large linkers in powder form. The interpenetration in these samples can be rationalized by the following. In order to minimize the energy in the larger networks in these MOFs due to bulky linkers (*i.e.*  $H_3TATB$ ), the free void space in the material is filled by the units of the framework, which can lead to interpenetration.<sup>13</sup> This interpenetration also affects the sorption behaviour.<sup>15</sup> A similar two-step behavior for  $N_2$  adsorption as shown in Fig. 2.5 for CuTATB has been reported earlier for other materials as well on the control of interpenetration in the framework.<sup>15, 32</sup> Moreover, other MOFs based on copper metal and  $H_3TATB$  or  $H_3BTB$  as similar organic linker have also shown interpenetration, resulting in materials like PCN-6<sup>26-27</sup> and MOF-14,<sup>10</sup> respectively. Non-interpenetrated alternatives of PCN-6 and MOF-14, PCN-6'<sup>16, 27</sup> and MOF-143<sup>33</sup> were also synthesized by modification of synthesis conditions. It should be noted that the electrochemically synthesized powder MOF did not show any resemblance with these MOFs. That can be attributed to a reduced solubility of the linkers in ethanol. In order to increase the solubility, the synthesis process was also carried out at 70 °C. It resulted in the formation of MOFs with similar properties as the room temperature prepared MOFs.

During the electrochemical synthesis, the generation of a high density of metal ions allows the formation of small crystals that end up in the solution. With the use of a pulsed current, the generation of these copper ions is controlled, which results in the growth of MOF on the surface, as the fast nucleation rate of copper MOFs allows crystallization taking place on the

electrode surface layer. Further, molecular reorientation of organic ligands near the copper surface can modify the morphological and structural characteristics of the formed MOF.<sup>34-35</sup> The controlled generation of copper ions, molecular reorientation of organic ligands near the copper surface and hence the growth kinetics by electrochemical synthesis can affect the interpenetration in the formed MOFs.

### 2.4 CONCLUSIONS

Copper-based metal-organic frameworks (MOFs) were prepared by electrochemical synthesis using an elongated linker with similar geometry to that of benzene 1,3,5-tricarboxylic acid (H<sub>3</sub>BTC). Our results demonstrate clear differences in the properties of the MOF grown in the bulk and the MOF grown on the surface of the electrodes. These differences can be attributed to the observation that growth on the surface decreases the degree of the interpenetration in the MOF network.



## REFERENCES

- [1] M. D. Allendorf, V. Stavila, *CrystEngComm* **2015**, 17, 229-246.
- [2] H. Furukawa, K. E. Cordova, M. O'Keeffe, O. M. Yaghi, *Science* **2013**, 341, 1230444.
- [3] S. L. James, *Chem. Soc. Rev.* **2003**, 32, 276-288.
- [4] T. Rodenas, I. Luz, G. Prieto, B. Seoane, H. Miro, A. Corma, F. Kapteijn, F. X. Llabres i. Xamena, J. Gascon, *Nat. Mater.* **2015**, 14, 48-55.
- [5] L. J. Murray, M. Dinca, J. R. Long, *Chem. Soc. Rev.* **2009**, 38, 1294-1314.
- [6] P. Horcajada, T. Chalati, C. Serre, B. Gillet, C. Sebrie, T. Baati, J. F. Eubank, D. Heurtaux, P. Clayette, C. Kreuz, J.-S. Chang, Y. K. Hwang, V. Marsaud, P.-N. Bories, L. Cynober, S. Gil, G. Ferey, P. Couvreur, R. Gref, *Nat. Mater.* **2010**, 9, 172-178.
- [7] J. Gascon, A. Corma, F. Kapteijn, F. X. Llabrés i Xamena, *ACS Catalysis* **2014**, 4, 361-378.
- [8] L. E. Kreno, K. Leong, O. K. Farha, M. Allendorf, R. P. Van Duyne, J. T. Hupp, *Chem. Rev.* **2012**, 112, 1105-1125.
- [9] A. Bétard, R. A. Fischer, *Chem. Rev.* **2012**, 112, 1055-1083.
- [10] B. Chen, M. Eddaoudi, S. T. Hyde, M. O'Keeffe, O. M. Yaghi, *Science* **2001**, 291, 1021-1023.
- [11] M. G. Goesten, F. Kapteijn, J. Gascon, *CrystEngComm* **2013**, 15, 9249-9257.
- [12] O. M. Yaghi, *Nat. Mater.* **2007**, 6, 92-93.
- [13] H.-L. Jiang, T. A. Makal, H.-C. Zhou, *Coord. Chem. Rev.* **2013**, 257, 2232-2249.
- [14] J. Zhang, L. Wojtas, R. W. Larsen, M. Eddaoudi, M. J. Zaworotko, *J. Am. Chem. Soc.* **2009**, 131, 17040-17041.
- [15] S. B. Choi, H. Furukawa, H. J. Nam, D.-Y. Jung, Y. H. Jhon, A. Walton, D. Book, M. O'Keeffe, O. M. Yaghi, J. Kim, *Angew. Chem., Int. Ed.* **2012**, 51, 8791-8795.
- [16] S. Ma, D. Sun, M. Ambrogio, J. A. Fillinger, S. Parkin, H.-C. Zhou, *J. Am. Chem. Soc.* **2007**, 129, 1858-1859.
- [17] O. Shekhah, H. Wang, M. Paradinas, C. Ocal, B. Schuepbach, A. Terfort, D. Zacher, R. A. Fischer, C. Woell, *Nat. Mater.* **2009**, 8, 481-484.
- [18] P. Falcaro, R. Ricco, C. M. Doherty, K. Liang, A. J. Hill, M. J. Styles, *Chem. Soc. Rev.* **2014**, 43, 5513-5560.
- [19] U. Mueller, M. Schubert, F. Teich, H. Puetter, K. Schierle-Arndt, J. Pastre, *J. Mater. Chem.* **2006**, 16, 626-636.
- [20] A. Martinez Joaristi, J. Juan-Alcañiz, P. Serra-Crespo, F. Kapteijn, J. Gascon, *Cryst. Growth Des.* **2012**, 12, 3489-3498.
- [21] U. Mueller, H. Puetter, M. Hesse, H. Wessel (BASF Aktiengesellschaft, Germany) *Patent WO2005049892A1*, **2005**.
- [22] R. Ameloot, L. Stappers, J. Fransaer, L. Alaerts, B. F. Sels, D. E. De Vos, *Chem. Mater.* **2009**, 21, 2580-2582.
- [23] I. Stassen, M. Styles, T. Van Assche, N. Campagnol, J. Fransaer, J. Denayer, J.-C. Tan, P. Falcaro, D. De Vos, R. Ameloot, *Chem. Mater.* **2015**, 27, 1801-1807.
- [24] A. Altomare, C. Cuocci, C. Giacomazzo, A. Moliterni, R. Rizzi, N. Corriero, A. Falcicchio, *J. Appl. Crystallogr.* **2013**, 46, 1231-1235.
- [25] Chui, Lo, Charmant, Orpen, Williams, *Science* **1999**, 283, 1148-1150.
- [26] D. Sun, S. Ma, Y. Ke, D. J. Collins, H.-C. Zhou, *J. Am. Chem. Soc.* **2006**, 128, 3896-3897.
- [27] J. Kim, S.-T. Yang, S. B. Choi, J. Sim, J. Kim, W.-S. Ahn, *J. Mater. Chem.* **2011**, 21, 3070-3076.

- [28] B. Mu, F. Li, K. S. Walton, *Chem. Commun.* **2009**, 2493-2495.
- [29] V. A. Blatov, A. P. Shevchenko, D. M. Proserpio, *Cryst. Growth Des.* **2014**, 14, 3576-3586.
- [30] I. A. Baburin, V. A. Blatov, L. Carlucci, G. Ciani, D. M. Proserpio, *J. Solid State Chem.* **2005**, 178, 2452-2474.
- [31] N. Campagnol, T. R. C. Van Assche, L. Stappers, J. F. M. Denayer, K. Binnemans, D. E. De Vos, J. Fransaer, *ECS Trans.* **2014**, 61, 25-40.
- [32] S. Bureekaew, H. Sato, R. Matsuda, Y. Kubota, R. Hirose, J. Kim, K. Kato, M. Takata, S. Kitagawa, *Angew. Chem., Int. Ed.* **2010**, 49, 7660-7664.
- [33] H. Furukawa, Y. B. Go, N. Ko, Y. K. Park, F. J. Uribe-Romo, J. Kim, M. O'Keeffe, O. M. Yaghi, *Inorg. Chem.* **2011**, 50, 9147-9152.
- [34] J. V. Barth, J. Weckesser, N. Lin, A. Dmitriev, K. Kern, *Appl. Phys. A: Mater. Sci. Process.* **2003**, 76, 645-652.
- [35] S. Stepanow, T. Strunskus, M. Lingenfelder, A. Dmitriev, H. Spillmann, N. Lin, J. V. Barth, C. Woell, K. Kern, *J. Phys. Chem. B* **2004**, 108, 19392-19397.



## APPENDIX A

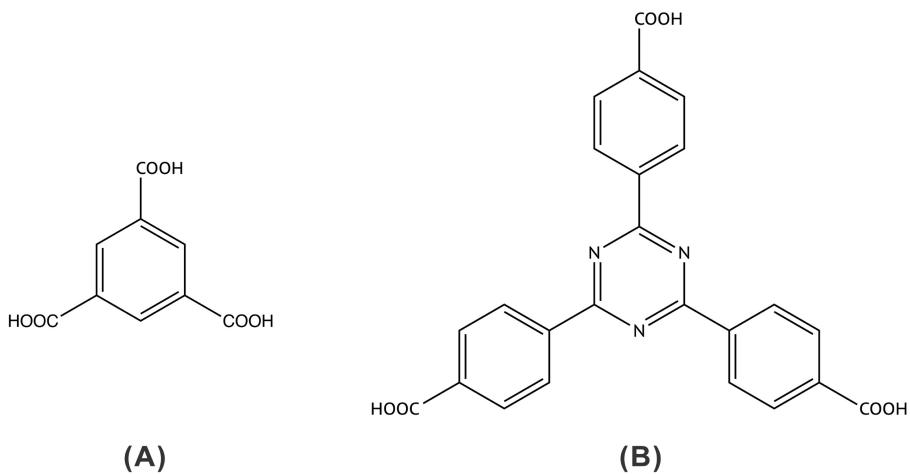


**Figure A1.** Molecular structures of the two linkers used in the study:  $\text{H}_3\text{BTC}$  (A) and  $\text{H}_3\text{TATB}$  (B).

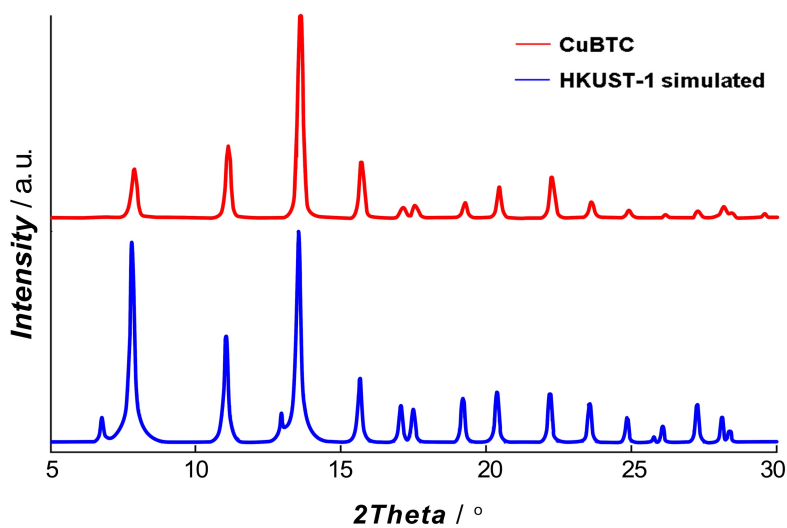


**Figure A2.** Comparison of XRD patterns of CuBTC obtained in bulk (experimental) and HKUST-1 (simulated).

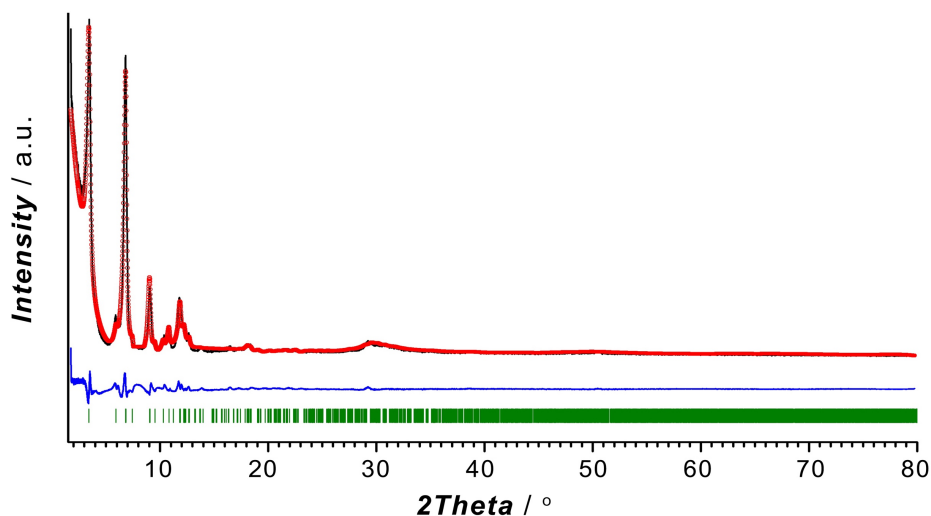


**Figure A3.** Rietveld refinement plot for CuTATB MOF obtained in bulk. The experimental data are presented as black solid line, the calculated data by red circles and difference as blue solid line. The Bragg positions of the peaks are represented as green sticks.

**Table A1.** Unit cell parameters for CuTATB (obtained in bulk) determined by Rietveld refinement of experimental XRD pattern and compared with CuBTB.<sup>A1</sup>

Compound	CuTATB	CuBTB
Formula	C <sub>100</sub> H <sub>57</sub> Cu <sub>4</sub> N <sub>12</sub> O <sub>28</sub>	C <sub>456</sub> H <sub>308</sub> Cu <sub>16</sub> O <sub>142</sub>
FW / g·mol <sup>-1</sup>	2128.78	9075.84
Crystal system	Orthorhombic	Orthorhombic
Space group	<i>Pbcm</i>	<i>Pbcm</i>
<i>a</i> / Å	29.9203(20)	28.0524(17)
<i>b</i> / Å	17.3963(9)	14.8658(9)
<i>c</i> / Å	34.5860(17)	28.7818(18)
<i>a</i> / °	90	90
<i>V</i> / Å <sup>3</sup>	18002.2(10)	12002.6(13)
<i>Z</i>	4	1
<i>R</i> <sub>1</sub> , <sup>i</sup> <i>wR</i> <sub>2</sub> <sup>ii</sup>	9.290, 12.917	–

$$^i R_P = \sum_i |y_{i,0} - y_{i,c}| / \sum_i |y_{i,0}|; ^{ii} R_{wp} = \left[ \sum_i w_i (y_{i,0} - y_{i,c})^2 / \sum_i w_i (y_{i,0})^2 \right]^{1/2}$$

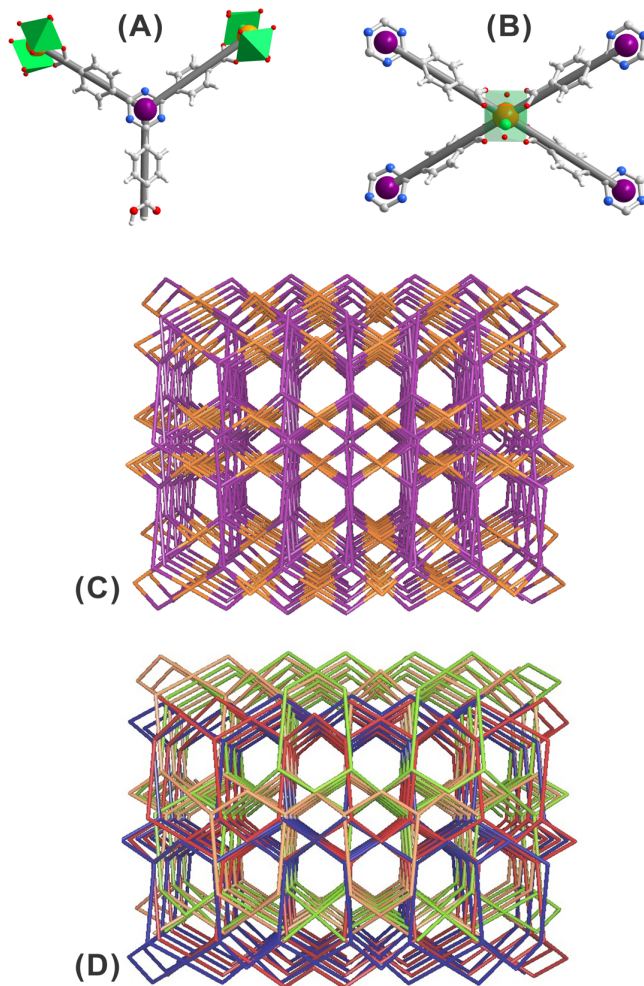


**Figure A4.** Simplification of CuTATB structural units: (A) TATB tripod linker represented as a 3-connected node; (B) paddlewheel copper unit represented as a 4-connected node. (C) Topological view of CuTATB highly interpenetrated net where 3-c nodes of TATB are drawn as violet centers and 4-c nodes of dimeric copper unit as orange centers. (D) The four-component interpenetration in CuTATB polymeric network where each independent polymeric frame is binodal 3,4-connected of *sur* topological type (each independent net is drawn with different color).

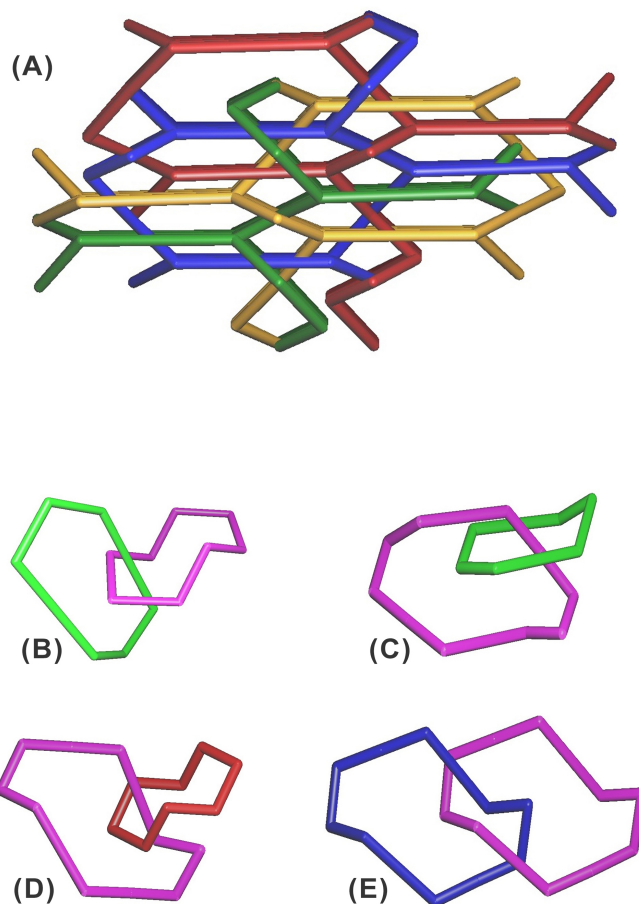


**Figure A5.** (A) Four interpenetrated nets forming array of CuTATB which show four different links (knots) of Hopf type between closed circles: (B) 6-membered (green) and 8-membered (magenta); (C) 8-membered (green) and 8-membered (magenta); (D) 8-membered (red) and 10-membered (magenta); (E) 10-membered (blue) and 10-membered (magenta)

Topological analyses of CuTATB structures have been performed using ToposPro software package.<sup>A2</sup> All the interpenetration nets have the topology of **sur**-type net and the interpenetration type belongs to a rare class IIIa.<sup>A3</sup> As shown in Fig. A5, the interpenetration of four equivalent **sur**-nets realized by four kinds of interwoven rings (Hopf links): six- and eight-membered rings (B); eight- and eight-membered rings (C); ten- and eight-membered rings (D); ten- and ten-membered rings (E).

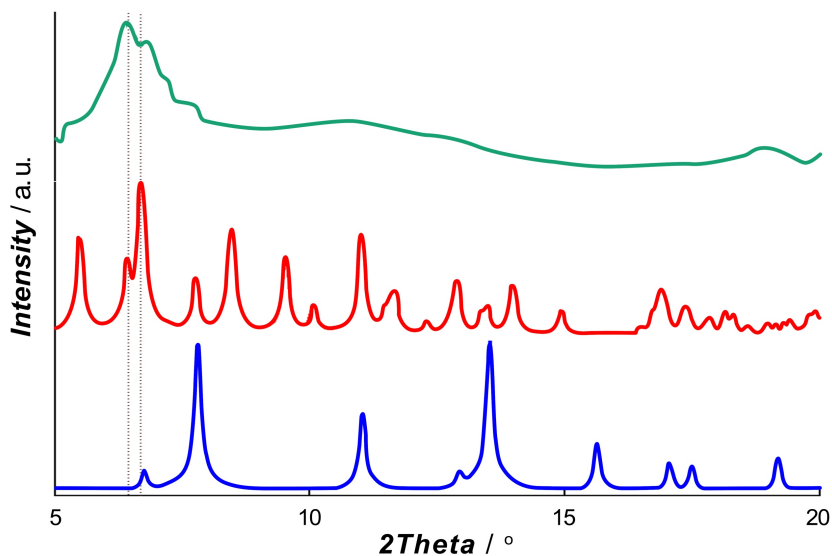


**Figure A6.** Comparison of the pattern of CuTATB scratched from the electrode surface (green) and simulated patterns of PCN-6 structure (red) and HKUST-1 (blue). The dashed lines indicate the most intense peak of the measured diffractogram.

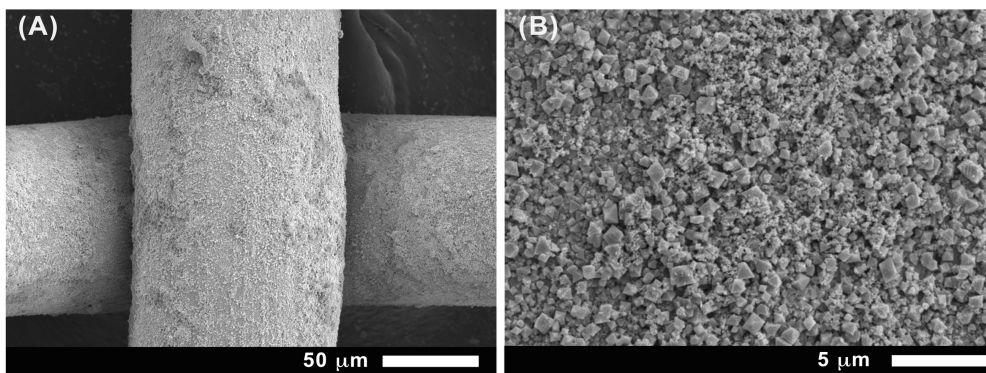


**Figure A7.** SEM micrographs of CuBTC grown on the surface of a copper mesh at different magnifications:  $\times 500$  (A) and  $\times 5000$  (B).



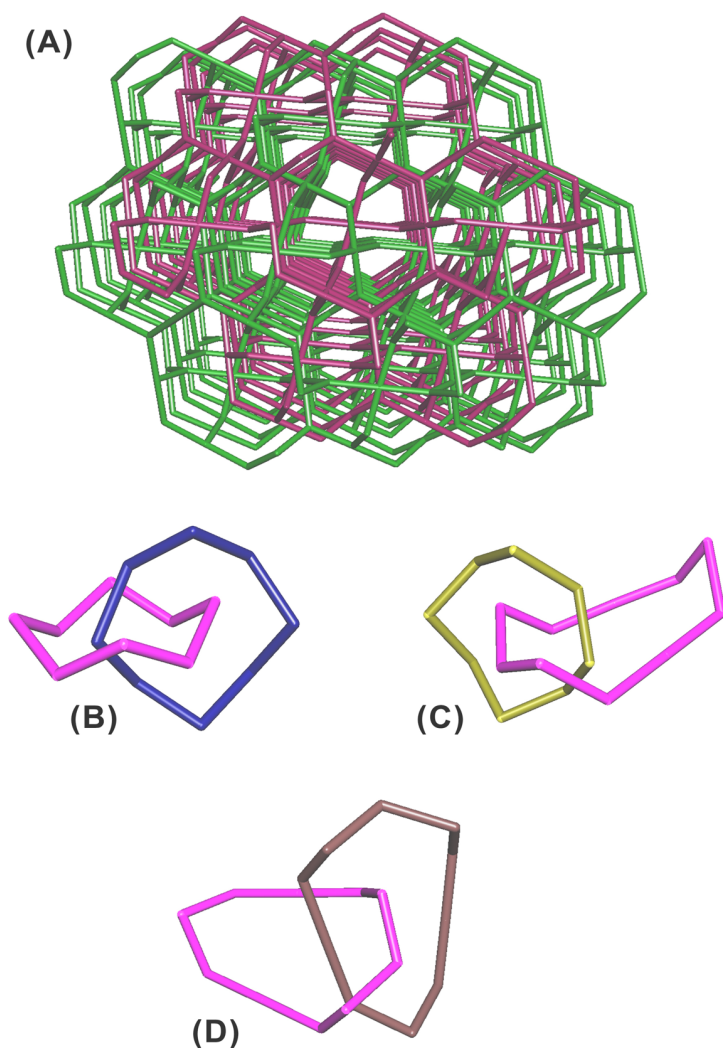


**Figure A8.** (A) Two interpenetrated nets of *tbo*-type forming array of CuTATB, which show three different links (knots) of Hopf type between closed circles: (B) 8-membered (blue) and 8-membered (magenta); (C) 8-membered (yellow) and 10-membered (magenta); (D) 10-membered (brown) and 10-membered (magenta).

Topological analysis of CuTATB structure grown on the electrode surface has been performed using ToposPro software package.<sup>A2</sup> All the interpenetration nets have the topology of *tbo*-type net and the interpenetration type belongs to a class IIa.<sup>A3</sup> As shown in Fig. A8, the interpenetration of two equivalent *tbo*-nets realized by three kinds of interweaved rings (Hopf links): eight- and eight-membered rings (B); eight- and ten-membered rings (C); ten- and ten-membered rings (D).

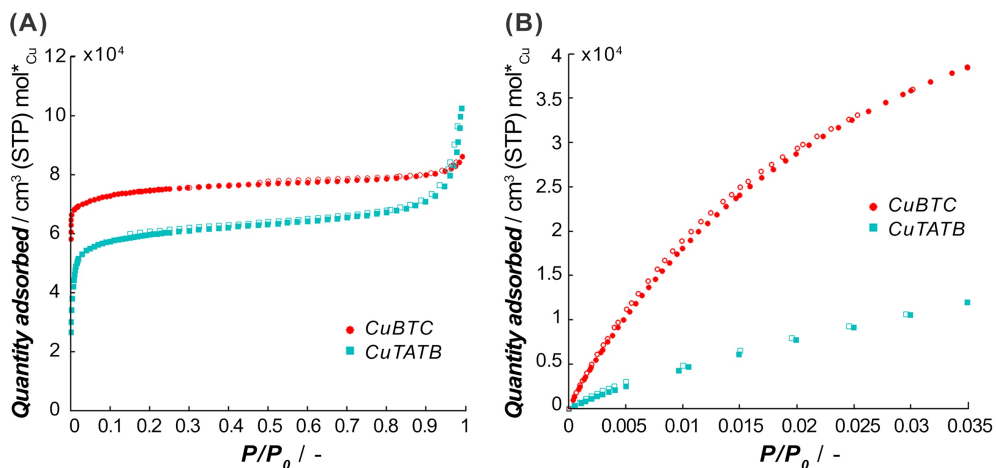


**Figure A9.** (A)  $N_2$  sorption isotherm (at 77 K) of CuBTC (red) and CuTATB (blue) synthesized as bulk powder. (B)  $CO_2$  sorption isotherm of bulk CuBTC (red) and CuTATB (blue) measured at 273 K. Solid symbols represent adsorption branch and open symbols desorption branch.

## REFERENCES

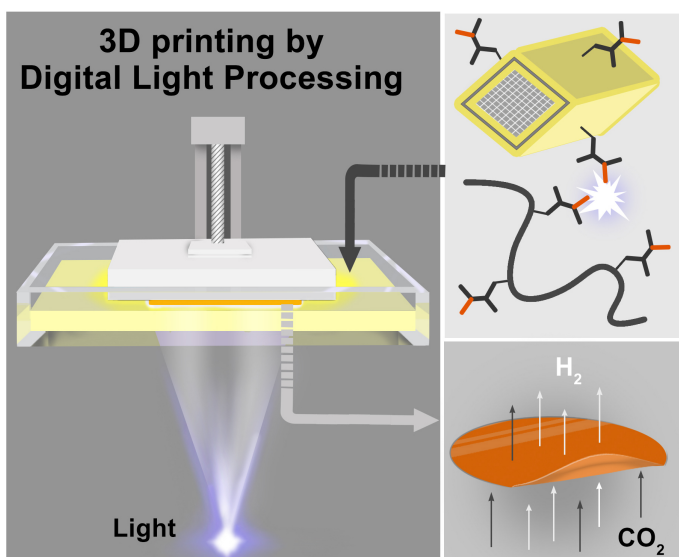
- [A1] B. Mu, F. Li, K. S. Walton, *Chem. Commun.* **2009**, 2493-2495.
- [A2] V. A. Blatov, A. P. Shevchenko, D. M. Proserpio, *Cryst. Growth Des.* **2014**, *14*, 3576-3586.
- [A3] I. A. Baburin, V. A. Blatov, L. Carlucci, G. Ciani, D. M. Proserpio, *J. Solid State Chem.* **2005**, *178*, 2452-2474.



# RAPID FABRICATION OF MOF-BASED MIXED MATRIX MEMBRANES THROUGH A 3D PRINTING BY DIGITAL LIGHT PROCESSING

## Chapter

## 3



This chapter is based on the following publication:

A. Pustovarenko, B. Seoane, E. Abou-Hamad, H. E. King, B. M. Weckhuysen, F. Kapteijn, J. Gascon

(in preparation)

---

### Abstract

3D printing, also known as additive manufacturing technology, has greatly expanded across multiple sectors of technology replacing classical manufacturing methods by combining processing speed and high precision. The scientific interest in this technology lies in the ability to create solid architectures with customized shapes and predetermined properties through exploration of formulations enriched with multifunctional microporous additives such as metal-organic frameworks (MOFs). The concept of additive manufacturing involving advanced materials could be fruitfully adapted for MOF-based mixed matrix membranes fabrication to be used in gas separation applications. In this work, we explore a digital light processing (DLP) approach for fast prototyping of MOF-based mixed matrix membranes (MOF-MMMs) with full control over the shape, size and thickness of the resulting composite using a conventionally available 3D printer. MOF-based printable inks have been formulated from a selection of commercially available acrylate oligomers and MIL-53(Al)-NH<sub>2</sub> additive post-synthetically modified with methacrylic functionality. The formulations and resulting composites have been extensively characterized to demonstrate the suitability of the inks for DLP processing into free-standing MOF-based membranes. The MOF filler anchored to the polymeric matrix enhances the overall permeability at constant selectivity when applied for H<sub>2</sub>/CO<sub>2</sub> separation. The obtained results confirm the applicability of the 3D DLP technology for fast prototyping of MOF-based MMMs and provide new opportunities for further development.

---

### 3.1 INTRODUCTION

3D printing technology is a rapidly developing field.<sup>1-4</sup> Nowadays, the fast prototyping is slowly displacing classical manufacturing methods for advanced materials, offering relative operational simplicity and the ability to render a customized product at high speeds and with high precision.<sup>5</sup> Bridging the gap between fast prototyping and functionality, additive manufacturing is a very interesting playground for the development of formulations that can enable fabrication of complex forms of matter with specific properties on demand.<sup>6-7</sup>

To amplify and broaden the applicability prospects of additive compositions, the incorporation of multifunctional components such as microporous solids can be considered to endow the additive formulations with additional properties.<sup>8-9</sup> From this perspective, metal-organic frameworks (MOFs) are promising filler candidates.<sup>10,11-15</sup>

Conceptually, the integration of a MOF component into additive formulations has been approached and then realized through different 3D printing techniques<sup>4</sup> – inkjet,<sup>16-17</sup> direct ink writing (DIW),<sup>18-27</sup> fused deposition modelling (FDM),<sup>28-30</sup> digital light processing (DLP)<sup>31</sup> and selective laser sintering (SLS).<sup>32-33</sup> For instance, photoluminescent lanthanide MOFs-based inks for inkjet printing were reported by da Luz *et al.*<sup>16</sup> In addition to examples of MOF coatings grown on 3D printed objects obtained by stereolithography (SLA)<sup>34</sup> or direct ink writing,<sup>24</sup> fabrication of monoliths with full integration of the MOF component within a melting matrix of acrylonitrile butadiene styrene (ABS),<sup>28-29</sup> poly(lactic acid) (PLA) or polyurethane (TPU) thermoplastics<sup>30</sup> have been achieved using fused deposition modelling. However, the FDM processable MOF/thermoplastic composites frequently suffer from a porosity loss that questions their further applicability.<sup>28</sup> Unlike in the FDM approach, firm monoliths with accessible internal porosity, suitable for applications involving adsorption, have been obtained via direct ink writing. Moreover, several representative examples of composites with high MOF loading<sup>22</sup> suitable for gas separation,<sup>18,20-21</sup> catalysis,<sup>26</sup> molecule sequestration and release have been reported.<sup>19,25</sup> Similarly, tailored shapes with high MOF contents<sup>32</sup> can be fabricated by means of selective laser sintering into self-standing MOF–polymer mixed matrix films.<sup>33</sup>

From the perspective of using 3D printable MOF-containing additives for gas separation and, particularly, for fast prototyping of MOF-based mixed matrix membranes (MOF-MMMs), the digital light processing (DLP) technique deserves particular attention. DLP printing proceeds through solidification of liquid resins by photoinduced crosslinking on locally illuminated areas, reproducing in this way a 3D shape in a stepwise manner (layer by layer). Thus, the process not only affords fast prototyping but also endows a control over resolution – thickness of the layer, which is an important aspect to consider while dealing with mixed matrix membranes. Building on Halevi *et al.*'s<sup>31</sup> work on DLP processing of a MOF/acrylate

admixture into 3D printed shapes and an early study of Zhang *et al.*<sup>35</sup> on copolymerization between post-synthetically functionalized with methyl methacrylate UiO-66-NH<sub>2</sub> particles and an acrylate monomer, we are targeting to adapt the previous contributions for a fast prototyping of MOF-based mixed matrix membranes (MOF-MMMs).

Herein, we explore a digital light processing (DLP) technology for fast prototyping of MOF-based mixed matrix membranes (MOF-MMMs). With this approach, MIL-53(Al)-NH<sub>2</sub> nanoparticles post-synthetically functionalized with a methacrylic moiety could be covalently integrated within a photopolymerizable matrix of commercially available acrylic oligomers for further fabrication of MOF-MMMs with controllable thickness and tailored shape just in a matter of minutes without the need of additional solvents or long post-synthetic treatment. Given the fact that DLP 3D printing technique involving MOF-based inks are currently poorly represented whilst the approach offers a range of attractive benefits such as rapidness of prototyping with no molds and solvents engaged in, herein we critically evaluate aspects relevant for DLP processing of several acrylate systems with and without MOF-additive into membranes aimed to be applied for separation of equimolar H<sub>2</sub>/CO<sub>2</sub> mixture.

## 3.2 EXPERIMENTAL SECTION

### 3.2.1 Materials

Aluminum nitrate nonahydrate (Al(NO<sub>3</sub>)<sub>3</sub>·9H<sub>2</sub>O, 99.997% trace metals basis), sodium hydroxide (NaOH, pellets), 2-aminoterephthalic acid (2-ATA, 99%), *N,N*-dimethylformamide (DMF, >99.8%), methacrylic anhydride (MMA, 94%), phenyl-bis(2,4,6-trimethylbenzoyl)phosphine oxide (Irgacure<sup>®</sup>-819, 97%), tetrahydrofuran (THF), chloroform (CHCl<sub>3</sub>) were purchased from Sigma-Aldrich. Methanol was supplied by VWR Chemicals (≥99.8% ACS). Ethoxylated-4-bisphenol-A-dimethacrylate (SR540), aliphatic urethane dimethacrylate (CN1963), trimethylolpropane trimethacrylate (SR350D) and amine-modified polyether acrylate (CN501) from Sartomer were kindly provided by Arkema.

### 3.2.2 Syntheses and protocols

#### 3.2.2.1 Synthesis of MIL-53(Al)-NH<sub>2</sub> nanoparticles

Nanoparticles of MIL-53(Al)-NH<sub>2</sub> were synthesized following a previously reported protocol,<sup>36</sup> where 1.90 g of 2-aminoterephthalic acid (10.50 mmol) was dissolved in 10.5 mL aqueous 2 M NaOH solution at room temperature. Afterwards, 6.11 g Al(NO<sub>3</sub>)<sub>3</sub>·9H<sub>2</sub>O (16.30 mmol) dissolved in 64.5 mL deionized water was added to the previous solution and the resulting mixture was magnetically stirred for 15 min. Then the reactant mixture was refluxed for 3 d without stirring resulting in a yellow product that was filtered under vacuum.

### 3.2.2.2 Post-synthetic modification of MIL-53(Al)-NH<sub>2</sub> with methacrylate functionality

Post-synthetic modification of MIL-53(Al)-NH<sub>2</sub> nanoparticles with photocrosslinkable functional groups was achieved through acylation of -NH<sub>2</sub> with methacrylic anhydride following a procedure adapted from previous works.<sup>35,37</sup> In a typical experiment, 300 mg dry MIL-53(Al)-NH<sub>2</sub> powder was transferred into a two-neck flask equipped with a condenser and a magnetic stirring bar and filled in with nitrogen gas using a Schlenk line. Then the powder was suspended in 20.0 mL of CHCl<sub>3</sub> and 1.0 mL methyl methacrylic (MMA) anhydride was added to the stirring mixture under a nitrogen atmosphere. The temperature of the reaction mixture was raised to 80 °C and left to react for 10 h. Afterwards, the suspension was cooled down and the resulting solid MIL-53(Al)-NH<sub>2</sub>/MMA was washed several times with CHCl<sub>3</sub>. The suspension was then dried under reduced pressure at 80 °C for 5 h after which it was activated by washing with *N,N*-dimethylformamide at 130 °C, and subsequently with methanol under reflux, both overnight. Finally, the powder was thoroughly washed twice with ethanol, dried at 100 °C under vacuum and stored in a glovebox for further experiments.

### 3.2.2.3 Photocurable ink formulation for the DLP process

DLP printable inks were prepared by admixing a certain mass of individual photocurable oligomers (Fig. B1), *i.e.* ethoxylated-4-bisphenol-A-dimethacrylate (**E**-component, SR540), aliphatic urethane dimethacrylate (**U**-component, CN1963), trimethylolpropane trimethacrylate (**T**-component, SR350D), amine modified polyether acrylate (**P**-component, CN501), and their mixtures with photoinitiator Irgacure<sup>®</sup>-819 (Fig. B2). For MOF-based ink variations, MIL-53(Al)-NH<sub>2</sub>/MMA PSM nanoparticles were admixed with commercial acrylate-based component (**E**-, **U**-, **T**-, **P**-oligomers) or a mixture of the components along with Irgacure<sup>®</sup>-819 photoinitiator in a mass proportion according to Table B1. Typically, photocurable MOF based formulations containing 12 wt.% of MIL-53(Al)-NH<sub>2</sub>/MMA were prepared by mixing the components and stirring for 20-30 min to reach stable suspensions. Afterwards the heterogeneous mixture was poured into the resin vat of a 3D printer.

### 3.2.2.4 3D printing of polyacrylate membranes

All printed materials were prepared using a Kudo3D model Titan 2 printer operating in a digital light processing (DLP) mode (Table B2, Figs. B3-B4) with parameter settings detailed in Table B4 (Appendix B). Spectral irradiance of the 3D printer light source was measured with an AvaSpec-3648-2-USB2 probe from Avantes (Fig. B5, Table B3). The printed membranes



were detached from the build platform, washed with isopropanol to remove remaining unpolymerized ink and dried at 80 °C for 1 h in a conventional oven.

### 3.2.3 Characterization methods

#### 3.2.3.1 Determination of crosslinking degree and methacrylic group conversion

The degree of crosslinking was determined following the Soxhlet extraction method detailed in ASTM with some adaptations.<sup>38</sup> According to this method, several specimens were cut from different segments of each photopolymerized membrane and weighed to determine the initial mass ( $m_i$ ), then the specimen was divided into smaller 0.5 cm × 0.5 cm pieces and soaked in tetrahydrofuran (THF) at room temperature for 24 h. As the photocurable precursors are soluble in THF, a non-crosslinked fraction of oligomers is expected to be removed from the composite leaving the crosslinked polymer matrix. Consequently, the remaining solid fraction was dried up at 80 °C for 24 h and weighted to determine its residual weight ( $m_f$ ). The degree of crosslinking (DC) was calculated as follows:

$$\text{Degree of crosslinking (DC, \%)} = \frac{m_f}{m_i} \cdot 100\% \quad (\text{eq. 3.1})$$

Methacrylic group conversion was followed by attenuated total reflection-Fourier transform infrared (ATR-FTIR) real-time measurements to evaluate the kinetics of cross-linking and to quantitatively express the degree of conversion in each studied ink formulation. The degree of methacrylic group conversion was derived from the intensity of the methacrylate group absorption centered at  $\sim 1640 \text{ cm}^{-1}$  and calculated according to the following equation:

$$\text{MMA conversion } (X_{\text{MMA}}, \%) = \left(1 - \frac{A_t}{A_i}\right) \cdot 100\% \quad (\text{eq. 3.2})$$

where  $A_t$  and  $A_i$  were the areas of the methacrylate group absorption in the beginning and at the moment  $t$  of exposure to the light, respectively.

#### 3.2.3.2 General characterization

Scanning Powder X-ray diffraction (PXRD) patterns were acquired on a Bruker D8 Advance operated with monochromatic  $\text{Cu-K}\alpha$  ( $\lambda = 1.5418 \text{ \AA}$ ) radiation with a scan speed of 0.5 s per step and a step size of  $0.1^\circ$  over the  $5\text{--}60^\circ$   $2\theta$  range.

*Physisorption* isotherms using nitrogen and argon gas probes were carried out at 77 K and at 87 K, respectively, using a Micromeritics ASAP 2040 instrument. Carbon dioxide physisorption isotherms were recorded in a Tristar II 3020 at 273 K. Before the measurement, composite samples were degassed at 150 °C for 8 h. The uptake measurements for MIL-53(Al)-

NH<sub>2</sub> and MIL-53(Al)-NH<sub>2</sub>/MMA were conducted on activated sample treated according to the well-known procedure described elsewhere.<sup>36,39–40</sup>

*Thermogravimetric data* (TG) were collected in nitrogen and air atmospheres using a Mettler-Toledo thermal analyzer at a heating rate of 5 °C·min<sup>-1</sup> in a 25–800 °C temperature range with a gas flow of 25 mL·min<sup>-1</sup>.

*Differential scanning calorimetry* (DSC) tests were carried out on Mettler-Toledo TGA/DSC1 Star system by heating 5–10 mg of each sample under nitrogen flow (50 mL·min<sup>-1</sup>) from 40 up to 230 °C applying a heating rate of 10 °C·min<sup>-1</sup> and cooling rate of 5 °C·min<sup>-1</sup>. Three consecutive runs were performed. The first cycle was intended to remove any previous thermal history of the samples. Two following cycles were performed using the same protocol.

*Transmission electron microscopy* (TEM) images were recorded on a JEOL JEM-2100F microscope operated at 120 kV and equipped with a field emission gun (FEG). The samples were dispersed in methanol, sonicated and sprayed on a carbon-coated copper grid and air dried.

*Scanning electron microscopy* (SEM) imaging was performed in a FEI TENE0 VS microscope equipped with an integrated SDD EDX detector. Photocured samples were mounted on a 45°/90° holder with help of double-sided carbon tape and grounded with strokes of conductive silver paint. For a cross-section evaluation, printed films were cryo-fractured in liquid nitrogen. FIB-SEM cross-section studies were carried out on Helios Nanolab 600 FIB.

*Solid-State Nuclear Magnetic Resonance (ssNMR) Spectroscopy.* One-dimensional <sup>1</sup>H MAS and <sup>13</sup>C CP/MAS solid state NMR spectra were recorded on Bruker AVANCE III spectrometers operating at 400 or 600 MHz resonance frequencies for <sup>1</sup>H. Experiments at 400 MHz employed a conventional double-resonance 4 mm CP/MAS probe, while experiments at 600 MHz utilized a 3.2 mm double-resonance probe. NMR chemical shifts are reported with respect to the external references TMS and adamantane. For <sup>13</sup>C CP/MAS NMR experiments, the following sequence was used: 90° pulse on the proton (pulse length 2.4 s), then a cross-polarization step with a contact time of typically 2 ms, and finally acquisition of the <sup>13</sup>C signal under high-power proton decoupling. The delay between the scans was set to 5 s to allow the complete relaxation of the <sup>1</sup>H nuclei, and the number of scans ranged between 10000 and 20000 for <sup>13</sup>C and was 32 for <sup>1</sup>H. An exponential apodization function corresponding to a line broadening of 80 Hz was applied prior to Fourier transformation.

The 2D <sup>1</sup>H–<sup>13</sup>C heteronuclear correlation (HETCOR) solid state NMR spectroscopy experiments were conducted on a Bruker AVANCE III spectrometer using a 3.2 mm MAS probe. The experiments were performed according to the following scheme: 90° proton pulse, *t*<sub>1</sub> evolution period, CP to <sup>13</sup>C, and detection of the <sup>13</sup>C magnetization under TPPM decoupling.

For the cross-polarization step, a ramped radio frequency (RF) field centered at 75 kHz was applied to the protons, while the  $^{13}\text{C}$  channel RF field was matched to obtain an optimal signal. A total of 64  $t_1$  increments with 2000 scans each were collected. The sample spinning frequency was 15 kHz. Using a contact time of 0.2 ms for the CP step, the polarization transfer in the dipolar correlation experiment was verified to be selective for the first coordination sphere ( $< 5 \text{ \AA}$ ).

*Dynamic Nuclear Polarization (DNP) NMR spectroscopy.* TEKPol was dried under high vacuum ( $10^{-4}$  mbar) and the solvents were stirred over calcium hydride and then distilled in vacuo. A radical solution consisting of 16 mM TEKPol (TEKPol,  $\text{MW} = 905 \text{ g}\cdot\text{mol}^{-1}$ ) in 1,1,2,2-tetrachloroethane (TCE) was used. The compounds and the corresponding nitrides synthesized were finely ground in a mortar and pestle prior to preparation of DNP experiments. DNP samples were then prepared by incipient wetness impregnation. In a typical experiment, 15 mg of the samples were impregnated with the appropriate volume of 16 mM solution of TEKPol ( $n\text{TEKPol} = 0.5 - 1.2 \text{ }\mu\text{mol/sample}$ ) and packed into a 3.2 mm (o.d.) sapphire rotor capped with a teflon plug. The packed samples were then immediately inserted into the pre-cooled DNP probe for experiments. Data were acquired using 263 GHz/400 MHz Avance III Bruker DNP solid-state NMR spectrometer equipped with a 3.2 mm Bruker triple resonance low temperature magic angle spinning (LTMAS) probe and the experiments were performed at ca. 100 K with a 263 GHz gyrotron. The sweep coil of the main magnetic field was set for the microwave irradiation occurring at the  $^1\text{H}$  positive enhancement maximum of the TEKPol biradical. For the  $^{15}\text{N}$  CP-MAS DNP experiments, the acquisition parameters included a 3 s repetition delay and a  $^1\text{H}$   $\pi/2$  pulse length of 2.3  $\mu\text{s}$  to afford 100 kHz  $^1\text{H}$  decoupling using the SPINAL 64 method. The contact time was typically 4 ms for the cross-polarization experiments. The MAS frequency varied between 8 and 12 kHz. The 2D  $^1\text{H}$ - $^{15}\text{N}$  HETCOR spectra were acquired with 2048 scans per  $t_1$  increment, 96 individual increments, and a contact time of 4 ms. During  $t_1$ , e-DUMBO-1 homonuclear  $^1\text{H}$  decoupling was applied, and the proton chemical shifts were corrected by applying a scaling factor of 0.57.

*Liquid state nuclear magnetic resonance* experiments were performed in a Bruker Avance-400. In the digestion experiment, 10 mg of MIL-53(Al)- $\text{NH}_2$ /MMA was dissolved in mixture of DMSO- $d_6$  / HF resulting in a clear solution.

*Attenuated total reflection (ATR) Fourier-transformed infrared spectroscopy (FTIR)* analyses were performed on a home-built setup that included a Nicolet 8700 FTIR spectrometer equipped with a Harrick Horizon multiple internal reflections accessory, coupled to a cell containing a ZnSe crystal. The photocurable ink formulations were layered on the top of the ZnSe crystal and illuminated by an ACER H5360 LED DLP projector. To observe the

spectral changes during the photopolymerization process, real-time ATR spectra were recorded in the range of 2000–1000  $\text{cm}^{-1}$  in 1.93 s intervals. The spectral resolution was 4  $\text{cm}^{-1}$  and 1 scan per time interval was used to achieve the maximum time resolution.

*Raman spectroscopy* studies were performed on a WITec alpha 300R Raman microscope operated with 532 nm laser (14 mW). 2D maps of the 3D printed object surface were acquired on 30  $\mu\text{m} \times 30 \mu\text{m}$  area advancing with 1  $\mu\text{m}$  step size along each of x, y directions.

*The stress–strain data* was collected using a Zwick Roell tensile testing machine at room temperature. UV polymerized samples were prepared in molds in form of 55  $\times$  5  $\times$  3 mm blocks and all tested with 150  $\text{mN}\cdot\text{min}^{-1}$  loading rate applied.

*Optic microscope* Leica DM750 equipped with HI Plan EPI 5/10/20/50 $\times$  objectives and a rotating diascopic polarizer was used to capture images of 3D printed objects in bright and dark fields.

### 3.2.4 Gas permeation measurements

Photocured rounded membranes with an area of 0.2  $\text{cm}^2$  were mounted in a flange between Viton<sup>®</sup> O-rings and placed inside an oven in a home-made permeation setup. The  $\text{H}_2/\text{CO}_2$  separation measurements were performed employing an equimolar  $\text{H}_2:\text{CO}_2$  gas mixture (20  $\text{mL}\cdot\text{min}^{-1}$   $\text{CO}_2$  and 20  $\text{mL}\cdot\text{min}^{-1}$   $\text{H}_2$ ) feed. Helium (2.0  $\text{mL}\cdot\text{min}^{-1}$ ) was used as a sweep gas at the permeate side. The absolute pressure of the feed stream was adjusted in a range of 1–2 bar using a back-pressure controller at the retentate side, keeping the permeate side at atmospheric pressure. The temperature in the permeation module was adjusted from room temperature to 100  $^\circ\text{C}$  through a convection oven. An on-line gas chromatograph (Interscience Compact GC) equipped with a packed Carboxen 1010 PLOT (30 m  $\times$  0.32 mm) column and TCD detector was used to periodically analyze the permeate stream.

The permeance of component  $j$  ( $P_j$ ) was calculated as follows:

$$P_j = \frac{\varphi_{n,j} \cdot \delta}{\Delta p_j \cdot A} \quad (\text{eq. 3.3})$$

where  $\varphi_{n,j}$  denotes the molar flow rate of component  $j$ ,  $\delta$  is the thickness of the membrane,  $\Delta p_j$  the partial pressure difference of component  $j$  across the membrane and  $A$  the membrane area.

The SI unit for the permeability is  $\text{mol}\cdot\text{s}^{-1}\cdot\text{m}^{-1}\cdot\text{Pa}^{-1}$ . However, here gas permeabilities are reported in the widely used non-SI unit Barrer, where 1 Barrer =  $3.35\cdot 10^{-16} \text{ mol}\cdot\text{m}\cdot\text{m}^{-2}\cdot\text{Pa}^{-1}\cdot\text{s}^{-1}$ .

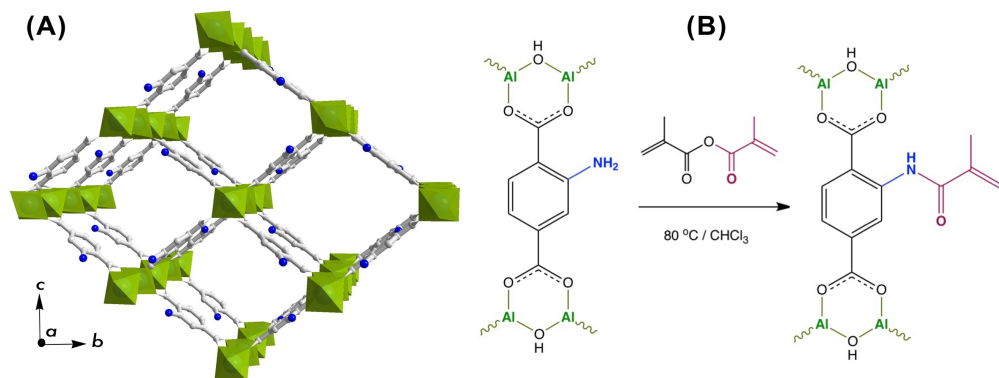


**Figure 3.1.** (A) Representation of MIL-53(Al)-NH<sub>2</sub> structure in the open pore configuration, where AlO<sub>6</sub> polyhedra are depicted in green, and grey and navy are carbon and nitrogen atoms, respectively. (B) Scheme of post-synthetic modification of MIL-53(Al)-NH<sub>2</sub> structure with methyl methacrylic anhydride.

The separation factor or mixed gas selectivity ( $\alpha$ ) was calculated as the ratio of the permeance of the faster permeating component (H<sub>2</sub>) to the permeance of the less permeable component (CO<sub>2</sub>) as given below:

$$\alpha = \frac{P_{H_2}}{P_{CO_2}} \quad (eq. 3.4)$$

### 3.3 RESULTS AND DISCUSSION

MIL-53(Al)-NH<sub>2</sub> framework is a MOF widely used for gas storage and separation purposes and reported to demonstrate remarkable performance when incorporated as a filler into mixed matrix membranes (MMMs).<sup>36,40</sup> In particular, the presence of NH<sub>2</sub>-groups endows this framework with diverse functionalization opportunities (Fig. 3.1A).<sup>41</sup> Thus, the amino groups were brought into play to introduce a photocrosslinkable functionality to MIL-53(Al)-NH<sub>2</sub> particles with the aim to improve its processability and integrability into DLP UV-curable inks.

To meet the requirements for an effective integrability into a polymer matrix, MIL-53(Al)-NH<sub>2</sub> material was synthesized in the form of nanoparticles with dimensions of about 30 – 100 nm (Figs. B6-B7). The post-synthetic functionalization was made on non-activated MOF to assure a restricted accessibility of the porous system and to favor preferential attachment to NH<sub>2</sub>-groups on the surface. Hence, as-synthesized MIL-53(Al)-NH<sub>2</sub> was post-synthetically modified (PSM) through an acylation reaction with a methyl methacrylic anhydride (Fig. 3.1B). Such modification leads to the framework transformation from *np*- to *lp*-conformation,<sup>42</sup> as suggested by Figure 3.2A. The latter can be attributed to a partial anchoring of NH<sub>2</sub>-groups

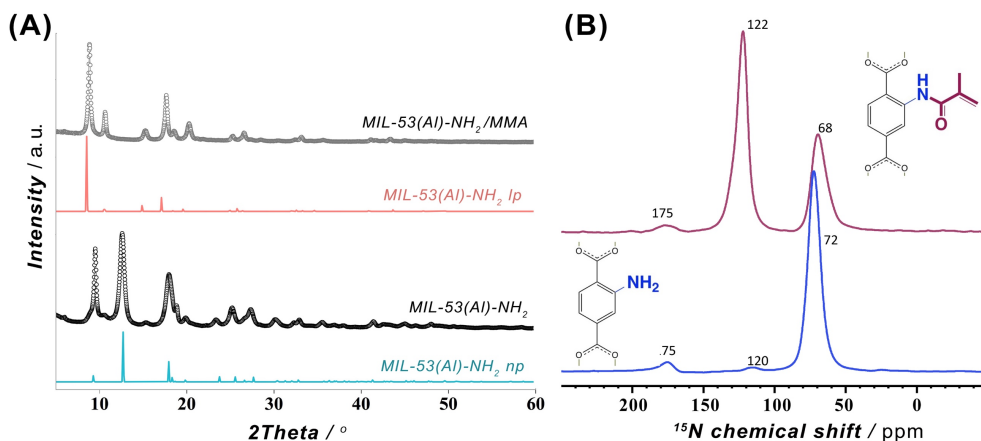


**Figure 3.2.** (A) Powder XRD patterns of MIL-53(Al)-NH<sub>2</sub> nanoparticles before (black) and after (grey) post-synthetic modification with MMA and compared to open (*lp*) and narrow pore (*np*) forms. (B) Solid-state DNP enhanced <sup>15</sup>N NMR spectrum for MIL-53(Al)-NH<sub>2</sub> before (blue) and after (wine) post-synthetic modification with MMA.

inside the pores of the MOF in addition to modifications occurring on the surface of the particles. Thus, the incorporation of a bulky MMA group in the pore space forces the framework to adopt the *lp*-configuration, in good agreement with previous reports on PSM of structures exhibiting “breathing behaviour”.<sup>39,41</sup>

In order to confirm a covalent character of the post-synthetic modification of MIL-53(Al)-NH<sub>2</sub> with MMA functionality, solid-state nuclear magnetic resonance (NMR) spectroscopy studies were carried out on a pristine MIL-53(Al)-NH<sub>2</sub> material and its PSM-NH<sub>2</sub>/MMA version. The <sup>1</sup>H MAS NMR spectrum (Fig. B8) of original MIL-53(Al)-NH<sub>2</sub> contains four peaks that can be assigned to the aromatic protons of the linker (unresolved peak at 6.9 ppm), protons of the amino group (5.5 ppm) and protons of bridging μ<sub>2</sub>-OH group in two possible chemical environments ( $\delta_{\text{iso}} = 2.8$  and 1.9 ppm) as expected.<sup>43-44</sup> In the 2D <sup>1</sup>H MAS DQ-SQ NMR correlation spectrum (Fig. B9), the aromatic proton resonances remain unresolved albeit manifesting two main pairs of correlation peaks: <sup>1</sup>H-<sup>1</sup>H correlations between i) aromatic protons and NH<sub>2</sub>-group ( $\delta_{\text{iso}}$  in F2 dimension: 5.5-6.8 ppm), ii) aromatic protons and bridging OH group ( $\delta_{\text{iso}}$  in F2 dimension: 1.9-6.8 ppm). The <sup>13</sup>C CPMAS NMR spectrum shows six resonances (Fig. B10) attributed to the carbonyl groups in NH<sub>2</sub>-BDC linker ( $\delta_{\text{iso}} = 175.6$  ppm) and carbons of the aromatic ring ( $\delta_{\text{iso}}$  in 116.4 – 150.5 ppm range). In addition, the intra-linker coupling interaction between carbon atoms and aromatic protons was complemented by means of 2D <sup>1</sup>H-<sup>13</sup>C HETCOR NMR (Fig. B11). The <sup>1</sup>H MAS NMR spectrum (Fig. B12) of PSM MIL-53(Al)-NH<sub>2</sub>/MMA material reveals additional weakly resolved resonances of CH<sub>3</sub>-protons ( $\delta_{\text{iso}} \sim 0.7$  ppm), CH<sub>2</sub> protons ( $\delta_{\text{iso}} \sim 5.2$  ppm) of MMA moiety and amide -NH- proton ( $\delta_{\text{iso}} \sim 10.7$  ppm) that affirm the

presence of acylated  $\text{NH}_2$ -groups. Expected changes of aromatic proton related chemical shifts upon PSM are also reflected in the presence of a shoulder resonance at  $\delta_{\text{iso}} \sim 9.0$  ppm. The 2D  $^1\text{H}$  MAS DQ-SQ NMR spectrum of MIL-53(Al)- $\text{NH}_2$ /MMA (Fig. B13) demonstrates off-diagonal signals that indicate i) a coupling of geminal  $-\text{CH}_2$  protons ( $\delta_{\text{iso}}$  in F2 dimension: 5.0-6.5 ppm) of MMA functionality; ii) a correlation between bridging  $\mu_2$ -OH of the framework and *trans*- $\text{CH}_2$  of MMA group ( $\delta_{\text{iso}}$  in F2 dimension: 1.6-5.1 ppm) due to their spatial proximity; iii) a correlation of the methyl-group of MMA ( $\delta_{\text{iso}}$  in F2 dimension: 0.7-8.0 ppm) and iv) bridging  $\mu_2$ -OH ( $\delta_{\text{iso}}$  in F2 dimension: 2.7-8.0 ppm) with the aromatic protons. The appearance of resonances at  $\sim 16.7$ , 122.7 and 166.0 ppm in  $^{13}\text{C}$  CP-MAS NMR spectrum (Fig. B14) can be associated with  $-\text{CH}_3$ ,  $-\text{CH}_2$  and  $\text{C}=\text{O}$  carbons of MMA moiety anchored to  $-\text{NH}_2$  site of the MOF. Additionally, correlations at  $\delta_{\text{iso}} \sim (16, 0.6)$  ppm, (123, 6.0) ppm and (160, 9.9) ppm corresponding to  $-\text{CH}_3$ ,  $-\text{CH}_2$  and  $\text{C}(=\text{O})\text{-NH}$  fragments of MMA functionality can be observed in 2D  $^1\text{H}$ - $^{13}\text{C}$  CP-MAS HETCOR NMR spectrum (Fig. B15).

To overcome sensitivity constraints of the  $^{15}\text{N}$  NMR measurement, DNP enhanced  $^{15}\text{N}$  NMR experiments were carried out on MIL-53(Al)- $\text{NH}_2$  and MIL-53(Al)- $\text{NH}_2$ /MMA samples. As shown in Figure 3.2B, the spectrum of PSM- $\text{NH}_2$ /MMA material reveals a resonance at  $\sim 122$  ppm attributed to newly formed  $\text{C}(=\text{O})\text{-NH}$  functionality in addition to the peak of  $-\text{NH}_2$  group at  $\sim 68$  ppm whereas only one strong signal at  $\sim 72$  ppm of the  $-\text{NH}_2$  group is observed in the spectrum of the pristine MOF. Furthermore, 2D DNP enhanced  $^{15}\text{N}$ - $^1\text{H}$  CP-MAS HETCOR NMR correlation map exposes two sets of cross-peaks attributed to couplings between nitrogens in  $-\text{NH}_2$  and  $\text{C}(=\text{O})\text{-NH}$  with aromatic and amide protons (Fig. B20). All observations above indicate the covalent anchoring of MMA in the framework of MIL-53(Al)- $\text{NH}_2$ .

Additionally, the post-synthetic event in the MIL-53(Al)- $\text{NH}_2$ /MMA structure was evidenced by thermogravimetric analysis (TGA) in an air atmosphere and argon physisorption measurements (Fig. B6C-D). Due to incorporation of an additional MMA group, the mass loss in the region 350-600  $^\circ\text{C}$ , where a total organic component decomposition takes place, expanded by 12 wt.% for PSM material compared to the pristine compound (Table B5). Furthermore, the surface measurements reveal that incorporation of several larger MMA group leads to a reduction in the intrinsic porosity from 370  $\text{m}^2\cdot\text{g}^{-1}$  down to 303  $\text{m}^2\cdot\text{g}^{-1}$  (Fig. B6D, Table B5). Supplementary, a comparison of FTIR spectra of pristine and modified MIL-53(Al)- $\text{NH}_2$ /MMA material reveals an increase in the relative intensity of absorption band situated  $\sim 1610$   $\text{cm}^{-1}$ , which is assigned to  $\text{C}=\text{C}$  vinylic group, further suggesting a conceivable PSM occurrence (Fig. B21).

In order to determine the percentage of amino groups acylated with MMA, the MIL-53(Al)- $\text{NH}_2$ /MMA material was digested in a DMSO- $d_6$  and HF mixture and evaluated by liquid state

$^1\text{H}$  NMR spectroscopy. The percentage of modified  $-\text{NH}_2$  groups was estimated to be 34% by comparing the integrals of characteristic geminal proton signals of the MMA group ( $\delta = 5.58, 5.95$  ppm) and aromatic protons of the pristine  $\text{NH}_2$ -BDC linker ( $\delta = 6.99 - 7.75$  ppm) (Fig. B22). Considering the size of the MIL-53(Al)- $\text{NH}_2$  nanoparticles (Fig. B7) and the orientation of the unit cell axes relative to the rod-shaped nanocrystal facets (Fig. B23),<sup>45-46</sup> the estimated amount of  $-\text{NH}_2$  groups located in the unit cells forming the crystal surface and exposed to PSM was approximated to be around 20%. Thus, this value concedes the percentage of  $-\text{NH}_2$  acylated with MMA determined from the liquid NMR of digested MIL-53(Al)- $\text{NH}_2$ /MMA material, which suggests that the PSM process does not only occur on the surface of the nanoparticles but also involves part of the porosity.

An essential criterion imposed on any photocurable ink formulation is the velocity of photo-crosslinking events set in motion when exposed to a light source. Thus, the commencing step in the design of MOF-containing ink formulation was to appraise the suitability of the precursor oligomer mixture for photopolymerization in terms of its behaviour under illumination. The corresponding transformation was followed by time-resolved ATR-FTIR on several commercially available acrylate-based systems (Fig. B1, Table B1 entries 1-6), which were intended to form a continuous matrix in printed composites, defining a decrease of  $\sim 1640\text{ cm}^{-1}$  band area as a merit of methacrylic group conversion (Fig. B24).<sup>47</sup> Figure 3.3A summarizes individual kinetic profiles of **T**, **P**, **E** and **U**-monomer photopolymerization and demonstrates a rapid MMA transformation in **P**-system (with  $2.4\text{ \%}\cdot\text{s}^{-1}$   $v_{X_{\text{MMA}}^{50\%}}$ ) with  $X_{\text{MMA}}$  conversion reaching 25 % compared to more moderate photopolymerization velocities in the **T**- and **E**-components ( $\sim 1.5\text{ \%}\cdot\text{s}^{-1}$ ) that demonstrated conversion of  $X_{\text{MMA}}$  of 27 % and 24 %, respectively (Fig. 3.3B). In contrast, the relatively slow behavior of the **U**-oligomer with a maximum degree of MMA conversion of 15 % and a rate of  $0.75\text{ \%}\cdot\text{s}^{-1}$  made it less desirable for further involvement in the DLP process. Viscosity of a photocurable formulation is one of the governing factors that determines the kinetics of MMA crosslinking. As observed (Table B6), a higher viscosity of the precursor is correlated with slower kinetics of the photopolymerization process. This should not exceed values of about 600 cP for the effective use with a moving build platform.

Subsequently, MOF-based blends with selected commercial oligomers (**T**, **P**, **E** components) were admixed in a certain proportion (Table B1, entries 7-8,10) and the kinetics of MMA conversion were elucidated. The polymerization rates of the heterogeneous formulations diminish by a factor of 3-4 compared to the systems without the MIL-53- $\text{NH}_2$ /MMA component (Fig. 3.3B), still reaching the same conversion levels observed for homogeneous mixtures (Fig. B25, Table B7). Among the tested blends **T**/MIL-53- $\text{NH}_2$ /MMA



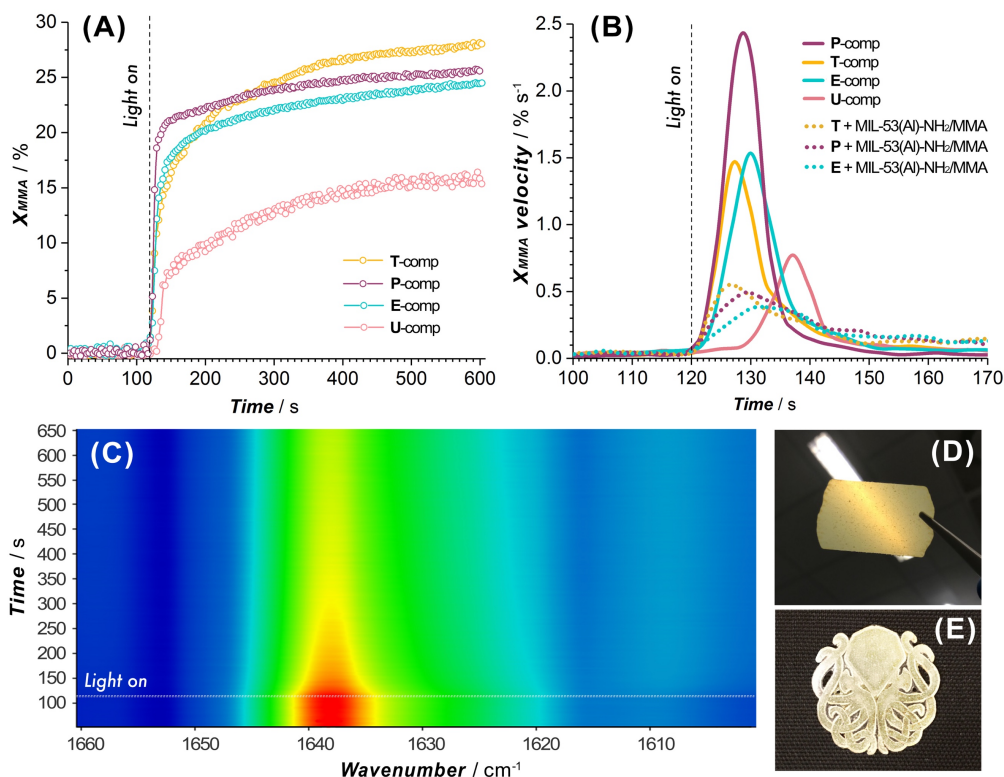


**Figure 3.3.** (A) Kinetic profiles of photopolymerization for individual oligomer mixtures (T, P, E and U-components). (B) Comparison of MMA-group conversion velocities for individual oligomers and MOF-contained formulations under the printer light source (turn on at 120 s). (C) 2D-resolved ATR-FTIR spectrum of T/MIL-53(Al)-NH<sub>2</sub>/MMA photopolymerization event (lamp on at 120 s). Image of 50 μm thick photocured film viewed against the light (D) and three layer printed model (E) both based on T/MIL-53(Al)-NH<sub>2</sub>/MMA ink.

demonstrated the fastest response to the light (Fig. 3.3B), as evidenced by a pronounced drop for the ca. 1640 cm<sup>-1</sup> band of the MMA group in a 2D ATR-FTIR spectra series (Fig. 3.3C), and can be used for the DLP printing process to yield solid films and 3D models of desired shapes (Figs. 3.3D-E).

As a covalent integration of MIL-53-NH<sub>2</sub>/MMA nanoparticles into the matrix is an important aspect to consider, the ability of functionalized MOF component to be grafted to the acrylic moieties of the matrix was elucidated with the help of confocal Raman spectroscopy. Figure 3.4A depicts the Raman maps on 30 × 30 μm<sup>2</sup> area of PSM-MOF containing 3DP composite membrane in which the contrast scale corresponds to intensity of C-(C=O)-O symmetrical stretching band (~600 cm<sup>-1</sup>) attributed to the MMA moieties involved in copolymerization. The contrast scale ranges from the strongest (*wine*) to the weakest (*navy*)

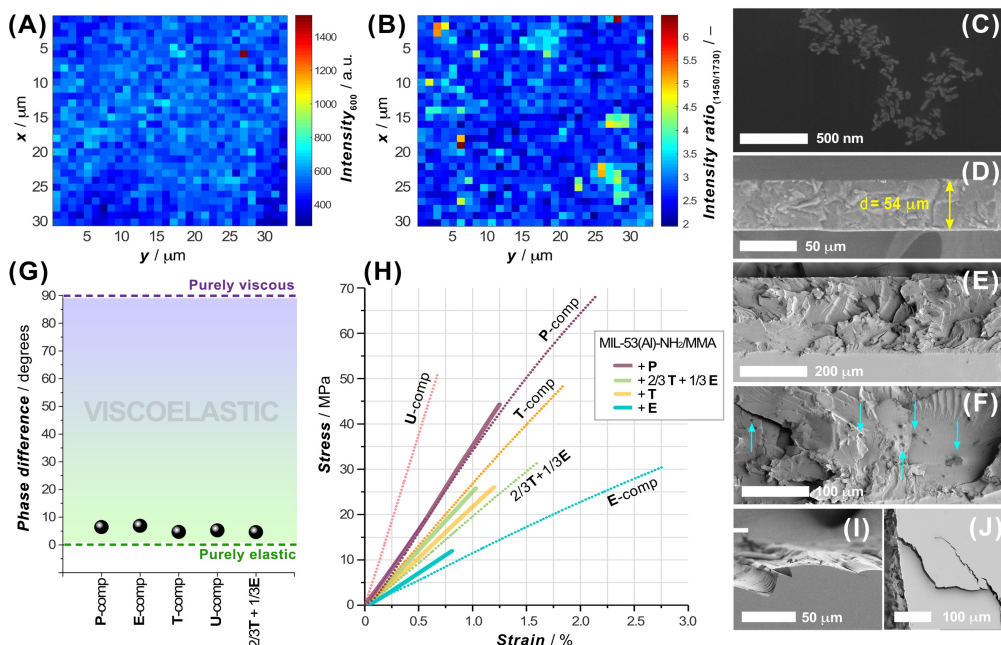


**Figure 3.4.** (A-B) Raman maps of a 3D printed membrane (30 × 30 μm<sup>2</sup> area, step size of 1 μm) depicting the spatial distribution of (A) the intensity of the characteristic band from MMA functionality and (B) the band intensity ratios of the distinguished frequencies in MIL-53(AI) relative to MMA component. (C) FIB-SEM cross-section and (D) SEM image of N<sub>2</sub> cracked 54 μm thick T/MIL-53-NH<sub>2</sub>/MMA 3DP membrane (3DP-M). (E-F) Cross-section (liquid N<sub>2</sub>) views of 3DP-M at different magnifications revealing MIL-53-NH<sub>2</sub>/MMA lumps (indicated with arrows). (G) Phase difference ( $\delta$ ) between stress and strain values of pure **P**, **E**, **T**, **U**- 3DP systems and 2/3T+1/3E mixture on a viscoelastic reference diagram. (H) Stress and strain curves of pure **P**, **E**, **T**, **U** and 2/3T+1/3E 3DP materials (dotted lines) and their MOF-based composites (solid lines). Brittle fracture (I) and cracks (J) produced by fracturing of a T/MIL-53-NH<sub>2</sub>/MMA 3DP-M.

scattering intensities, sketching zones with lower crosslinking density of MMA in dark blue and cyan regions visualize regions where the concentration of crosslinked MMA moieties is higher. Taking into account previous findings that the MMA conversion in MIL-53-NH<sub>2</sub>/MMA-acrylate systems usually does not exceed 27-30 % in total and considering that MIL-53-NH<sub>2</sub>/MMA component and matrix oligomer mixtures both have the crosslinked functionality, relatively homogenous cross-linking in the 3D printed composite despite PSM-MOF additive inclusion can be achieved.

Furthermore, the intensity ratios of specific Raman bands related to acrylic part (both matrix and PSM-NH<sub>2</sub>/MMA MOF) and aromatic component of the linker (PSM-NH<sub>2</sub>/MMA MOF) were compared on 2D contrast maps to provide information on the local chemical composition and distribution of the MOF additive in the accessible depth of the 3DP material. The distribution of MIL-53-NH<sub>2</sub>/MMA nanoparticles within acrylic matrix was evaluated from the

intensity ratios of Raman band centered at  $\sim 1450\text{ cm}^{-1}$  (aromatic ring C-C chain vibration in MIL-53(Al) framework) relative to C=O symmetric stretching vibration in MMA group located at  $\sim 1730\text{ cm}^{-1}$  (Fig. B26). As shown in Figure 3.4B, the distinguished regions of PSM-NH<sub>2</sub>/MMA MOF component can be mapped where the pixels of colours from cyan to yellow are located, occupying areas one order of magnitude bigger than the average nanoparticle size of MIL-53-NH<sub>2</sub>/MMA additive. FIB-SEM cross-sectioning studies of 3DP composite membrane further disclose MIL-53-NH<sub>2</sub>/MMA clustering and unveil a structural feature of the observed lumps (Fig. 3.4C). Although the MOF distribution within the polymerized matrix is not perfectly uniform (Figs. 3.4E-F), individual MIL-53-NH<sub>2</sub>/MMA nanoparticles are surrounded by the polymer, suggesting proper integration of the filler without formation of voids. Notably, the structure of polyacrylate matrix itself does not possess visible intrinsic porosity compared to conventional polymeric matrices used in MMMs preparation (Fig. 3.4D). The gas adsorption measurements using CO<sub>2</sub> as a probe molecule further corroborate this observation (Fig. B27). Despite the chemical differences in the acrylate systems employed as matrix precursor, shapes of adsorption isotherms reveal large sorption-desorption hysteresis loops along a wide range of pressures as a common attribute of glassy polymers<sup>48</sup> albeit severe divergence in a total adsorption capacity from 0.01 mmol·g<sup>-1</sup> for **T**- to 0.14 mmol·g<sup>-1</sup> for **U**-component and  $\sim 0.17\text{ mmol}\cdot\text{g}^{-1}$  for 2/3**T**+1/3**U** mixture (Fig. B27A).

The hysteresis loop feature is a characteristic aspect of many polymethylmethacrylate systems and is caused by the ability of these systems to undergo CO<sub>2</sub>-induced swelling associated with a glassy-to-rubbery state transition.<sup>49-51</sup> As expected, the adsorption capacity of a photocurable composite increases with an inclusion of a MIL-53-NH<sub>2</sub>/MMA component (Fig. B27B) which contributes to the boost of the total gas uptake at its microporous surface.

In order to be used in gas separation, either purely polymeric or composite membranes require sufficient mechanical stability and flexible resistivity at the conditions close to real operation settings.<sup>52</sup> To assess the mechanical properties of the here studied DLP 3D printed materials, specimens of various photocurable systems and blends were tested by applying dynamic mechanical and uniaxial tensile analyses. The dynamic tensile data for a commercially available acrylate ink (**P**, **E**, **T** and **U**), used as a matrix component in our formulations, and a mixture (2/3**T**+1/3**E**) were compared on a viscoelastic reference diagram (Fig. 3.4G). Evidently, the elastic nature in these photocurable matrix systems significantly prevails over its viscous counterpart and the phase difference ( $\delta$ ) in stress-strain responses deviates slightly from one component to another. As anticipated, the MIL-53-NH<sub>2</sub>/MMA-based composites exhibit lower damping factor ( $\tan \delta$ ) compared to pure polymeric material that agreeing well with commonly observed trends (Table B8).<sup>53</sup> Furthermore, the shape of the stress-strain curves for 3DP

stress-strain curves for 3DP polymeric and MOF based materials suggests the brittle nature of the acrylate crosslinked systems, whose chemical composition defines mechanical properties expressed in terms of Young's modulus ( $E$ ), stress ( $\sigma_R$ ) and strain at break ( $\varepsilon_R$ ) values (Table B8). Hence, the 3DP **U**-component shows the highest tensile strength ( $\sigma_R = 50.6$  MPa,  $\varepsilon_R = 0.67\%$ ) among other matrix inks, while the **E**-system, in turn, reveals superior toughness ( $\sigma_R = 30.2$  MPa,  $\varepsilon_R = 2.75\%$ ). Certainly, the brittle behaviour of 3DP composite can also be noted on corresponding cross-section views (Figs. 3.4E,I-J) where typical brittle fracture patterns and cracks can be observed. It is worth noting that the MOF filler commonly contributes to an earlier rupture of 3DP composites presumably due to formation of discretely localized heterogeneous inclusions and defects that can contribute to the origin and propagation of cracks. Overall, MIL-53-NH<sub>2</sub>/MMA-based acrylate 3DP materials display high tensile strengths and are able to withstand the conditions applied in gas separation processes.

Membranes based on a polymer in the glassy state are known to be particularly attractive for the selective separation of H<sub>2</sub> from H<sub>2</sub>/CO<sub>2</sub> mixtures.<sup>54</sup> Considering the above information, the 3DP acrylate-based membranes were assumed to be applicable in H<sub>2</sub>/CO<sub>2</sub> separation and therefore subjected to mixed gas separation tests to unveil their potential. The selection of the 3DP membrane formulation was rationalized considering the optimal DLP processing parameters, mechanical properties discussed above and glass transition temperatures ( $T_g$ ) of pure continuous phases and MIL-53-NH<sub>2</sub>/MMA-based composites (Table B11). The **U**-based formulations were excluded due to their poor DLP processing performance whereas **P**-systems show comparatively low  $T_g$  value (Table B11) limiting the available temperature range of H<sub>2</sub>/CO<sub>2</sub> gas separation. Thus, **T**-component system was selected for further separation of an equimolar mixture of H<sub>2</sub> and CO<sub>2</sub> at two different temperatures (323 K and 373 K) and 2 bar absolute feed pressure. All the prepared membranes can withstand the permeation test conditions. Figure 3.5A summarizes the separation data for pure **T**-matrix and **T**+MIL-53-NH<sub>2</sub>/MMA composite 3DP membranes.

The incorporation of MIL-53-NH<sub>2</sub>/MMA nanoparticles (12 wt.% loading) crosslinked with a continuous matrix leads to a significant increase in H<sub>2</sub> and CO<sub>2</sub> permeabilities preserving the original **T**-component membrane selectivity at 323 K. These observations agree with the fact that porous filler can provide additional pathways for the permeating gases. However, the low H<sub>2</sub>/CO<sub>2</sub> selectivity in the studied membranes compared to other reported relevant MMMs<sup>55-56</sup> (Fig. 3.5B) suggests the presence non-selective paths for penetrant gas molecules around filler particles. Upon the temperature increase up to 373 K, the permeabilities of bare **T**-polymer and **T**+MIL-53-NH<sub>2</sub>/MMA composite both rise about one order of magnitude ( $P_{H_2} = 41.9 \pm 12.6$ ,

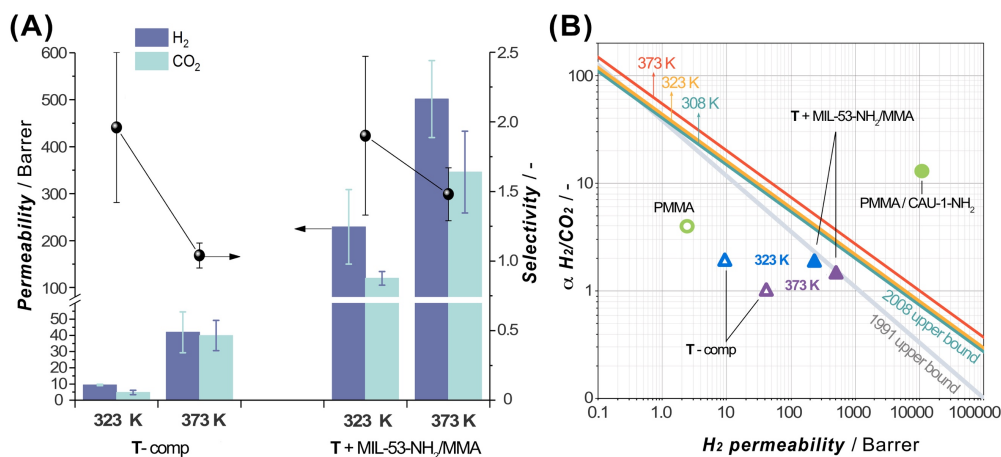


**Figure 3.5.** (A) H<sub>2</sub> (violet column, mint error bars) and CO<sub>2</sub> (mint columns, violet error bars) permeabilities and H<sub>2</sub>/CO<sub>2</sub> selectivity (black spheres, black error bars) for 3DP membrane containing pure **T**-comp or **T**+MIL-53-NH<sub>2</sub>/MMA (12 wt.% of MOF component) formulation in equimolar H<sub>2</sub>/CO<sub>2</sub> gas mixture at different temperatures (323 K and 373 K) and measured at 2 bar absolute feed pressure. (B) Comparison of separation performance for **T**-comp (empty triangle) or **T**+MIL-53-NH<sub>2</sub>/MMA (solid triangle) 3DP membranes (at 323 K and 373 K, blue and violet, respectively) with previously reported pure PMMA (2 bar, 303 K, green empty circle),<sup>56</sup> PMMA/CAU-1-NH<sub>2</sub> (green solid circle, 3 bar, 298 K, 15 wt.% of MOF) composite.<sup>55</sup> The lines represent Robeson's upper bonds for 1991 (grey line) and updated for 2008, plotted for 308 K (green), 323 K (yellow) and 373 K (red).<sup>57-58</sup>

$P_{\text{CO}_2} = 39.9 \pm 9.3$  versus  $P_{\text{H}_2} = 9.4 \pm 0.4$ ,  $P_{\text{CO}_2} = 4.8 \pm 1.4$  Barrer and  $P_{\text{H}_2} = 501.4 \pm 81.9$ ,  $P_{\text{CO}_2} = 345.9 \pm 87.1$  versus  $P_{\text{H}_2} = 229.3 \pm 79.3$ ,  $P_{\text{CO}_2} = 119.6 \pm 14.4$  Barrer, respectively, Table B12) meanwhile the H<sub>2</sub>/CO<sub>2</sub> selectivity drops down reflecting a loss of the size sieving ability, most significantly in the case of pure **T**-acrylate matrix. The permeability enhancement can be attributed to an increase in diffusivity of the gases through the polymeric matrix at higher temperatures. It should be noted that the milder drop of the selectivity in MIL-53-NH<sub>2</sub>/MMA-grafted **T**-composite membrane at 373 K indicate a beneficial collaborative interaction between the continuous and dispersed phases resulting in selective contribution of the filler to the total H<sub>2</sub>/CO<sub>2</sub> sieving performance.

The permeation results of pure **T**-matrix and **T**+MIL-53-NH<sub>2</sub>/MMA composite membranes at 323 K and 373 K are plotted against the 2008 Robeson upper bound<sup>58</sup> for selected temperatures (Fig. 3.5B).<sup>57</sup> Specifically, the separation performance of 3DP membranes explored in this study lies below the empirical selectivity-permeability trend line for the H<sub>2</sub>/CO<sub>2</sub> gas pair and occupies a modest position in the graph. Compared to the best performing and chemically related polymethyl methacrylate (PMMA)-based MMM containing CAU-1-NH<sub>2</sub> filler (Fig. 3.5B), 3DP **T**+MIL-53-NH<sub>2</sub>/MMA membrane demonstrates significantly lower permeability and selectivity. This can be explained in light of chemical, textural and structural differences

and selectivity. This can be explained in light of chemical, textural and structural differences between these two systems. As 3DP DLP processing requires highly crosslinked methacrylic matrices to enable the control over the resulting solid shape, the low permeability is an expected and inevitable outcome whereas MMMs prepared by conventional casting method can possess large free volumes that results in high permeabilities.<sup>55</sup> Moreover, preliminary obtained gas separation results for **T**+MIL-53-NH<sub>2</sub> formulation comprising pristine MOF revealed a non-selective behaviour caused by poor interaction between the filler and polymer which leads to formation of defects and approved using the MOF grafted with methacrylic functionality. Overall, the obtained results suggest that 3D DLP technology can be used in fast prototyping of MOF-based MMMs, leaving room for further development of the ink formulations by varying of polymeric matrix content along with type of MOF component. Additionally, to overcome the small free volume drawback, some approaches can be applied, such as use of hard templates<sup>59</sup> or employment of scCO<sub>2</sub> treatment.<sup>60</sup> Nevertheless, possible applications of 3D printable MOF-based composites are not exhausted by the gas separation field and can be tested out in tasks which require custom prototyping, e.g. fabrication of monoliths and fluidic devices for catalysis, pollutant removal, biomedical applications or patterned deposition on sensors.

### 3.4 CONCLUSIONS

In this work, we have demonstrated a fast and convenient approach to manufacture MOF-based polymer composite membranes using a conventional DLP 3D printer. MOF-based photocurable inks formulated from post-synthetically functionalized MIL-53(Al)-NH<sub>2</sub>/MMA nanoparticles and acrylate oligomers are fully compatible with conventional 3D printing. It was evidenced that the MOF-based photocurable systems undergo a photoinduced crosslinking with the matrix components at a relatively fast rate reaching the degree of crosslinking comparable with the pure oligomer mixtures. Hence, fulfilling the criteria for DLP process, the MIL-53(Al)-NH<sub>2</sub>/MMA containing inks can be transformed into free-standing composite membranes with desirable thickness and shape. Mechanical properties of the resulting 3D printed composites, glassy state of the polymeric media and microporosity provided by the MOF component enables their use as mixed matrix membranes for gas separation applications. The sieving behavior of the 3D printed MOF-MMMs in equimolar H<sub>2</sub>/CO<sub>2</sub> gas mixture indicate the enhanced permeability of MIL-53(Al)-NH<sub>2</sub>/MMA containing composite in comparison to that observed for the bare polymer. Finally, it was shown that 3D printing technology involving digital light processing could be successfully applied for fast prototyping of MOF-based mixed membranes and sets a basis for further development in this field.

## REFERENCES

- [1] S. C. Ligon, R. Liska, J. Stampfl, M. Gurr, R. Mülhaupt, *Chem. Rev.* **2017**, 117, 10212-10290.
- [2] M. R. Hartings, Z. Ahmed, *Nat. Rev. Chem.* **2019**, 3, 305-314.
- [3] L. D. Tijing, J. R. C. Dizon, I. Ibrahim, A. R. N. Nisay, H. K. Shon, R. C. Advincula, *Appl. Mater. Today* **2020**, 18, 100486.
- [4] C. Parra-Cabrera, C. Achille, S. Kuhn, R. Ameloot, *Chem. Soc. Rev.* **2018**, 47, 209-230.
- [5] R. L. Truby, J. A. Lewis, *Nature* **2016**, 540, 371-378.
- [6] T. D. Ngo, A. Kashani, G. Imbalzano, K. T. Q. Nguyen, D. Hui, *Compos. B: Eng.* **2018**, 143, 172-196.
- [7] X. Zhou, C.-j. Liu, *Adv. Funct. Mater.* **2017**, 27, 1701134.
- [8] X. Yun, B. Lu, Z. Xiong, B. Jia, B. Tang, H. Mao, T. Zhang, X. Wang, *RSC Adv.* **2019**, 9, 29384-29395.
- [9] E. Davoodi, H. Montazerian, R. Haghniaz, A. Rashidi, S. Ahadian, A. Sheikhi, J. Chen, A. Khademhosseini, A. S. Milani, M. Hoorfar, E. Toyserkani, *ACS Nano* **2020**, 14, 1520-1532.
- [10] H. Furukawa, K. E. Cordova, M. O'Keeffe, O. M. Yaghi, *Science* **2013**, 341, 1230444.
- [11] A. Bavykina, N. Kolobov, I. S. Khan, J. A. Bau, A. Ramirez, J. Gascon, *Chem. Rev.* **2020**, DOI: 10.1021/acs.chemrev.9b00685.
- [12] A. Pustovarenko, A. Dikhtiarenko, A. Bavykina, L. E. M. Gevers, A. Ramirez, A. Russkikh, S. Telalovic, A. A. Tapia, J. L. Hazemann, S. Ould-Chikh, J. Gascon, *ACS Catal.* **2020**, 10, 5064-5076.
- [13] B. Seoane, J. Coronas, I. Gascon, M. E. Benavides, O. Karvan, J. Caro, F. Kapteijn, J. Gascon, *Chem. Soc. Rev.* **2015**, 44, 2421-2454.
- [14] J. Yang, Y.-W. Yang, *Small* **2020**, 16, 1906846.
- [15] W.-T. Koo, J.-S. Jang, I.-D. Kim, *Chem* **2019**, 5, 1938-1963.
- [16] L. L. da Luz, R. Milani, J. F. Felix, I. R. B. Ribeiro, M. Talhavini, B. A. D. Neto, J. Chojnacki, M. O. Rodrigues, S. A. Júnior, *ACS Appl. Mater. Interfaces* **2015**, 7, 27115-27123.
- [17] J. L. Zhuang, D. Ar, X. J. Yu, J. X. Liu, A. Terfort, *Adv. Mater.* **2013**, 25, 4631-4635.
- [18] H. Thakkar, S. Eastman, Q. Al-Naddaf, F. Rezaei, *ACS Appl. Mater. Interfaces* **2017**, 9.
- [19] P. Pei, Z. Tian, Y. Zhu, *Microporous Mesoporous Mater.* **2018**, 272, 24-30.
- [20] H. Thakkar, Q. Al-Naddaf, N. Legion, M. Hovis, A. Krishnamurthy, A. A. Rownaghi, F. Rezaei, *ACS Sustain. Chem. Eng.* **2018**, 6, 15228-15237.
- [21] J. Lefevre, B. Claessens, S. Mullens, G. Baron, J. Cousin-Saint-Remi, J. F. M. Denayer, *ACS Appl. Nano Mater.* **2019**, 2, 4991-4999.
- [22] G. J. H. Lim, Y. Wu, B. B. Shah, J. J. Koh, C. K. Liu, D. Zhao, A. K. Cheetham, J. Wang, J. Ding, *ACS Mater. Lett.* **2019**, 1, 147-153.
- [23] Z. Lyu, G. J. H. Lim, R. Guo, Z. Kou, T. Wang, C. Guan, J. Ding, W. Chen, J. Wang, *Adv. Funct. Mater.* **2019**, 29, 1806658.
- [24] S. Lawson, Q. Al-Naddaf, A. Krishnamurthy, M. S. Amour, C. Griffin, A. A. Rownaghi, J. C. Knox, F. Rezaei, *ACS Appl. Mater. Interfaces* **2018**, 10, 19076-19086.
- [25] S. Sultan, H. N. Abdelhamid, X. D. Zou, A. P. Mathew, *Adv. Funct. Mater.* **2019**, 29, 1805372.
- [26] A. J. Young, R. Guillet-Nicolas, E. S. Marshall, F. Kleitz, A. J. Goodhand, L. B. L. Glanville, M. R. Reithofer, J. M. Chin, *Chem. Commun.* **2019**, 55, 2190-2193.
- [27] J. Dhainaut, M. Bonneau, R. Ueoka, K. Kanamori, S. Furukawa, *ACS Appl. Mater. Interfaces* **2020**, 12, 10983-10992.

- [28] M. Bible, M. Sefa, J. A. Fedchak, J. Scherschligt, B. Natarajan, Z. Ahmed, M. R. Hartings, *3D Print. Addit. Manuf.* **2018**, 5, 63-72.
- [29] M. N. Channell, M. Sefa, J. A. Fedchak, J. Scherschligt, M. Bible, B. Natarajan, N. N. Klimov, A. E. Miller, Z. Ahmed, M. R. Hartings, *Polym. Adv. Technol.* **2018**, 29, 867-873.
- [30] K. A. Evans, Z. C. Kennedy, B. W. Arey, J. F. Christ, H. T. Schaef, S. K. Nune, R. L. Erikson, *ACS Appl. Mater. Interfaces* **2018**, 10, 15112-15121.
- [31] O. Halevi, J. M. R. Tan, P. S. Lee, S. Magdassi, *Adv. Sustain. Syst.* **2018**, 2, 1700150.
- [32] E. Lahtinen, R. L. M. Precker, M. Lahtinen, E. Hey-Hawkins, M. Haukka, *ChemPlusChem* **2019**, 84, 222-225.
- [33] R. Li, S. Yuan, W. Zhang, H. Zheng, W. Zhu, B. Li, M. Zhou, A. Wing-Keung Law, K. Zhou, *ACS Appl. Mater. Interfaces* **2019**, 11, 40564-40574.
- [34] A. Figuerola, D. A. V. Medina, A. J. Santos-Neto, C. P. Cabello, V. Cerdà, G. T. Palomino, F. Maya, *Appl. Mater. Today* **2019**, 16, 21-27.
- [35] Y. Zhang, X. Feng, H. Li, Y. Chen, J. Zhao, S. Wang, L. Wang, B. Wang, *Angew. Chem., Int. Ed.* **2015**, 54, 4259-4263.
- [36] A. Sabetghadam, B. Seoane, D. Keskin, N. Duim, T. Rodenas, S. Shahid, S. Sorribas, C. Le Guillouzer, G. Clet, C. Tellez, M. Daturi, J. Coronas, F. Kapteijn, J. Gascon, *Adv. Funct. Mater.* **2016**, 26, 3154-3163.
- [37] M. Kandiah, S. Usseglio, S. Svelle, U. Olsbye, K. P. Lillerud, M. Tilset, *J. Mater. Chem.* **2010**, 20, 9848-9851.
- [38] A. S. f. T. a. Materials, ASTM, *Standard Test Methods for Determination of Gel Content and Swell Ratio of Crosslinked Ethylene Plastics*, ASTM D2765-11, 2006.
- [39] P. Serra-Crespo, E. Gobechiya, E. V. Ramos-Fernandez, J. Juan-Alcañiz, A. Martinez-Joaristi, E. Stavitski, C. E. A. Kirschhock, J. A. Martens, F. Kapteijn, J. Gascon, *Langmuir* **2012**, 28, 12916-12922.
- [40] A. Pustovarenko, M. G. Goesten, S. Sachdeva, M. Shan, Z. Amghouz, Y. Belmabkhout, A. Dikhtiarenko, T. Rodenas, D. Keskin, I. K. Voets, B. M. Weckhuysen, M. Eddaoudi, L. C. P. M. de Smet, E. J. R. Sudhölter, F. Kapteijn, B. Seoane, J. Gascon, *Adv. Mater.* **2018**, 30, 1707234.
- [41] S. Castellanos, K. B. Sai Sankar Gupta, A. Pustovarenko, A. Dikhtiarenko, M. Nasalevich, P. Atienzar, H. García, J. Gascon, F. Kapteijn, *Eur. J. Inorg. Chem.* **2015**, 2015, 4648-4652.
- [42] S. Couck, E. Gobechiya, C. E. A. Kirschhock, P. Serra-Crespo, J. Juan-Alcañiz, A. Martinez-Joaristi, E. Stavitski, J. Gascon, F. Kapteijn, G. V. Baron, J. F. M. Denayer, *ChemSusChem* **2012**, 5, 740-750.
- [43] S. Devautour-Vinot, G. Maurin, C. Serre, P. Horcajada, D. Paula da Cunha, V. Guillermin, E. de Souza Costa, F. Taulelle, C. Martineau, *Chem. Mater.* **2012**, 24, 2168-2177.
- [44] M. Haouas, C. Volkringer, T. Loiseau, G. Férey, F. Taulelle, *Chem. Eur. J.* **2009**, 15, 3139-3146.
- [45] J. M. Chin, E. Y. Chen, A. G. Menon, H. Y. Tan, A. T. S. Hor, M. K. Schreyer, J. Xu, *CrystEngComm* **2013**, 15, 654-657.
- [46] B. Seoane, S. Castellanos, A. Dikhtiarenko, F. Kapteijn, J. Gascon, *Coord. Chem. Rev.* **2016**, 307, 147-187.
- [47] E. Gulari, K. McKeigue, K. Y. S. Ng, *Macromolecules* **1984**, 17, 1822-1825.
- [48] R. M. Conforti, T. A. Barbari, *Macromolecules* **1993**, 26, 5209-5212.
- [49] X.-K. Li, G.-P. Cao, L.-H. Chen, R.-H. Zhang, H.-L. Liu, Y.-H. Shi, *Langmuir* **2013**, 29, 14089-14100.
- [50] D. Liu, H. Li, M. S. Noon, D. L. Tomasko, *Macromolecules* **2005**, 38, 4416-4424.
- [51] A. Rajendran, B. Bonavoglia, N. Forrer, G. Storti, M. Mazzotti, M. Morbidelli, *Ind. Eng. Chem. Res.* **2005**, 44, 2549-2560.



- [52] K. Wang, A. A. Abdala, N. Hilal, M. K. Khraisheh, in *Membrane Characterization*, (Eds: N. Hilal, A. F. Ismail, T. Matsuura, D. Oatley-Radcliffe), Elsevier **2017**, 259-306.
- [53] V. Panwar, K. Pal, in *Clay-Polymer Nanocomposites*, (Eds: K. Jlassi, M. M. Chehimi, S. Thomas), Elsevier **2017**, 413-441.
- [54] L. Shao, B. T. Low, T.-S. Chung, A. R. Greenberg, *J. Membr. Sci.* **2009**, 327, 18-31.
- [55] L. Cao, K. Tao, A. Huang, C. Kong, L. Chen, *Chem. Commun.* **2013**, 49, 8513-8515.
- [56] C. J. Orme, M. L. Stone, M. T. Benson, E. S. Peterson, *Sep. Sci. Technol.* **2003**, 38, 3225-3238.
- [57] B. W. Rowe, L. M. Robeson, B. D. Freeman, D. R. Paul, *J. Membr. Sci.* **2010**, 360, 58-69.
- [58] L. M. Robeson, *J. Membr. Sci.* **2008**, 320, 390-400.
- [59] M. Stucki, M. Loepfe, W. J. Stark, *Adv. Eng. Mater.* **2018**, 20, 1700611.
- [60] R. W. Sharudin, A. Nabil, K. Taki, M. Ohshima, *J. Appl. Polym. Sci.* **2011**, 119, 1042-1051.

## APPENDIX B

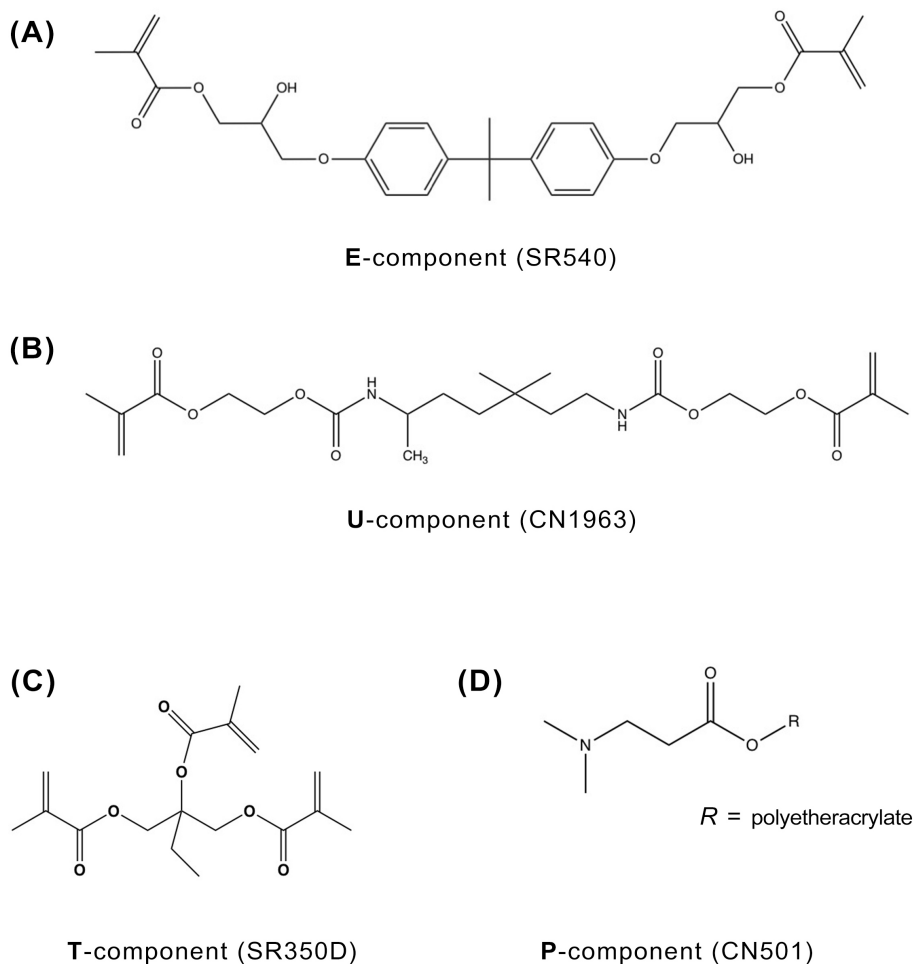


**Figure B1.** Chemical schemes and corresponding codes for photocurable oligomers used in this study: (A) ethoxylated-4-bisphenol-A-dimethacrylate (**E**-component), (B) aliphatic urethane dimethacrylate (**U**-component), (C) trimethylolpropane trimethacrylate (**T**-component) and (D) amine modified polyether acrylate (**P**-component)

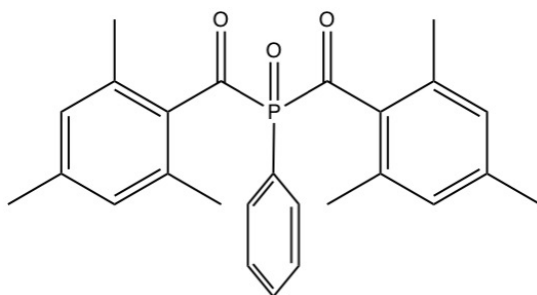


**Figure B2.** Chemical scheme of photoinitiator Irgacure<sup>®</sup>-819.

**Table B1.** Summary of photocurable systems and MIL-53(Al)-NH<sub>2</sub>/MMA containing ink formulations.

Entry	Sample code	Commercial oligomer*		Photoinitiator Irgacure <sup>®</sup> -819 (wt.%)	MIL-53- NH <sub>2</sub> /MMA (wt.%)
		1 <sup>st</sup> (wt.%)	2 <sup>nd</sup> (wt.%)		
1	<b>T</b> -comp.	98	–	2	–
2	<b>P</b> -comp.	98	–	2	–
3	<b>U</b> -comp.	98	–	2	–
4	<b>E</b> -comp.	98	–	2	–
5	2/3 <b>T</b> +1/3 <b>U</b> -comps.	65	33	2	–
6	2/3 <b>T</b> +1/3 <b>E</b> -comps.	65	33	–	–
7	<b>T</b> / MIL-53-NH <sub>2</sub> /MMA	86	–	2	12
8	<b>P</b> / MIL-53-NH <sub>2</sub> /MMA	86	–	2	12
9	<b>U</b> / MIL-53-NH <sub>2</sub> /MMA	86	–	2	12
10	<b>E</b> / MIL-53-NH <sub>2</sub> /MMA	86	–	2	12
11	2/3 <b>T</b> +1/3 <b>E</b> / MIL-53-NH <sub>2</sub> /MMA	58	28	2	12

\* Acrylate systems contain 4-methoxyphenol as a stabilizer (~ 500-600 ppm)

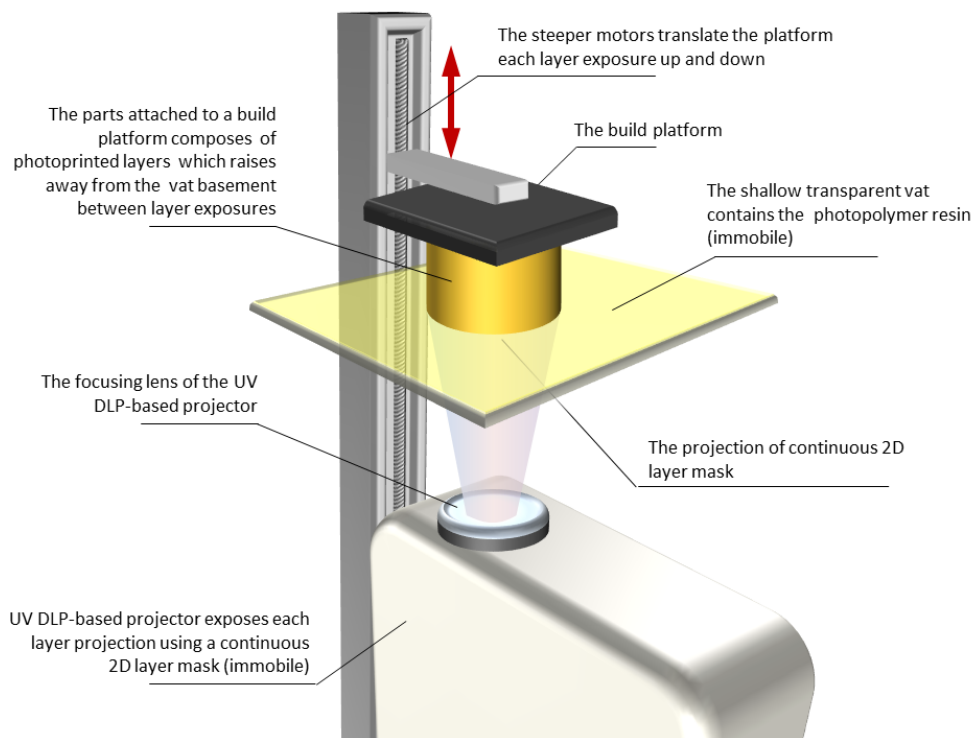


**Figure B3.** Scheme of 3D printer with DLP configuration.

The DLP printer setup consists of three main components: the projector, the resin basin (vat) and the build platform. The projector is placed under the transparent vat. The build platform enters the vat from the top and can be moved upwards to “pull” the print out of the vat layer by layer.

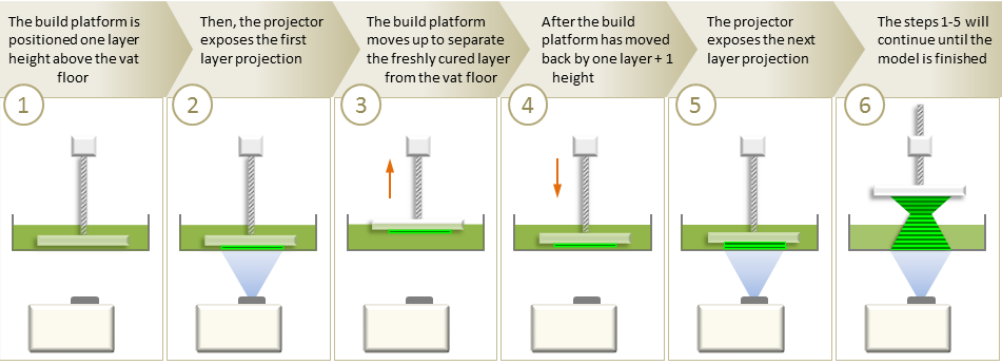


**Figure B4.** The six-step printing process using 3D DLP printer.

**Table B2.** Technical characteristics of 3D DLP printer Kudo3D model Titan 2.

Specifications		DLP Kudo3D Titan 2
Hardware	Machine size	40.9 cm × 34.8 cm × 85.3 cm
	Weight	13.6 kg
	Resin container	Flexible PSP
	Linear stage module	THK's high precision
	Projector	ACER H5360 LED DLP projector with a 2 cm native 1920 × 1080 DMD chip by Texas Instruments
Printing properties	XY resolution	38 – 92 μm
	Finest Z resolution	5 μm
	Maximum build size	<b>XY: 92 μm resolution</b> 17.5 cm × 9.6 cm × 24.9 cm <b>XY: 100 μm resolution</b> 19.0 cm × 10.9 cm × 24.9 cm
	Maximum print speed (for XY = 50 μm and Z = 100 μm)	6.86 cm/h
Control	Control software	Web-based
	Connectivity	LAN cable
	Printer control	PC
Calibration and assembly	Pre-calibration	At 50 μm / 75 μm
	Assembly	Fully assembled body

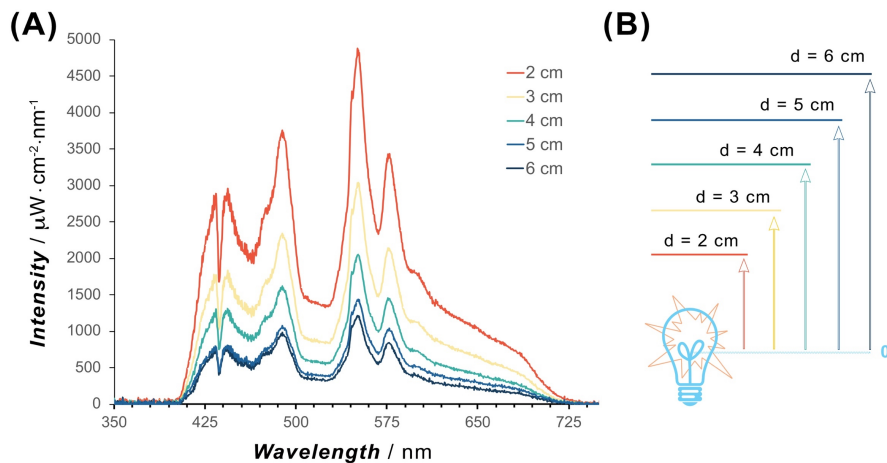


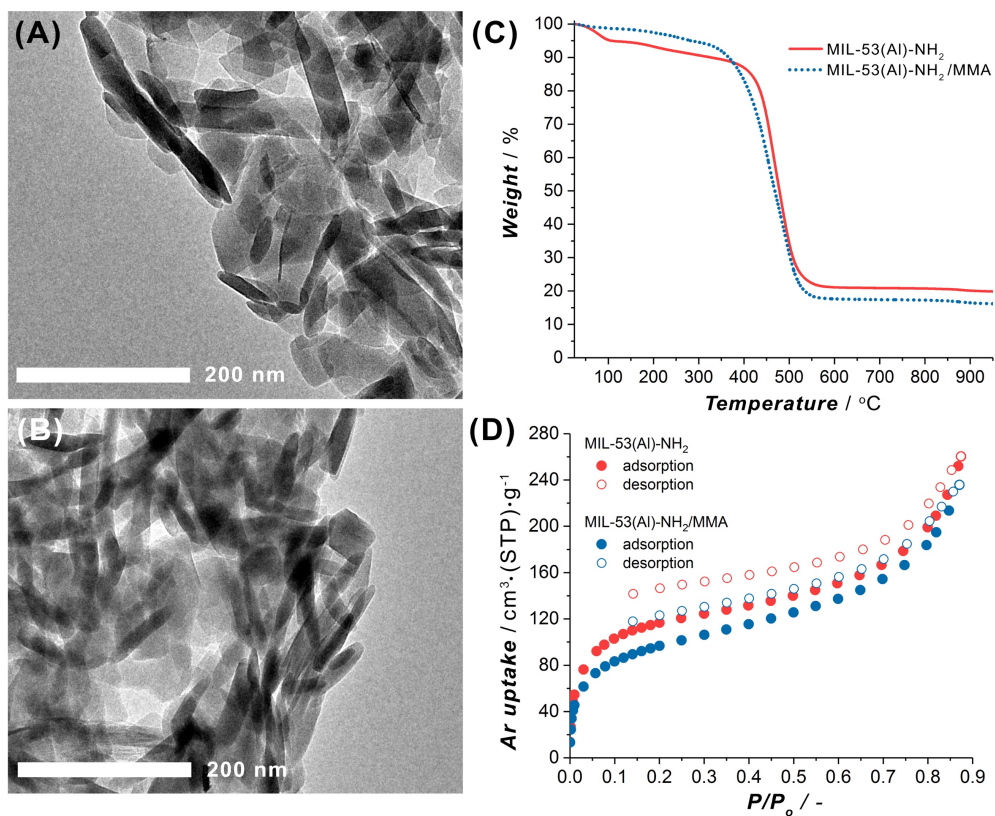
**Figure B5.** (A) Spectral irradiance of the 3D printer light source as a function of the distance (B) between the printer light source and resin vat.

**Table B3.** Summary of power density of the 3D printer light source as a function of the separation distance between the printer light source and resin vat.

d (cm)	P ( $\text{mW} \cdot \text{cm}^{-2}$ )
2	566.6
3	240.3
4	212.5
5	164.3
6	137.3

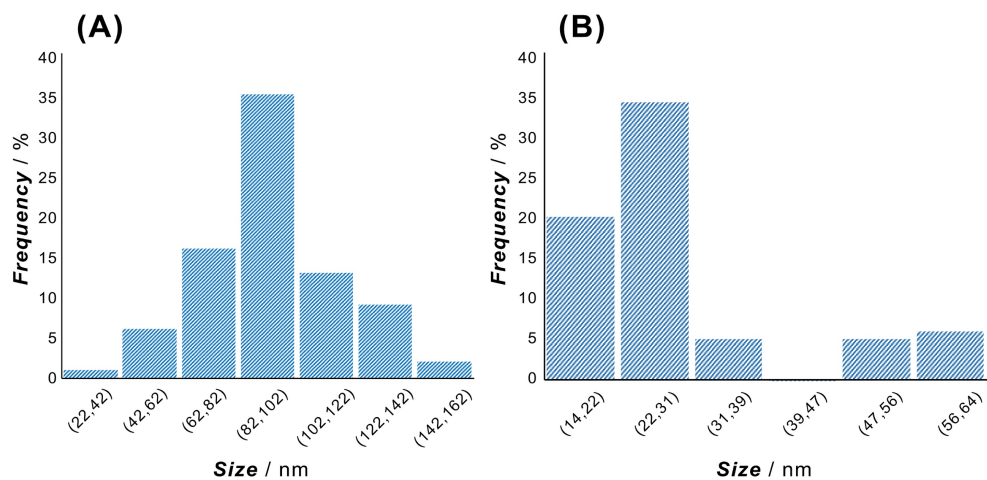
**Table B4.** Typical operative parameters for DLP 3D printing used in this study.

Parameter	Value
Exposure time	10 s
Layer thickness	50 $\mu\text{m}$
Lifting height	3.5 mm
Lifting speed	10 $\text{mm}\cdot\text{min}^{-1}$
Projected width	28 mm
Projected length	49.8 mm
Projected area	1393.7 $\text{mm}^2$
Temperature	RT
Light intensity	212.5 $\text{mW}\cdot\text{cm}^{-2}$

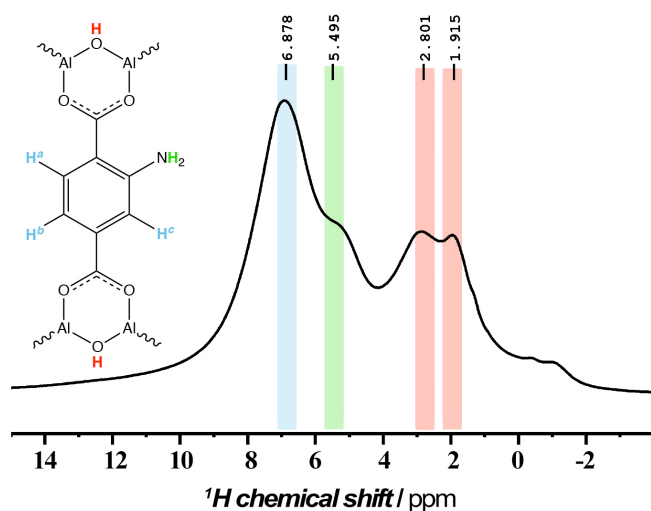


**Figure B6.** TEM images of MIL-53(Al)-NH<sub>2</sub> (A) and MIL-53(Al)-NH<sub>2</sub>/MMA (B). Thermogravimetric curves in air atmosphere (C) and N<sub>2</sub> adsorption isotherms (D) for MIL-53(Al)-NH<sub>2</sub> and MIL-53(Al)-NH<sub>2</sub>/MMA.

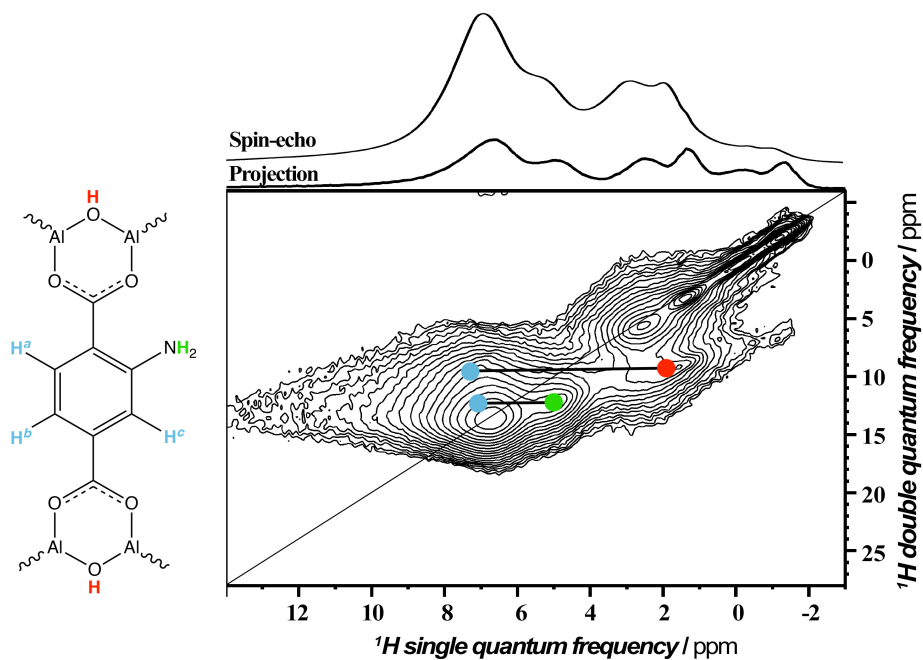




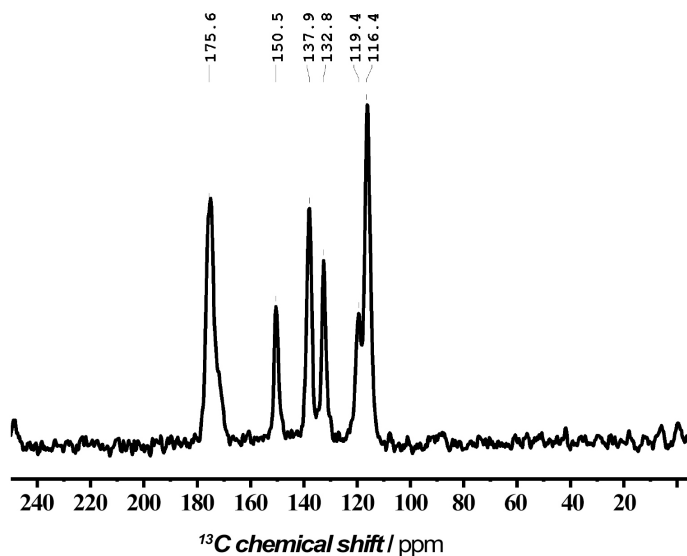
**Figure B7.** Particle size distributions of MIL-53(Al)-NH<sub>2</sub> nanoparticles measuring (A) length (mean of 95 ± 24 nm) or (B) width (mean of 28 ± 13 nm). Measurements were performed on several TEM images accounting of more than 100 particles.



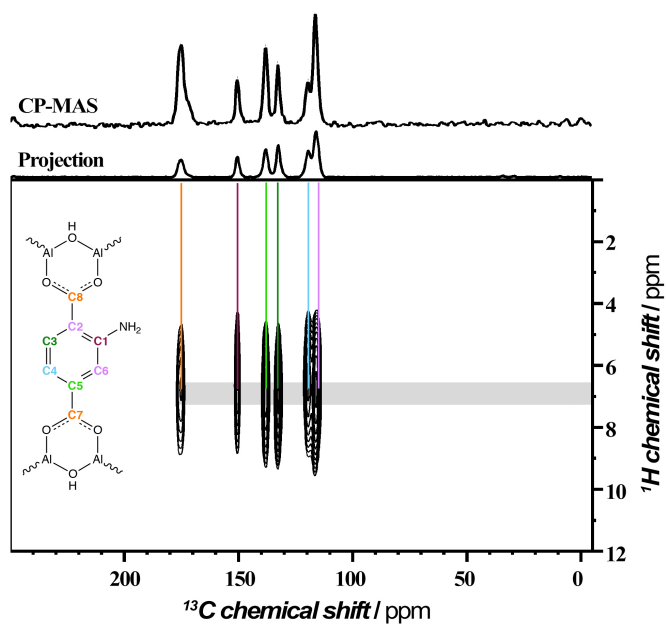
**Figure B8.** Solid-state one-dimensional <sup>1</sup>H MAS NMR spectrum of MIL-53(Al)-NH<sub>2</sub> before post-synthetic modification.



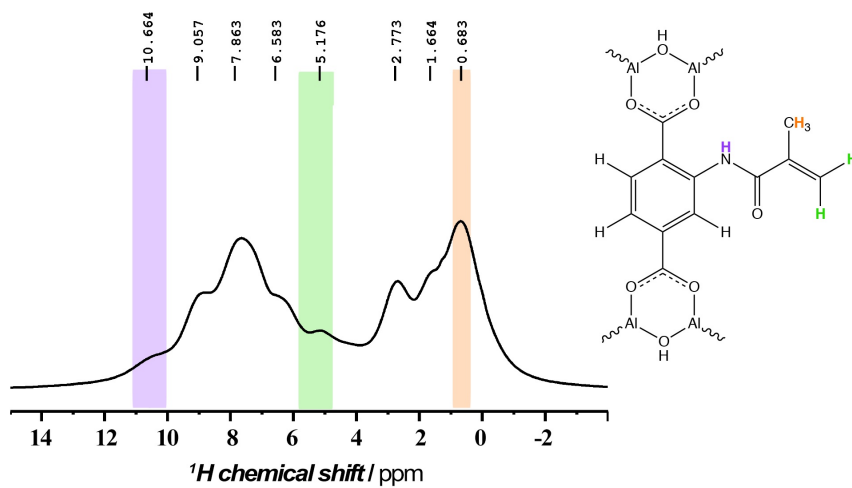
**Figure B9.** Solid state 2D  $^1\text{H}$  MAS DQ-SQ NMR correlation spectrum for MIL-53(Al)- $\text{NH}_2$  before post-synthetic modification.



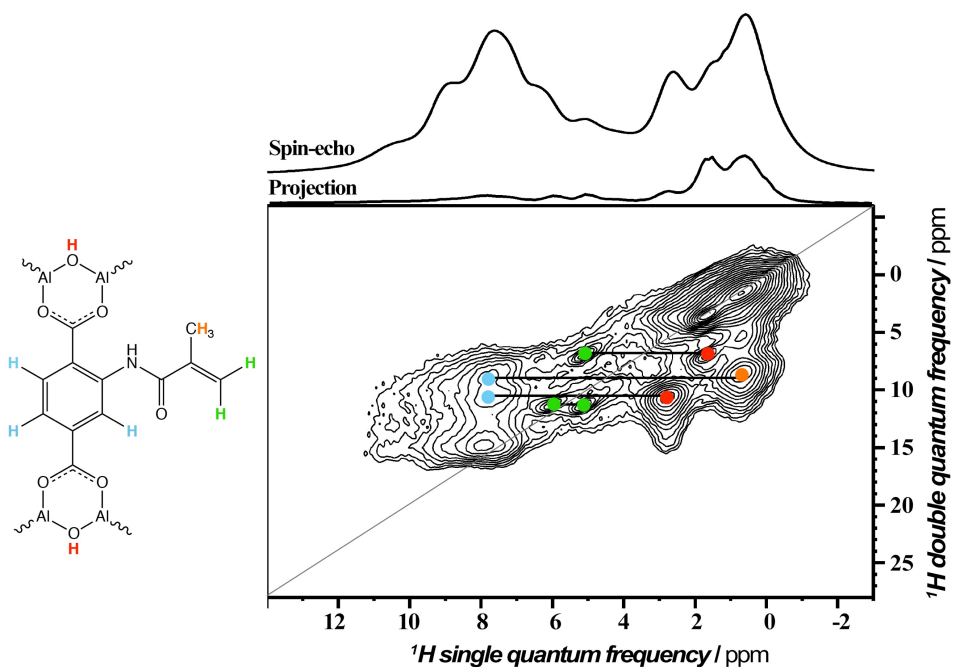
**Figure B10.** Solid-state one-dimensional  $^{13}\text{C}$  CP-MAS NMR spectrum of MIL-53(Al)- $\text{NH}_2$  before post-synthetic modification.



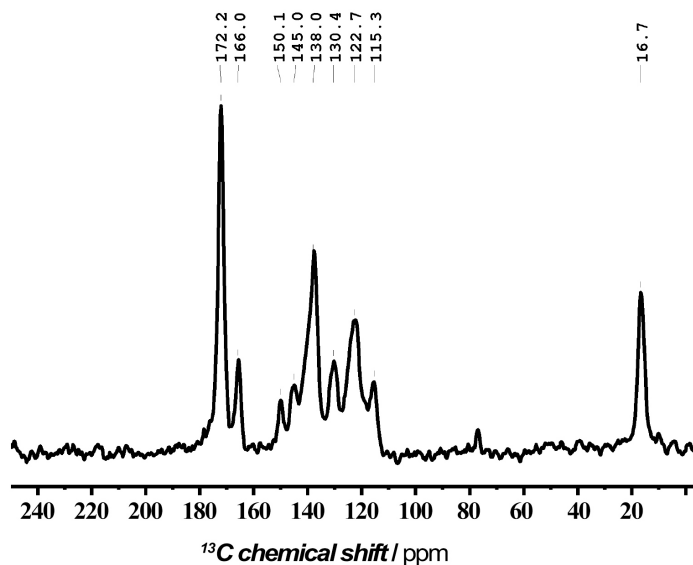
**Figure B11.** Solid-state two-dimensional (2D)  $^{13}\text{C}$ - $^1\text{H}$  heteronuclear single quantum correlation NMR spectrum of MIL-53(Al)- $\text{NH}_2$  before post-synthetic modification.



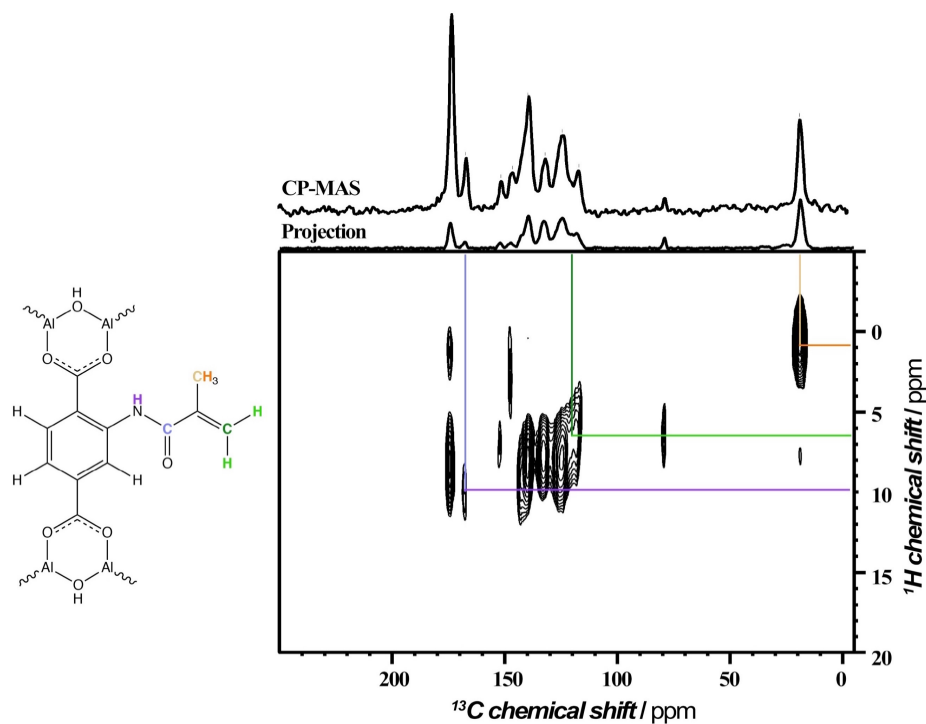
**Figure B12.** Solid-state  $^1\text{H}$  MAS NMR spectrum of MIL-53(Al)- $\text{NH}_2$ /MMA after post-synthetic modification. Characteristic resonances expected to be in PSM material with MMA moiety are shown in color.



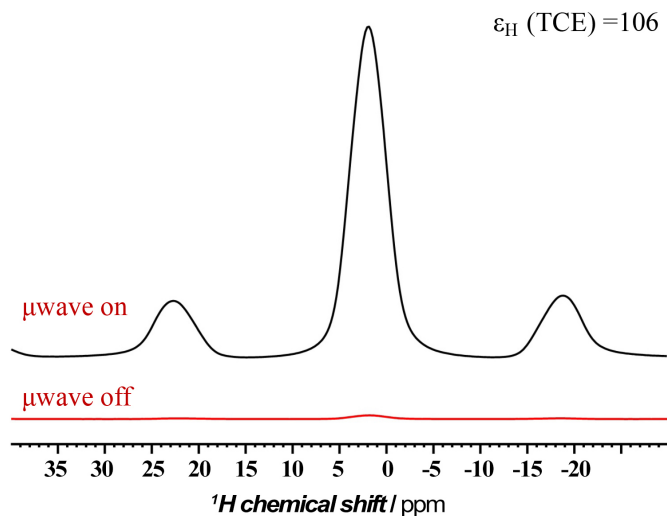
**Figure B13.** Solid-state 2D <sup>1</sup>H MAS DQ-SQ NMR correlation spectrum of MIL-53(Al)-NH<sub>2</sub>/MMA after post-synthetic modification.



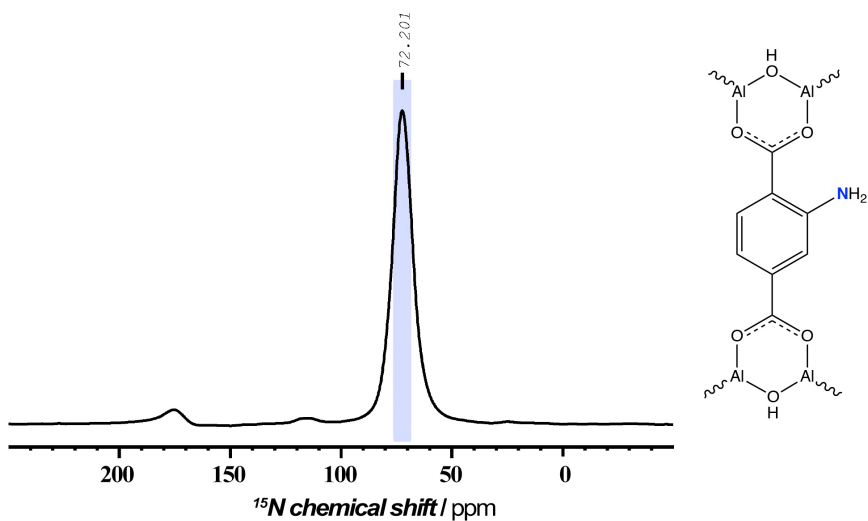
**Figure B14.** Solid-state <sup>13</sup>C CP-MAS NMR spectrum of MIL-53(Al)-NH<sub>2</sub>/MMA after post-synthetic modification.



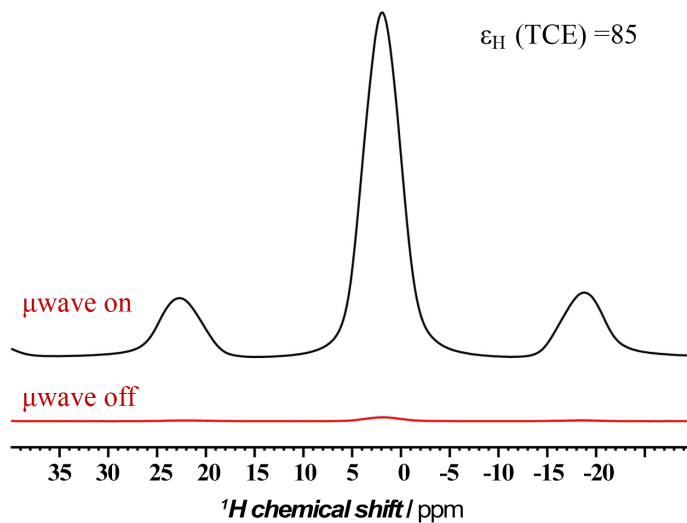
**Figure B15.** Solid-state two-dimensional (2D) <sup>13</sup>C-<sup>1</sup>H heteronuclear single quantum spectrum of MIL-53(Al)-NH<sub>2</sub>/MMA after post-synthetic modification.



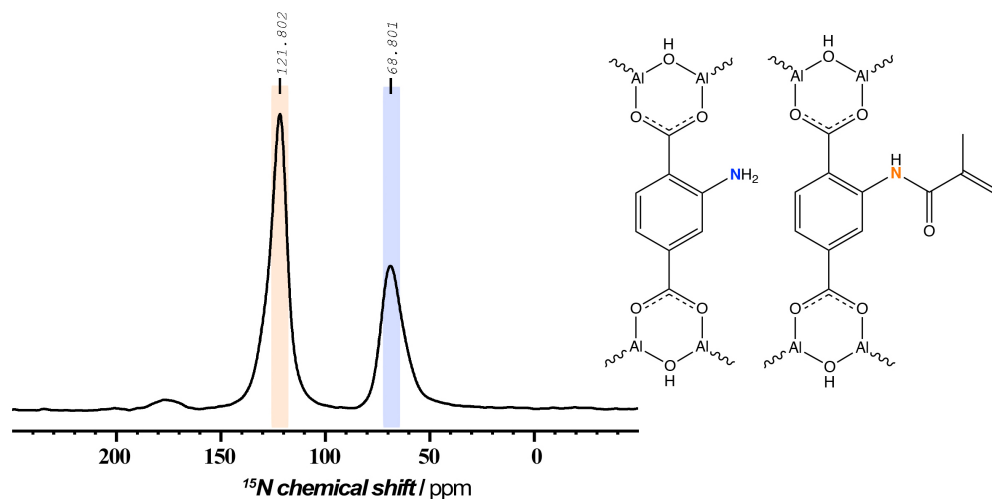
**Figure B16.** Solid-state DNP enhanced <sup>1</sup>H NMR spectrum of MIL-53(Al)-NH<sub>2</sub> before post-synthetic modification with and without DNP microwave applied.



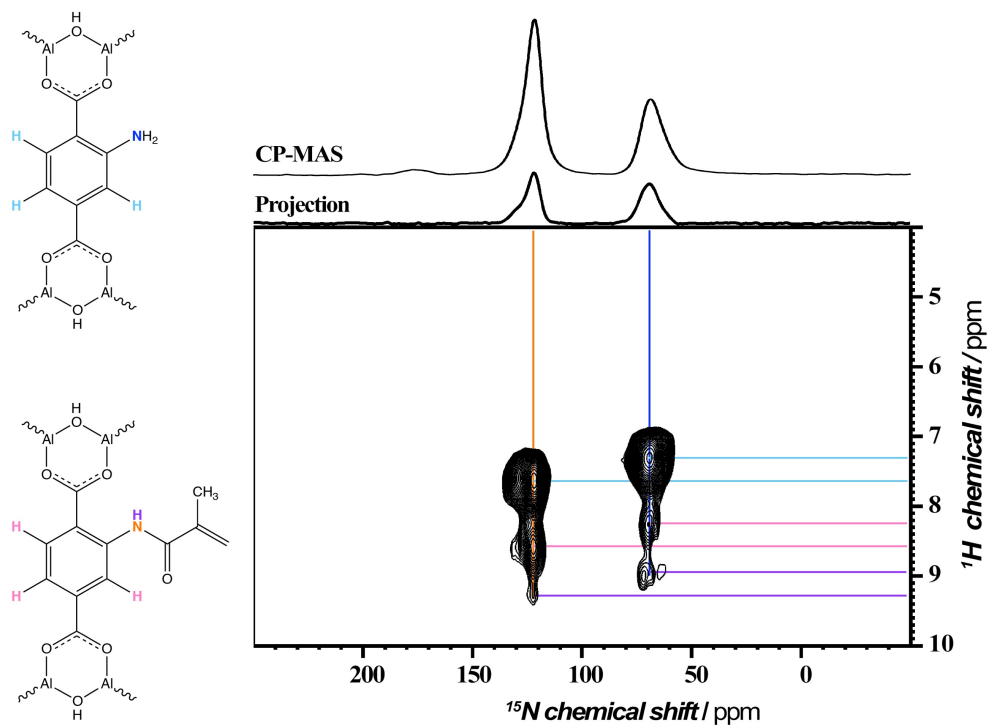
**Figure B17.** Solid-state DNP enhanced  $^{15}\text{N}$  NMR spectrum of MIL-53(Al)- $\text{NH}_2$  before post-synthetic modification.



**Figure B18.** Solid-state DNP enhanced  $^1\text{H}$  NMR spectrum of MIL-53(Al)- $\text{NH}_2/\text{MMA}$  after post-synthetic modification with and without DNP microwave applied.



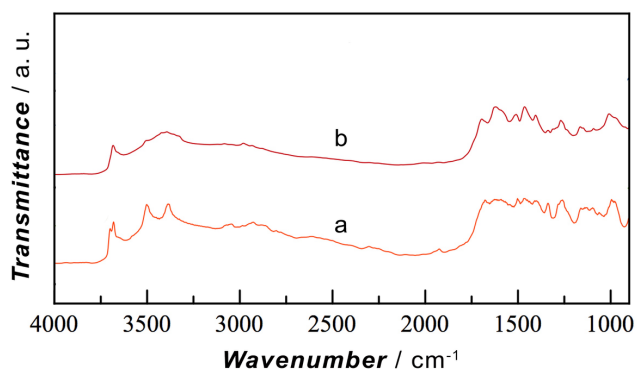
**Figure B19.** Solid-state DNP enhanced  $^{15}\text{N}$  NMR spectrum of MIL-53(Al)-NH<sub>2</sub>/MMA after post-synthetic modification.



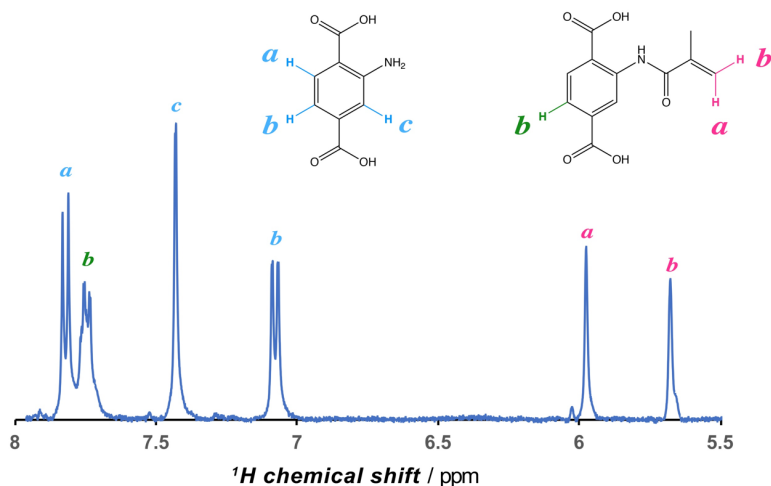
**Figure B20.** Solid-state DNP enhanced  $^{15}\text{N}$ - $^1\text{H}$  CP-MAS HETCOR NMR spectrum of MIL-53(Al)-NH<sub>2</sub>/MMA after post-synthetic modification.

**Table B5.** TGA and Ar physisorption data for MIL-53(Al)-NH<sub>2</sub> and MIL-53(Al)-NH<sub>2</sub>/MMA.

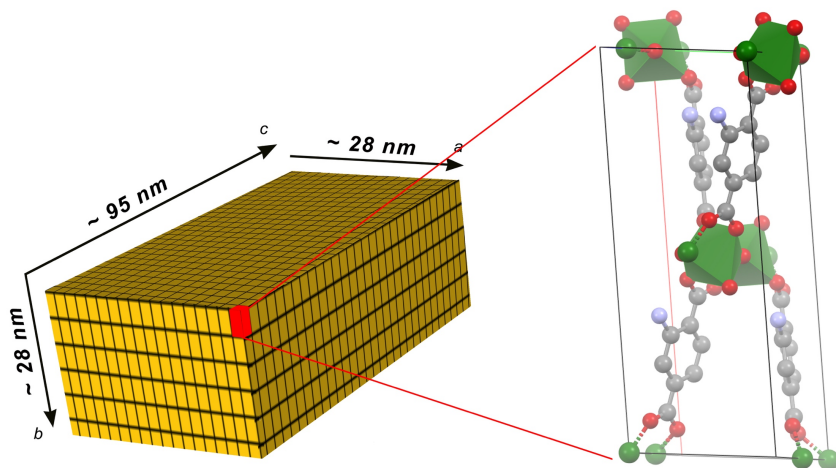
Sample	Surface area (m <sup>2</sup> ·g <sup>-1</sup> )			TGA
	S <sub>BET</sub>	S <sub>micro</sub>	S <sub>ext</sub> <sup>a</sup>	Δm/m <sub>0</sub> (%) <sup>b</sup>
MIL-53(Al)-NH <sub>2</sub>	370	150	220	68
MIL-53(Al)-NH <sub>2</sub> /MMA	303	43	260	80

<sup>a</sup> Mesopore surface area is obtained from the *t*-plot applied to the Ar isotherm<sup>b</sup> Value corresponds to the mass loss step observed on thermogravimetric curve in region 350-600 °C**Figure B21.** FTIR spectra of MIL-53(Al)-NH<sub>2</sub> before (a) and after (b) post-synthetic modification with MMA group.





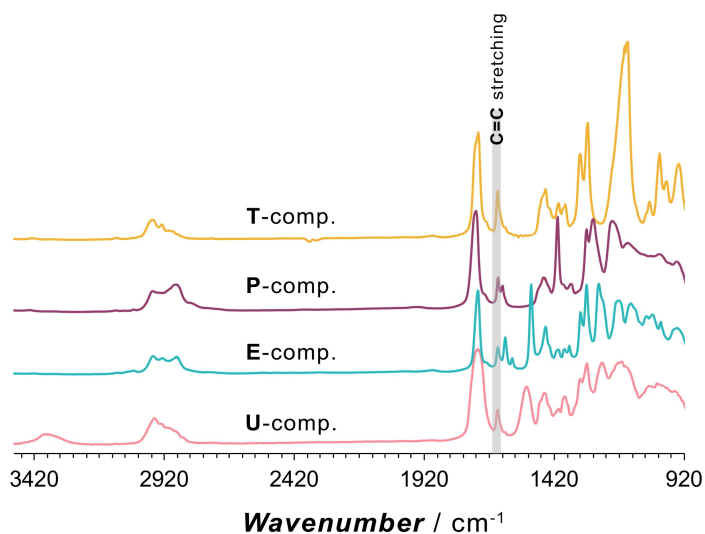
**Figure B22.** Liquid state  $^1\text{H}$  NMR spectrum of MIL-53(Al)-NH<sub>2</sub>/MMA digestion crude in DMSO-d<sub>6</sub>.



**Figure B23.** Schematic representation of MIL-53(Al)-NH<sub>2</sub> nanoparticle with ~95 nm × 28 nm × 28 nm dimensions (Fig. B7) and unit cell arrangement of *np*-form of the framework with respect to the crystal faces. Image showing the surface fraction of the linkers (20%) exposed to PSM and structure orientation within unit cell respective to the nanocrystal facets.

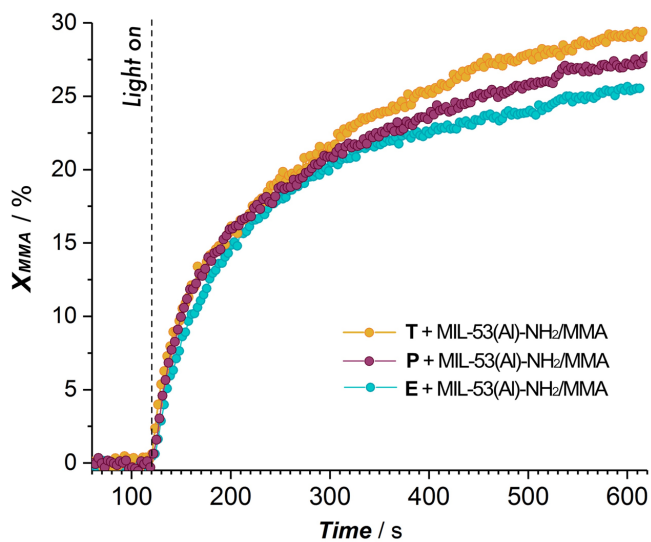
**Table B6.** Viscosity of commercial photocurable methacrylic systems at 25 °C.

Component	Sample code	Viscosity (cP)
SR350D	<b>T</b>	65.7
CN501	<b>P</b>	65
SR540	<b>E</b>	575
CN1963	<b>U</b>	1740

**Figure B24.** ATR-FTIR spectra for T-, P-, E- and U-components with the highlight of characteristic C=C stretching ( $\sim 1640\text{ cm}^{-1}$ ) of methacrylic group.

**Table B7.** Data of kinetic characteristics of photocurable systems with and without MOF additive.

Components		Sample code	$X_{\text{MMA}}^{\text{total}}$ (%)	$v_{\text{XMMA}}^{50\%}$ (%·s <sup>-1</sup> )
Comm.	MOF			
SR350D	–	<b>T</b>	27	1.50
CN501	–	<b>P</b>	25	2.40
SR540	–	<b>E</b>	24	1.55
CN1963	–	<b>U</b>	15	0.75
SR350D	MIL-53-NH <sub>2</sub> /MMA	<b>T/MIL-53-NH<sub>2</sub>/MMA</b>	30	0.55
CN501	MIL-53-NH <sub>2</sub> /MMA	<b>P/MIL-53-NH<sub>2</sub>/MMA</b>	27	0.50
SR540	MIL-53-NH <sub>2</sub> /MMA	<b>E/MIL-53-NH<sub>2</sub>/MMA</b>	25	0.39

**Figure B25.** Methacrylate group conversion ( $X_{\text{MMA}}$ , %) curves for formulations containing MIL-53(Al)-NH<sub>2</sub>/MMA and different oligomers.

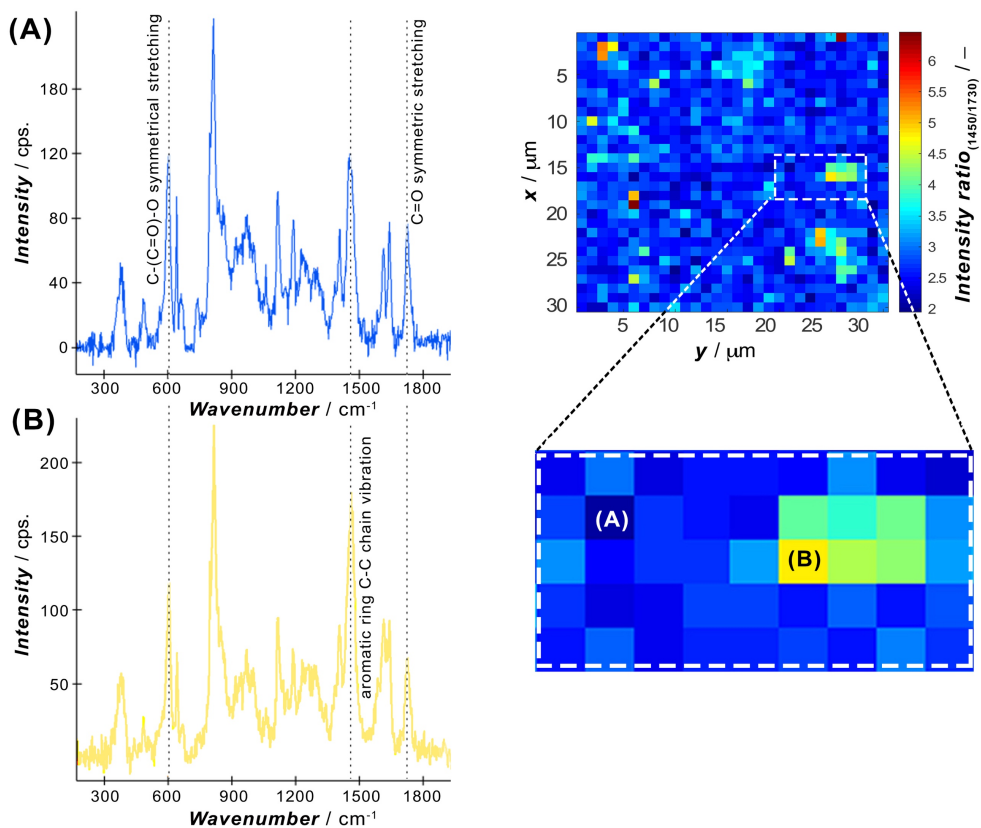


**Figure B26.** Raman spectra and characteristic band assignment corresponding to (A) and (B) pixels on the color scaled confocal microscopy map (inset).

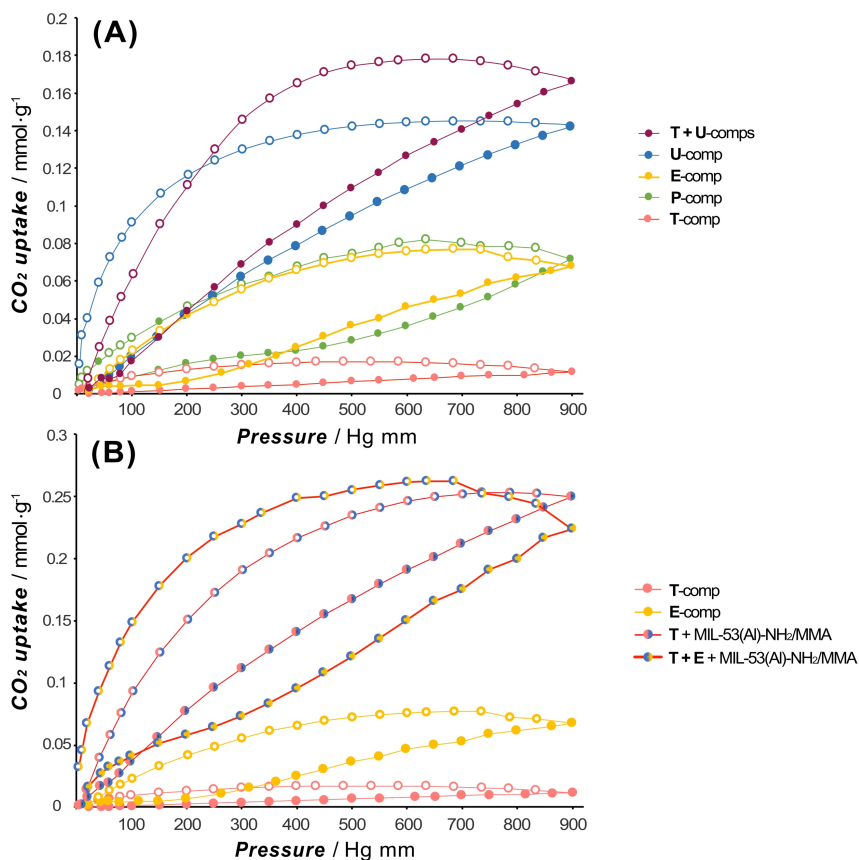


**Figure B27.** CO<sub>2</sub> adsorption isotherms of (A) membranes 3D printed from T-, P-, E- and U-commercial oligomers and T+U mixture, and (B) of membranes 3D printed from MIL-53(Al)-NH<sub>2</sub>/MMA containing ink mixtures acquired at 273 K. Filled symbols correspond to the adsorption branch and open symbols to the desorption.

**Table B8.** Mechanical data of photocurable systems and MIL-53(Al)-NH<sub>2</sub>/MMA contained ink formulations.

Sample code	$\epsilon_R$ (%) <sup>a</sup>	$\sigma_R$ (MPa) <sup>b</sup>	Young's modulus (GPa)	$\tan \delta$ (-) <sup>c</sup>	$\delta$ (°) <sup>d</sup>
U-comp	0.67	50.6	7.6	0.092	5.25
T-comp	1.82	47.8	2.7	0.081	4.66
T / MIL-53-NH <sub>2</sub> /MMA	1.20	26.0	2.2	0.076	4.36
P-comp	2.15	68.3	3.3	0.112	6.42
P / MIL-53-NH <sub>2</sub> /MMA	1.25	44.4	3.6	0.091	5.20
E-comp	2.75	30.2	1.1	0.120	6.86
E / MIL-53-NH <sub>2</sub> /MMA	0.80	11.9	1.6	0.113	6.47
2/3T+1/3E-comps	1.58	31.3	2.0	0.080	4.59
2/3T+1/3E / MIL-53-NH <sub>2</sub> /MMA	1.04	25.9	2.5	0.071	4.06

<sup>a</sup> Strain at break ( $\epsilon_R$ , %).

<sup>b</sup> Stress at break ( $\sigma_R$ , MPa).

<sup>c</sup> Phase difference in stress and strain ( $\delta$ , degrees).

<sup>d</sup> Damping factor ( $\tan \delta$ )

Mechanical analyses were performed on stress-strain data curves determining the strain at break ( $\epsilon_R$ ) and stress at break ( $\sigma_R$ ) values by extrapolating the last point of the curve on abscise and ordinate axes, respectively.

Young's modulus was determined from corresponding stress-strain curves as a slope coefficient on the linear fits.

The damping properties of the composites during tension or compression were expressed in terms of the stress and strain relations, and defined by following equation:

$$\tan \delta = \frac{E''}{E'} \quad (\text{eq. B1})$$

where  $\tan \delta$  is so-called damping factor,  $E''$  and  $E'$  are loss modulus and storage modulus, respectively.

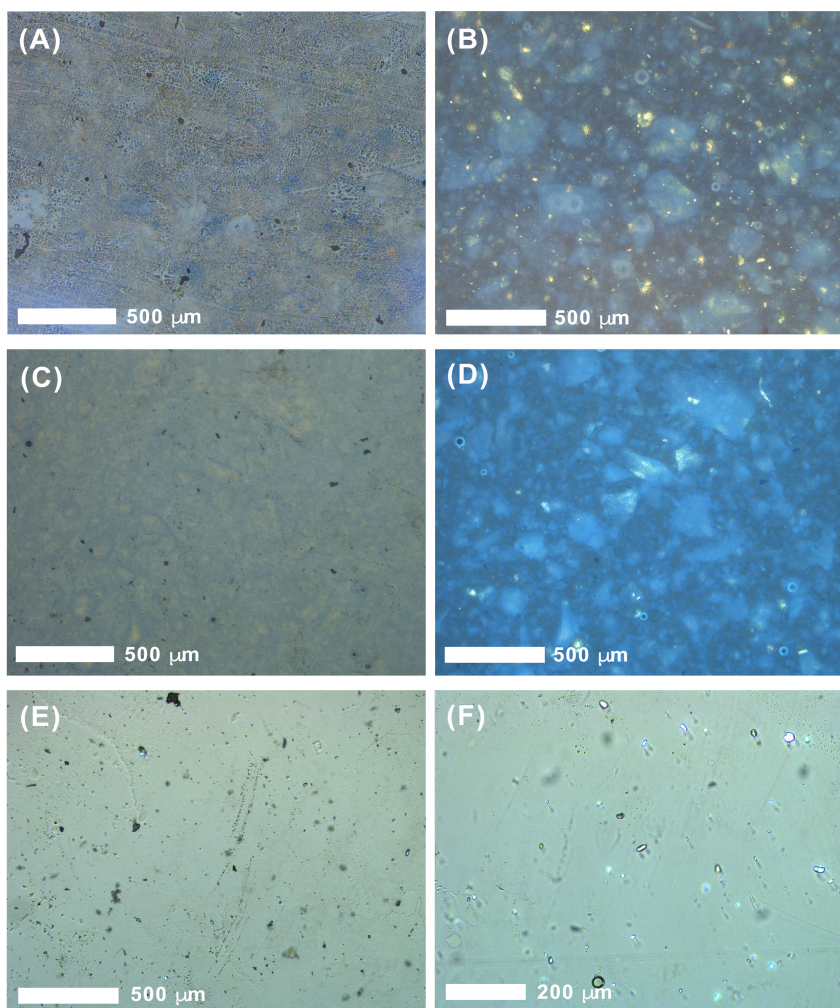


**Figure B28.** Micrographs of 3D printed composites containing MIL-53(Al)-NH<sub>2</sub>/MMA in T- (A), P- (C) and E-matrix (E) under reflected light and (B, D, F) the same under crossed polarizers.



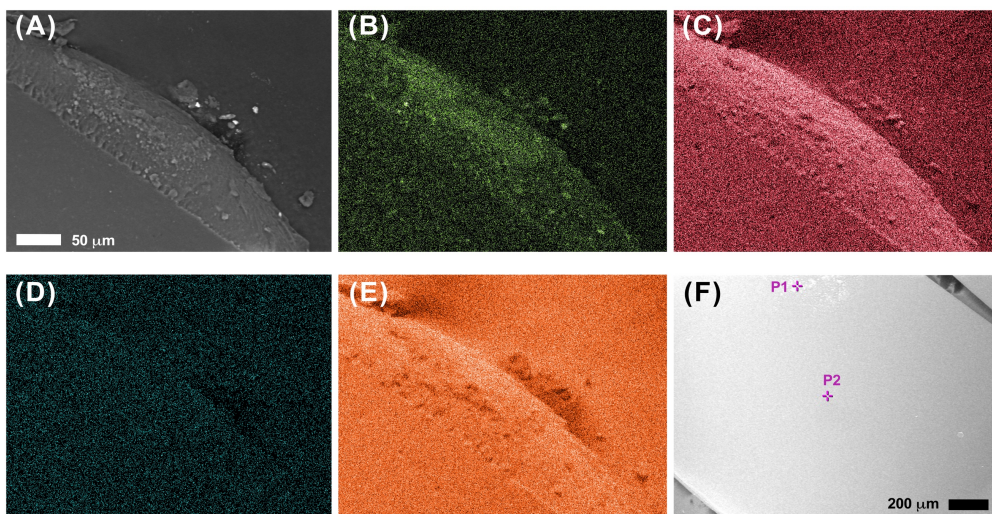


**Figure B29.** SEM-EDX maps of **T/MIL-53(Al)-NH<sub>2</sub>/MMA** 3DP composite: (A) survey image and corresponding to Al (B), O (C), P (D), C (E) *K*-edges maps. (F) SEM image of the membrane and two locations used for the elemental analysis.

**Table B9.** Elemental analysis data derived obtained by EDX from the two locations of 3DP membrane according to Figure B29F.

Element	Relative mass (%)	
	Point 1 (P1)	Point 2 (P2)
Al	1.42	1.81
C	76.81	69.54
O	21.47	28.49
P	0.30	0.16



**Table B10.** Degree of the crosslinking (DC, %) of photocurable systems with and without MOF additive.

Components		Sample code	DC (%)
Comm.	MOF		
SR350D	–	<b>T</b>	96.2
CN501	–	<b>P</b>	97.4
SR540	–	<b>E</b>	99.7
CN1963	–	<b>U</b>	93.6
SR350D	MIL-53-NH <sub>2</sub> /MMA	<b>T/MIL-53-NH<sub>2</sub>/MMA</b>	93.9
CN501	MIL-53-NH <sub>2</sub> /MMA	<b>P/MIL-53-NH<sub>2</sub>/MMA</b>	94.7
SR540	MIL-53-NH <sub>2</sub> /MMA	<b>E/MIL-53-NH<sub>2</sub>/MMA</b>	92.8

**Table B11.** Thermogravimetric (TGA) and differential scanning calorimetry (DSC) data for photocurable inks with and without MOF additive.

Components		Sample code	$T_d$ (°C)	$T_g$ (°C)	$\Delta m/m_0$ (%)
Comm.	MOF				
SR350D	–	<b>T</b>	461.0	155.7	96.5
CN501	–	<b>P</b>	432.5	84.4	98.0
SR540	–	<b>E</b>	428.0	180.4	97.3
CN1963	–	<b>U</b>	387.5	173.6	99.4
SR350D	MIL-53-NH <sub>2</sub> /MMA	<b>T/MIL-53-NH<sub>2</sub>/MMA</b>	438.0	145.3	87.3
CN501	MIL-53-NH <sub>2</sub> /MMA	<b>P/MIL-53-NH<sub>2</sub>/MMA</b>	429.5	79.5	89.7
SR540	MIL-53-NH <sub>2</sub> /MMA	<b>E/MIL-53-NH<sub>2</sub>/MMA</b>	432.5	190.3	86.3

$T_d$  - temperature at which a maximum mass loss velocity is observed.

$T_g$  - glass transition temperature.

$\Delta m$  - total mass loss in air atmosphere.

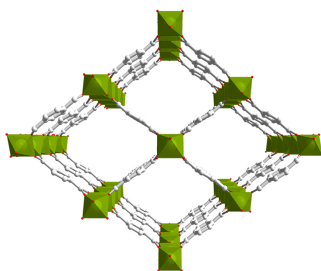
**Table B12.** Summary of gas separation performance obtained with 3DP polymer and 3DP MOF-polymer composite membranes (12 wt.% MOF loading) under several operation conditions.

Membrane	T-comp.		T + MIL-53-NH <sub>2</sub> /MMA	
Thickness (μm)	48 ± 2		57 ± 1	
Temperature	323 K	373 K	323 K	373 K
ΔP (bar)	1	1	1	1
P <sub>H<sub>2</sub></sub> (Barrer)	9.4 ± 0.4	41.9 ± 12.6	229.3 ± 79.3	501.4 ± 81.9
P <sub>CO<sub>2</sub></sub> (Barrer)	4.8 ± 1.4	39.9 ± 9.3	119.6 ± 14.4	345.9 ± 87.1
H <sub>2</sub> /CO <sub>2</sub> selectivity (-)	1.9 ± 0.5	1.1 ± 0.1	1.9 ± 0.6	1.5 ± 0.2

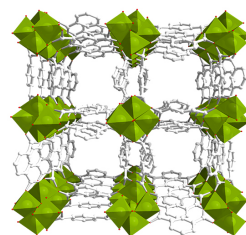


# NANOSHEETS OF NON-LAYERED ALUMINIUM METAL-ORGANIC FRAMEWORKS THROUGH A SURFACTANT-ASSISTED METHOD

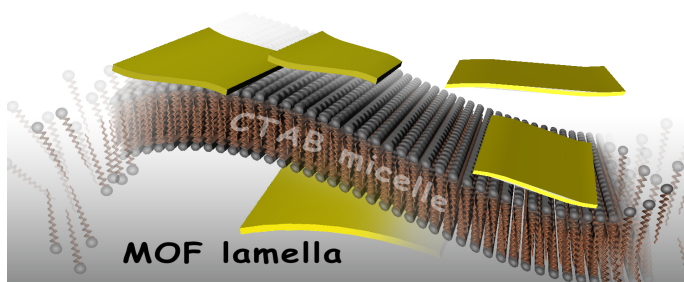
## Chapter



MIL-53(**Al, Ga**)-NH<sub>2</sub>



CAU-10(**Al**)-**R**  
**R** = **H, NH<sub>2</sub>**



This chapter is based on the following publication:

A. Pustovarenko, M. G. Goesten, S. Sachdeva, M. Shan,  
Z. Amghouz, Y. Belmabkhout, A. Dikhtiarenko, T. Rodenas,  
D. Keskin, I. K. Voets, B. M. Weckhuysen, M. Eddaoudi,  
L. C. P. M. de Smet, E. J. R. Sudhölter, F. Kapteijn, B. Seoane,  
J. Gascon

*Adv. Mater.* **2018**, 30, 1707234

## 4

---

### Abstract

During the last decade, the synthesis and application of metal-organic framework (MOF) nanosheets has received growing interest, showing unique performances for different technological applications. Despite the potential of this type of nanolamellar materials, the synthetic routes developed so far are restricted to MOFs possessing layered structures, limiting further development in this field. Here, a bottom-up surfactant-assisted synthetic approach is presented for the fabrication of nanosheets of various nonlayered MOFs, broadening the scope of MOF nanosheets application. Surfactant-assisted preorganization of the metallic precursor prior to MOF synthesis enables the manufacture of nonlayered Al-containing MOF lamellae. These MOF nanosheets are shown to exhibit a superior performance over other crystal morphologies for both chemical sensing and gas separation. As revealed by electron microscopy and diffraction, this superior performance arises from the shorter diffusion pathway in the MOF nanosheets, whose 1D channels are oriented along the shortest particle dimension.

---

## 4.1 INTRODUCTION

The synthesis of 2D nanomaterials has arisen keen interest within the scientific and technological communities.<sup>1-4</sup> This interest originates from their unique physicochemical properties, highly desirable for a wide range of applications.<sup>3-5</sup> Examples of 2D nanomaterials that have been synthesized as single- and few-layer nanosheets are graphene and its group 14 analogues, transition-metal dichalcogenides, boron nitride, 2D layered oxides and hydroxides,<sup>3-4</sup> and recently, metal-organic frameworks (MOFs).<sup>6-7</sup> The last example is particularly exciting: MOFs are crystalline coordination compounds built-up from metal atoms or clusters linked together by the organic ligands.<sup>8-9</sup> Their metal-organic make-up allows for rich pre and post-synthetic chemistry, which in some cases can lead to a degree of rational design.<sup>10-11</sup> This opportunity for design, together with exceptional porosity, endows the MOFs with great potential in many different technological fields,<sup>12-19</sup> their first commercial applications being recently announced.<sup>20</sup>

MOF nanosheets have been prepared by various top-down and bottom-up approaches. As a top-down approach, the MOF nanosheets have been isolated by exfoliation,<sup>18-19,21-28</sup> one of the most extended strategies to synthesize 2D nanomaterials.<sup>1-4</sup> Bottom-up approaches rely on diffusion-mediated<sup>17</sup> and templated synthesis<sup>3,12,14-15,29-35</sup> and the use of small capping agents or modulators to control crystal growth in certain directions.<sup>16, 32-33</sup> Despite the advances reported, the applicability of the synthetic methods developed so far is mainly restricted to the MOFs possessing a layered structure. These MOFs consist of stacked 2D layers, being more prone to the formation of nanosheets. However, this subfamily of compounds only embodies a small fraction of the MOF structures reported to date, severely limiting the potential of this promising type of 2D nanomaterials. To the best of our knowledge, only one very recent example has been reported so far on the top-down exfoliation of 3D MOFs.<sup>34</sup> However, top-down approaches are often associated with particle fragmentation and reaggregation of the detached sheets. A bottom-up approach for the synthesis of 3D MOF has never been reported.

Within this context, we report a novel bottom-up surfactant-assisted approach whereby several well-known nonlayered 3D Al-containing MOFs can be prepared as freestanding lamellae. Our approach is based on decoupling the surfactant-assisted preassembly of the metallic species in solution from the MOF synthesis, gaining control over the crystallization process. In particular, we have selected MIL-53(Al)-NH<sub>2</sub>,<sup>35</sup> CAU-10(Al)-H and CAU-10(Al)-NH<sub>2</sub>.<sup>36</sup> Both MOF topologies, *i.e.* MIL-53 and CAU-10, are based on inorganic *trans*-connected AlO<sub>4</sub>(μ<sub>2</sub>-OH)<sub>2</sub> octahedra forming linear chains and *cis*-connected AlO<sub>6</sub> octahedra forming helical chains, respectively. For both topologies, these inorganic chains are connected through dicarboxylate linkers to make up the scaffold.<sup>36-37</sup> In this work we demonstrate that the new 2D

materials based on these MOF topologies provide a remarkable playground for membrane separation, chemical sensing, and device fabrication in general.

## 4.2 EXPERIMENTAL SECTION

### 4.2.1 Materials

All chemicals were used as received, without further purification.  $\text{Al}(\text{NO}_3)_3 \cdot 9\text{H}_2\text{O}$ ,  $\text{AlCl}_3 \cdot 6\text{H}_2\text{O}$ ,  $\text{Ga}(\text{NO}_3)_3$ , 2-aminoterephthalic acid (2-ATA), isophthalic acid (IPA), 5-aminoisophthalic acid (5-AIPA), sodium hydroxide (NaOH), hexadecyltrimethylammonium bromide (CTAB, Sigma-Aldrich,  $\geq 98\%$ ), tetramethylammonium hydroxide 25 wt.% aqueous solution (25% w/w TMAOH), chloroform ( $\text{CHCl}_3$ ), tetrahydrofuran (THF), anhydrous N,N-dimethylformamide (DMF), anhydrous acetonitrile ( $\text{CH}_3\text{CN}$ ), anhydrous methanol (MeOH), anhydrous 2-propanol ( $\text{C}_3\text{H}_7\text{OH}$ ), anhydrous 1-butanol ( $\text{C}_4\text{H}_9\text{OH}$ ), anhydrous dichloromethane ( $\text{CH}_2\text{Cl}_2$ ) were of analytical grade (Sigma-Aldrich). Polyimide (PI) Matrimid® 5218 (kindly supplied by Huntsman Advanced Materials,  $M_w \approx 80000 \text{ g}\cdot\text{mol}^{-1}$  and  $M_n \approx 11000 \text{ g}\cdot\text{mol}^{-1}$ ) was degassed at 453 K overnight under vacuum to remove the adsorbed water.

### 4.2.2 Syntheses and protocols

#### 4.2.2.1 Synthesis of MIL-53(Al)-NH<sub>2</sub> nanoparticles

MIL-53(Al)-NH<sub>2</sub> nanoparticles were synthesized following our previously reported reflux procedure.<sup>38</sup> In a typical synthesis, 1.90 g 2-aminoterephthalic acid (10.50 mmol, Sigma-Aldrich, 99 %) was dissolved in 10.5 mL of a 2 M NaOH aqueous solution at room temperature. Then, 3.94 g  $\text{AlCl}_3 \cdot 6\text{H}_2\text{O}$  (16.30 mmol, Sigma-Aldrich,  $\geq 99.0\%$ ) was added to a separated vial and both volumes were increased to a total of 75 mL by addition of distilled water. The reactants were mixed and treated at reflux temperature for 3 days without stirring. The resulting yellow powder was filtered under vacuum and activated to remove organic species trapped within the pores with N,N'-dimethylformamide (DMF, Sigma-Aldrich,  $>99.8\%$ ) at 403 K, and subsequently with methanol under reflux, overnight. Finally, the powder was thoroughly washed twice with ethanol and dried at 373 K under vacuum.

#### 4.2.2.2 Synthesis of MIL-53(Al)-NH<sub>2</sub> MOF nanosheets and optimization procedures

Freestanding MIL-53(Al)-NH<sub>2</sub> nanosheets were synthesized from two different aqueous solutions: one containing 0.84 g  $\text{Al}(\text{NO}_3)_3 \cdot 9\text{H}_2\text{O}$  (2.2 mmol, Sigma-Aldrich,  $>98\%$ ) and the corresponding amount of CTAB (Sigma-Aldrich,  $\geq 98\%$ ), see Table C1, and the other containing 0.29 g 2-aminoterephthalic acid (1.6 mmol, Sigma-Aldrich, 99%) and 2 mL tetramethylammonium hydroxide (TMAOH, Sigma-Aldrich, 25 wt.%) in 10 and 5 mL distilled

water, respectively. Both mixtures were separately stirred until complete dissolution and transferred into two different wall-separated compartments of a Teflon<sup>®</sup>-lined stainless-steel autoclave. Our custom designed Teflon<sup>®</sup> autoclave is 45 mL of total volume and divided up to the half of its height on two chambers of 10 mL and 5 mL of volume each. The autoclave was then placed in an oven and heated to 373 K, temperature at which it was kept for 1 h. Then, the autoclave was turned upside down to let the two solutions from the separate chambers mix and react at 373 K for 16 h. After cooling, the formed yellow solid product was collected by centrifugation for 10 min at 6000 rpm and washed three times with water followed by another three times with ethanol through redispersion and centrifugation. The resulting washed material was finally transferred to a Petri dish and dried under vacuum at 353 K for 16 h or left suspended in THF (Sigma-Aldrich, anhydrous) until the preparation of the MOF composites. The optimal CTAB amount at which the freestanding nanolamellae formed is 0.40 g (1.1 mmol) following the standard synthetic protocol detailed above.

#### 4.2.2.3 Generalization of the surfactant-assisted synthesis approach to other MOFs

To investigate the scope of our surfactant-assisted MOF nanosheet synthesis strategy, the method was extended to other MOF structures.

CAU-10(Al)-H lamellae were synthesized from two different aqueous solutions: one containing 0.84 g  $\text{Al}(\text{NO}_3)_3 \cdot 9\text{H}_2\text{O}$  (2.2 mmol, Sigma-Aldrich, >98 %) and the corresponding amount of hexadecyltrimethylammonium bromide (CTAB, Sigma-Aldrich, ≥98 %), see Table C1 entry 1-7, and the other containing 0.27 g isophthalic acid (1.6 mmol, Sigma-Aldrich, 99 %) and 2 mL tetramethylammonium hydroxide (TMAOH, Sigma-Aldrich, 25 wt.%) in 8 and 5 mL distilled water, respectively. Both mixtures were separately stirred until complete dissolution and transferred into two different wall-separated compartments of a Teflon<sup>®</sup>-lined stainless-steel autoclave. The autoclave was then placed in an oven and heated to 373 K, temperature at which it was kept for 1 h. Afterwards, the autoclave was turned upside down so as to let the two solutions from the separate chambers mix and react at 373 K for 16 h. After cooling, the formed solid product was collected by centrifugation for 10 min at 6000 rpm and washed 3 times with water followed by another 3 times with ethanol through re-dispersion and centrifugation. The resulting washed material was finally transferred to a Petri dish and dried under vacuum at 353 K for 16 h or left suspended in tetrahydrofuran (THF, Sigma-Aldrich, anhydrous) until the preparation of the MOF composites. Exfoliation of CAU-10(Al)-H material was performed by ultrasonication of the suspension in THF for 40 min.



CAU-10(Al)-NH<sub>2</sub> lamellae were synthesized following a similar procedure to that used to prepare CAU-10(Al)-H, but using 0.28 g 5-aminoisophthalic acid (1.6 mmol, Sigma-Aldrich, 99 %) instead of 0.27 g isophthalic acid.

Similarly to MIL-53(Al)-NH<sub>2</sub>, CAU-10(Al)-H and CAU-10(Al)-NH<sub>2</sub>, MIL-53(Ga)-NH<sub>2</sub> sheets were synthesized from two different aqueous solutions: one containing 0.56 g Ga(NO<sub>3</sub>)<sub>3</sub> (2.2 mmol, Sigma-Aldrich, >98 %) and 0.40 g CTAB (1.1 mmol, CTAB, Sigma-Aldrich, ≥98 %) and the other containing 0.28 g 2-aminoterephthalic acid (1.6 mmol, Sigma-Aldrich, 99 %) and 2 mL tetramethylammonium hydroxide (TMAOH, Sigma-Aldrich, 25 wt.%) in 8 and 5 mL distilled water, respectively. All preparation procedures, synthesis conditions and post-synthetic treatments were the same as in case of the MIL-53(Al)-NH<sub>2</sub> nanosheets synthesis.

#### 4.2.2.4 Synthesis of MOF-polymer composite materials and membrane casting

To prepare the MOF-based MMMs, the protocol previously reported by Rodenas *et al.*<sup>17</sup> was followed in which MIL-53(Al)-NH<sub>2</sub> nanosheets were dispersed in tetrahydrofuran and sonicated for 1 h in an ultrasonic bath (50 W and 60 Hz). The polymer Matrimid® 5218 (0.4 g), previously degassed under vacuum at 453 K for 24 h, was subsequently added stepwise to the MIL-53(Al)-NH<sub>2</sub> suspension in two portions of 0.2 g, keeping a mass ratio solvent/(MOF+polymer) of 90/10. The MOF/polymer mass ratio was selected to achieve the desired final MOF loading in the composite materials (*i.e.* 8 and 16 wt.%). The resulting suspensions were shaken in a laboratory shaker (5.3 kHz) at room temperature for 12 h. Prior to the membrane casting, three cycles were carried out each consisting of dispersing the casting suspension in an ultrasonic bath for 15 min, followed by shaking for 30 min. Afterwards, the viscous suspension was poured on a flat surface and shaped as a thin film under shear forces by a doctor blade knife. The solvent was then removed by evaporation, first by natural convection at room temperature for 16 h, followed by a treatment at 453 K for 12 h under vacuum. This temperature was selected below the glass transition temperature ( $T_g$ ) of the polymer (590 K) to prevent the transition into a rubbery-state. The final thickness of the resulting composite films was evaluated using a digital micrometer (Mitutoyo, Quickmike Series). For reference purposes, neat polymer membranes were prepared following an identical procedure without MOF incorporation.

#### 4.2.2.5 Fabrication of MOF-coated devices

The sensor devices were fabricated over *p*-doped silicon substrates to obtain planar capacitive electrodes as described in our previous study.<sup>39</sup> Briefly, the devices were designed to obtain 4 parallel meander-patterned aluminium electrodes by photolithography with width

of 0.52  $\mu\text{m}$  and a gap of 1  $\mu\text{m}$ . The total electrode area was obtained as  $\sim 2.1 \text{ mm}^2$  leading to high bare capacitance of the sensor devices ( $\sim 22 \text{ pF}$ ). In order to prepare  $\sim 10 \text{ }\mu\text{m}$  thick layers of MIL-53(Al)- $\text{NH}_2$  nanoparticles and nanosheets over these devices, 22.5 mg MOF particles were dispersed in 480 mg tetrahydrofuran (THF). 5  $\mu\text{L}$  of the prepared dispersions were drop-casted over the electrode area of the devices followed by drying in vacuum at 393 K.

### 4.2.3 Characterization methods

#### 4.2.3.1 General characterizations

Small-Angle X-ray Scattering (SAXS) measurements were performed on a SAXSLAB GANESHA 300 XL SAXS system equipped with a GeniX 3D Cu Ultra Low Divergence micro focus sealed tube source producing X-rays with a wavelength  $\lambda = 1.54 \text{ \AA}$  at a flux of  $1 \times 10^8$  ph/s and a Pilatus 300K silicon pixel detector with  $487 \times 619$  pixels of  $172 \times 172 \text{ }\mu\text{m}$ . Silver behenate was used for calibration of the beam center and the  $q$  range. An aqueous solution containing  $\text{Al}(\text{NO}_3)_3 \cdot 9\text{H}_2\text{O}$  and CTAB in 10 mL of distilled water was loaded into a 1 mm borosilicate capillary (Hilgenberg GmbH, Germany). The solution was then heated up to 373 K, temperature at which small-angle (SAXS) patterns were acquired. Subsequently, a solution of deprotonated linker was pre-heated at 373 K and added to the reaction mixture. Immediately thereafter, another SAXS pattern was acquired.

*Scanning electron microscopy* (SEM) experiments were conducted in a JEOL JSM 6010LA microscope equipped with a Field-Emission (FE) electron beam source and operated at an accelerating voltage of 20 kV. MOF lamellae specimens were prepared by applying a couple of drops from a suspension of the material in tetrahydrofuran and let dry over the sample holder. To acquire the FE-SEM images shown, it was necessary to sputter the specimens with Au conductive layer.

*High resolution transmission electron microscopy* (HRTEM), selected area electron diffraction (SAED) and energy-dispersive X-ray (EDX) line profiles were recorded on a JEOL JEM-2100F microscope operated at an accelerating voltage of 120 kV, equipped with a field emission gun (FEG) and an ultra-high resolution pole-piece that provided a point-resolution better than 0.19 nm. The samples for TEM were dispersed in methanol, sonicated and sprayed on a carbon-coated copper grid and then allowed to air-dry. The analysis of MOF-polymer composites was performed using cryo-TEM.

*Atomic force microscopy* (AFM) topography images were recorded in air with a NTEGRA (NT-MDT) microscope operating in tapping mode. Rectangular silicon cantilevers HA\_NC from NT-MDT with a spring constant of  $k \sim 12 \text{ N/m}$ , resonance frequency of  $\omega_0 \sim 235 \text{ kHz}$  and tip

radius of  $r \sim 8$  nm were used. The MOF samples were applied to a previous annealed silicon wafer substrate. Before microscopy inspection, a couple of drops from a suspension of MOF nanosheets in tetrahydrofuran were drop cast and let dry over the silicon substrate.

*Thermogravimetric analysis* (TGA) was applied to determine the MOF purity and content in the MOF-polymer composites. The experiments were performed in a Mettler Toledo TGA/SDTA851e apparatus by heating the sample from room temperature to 1273 K at a rate of  $5 \text{ K} \cdot \text{min}^{-1}$  in flow of synthetic air ( $100 \text{ mL} \cdot \text{min}^{-1}$ ). The MOF content was derived from the mass of the residual  $\text{Al}_2\text{O}_3$  after complete combustion.

*Surface tension.* The Wilhelmy plate method was employed to measure the equilibrium surface tension of CTAB/ $\text{Al}^{3+}$  solutions, making use of a KRÜSS GmbH digital tensiometer K100MK2 equipped with a platinum plate. The plate was washed thoroughly with ethanol and carefully dried after each series of measurements. The CTAB solutions were prepared separately at two concentration ranges: low concentrations and high concentrations which have been explored in the MIL-53(Al)- $\text{NH}_2$  nanolamellae synthesis optimization. The amount of  $\text{Al}(\text{NO}_3)_3$  salt was kept constant,  $0.22 \text{ mol} \cdot \text{L}^{-1}$ . Special attention has been paid to the temperature stabilization of the solution in the measuring vessel in the tensiometer chamber (20 min).

*Dynamic light scattering* (DLS) was measured at  $30^\circ \text{C}$  using a Zetasizer Nano ZEN 3600 instrument (Malvern Instruments) equipped with a helium-neon 4-mW laser (wavelength of 632.8 nm). The scattering angle was equal to  $173^\circ$ . Prior to measurements, the samples of low CTAB concentrations (see caption of Fig. C1, Appendix C) were dust-removed by filtration into the measurement cell through Millipore membrane filters with pore diameter of  $0.45 \mu\text{m}$ . The samples of high CTAB concentrations were filtered warm (at  $100^\circ \text{C}$ ) directly into the measurement cell, cooled down and kept at  $30^\circ \text{C}$  for 1 h prior the measurements. The concentration of  $\text{Al}(\text{NO}_3)_3$  in all prepared sample solutions was  $0.22 \text{ mol} \cdot \text{L}^{-1}$ .

#### 4.2.3.2 Powder X-ray diffraction (PXRD)

Powder X-ray diffraction (PXRD) was used to study the crystalline structure of the MOF materials. PXRD patterns were recorded using a Bruker D8 Advance diffractometer operated with  $\text{Co } K\alpha$  radiation ( $\lambda = 1.78897 \text{ \AA}$ ). The samples were scanned using a step size of  $0.02$ – $0.04^\circ$  and a scan speed of  $1 \text{ s}$  per step in a continuous scanning mode. MOF nanoparticles specimens were prepared by filling the holder with the dry powder. In the case of MOF lamellae, the specimen was prepared by slow evaporation of a couple of drops from a suspension of the material in tetrahydrofuran over a zero-background single-crystal silicon sample holder.

The mass ratios of MIL-53(Al)-NH<sub>2</sub> orthorhombic *Imma* and monoclinic *Cc* framework configurations were determined via quantitative calculation based on the PXRD data using the PowderCell software.<sup>40</sup> Quantification of phase content was carried out with whole powder pattern decomposition method (WPPM) routine<sup>41</sup> where the percentage of each phase was calculated as

$$c_i = I_i \cdot \rho_i \cdot k_i \cdot \mu^* = I_i \cdot \rho_i \cdot k_i \cdot \sum c_i \cdot \mu_i^* \quad (eq. 4.1)$$

where  $c_i$  is the percentage of  $i$ -phase,  $\rho_i$  the X-ray density of  $i$ -phase,  $k_i$  the calibration coefficient of  $i$ -phase,  $\mu^*$  the mass absorption coefficient of the specimen and  $I_i$  is the intensity of the peaks of  $i$ -phase. In our case, the density and mass absorption coefficient for orthorhombic *Imma* and monoclinic *Cc* phases were known from crystallographic information files reported previously.<sup>42</sup> During the analysis of each experimental data, simulated PXRD patterns for both orthorhombic *Imma* and monoclinic *Cc* components was normalized according to

$$I_i = \frac{I_i^0}{(V_{uc}^2 \cdot \rho_i)} = \frac{I_i^0}{(V_{uc} \cdot m_i)} \quad (eq. 4.2)$$

where  $\rho_i$  is the X-ray density of  $i$ -phase,  $V_{uc}$  the unit cell volume of  $i$ -phase,  $m_i$  is unit cell mass of  $i$ -phase. Thus, the weight fractions are easily determined since the scale factors are normally refined by the program and the densities can be evaluated as long as the unit cell volume and contents are known. So, the weight fraction for  $i$ -component in a mixture of  $n$  phases can be obtained from the equation:

$$W_i \% = \frac{c_{Ni}}{\sum_{i=1}^n c_{Ni}} \cdot 100\% \quad (eq. 4.3)$$

where  $c_{Ni}$  is normalized content value of the  $i$ -phase and  $n$  is number of the phases.

During the WPPM procedure the scale factors for *Imma* and monoclinic *Cc* phases are calculated and their values are used for the percentage determination. The ratio of the scaling factors is used to determine the partial content of each phase within a two-phase sample. Additionally, the background function with the polynomial of the seventh degree, a constant peak width  $W$ , the lattice parameters of both phases, the zero shift of the powder pattern have been fitted during the analysis.

### 4.2.3.3 Gas sorption isotherms

Sorption isotherms of the MOF materials were determined with N<sub>2</sub> (at 77 K) and CO<sub>2</sub> (at 273 K, low pressure region) using a Tristar II 3020 Micromeritics equipment. Prior to the measurements, the adsorbent was outgassed at 423 K under dynamic vacuum for 16 h.

Adsorption equilibrium measurements (high pressure region) of carbon dioxide were performed using a Rubotherm gravimetric-densimetric apparatus G-Hp-Flow, composed mainly of a magnetic suspension balance (MSB) and a network of valves, mass flow meters, and temperature and pressure sensors. The adsorption temperature can be controlled within the range of 77 K to 423 K. In a typical adsorption experiment, the adsorbent is precisely weighed and placed in a basket suspended by a permanent magnet through an electromagnet. Then the cell housing the basket is closed and vacuum or high pressure is applied. The gravimetric method allows the direct measurement of the reduced gas adsorbed amount ( $\Omega$ ). Correction for the buoyancy effect is required to determine the excess amount using equation 4.4:

$$\Omega = m_{\text{excess}} - \rho_{\text{gas}} \cdot (V_{\text{adsorbent}} + V_{\text{ss}}) \quad (\text{eq. 4.4})$$

where  $V_{\text{adsorbent}}$  and  $V_{\text{ss}}$  refer to the volume of the adsorbent and the volume of the suspension system, respectively.

The buoyancy effect resulting from the adsorbed phase may be taken into account *via* correlation with the pore volume or with the theoretical density of the sample. These volumes are determined using the helium isotherm method by assuming that helium penetrates in all open pores of the material without being adsorbed. The density of the gas is determined experimentally using a volume-calibrated titanium cylinder. By weighing this calibrated volume in the gas atmosphere, the local density of the gas is determined. Therefore, simultaneous measurement of adsorption capacity and gas-phase density as a function of pressure and temperature is possible. The pressure is measured using two Drucks high-pressure transducers ranging from 0.5 to 34 bar and 1 to 200 bar, respectively, and one low pressure transducer ranging from 0 to 1 bar. Prior to each adsorption experiment, about 100 mg of the sample was outgassed at 423 K for 12 h under a residual pressure of 10<sup>-6</sup> mbar. The temperature during adsorption measurements was maintained constant using a thermostat-controlled circulating fluid at 273 K.

### 4.2.4 Gas permeation experiments

Round-shaped membrane areas of 3.14 cm<sup>2</sup> were cut from the casted films, placed on a macroporous stainless steel support (316L, 20  $\mu$ m pore size) and mounted in a flange between

Viton O-rings. This flange fit in a permeation module which was placed inside an oven in a permeation setup described elsewhere.<sup>43</sup> An equimolar mixture of CO<sub>2</sub>/CH<sub>4</sub> (100 mL·min<sup>-1</sup> total flow rate) was employed as gas feed. He (3.3 mL·min<sup>-1</sup>) was used as sweep gas for the permeate stream and kept at atmospheric pressure. The trans-membrane pressure difference was adjusted in the range of 3 – 9 bar using a back-pressure controller at the retentate side, being the permeate side at atmospheric pressure. An on-line gas chromatograph equipped with a packed Carboxen 1010 PLOT (30 m × 0.32 mm) column and TCD and FID detectors was used to periodically analyse the permeate stream. Gas separation performance was defined by the separation selectivity and the gas permeabilities ( $P$ ) of the individual components.<sup>44</sup> The permeability for component  $j$  ( $P_j$ ) was calculated as shown in equation (4.5):

$$P_j = \frac{\varphi_{n,j} \cdot \delta}{\Delta p_j \cdot A} \quad (eq. 4.5)$$

where  $\varphi_{n,j}$  denotes the molar flow rate of component  $j$ ,  $\delta$  is the thickness of the membrane,  $\Delta p_j$  the partial pressure difference of component  $j$  across the membrane and  $A$  the membrane area. The SI unit for the permeability is mol·s<sup>-1</sup>·m<sup>-1</sup>·Pa<sup>-1</sup>. However, here gas permeabilities are reported in the widely used non-SI unit Barrer, where 1 Barrer = 3.35·10<sup>-16</sup> mol·m·m<sup>-2</sup>·Pa<sup>-1</sup>·s<sup>-1</sup>. The separation factor or mixed gas selectivity ( $\alpha$ ) was calculated as the ratio of the permeability of the more permeable compound (CO<sub>2</sub>) to the permeability of the less permeable compound (CH<sub>4</sub>) as given in equation (4.6).

$$\alpha = \frac{P_{CO_2}}{P_{CH_4}} \quad (eq. 4.6)$$

#### 4.2.5 Sensing studies

Sensing measurements were performed in a custom-built gas mixing and sensing equipment.<sup>39</sup> The addition of gas vapours to the measurement chamber was carried out by first generating a saturated stream of the vapours in dry N<sub>2</sub> gas and then further diluting it with N<sub>2</sub> to obtain the desired concentration. The saturated stream was generated by passing the dry N<sub>2</sub> through a series of bubblers containing either methanol, 2-propanol or 1-butanol at room temperature. Changes in the concentration of the vapours in gas phase were analysed by correlating it with the changes in the capacitive response of the MOF-coated sensor devices. These measurements were performed by impedance spectroscopy using HP 4284A LCR Meter at a frequency of 20 kHz and voltage of 1 V in a four-probe configuration. Total gas flow rate and temperature during the measurement were kept constant at 200 mL·min<sup>-1</sup> and 301 K.

### 4.3 RESULTS AND DISCUSSION

The bottom-up approach we developed here to synthesize MIL-53(Al)-NH<sub>2</sub> nanosheets makes use of surfactants to gain control over the MOF particle morphology.<sup>33</sup> As schematically shown in Figure 4.1A the synthesis was performed from two different solutions: i) one containing the cationic surfactant hexadecyltrimethylammonium bromide (CTAB) and the metal precursor (Al(NO<sub>3</sub>)<sub>3</sub>·9H<sub>2</sub>O), ii) the other the deprotonated linker, 2-aminoterephthalic acid (2-ATA). Both the solutions were separately heated in order to reach the MIL-53(Al)-NH<sub>2</sub> synthesis temperature, 373 K, and mixed after 1 h. This allows for the surfactant-assisted preorganization of aluminium species, favoured by the known ability of aluminium to form oligomeric structures in solution,<sup>45-46</sup> prior to the MOF formation.

Small-angle X-ray Scattering (SAXS) provides some initial insight into the formation of the 2D material for MIL-53(Al)-NH<sub>2</sub>. After being dissolved in a CTAB solution, the aluminium precursor, Al(NO<sub>3</sub>)<sub>3</sub>·9H<sub>2</sub>O, forms a pre-organized vesicular system (blue points). The appearance of the quasi-Bragg peak, around  $q = 1.6 \text{ nm}^{-1}$ , is typical for an assembly of stacked sheets - a paracrystalline system.<sup>47</sup> The line shape of the quasi Bragg peak, deviates from a Gaussian profile. It is broad, and sharpens towards the top. This indicates secondary disorder within the paracrystalline order; a root-mean square deviation of the  $d$ -spacing, in this case the distance between the stacked sheets.<sup>48</sup> We used a Caillé structure factor to approach this factor of disorder,<sup>49</sup> and obtained an accurate fitting of the quasi-Bragg peak (orange curve). The Caillé model takes into account bending fluctuations within the stacked-sheet system. Its central parameter, the Caillé parameter  $\delta$ , is inversely proportional to the bulk modulus  $B$  and the bending modulus  $K$  of the sheets,  $\delta \propto (KB)^{-1/2}$ . The fitting produces a  $d$ -spacing of 4.34 nm and a Caillé parameter  $\delta$  of 0.42. This signals an ordered yet soft system of stacked sheets that engage in a process of bending deformations.<sup>50</sup> That this soft system is easily perturbed, is seen when linker, 2-ATA, is added. The system reorganizes, paracrystallinity breaks up and the scattering in the low- $q$  region vanishes. Yet now, intensity falls off as  $I(q) \propto q^{-1}$ , which indicates that the scattering entities have retained the high aspect ratio we expect from nanosheets with 1D channels. As confirmed by transmission electron microscopy (TEM), these entities indeed involve free-standing nanolamellae and display an extent of nanosheet bending and folding. We note that this was also reported for other cases of MOF nanosheets.<sup>16,18,28,31</sup> This effect of flexibility hinders an adequate determination of the particle size distribution, but it is clear that nanosheets with submicron lateral dimensions are obtained. Furthermore, from atomic-force microscopy (Fig. C2, Appendix C) the lateral dimensions and thickness of the nanosheets can be assessed, being in the range 140 – 400 nm and 35 – 45 nm.

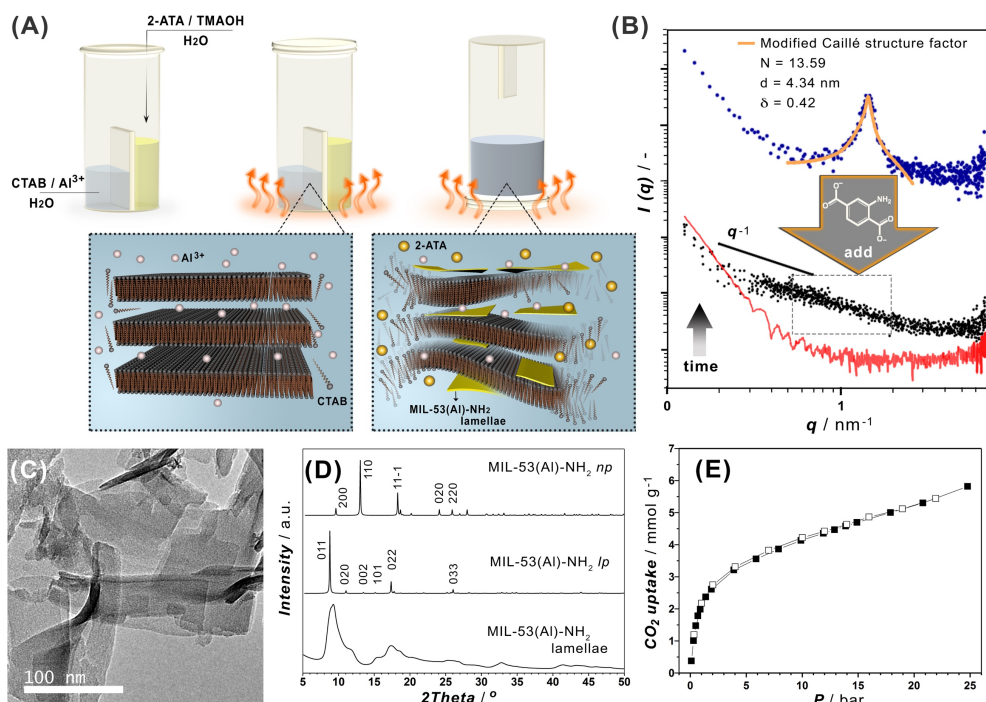


**Figure 4.1.** (A) Schematic representation of the synthetic procedure developed and the formation mechanism of the MIL-53(Al)-NH<sub>2</sub> lamellae. The synthesis was performed from two different solutions: one containing the cationic surfactant hexadecyltrimethylammonium bromide (CTAB) and the metal precursor, the other the linker, 2-aminoterephthalic acid (2-ATA) and a base to deprotonate the linker, tetramethylammonium hydroxide (TMAOH). Both solutions were separately heated at 373 K, and mixed after 1 h. (B) SAXS patterns acquired at 373 K for an aqueous solution of CTAB and Al(NO<sub>3</sub>)<sub>3</sub>·9H<sub>2</sub>O before and after adding the deprotonated linker (blue and black points, respectively). The former pattern is fitted with the Modified Caillé structure factor, orange curve. The red line depicts a background profile. (C) TEM micrograph of the MIL-53(Al)-NH<sub>2</sub> lamellae. (D) XRD pattern of the MOF nanosheets together with the simulated patterns for the *np* and *lp* configurations of MIL-53(Al)-NH<sub>2</sub>. (E) High-pressure CO<sub>2</sub> isotherm for MIL-53(Al)-NH<sub>2</sub> nanosheets at 273 K.

In order to optimize this synthetic methodology allowing the formation of MIL-53(Al)-NH<sub>2</sub> nanosheets, a systematic experimental study was performed by varying CTAB/Al<sup>3+</sup> ratios, ranging from 0.1 to 1.5 (Table C1 and Fig. C3). Among the different CTAB/Al<sup>3+</sup> ratios, we found 0.5 to be the optimal in the synthesis of MOF lamellae. This is demonstrated by TEM, X-ray diffraction (XRD) and gas adsorption (Figs. C3 and C5). XRD confirmed the formation of MIL-53(Al)-NH<sub>2</sub>, the observed reflections corresponding to those expected for the large pore (*lp*) MOF configuration. This is noteworthy – since MIL-53(Al)-NH<sub>2</sub> is usually found in the narrow pore (*np*) form.<sup>51</sup> Nevertheless, the relationship between crystal size and framework flexibility has been extensively studied revealing that with changing the crystal size and surface in the flexible MOFs structures, the kinetic behaviour of the crystal structure transformation could be



altered drastically.<sup>38,52-53</sup> In particular, Kitagawa and co-workers demonstrated that crystal downsizing to the nanometre scale range can stabilize the transient pore configuration in the flexible MOF structures, leading to the further thermodynamic and/or kinetic suppression of *lp-np* phase transitions.<sup>52</sup> This behavior is not surprising and can be related to the fact that reducing crystal dimensions can generally accelerate guest diffusion/mobility and hence constrain the structural transformations of the flexible MOFs. Thus, we attribute the dominance of the *lp* configuration of MIL-53(Al)-NH<sub>2</sub> nanolamellae to both nanocrystal size and shorter diffusion length along the crystallographic *a*-direction.

CO<sub>2</sub> adsorption further corroborated this. The step in the CO<sub>2</sub> isotherm (Fig. 4.1E), commonly attributed to the MIL-53 breathing behaviour (starting at  $\approx 7$  bar for the submicron-sized MIL-53(Al)-NH<sub>2</sub> crystals),<sup>54</sup> does not appear in the case of the MOF nanosheets. In fact, an isotherm archetypical for the rigid porous materials is obtained, the high uptake at low pressures corresponding to the filling of the MOF micropores. Furthermore, the slope observed at higher pressures can be attributed to multilayer adsorption on the external surface area exposed by the MOF nanosheets. This interparticle porosity was also found for N<sub>2</sub> adsorption, where the H1-type hysteresis loops observed have been commonly encountered for other delaminated materials (Fig. C5B).<sup>17</sup> Systematic study on the effect of low CTAB/Al<sup>3+</sup> ratio and the operating temperature is necessary to delineate the mechanism governing the dominance of the large pore configuration.

Once the suitability of our surfactant-assisted approach to synthesize MIL-53(Al)-NH<sub>2</sub> nanosheets was confirmed, the question then arose, how the 1D diamond-shaped MIL-53 channels are oriented within the MOF lamellae. This orientation of the 1D channels has significant implications for different applications, as the diffusion pathway is much longer if the 1D channels run parallel to the surface of the nanosheets than if they do in the perpendicular direction. To gain some insight, high-resolution TEM (HRTEM) and selected-area electron diffraction (SAED) experiments were performed. Lattice fringes with interplanar distances of 13.4 and 16.2 Å were observed by HRTEM, corresponding to the (001) and (010) planes of MIL-53(Al)-NH<sub>2</sub>, respectively (Fig. 4.2). Moreover, SAED patterns were acquired along the [100] axis and showed diffraction spots corresponding to the (*0kl*) planes of the MIL-53(Al)-NH<sub>2</sub> nanosheets. Interestingly, comparison between the simulated and experimental SAED patterns and the MIL-53(Al)-NH<sub>2</sub> structure along [100] (Fig. 4.2C and insets) points to an orientation of the 1D diamond-shaped channels perpendicular to the surface of the MOF nanosheets. Thus, besides the successful synthesis of MOF nanosheets, a further advantage of this surfactant-assisted synthetic route is the orientation of the MIL-53(Al)-NH<sub>2</sub> channels along the shortest particle dimension. This interesting feature of MIL-53(Al)-NH<sub>2</sub> nanolamellae is presumably

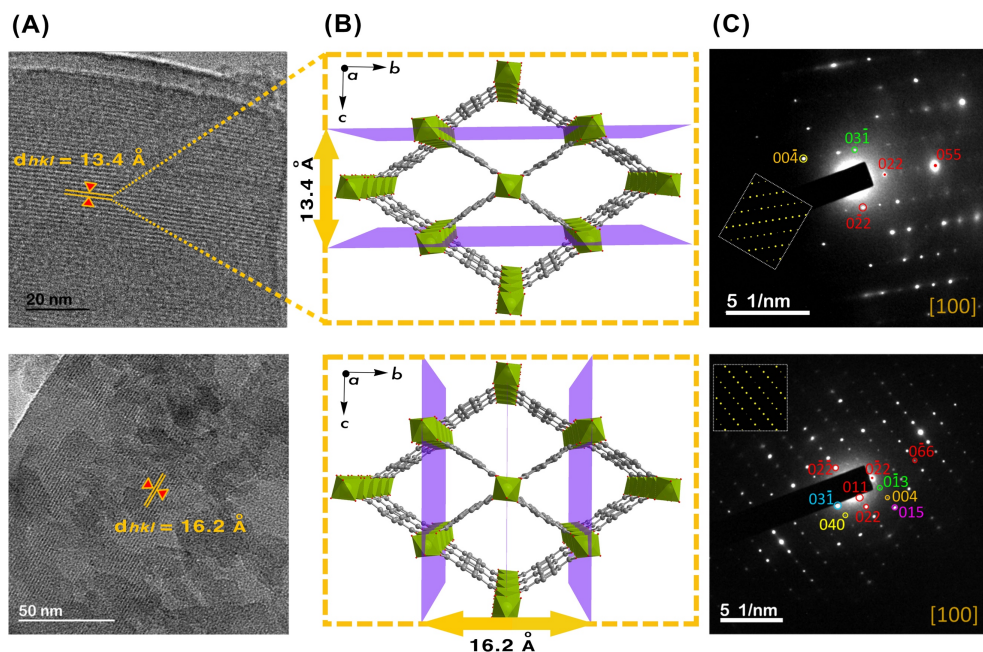


**Figure 4.2.** (A) HRTEM images acquired for the MIL-53(Al)-NH<sub>2</sub> nanosheets. Lattice fringes with interplanar distances of 13.4 and 16.2 Å were observed, corresponding to the crystallographic *c*- and *b*-axis, respectively. (B) MIL-53 topology represented along the [100] direction. (C) SAED patterns of MIL-53(Al)-NH<sub>2</sub> lamellae showing the diffraction from (*okl*) planes. Inset: simulated SAED pattern of MIL-53(Al)-NH<sub>2</sub> along the [100] axis.

caused by preorganization of the CTAB/Al<sup>3+</sup> system. In order to understand the formation mechanism of the nanolamellae, dynamic light scattering (DLS) measurements were performed for CTAB/Al<sup>3+</sup> precursor mixtures. The corresponding data for DLS measurements are summarized in the Appendix C (Fig. C1). Notably, the value of critical micelle concentration observed by DLS technique ( $8.2 \cdot 10^{-6} \text{ mol} \cdot \text{L}^{-1}$ ) is close to that determined by surface tension measurements. The increase in the hydrodynamic radius ( $R_h$ ) above CMC suggests a progressive growth of CTAB micelles until reaching a maximum at  $2.2 \cdot 10^{-2} \text{ mol} \cdot \text{L}^{-1}$  which corresponds to CTAB/Al<sup>3+</sup> molar ratio of 0.1, first point of high CTAB concentration series (Fig. C1D). When compared to the measured thickness of independent lamellae, the hydrodynamic radii obtained from DLS are very similar. Thus, we hypothesize that at CTAB concentration  $\approx 1.5 \cdot 10^{-4} \text{ mol} \cdot \text{L}^{-1}$ , which corresponds to a CTAB/Al<sup>3+</sup> ratio of 0.5, the aluminum oligomeric structures include themselves between the stacked CTAB lamellae micelles (Fig. C1E). As soon as the 2-aminoterephthalate anion is added to the system, the substitution of CTAB molecules in micelles by the linker occurs, initiating the formation of MIL-53(Al)-NH<sub>2</sub> following the stacking predefined by the CTAB micelle (Fig. C1F) and resulting in pore alignment along the channel direction.

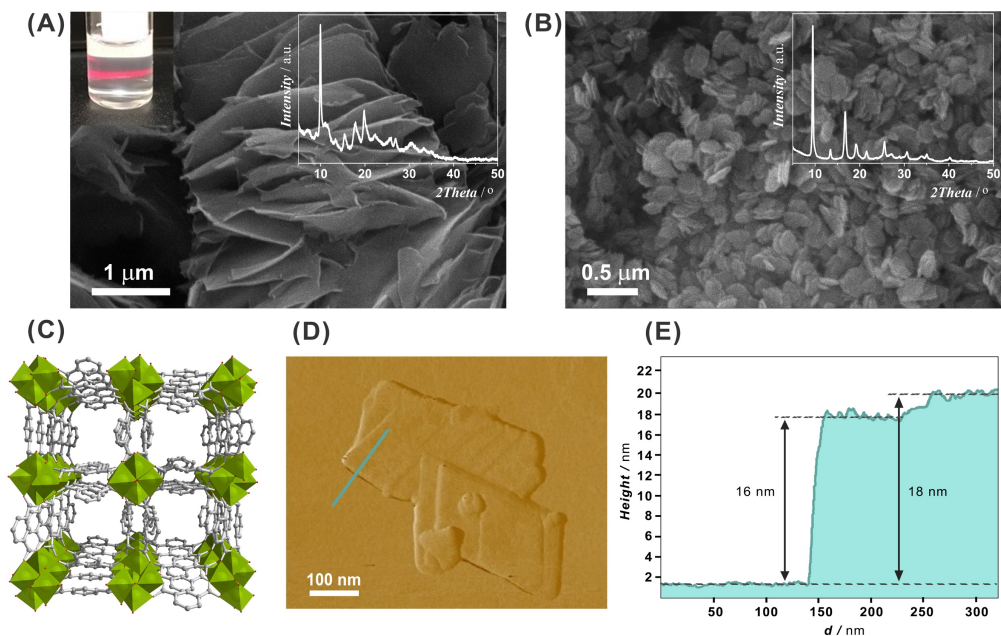


**Figure 4.3.** SEM images of the as-synthesized bulk particles of (A) CAU-10(Al)-H and (B) CAU-10(Al)-NH<sub>2</sub> synthesized for a CTAB/Al<sup>3+</sup> ratio of 0.5 and 0.6, respectively. Insets: Photograph demonstrating the Tyndall effect for the CAU-10(Al)-H nanosheets colloidal suspension obtained upon sonication and XRD patterns of (A) CAU-10(Al)-H and (B) CAU-10(Al)-NH<sub>2</sub>. (C) Crystalline structure of CAU-10(Al)-H viewed along *c*-axis and showing the channel system. Aluminium, oxygen and carbon atoms are shown in green, red and grey, respectively. Hydrogen atoms have been omitted for clarity. (D) AFM image of the exfoliated CAU-10(Al)-H nanosheets. (E) Height profile corresponds to the blue line shown in the AFM image.

Exploring the versatility of this synthetic approach, this surfactant-assisted method was applied to two different well-known Al-containing MOFs, bearing different functionalities, namely CAU-10(Al)-H and CAU-10(Al)-NH<sub>2</sub>. Similar to MIL-53(Al)-NH<sub>2</sub> nanosheets (*vide supra*), screening of different CTAB/Al<sup>3+</sup> ratios led to optimum values of 0.5 for CAU-10(Al)-H and 0.6 for CAU-10(Al)-NH<sub>2</sub>, suggesting that preorganization of Al is crucial for the successful synthesis of nanosheets. The XRD patterns of the product for this CTAB/Al<sup>3+</sup> ratio demonstrated formation of CAU-10(Al)-H and CAU-10(Al)-NH<sub>2</sub> (Fig. C6), while SEM micrographs evidenced the formation of MOF lamellae. In this case, however, the as-synthesized nanosheets were stacked into larger MOF particles with lateral dimensions of  $2.5 \pm 0.2 \mu\text{m}$  and  $250 \pm 25 \text{ nm}$  for CAU-10(Al)-H and CAU-10(Al)-NH<sub>2</sub>, respectively (Fig. C9). Interestingly, mild sonication of these stacked particles in THF for 40 min led to exfoliation. Indeed, the supernatant of the product obtained exhibits the Tyndall effect with laser beam irradiation, pointing to the high dispersion of particles of hundreds of nanometres in the colloidal suspension. Atomic force

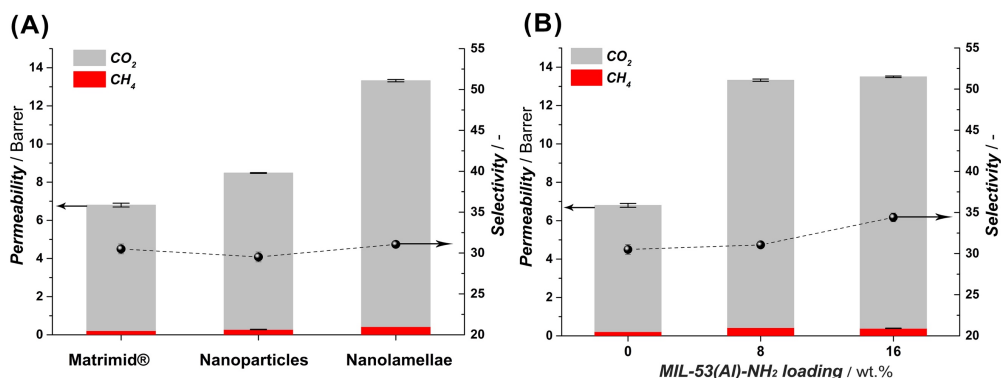


**Figure 4.4.** (A) Influence of the filler morphology on the CO<sub>2</sub> and CH<sub>4</sub> permeability and on the CO<sub>2</sub>/CH<sub>4</sub> selectivity for MMMs containing 8 wt.% MIL-53(Al)-NH<sub>2</sub> nanoparticles and lamellae; (B) influence of the MOF loading on CO<sub>2</sub> and CH<sub>4</sub> permeability and CO<sub>2</sub>/CH<sub>4</sub> mixed gas selectivity for MMM containing MIL-53(Al)-NH<sub>2</sub> lamellae measured at 308 K and a transmembrane pressure difference of 3 bar. Error bars correspond to standard deviation.

microscopy (AFM) confirmed that CAU-10(Al)-H nanosheets were isolated upon exfoliation (Fig. 4.3D,E). It should be noted however that this occurs together with particle fragmentation, which leads to lamellae with reduced lateral dimensions.

Furthermore, next to the successful synthesis of several MOF topologies bearing different functionalities as nanosheets, preliminary data with other trivalent metals show that this approach could be extended to other MOFs, provided that the metal preassembles in the presence of CTAB. Indeed, MIL-53-NH<sub>2</sub> containing different metals, *i.e.* Ga, have also shown the use of surfactants as a potential approach to gain control over the MOF particle morphology (Fig. C11). Collectively, these results underscore the potential of our surfactant-assisted method to synthesize lamellae of different nonlayered Al-containing MOFs. This complements the existing methods to synthesize MOF nanosheets, with a unique method for a bottom-up synthesis of MOF lamellae for topologies with a prevalent isotropic growth.

MIL-53(Al)-NH<sub>2</sub> nanosheets and nanoparticles (Figs. 4.1 and C12) were applied in gas separation and molecular recognition applications to assess the potential of MOF lamellae as materials with superior performance. In the application of MOFs for gas separation, the use of MOFs as fillers in MOF-based mixed-matrix membranes (MMMs), a blend of the MOF particles in a polymeric matrix, has shown great potential.<sup>44</sup> Specifically, the use of MOF nanosheets as fillers has been recently identified by some of us as a particular attractive strategy to synthesize advanced composite membranes for gas separation.<sup>17</sup>

Matrimid®-based MMMs containing MIL-53(Al)-NH<sub>2</sub> with two different morphologies: nanoparticles and nanosheets were prepared. Figure 4.4A and Table C3 show the performance of these membranes in the separation of an equimolar mixture of CO<sub>2</sub> and CH<sub>4</sub> at 308 K and 3

bar of transmembrane pressure difference. For both nanoparticle and nanosheet fillers, the membrane permeability increases upon 8 wt.% MOF loading, which can be attributed to the additional gas transport pathways provided by the porous MOF. This increase in permeability is however more pronounced in the case of the MIL-53(Al)-NH<sub>2</sub> nanosheets, reaching permeability values nearly twice than that for the bare polymer. The superior performance of the lamellae-based membranes can be ascribed to the more efficient utilization of the MOF's porosity. On the one hand, MOF nanosheets have been reported to orient parallel to the plane of the membrane, leading to a superior degree of coverage by the filler.<sup>17</sup> On the other hand, the 1D channels of MIL-53 are oriented along the shortest particle dimension, perpendicular to this plane. This results in the orientation of the MOF channels along the direction of the gas flux, facilitating gas transport through the membrane. As for the selectivity, it remains unchanged upon MOF loading. This was expected given that MIL-53(Al)-NH<sub>2</sub> is in its large pore form (*vide supra*), which is known to have moderate CO<sub>2</sub>/CH<sub>4</sub> selectivity.<sup>55</sup> Figure 4.4B further shows the influence of the MIL-53(Al)-NH<sub>2</sub> nanosheets loading on the performance of the MMMs. Upon increasing the MOF loading, permeability remains unchanged while selectivity slightly increases. We hypothesize that this behaviour is related to the rigidification of the polymeric chains surrounding the MOF nanosheets. This would result in higher selectivities and to a decrease in membrane permeability. Indeed, upon an increase in MOF loading from 8 to 16 wt.% the permeability remains unchanged, given that the rigidification of the polymeric chains counteracts the improved transport at higher MOF loading.

MIL-53(Al)-NH<sub>2</sub> nanosheets were further investigated for its gas sensing properties towards alcohols. These materials were first drop-casted over meander-patterned, planar transducer devices (Fig. C14) to form a uniform layer over the sensing area (see Appendix C for details).<sup>39, 56</sup> The thickness of the layer was kept at 10 µm to ensure that the majority of the electric field lines remain within the MOF layer, avoiding the influence of possible MOF coating variations on the sensor response. The coated devices were then exposed to different concentrations of alcohols (0-2500 ppm of methanol, 2-propanol and 1-butanol) and the capacitive response was measured by impedance spectroscopy in a 4-probe configuration at 301 K. Figures 4.5 and C15 clearly show a change in the sensing device capacitance upon alcohol exposure, the capacitance response increasing with higher alcohol concentrations. The response showed complete reversibility and a return to baseline in ~15 min over replacing the alcohol vapours in gas phase with dry N<sub>2</sub>. Hence, the completely reversible and sensitive response of MIL-53(Al)-NH<sub>2</sub> nanosheets-coated transducer devices towards methanol, 2-propanol and 1-butanol indicated capabilities of these materials for sensing applications. Comparison of the sensor response with that of MIL-53(Al)-NH<sub>2</sub> nanoparticle-coated devices

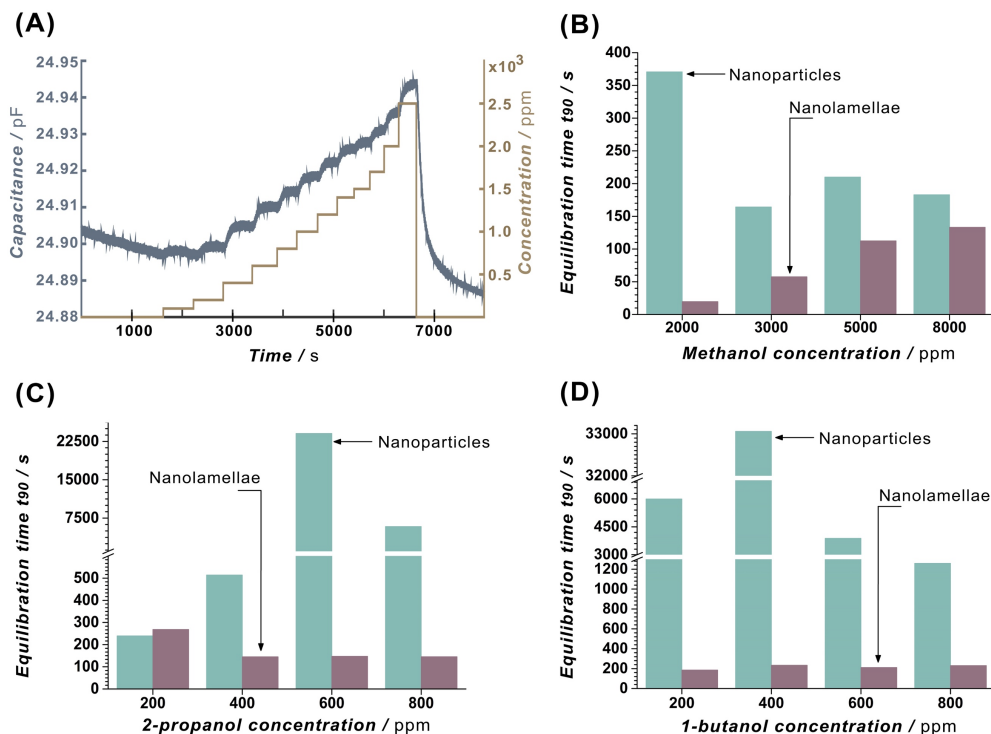


**Figure 4.5.** (A) Capacitance sensing behaviour of MIL-53(Al)-NH<sub>2</sub> lamellae toward increasing concentration of 2-propanol.  $t_{90}$  equilibration time for MIL-53(Al)-NH<sub>2</sub> lamellae and nanoparticles toward increasing concentration of methanol (B), 2-propanol (C) and 1-butanol (D) in a nitrogen flow.

learnt that the time required to reach half of the equilibration ( $t_{50}$ ) and 90% of the equilibrium response ( $t_{90}$ ) upon exposure to different alcohol concentrations was significantly reduced for the devices coated with nanosheets. In the particular case of 2-propanol for instance, after exposure to 600 ppm, the response time was reduced by ~180 times (Fig. 4.5). This decrease in the response time can be attributed to the shorter diffusion pathways in the case of the MOF nanosheets, for which the 1D diamond-shaped MIL-53(Al)-NH<sub>2</sub> channels are oriented along the smallest particle dimension.

#### 4.4 CONCLUSIONS

Our results underline the significance of the development of synthetic routes for the fabrication of MOF nanosheets to reveal the true potential of these promising materials. We envision that the surfactant-assisted approach presented in this work will lead to the development of different methods to fabricate lamellae of MOFs that do not possess an intrinsic layered structure. This is crucial for the efficient utilization of MOF materials as demonstrated here for gas separation and molecular recognition.

## REFERENCES

- [1] R. Mas-Balleste, C. Gomez-Navarro, J. Gomez-Herrero, F. Zamora, *Nanoscale* **2011**, 3, 20-30.
- [2] S. Z. Butler, S. M. Hollen, L. Y. Cao, Y. Cui, J. A. Gupta, H. R. Gutierrez, T. F. Heinz, S. S. Hong, J. X. Huang, A. F. Ismach, E. Johnston-Halperin, M. Kuno, V. V. Plashnitsa, R. D. Robinson, R. S. Ruoff, S. Salahuddin, J. Shan, L. Shi, M. G. Spencer, M. Terrones, W. Windl, J. E. Goldberger, *ACS Nano* **2013**, 7, 2898-2926.
- [3] A. Gupta, T. Sakthivel, S. Seal, *Prog. Mater. Sci.* **2015**, 73, 44-126.
- [4] G. R. Bhimanapati, Z. Lin, V. Meunier, Y. Jung, J. Cha, S. Das, D. Xiao, Y. Son, M. S. Strano, V. R. Cooper, L. B. Liang, S. G. Louie, E. Ringe, W. Zhou, S. S. Kim, R. R. Naik, B. G. Sumpter, H. Terrones, F. N. Xia, Y. L. Wang, J. Zhu, D. Akinwande, N. Alem, J. A. Schuller, R. E. Schaak, M. Terrones, J. A. Robinson, *ACS Nano* **2015**, 9, 11509-11539.
- [5] G. P. Liu, W. Q. Jin, N. P. Xu, *Angew. Chem. Int. Ed.* **2016**, 55, 13384-13397.
- [6] P. Amo-Ochoa, L. Welte, R. Gonzalez-Prieto, P. J. S. Miguel, C. J. Gomez-Garcia, E. Mateo-Marti, S. Delgado, J. Gomez-Herrero, F. Zamora, *Chem. Commun.* **2010**, 46, 3262-3264.
- [7] L. Peng, J. Zhang, J. Li, B. Han, Z. Xue, G. Yang, *Chem. Commun.* **2012**, 48, 8688-8690.
- [8] H. Li, M. Eddaoudi, M. O'Keeffe, O. M. Yaghi, *Nature* **1999**, 402, 276-279.
- [9] S. R. Batten, N. R. Champness, X. M. Chen, J. Garcia-Martinez, S. Kitagawa, L. Ohrstrom, M. O'Keeffe, M. P. Suh, J. Reedijk, *Pure Appl. Chem.* **2013**, 85, 1715-1724.
- [10] M. Eddaoudi, J. Kim, N. Rosi, D. Vodak, J. Wachter, M. O'Keeffe, O. M. Yaghi, *Science* **2002**, 295, 469-472.
- [11] K. K. Tanabe, S. M. Cohen, *Chem. Soc. Rev.* **2011**, 40, 498-519.
- [12] Z. C. Zhang, Y. F. Chen, S. He, J. C. Zhang, X. B. Xu, Y. Yang, F. Nosheen, F. Saleem, W. He, X. Wang, *Angew. Chem. Int. Ed.* **2014**, 53, 12517-12521.
- [13] Y. X. Wang, M. T. Zhao, J. F. Ping, B. Chen, X. H. Cao, Y. Huang, C. L. Tan, Q. L. Ma, S. X. Wu, Y. F. Yu, Q. P. Lu, J. Z. Chen, W. Zhao, Y. B. Ying, H. Zhang, *Adv. Mater.* **2016**, 28, 4149-4155.
- [14] G. W. Zhan, H. C. Zeng, *Adv. Funct. Mater.* **2016**, 26, 3268-3281.
- [15] M. T. Zhao, Y. X. Wang, Q. L. Ma, Y. Huang, X. Zhang, J. F. Ping, Z. C. Zhang, Q. P. Lu, Y. F. Yu, H. Xu, Y. L. Zhao, H. Zhang, *Adv. Mater.* **2015**, 27, 7372-7378.
- [16] L. Y. Cao, Z. K. Lin, F. Peng, W. W. Wang, R. Y. Huang, C. Wang, J. W. Yan, J. Liang, Z. M. Zhang, T. Zhang, L. S. Long, J. L. Sun, W. B. Lin, *Angew. Chem. Int. Ed.* **2016**, 55, 4962-4966.
- [17] T. Rodenas, I. Luz, G. Prieto, B. Seoane, H. Miro, A. Corma, F. Kapteijn, F. X. L. I. Xamena, J. Gascon, *Nat. Mater.* **2015**, 14, 48-55.
- [18] Y. Peng, Y. S. Li, Y. J. Ban, H. Jin, W. M. Jiao, X. L. Liu, W. S. Yang, *Science* **2014**, 346, 1356-1359.
- [19] H. Xu, J. K. Gao, X. F. Qian, J. P. Wang, H. J. He, Y. J. Cui, Y. Yang, Z. Y. Wang, G. D. Qian, *J. Mater. Chem. A* **2016**, 4, 10900-10905.
- [20] T. Faust, O. Farha, B. Hernandez, *Nat. Chem.* **2016**, 8, 990-991.
- [21] C. Hermosa, B. R. Horrocks, J. I. Martinez, F. Liscio, J. Gomez-Herrero, F. Zamora, *Chem. Sci.* **2015**, 6, 2553-2558.
- [22] P. Z. Li, Y. Maeda, Q. Xu, *Chem. Commun.* **2011**, 47, 8436-8438.
- [23] P. J. Saines, J. C. Tan, H. H. M. Yeung, P. T. Barton, A. K. Cheetham, *Dalton Trans.* **2012**, 41, 8585-8593.
- [24] J. C. Tan, P. J. Saines, E. G. Bithell, A. K. Cheetham, *ACS Nano* **2012**, 6, 615-621.

- [25] P. J. Beldon, S. Tominaka, P. Singh, T. S. Dasgupta, E. G. Bithell, A. K. Cheetham, *Chem. Commun.* **2014**, 50, 3955-3957.
- [26] A. Gallego, C. Hermosa, O. Castillo, I. Berlanga, C. J. Gomez-Garcia, E. Mateo-Marti, J. I. Martinez, F. Flores, C. Gomez-Navarro, J. Gomez-Herrero, S. Delgado, F. Zamora, *Adv. Mater.* **2013**, 25, 2141-2146.
- [27] T. Araki, A. Kondo, K. Maeda, *Chem. Commun.* **2013**, 49, 552-554.
- [28] A. Kondo, C. C. Tiew, F. Moriguchi, K. Maeda, *Dalton Trans.* **2013**, 42, 15267-15270.
- [29] Y. P. Yuan, W. Wang, L. G. Qiu, F. M. Peng, X. Jiang, A. J. Xie, Y. H. Shen, X. Y. Tian, L. D. Zhang, *Mater. Chem. Phys.* **2011**, 131, 358-361.
- [30] W. T. Shang, X. C. Kang, H. Ning, J. L. Zhang, X. G. Zhang, Z. H. Wu, G. Mo, X. Q. Xing, B. X. Han, *Langmuir* **2013**, 29, 13168-13174.
- [31] S. C. Junggeburth, L. Diehl, S. Werner, V. Duppel, W. Sigle, B. V. Lotsch, *J. Am. Chem. Soc.* **2013**, 135, 6157-6164.
- [32] M. H. Pham, G. T. Vuong, F. G. Fontaine, T. O. Do, *Cryst. Growth. Des.* **2012**, 12, 3091-3095.
- [33] B. Seoane, S. Castellanos, A. Dikhtiarenko, F. Kapteijn, J. Gascon, *Coord. Chem. Rev.* **2016**, 307, 147-187.
- [34] M. J. Cliffe, E. Castillo-Martínez, Y. Wu, J. Lee, A. C. Forse, F. C. N. Firth, P. Z. Moghadam, D. Fairen-Jimenez, M. W. Gaultois, J. A. Hill, O. V. Magdysyuk, B. Slater, A. L. Goodwin, C. P. Grey, *J. Am. Chem. Soc.* **2017**, 139, 5397-5404.
- [35] J. Gascon, U. Aktay, M. D. Hernandez-Alonso, G. P. M. van Klink, F. Kapteijn, *J. Catal.* **2009**, 261, 75-87.
- [36] H. Reinsch, M. A. van der Veen, B. Gil, B. Marszalek, T. Verbiest, D. de Vos, N. Stock, *Chem. Mater.* **2013**, 25, 17-26.
- [37] T. Ahnfeldt, D. Gunzelmann, T. Loiseau, D. Hirsemann, J. Senker, G. Ferey, N. Stock, *Inorg. Chem.* **2009**, 48, 3057-3064.
- [38] A. Sabetghadam, B. Seoane, D. Keskin, N. Duim, T. Rodenas, S. Shahid, S. Sorribas, C. Le Guillouzer, G. Clet, C. Tellez, M. Daturi, J. Coronas, F. Kapteijn, J. Gascon, *Adv. Funct. Mater.* **2016**, 26, 3154-3163.
- [39] S. Sachdeva, D. Soccol, D. J. Gravesteyn, F. Kapteijn, E. J. R. Sudholter, J. Gascon, L. C. P. M. de Smett, *ACS Sensors* **2016**, 1, 1188-1192.
- [40] W. Kraus, G. Nolze, *J. Appl. Crystallogr.* **1996**, 29, 301-303.
- [41] J. Martín-Ramos, J. Díaz-Hernández, A. Cambeses, J. Scarrow, A. López-Galindo, *An introduction to the study of Mineralogy. Croatia, webpage: Intechweb. org (checked on February 2013)* **2012**, 73-92.
- [42] S. Couck, E. Gobechiya, C. E. A. Kirschhock, P. Serra-Crespo, J. Juan-Alcañiz, A. Martinez Joaristi, E. Stavitski, J. Gascon, F. Kapteijn, G. V. Baron, J. F. M. Denayer, *ChemSusChem* **2012**, 5, 740-750.
- [43] B. Zornoza, A. Martinez-Joaristi, P. Serra-Crespo, C. Tellez, J. Coronas, J. Gascon, F. Kapteijn, *Chem. Commun.* **2011**, 47, 9522-9524.
- [44] B. Seoane, J. Coronas, I. Gascon, M. E. Benavides, O. Karvan, J. Caro, F. Kapteijn, J. Gascon, *Chem. Soc. Rev.* **2015**, 44, 2421-2454.
- [45] S. P. Bi, C. Y. Wang, Q. Cao, C. H. Zhang, *Coord. Chem. Rev.* **2004**, 248, 441-455.
- [46] M. Haouas, C. Volkringer, T. Loiseau, G. Ferey, F. Taulelle, *Chem. Mater.* **2012**, 24, 2462-2471.
- [47] X. C. Zhu, M. G. Goesten, A. J. J. Koekkoek, B. Mezari, N. Kosinov, G. Filonenko, H. Friedrich, R. Rohling, B. M. Szyja, J. Gascon, F. Kapteijn, E. J. M. Hensen, *Chem. Sci.* **2016**, 7, 6506-6513.



- [48] A. Guinier, *X-ray Diffraction in Crystals, Imperfect Crystals, and Amorphous Bodies*, Dover Publications, **1994**.
- [49] R. T. Zhang, R. M. Suter, J. F. Nagle, *Phys. Rev. E* **1994**, 50, 5047-5060.
- [50] G. Brotons, M. Dubois, L. Belloni, I. Grillo, T. Narayanan, T. Zemb, *J. Chem. Phys.* **2005**, 123, 024704.
- [51] A. Boutin, S. Couck, F. X. Coudert, P. Serra-Crespo, J. Gascon, F. Kapteijn, A. H. Fuchs, J. F. M. Denayer, *Micropor. Mesopor. Mat.* **2011**, 140, 108-113.
- [52] Y. Sakata, S. Furukawa, M. Kondo, K. Hirai, N. Horike, Y. Takashima, H. Uehara, N. Louvain, M. Meilikhov, T. Tsuruoka, S. Isoda, W. Kosaka, O. Sakata, S. Kitagawa, *Science* **2013**, 339, 193-196.
- [53] P. Serra-Crespo, E. Gobechiya, E. V. Ramos-Fernandez, J. Juan-Alcañiz, A. Martinez-Joaristi, E. Stavitski, C. E. A. Kirschhock, J. A. Martens, F. Kapteijn, J. Gascon, *Langmuir* **2012**, 28, 12916-12922.
- [54] C. Serre, S. Bourrelly, A. Vimont, N. A. Ramsahye, G. Maurin, P. L. Llewellyn, M. Daturi, Y. Filinchuk, O. Leynaud, P. Barnes, G. Ferey, *Adv. Mater.* **2007**, 19, 2246-2251.
- [55] S. Couck, J. F. M. Denayer, G. V. Baron, T. Remy, J. Gascon, F. Kapteijn, *J. Am. Chem. Soc.* **2009**, 131, 6326-6327.
- [56] S. Sachdeva, S. J. H. Koper, A. Sabetghadam, D. Soccol, D. J. Gravesteijn, F. Kapteijn, E. J. R. Sudhölter, J. Gascon, L. C. P. M. de Smet, *ACS Appl. Mater. Interfaces* **2017**, 9, 24926-24935.

## APPENDIX C

**Table C1.** Synthesis optimization of MIL-53(Al)-NH<sub>2</sub> nanosheets through the screening of different CTAB/Al<sup>3+</sup> ratios.

Entry	Sample	Al(NO <sub>3</sub> ) <sub>3</sub> ·9H <sub>2</sub> O		CTAB		CTAB/Al <sup>3+</sup> ratio
		[g]	[mmol]	[g]	[mmol]	
1	MIL-53(Al)-NH <sub>2</sub> _0.1	0.84	2.2	0.08	0.22	0.1
2	MIL-53(Al)-NH <sub>2</sub> _0.2	0.84	2.2	0.16	0.44	0.2
3	MIL-53(Al)-NH <sub>2</sub> _0.3	0.84	2.2	0.24	0.66	0.3
4	MIL-53(Al)-NH <sub>2</sub> _0.4	0.84	2.2	0.32	0.88	0.4
5	MIL-53(Al)-NH <sub>2</sub> _0.5	0.84	2.2	0.40	1.10	0.5
6	MIL-53(Al)-NH <sub>2</sub> _0.6	0.84	2.2	0.48	1.32	0.6
7	MIL-53(Al)-NH <sub>2</sub> _1.0	0.84	2.2	0.80	2.20	1.0
8	MIL-53(Al)-NH <sub>2</sub> _1.1	0.84	2.2	0.88	2.42	1.1
9	MIL-53(Al)-NH <sub>2</sub> _1.5	0.84	2.2	1.23	3.30	1.5

Surface active behavior of CTAB/Al(NO<sub>3</sub>)<sub>3</sub> aqueous solution was measured over low- and high CTAB concentration ranges, whereas the content of Al(NO<sub>3</sub>)<sub>3</sub> in each solution was kept constant (0.22 mol·L<sup>-1</sup>). The surface tension versus CTAB concentrations in the low concentration region is shown in Fig. C1A. The surface tension decreases progressively as CTAB concentration increases up to a plateau, beyond which no considerable change is noticed. The critical micelle concentration (CMC) of the studied CTAB/Al(NO<sub>3</sub>)<sub>3</sub> system was determined as the inflection point on the surface tension curve (see inset Fig. C1A) and found to be 7.5·10<sup>-6</sup> mol·L<sup>-1</sup>. Notably, the series of CTAB/Al(NO<sub>3</sub>)<sub>3</sub> solutions with high CTAB content (Fig. C1B) exhibit almost constant surface tension values over the CTAB concentration range explored for the MIL-53(Al)-NH<sub>2</sub> nanolamellae synthesis optimization (Table C1). This observation indicates that MIL-53(Al)-NH<sub>2</sub> nanolamellae synthesis was carried out in the range of CTAB concentrations above CMC at which the CTAB micelles were formed. Dynamic light scattering was used to probe the variation in the micellar size at increasing CTAB concentration. Similar to surface tension measurements, two ranges of CTAB concentrations (low and high content) were evaluated by dynamic light scattering. The plot of Z-average (hydrodynamic radius,  $R_h$ ) versus CTAB concentration in low-concentration regime (Fig. C1C) shows a break at the vicinity of the CMC. Notably, the value of critical micelle concentration

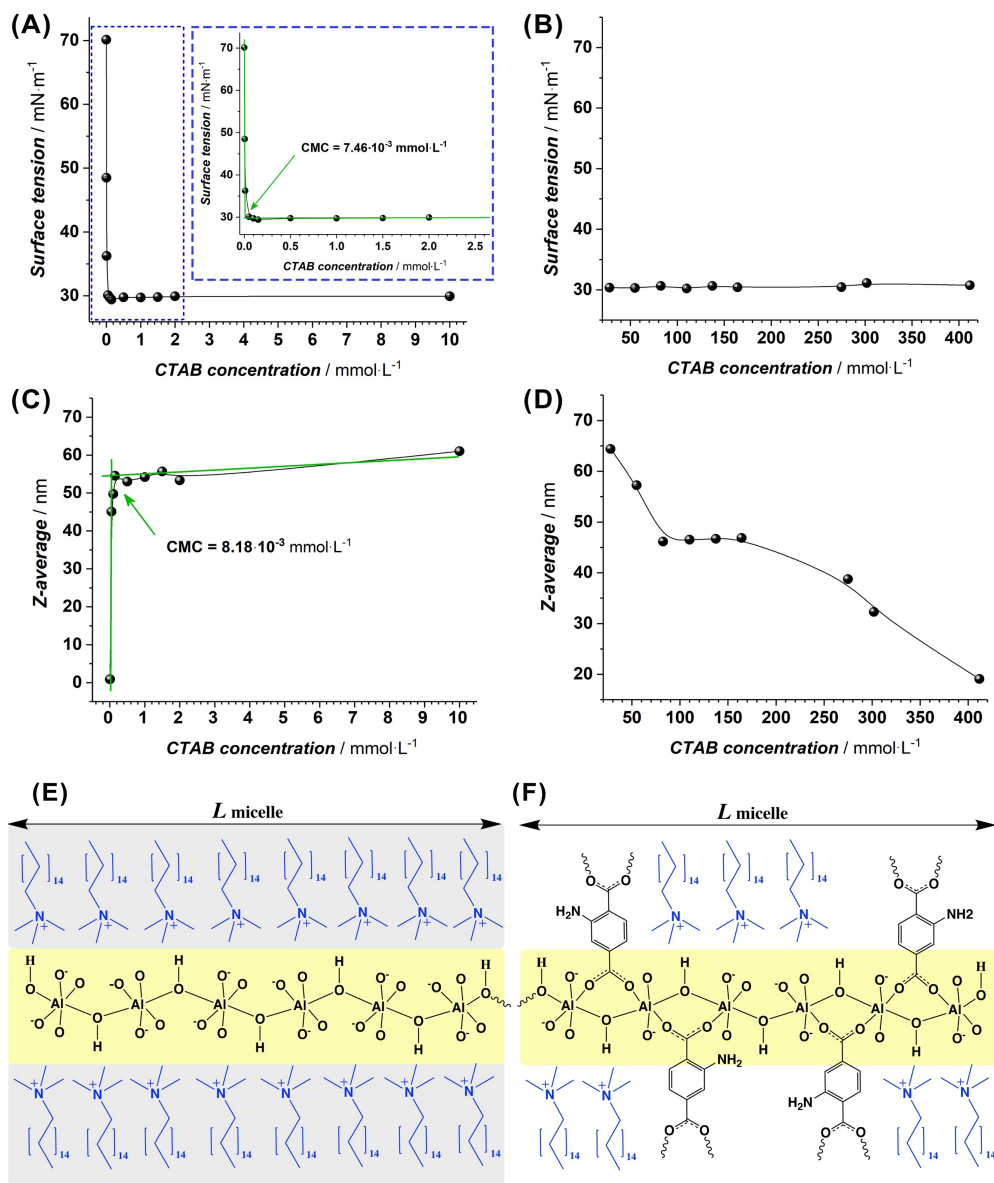


**Figure C1.** Surface tension measurements taken from the CTAB/ $\text{Al}^{3+}$  solutions of (A) low-concentration range (0;  $0.5 \cdot 10^{-5}$ ;  $1.0 \cdot 10^{-5}$ ;  $5.0 \cdot 10^{-5}$ ;  $1.0 \cdot 10^{-4}$ ;  $1.5 \cdot 10^{-4}$ ;  $5 \cdot 10^{-4}$ ;  $1.0 \cdot 10^{-3}$ ;  $1.5 \cdot 10^{-3}$ ;  $2.0 \cdot 10^{-3}$ ;  $1.0 \cdot 10^{-2} \text{ mol L}^{-1}$ ) and (B) high concentration range ( $2.2 \cdot 10^{-2}$ ;  $4.4 \cdot 10^{-2}$ ;  $6.6 \cdot 10^{-2}$ ;  $8.8 \cdot 10^{-2}$ ; 0.11; 0.132; 0.22; 0.242;  $0.33 \text{ mol L}^{-1}$ ) used for nanolamellae synthesis optimization. Inset shows a zoomed area of CMC region (blue dashed line). Z-average (hydrodynamic radius,  $R_h$ ) of CTAB micelles formed in solutions of (C) low-concentration range and (D) high concentration range determined by dynamic light scattering measurements. The concentration of  $\text{Al}^{3+}$  in all studied solution was kept constant,  $0.22 \text{ mol L}^{-1}$ . (E-F) Schematic representation of hypothesized mechanism of MIL-53(Al)-NH<sub>2</sub> nanolamellae formation.

observed by DLS technique ( $8.2 \cdot 10^{-6} \text{ mol} \cdot \text{L}^{-1}$ ) is close to that determined by surface tension measurements. The increase in the hydrodynamic radius above CMC suggests a progressive growth of CTAB micelles until reaching a maximum at  $2.2 \cdot 10^{-2} \text{ mol} \cdot \text{L}^{-1}$  which corresponds to CTAB: $\text{Al}^{3+}$  molar ratio of 0.1, the first point of high CTAB concentration series (Fig. C1D). In high concentration region, the hydrodynamic radius of micelles decreases up to 46 nm following by plateau zone for CTAB concentration of  $6.6 \cdot 10^{-2}$ ;  $8.8 \cdot 10^{-2}$ ; 0.11;  $0.132 \text{ mol} \cdot \text{L}^{-1}$  after which the decrement continues. This decreasing behavior can be attributed to high charge repulsion forces between the CTAB micelles which increase their diffusion. Noteworthy, at CTAB concentration of  $1.5 \cdot 10^{-4} \text{ mol} \cdot \text{L}^{-1}$  the micelles are packed as stacked sheets, according to the SAXS data (Fig. 4.1). Thus, we hypothesize that at CTAB concentration ca.  $1.5 \cdot 10^{-4} \text{ mol} \cdot \text{L}^{-1}$ , which corresponds to the CTAB/ $\text{Al}^{3+}$  ratio of 0.5, the aluminium oligomeric structures include themselves between the stacked CTAB lamellae micelles (Fig. C1E). As soon as the 2-aminoterephthalate anion is added to the system, the substitution of CTAB molecules in micelles by the linker occurs initiating the MIL-53(Al)- $\text{NH}_2$  growth in a specific manner where the thickness of the MOF lamellae particle determined by length of the former CTAB micelle (Fig. C1F).

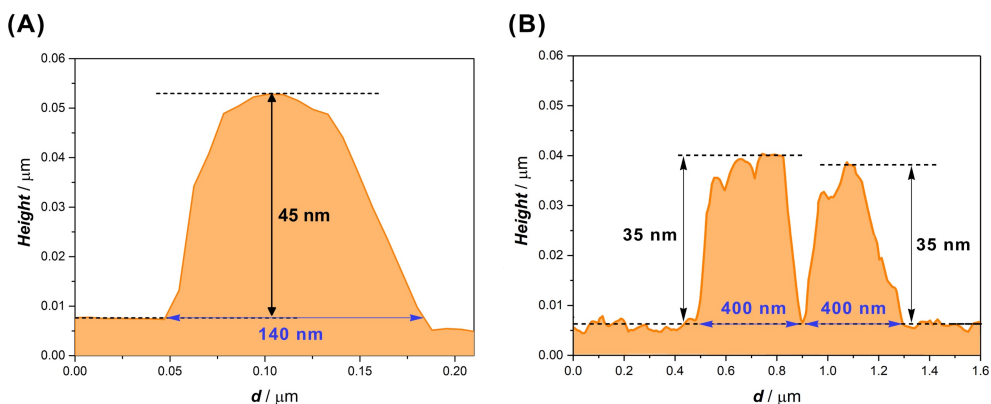


**Figure C2.** (A-B) AFM height profile of the MIL-53(Al)- $\text{NH}_2$  nanosheets synthesized at 0.5 CTAB/ $\text{Al}^{3+}$  molar ratio.

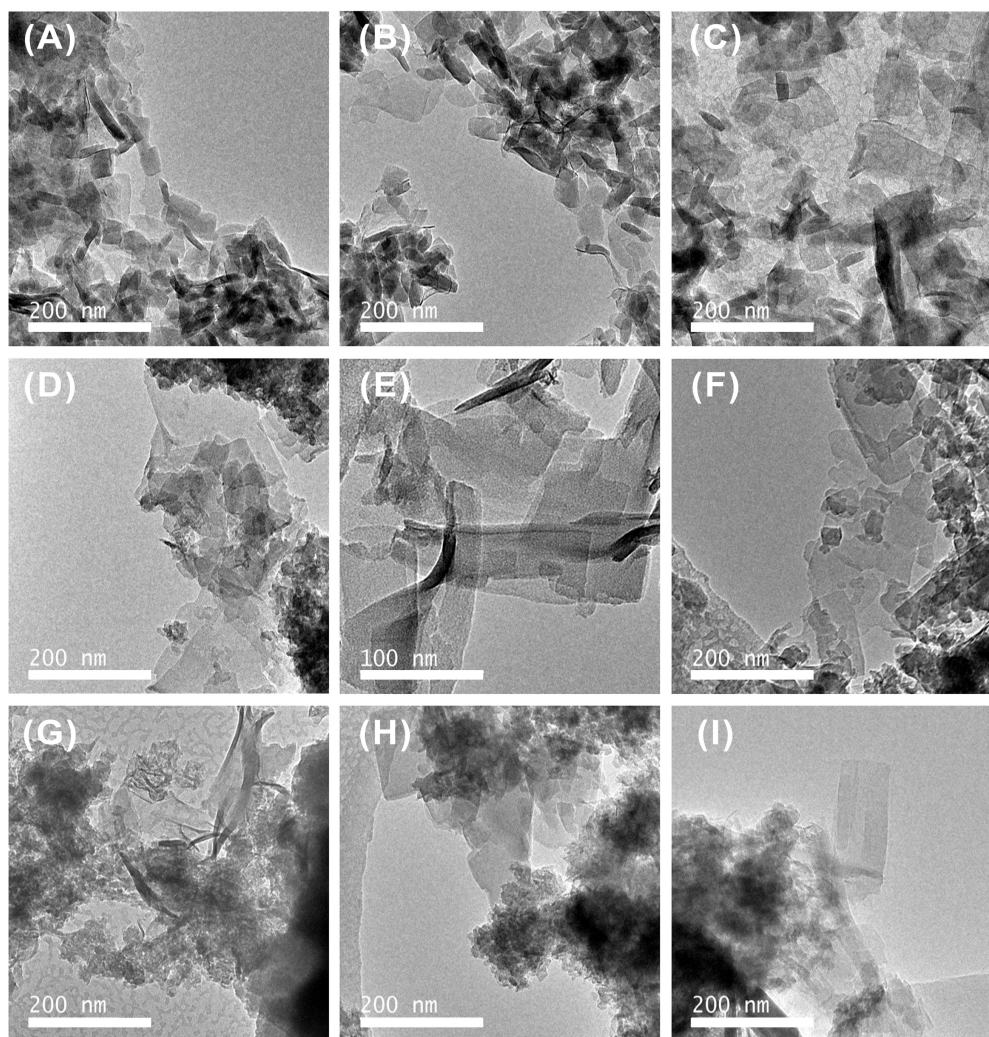


**Figure C3.** Transmission electron microscopy images for MIL-53(Al)-NH<sub>2</sub> synthesized at different CTAB/Al<sup>3+</sup> molar ratios: 0.1 (A); 0.2 (B); 0.3 (C); 0.4 (D); 0.5 (E); 0.6 (F); 1.0 (G); 1.1 (H) and 1.5 (I).

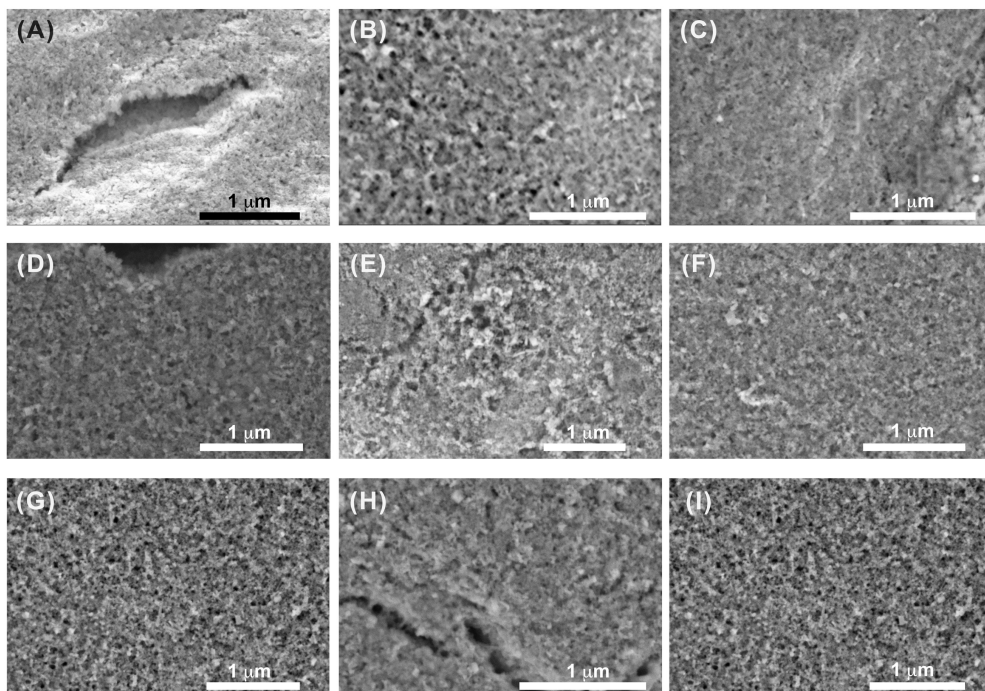


**Figure C4.** SEM micrographs of MIL-53(Al)-NH<sub>2</sub> synthesized at 0.1 (A), 0.2 (B), 0.3 (C), 0.4 (D), 0.5 (E), 0.6 (F), 1.0 (G), 1.1 (H) and 1.5 (I) CTAB/Al<sup>3+</sup> molar ratio *via* surfactant-assisted synthesis method.

The XRD patterns of the MIL-53(Al)-NH<sub>2</sub> synthesized at different CTAB/Al<sup>3+</sup> molar ratios are shown in Figure C5A. The expected diffractograms for orthorhombic *Imma* (*lp*) and monoclinic *Cc* (*np*) were built basing on the reported structural models.<sup>C1</sup> The corresponding diffraction patterns of the *lp* phase and *np* phase possess typical reflections at  $2\theta \approx 10, 12, 14.5, 16, 18.5$  and  $2\theta \approx 8.9, 12.5, 17.5$ , respectively. By comparing with the simulated XRD pattern of *lp* and *np* phases, it is clear that all MIL-53(Al)-NH<sub>2</sub> synthesized at different CTAB/Al<sup>3+</sup> molar ratios contain different amount of *Imma* (*lp*) and monoclinic *Cc* (*np*) forms and mainly consist of the mixture of both phases coexisting in the samples. Their relative content was determined by quantitative X-ray analysis and summarized in the Table C2. The typical XRD pattern of MIL-53(Al)-NH<sub>2</sub>-0.1, 0.2, 0.3, 0.6, 1.0, 1.1 and 1.5 is a combination of signals of *lp* and *np* phases, which agrees with the simulated pattern of *lp* and *np*. However, the XRD pattern of MIL-53(Al)-NH<sub>2</sub>-0.4 and 0.5 mainly consist of the *lp* form and a minor fraction *np*, as suggested by quantitative analysis (Table C2). Notably, the MIL-53(Al)-NH<sub>2</sub> nanoparticles (Fig. C12) and nanolamellae synthesized at CTAB/Al<sup>3+</sup> molar ratio of 0.5 have a very similar content of orthorhombic *Imma* (*lp*) and monoclinic *Cc* (*np*) phases, *ca.* 90:10 wt.%, respectively.

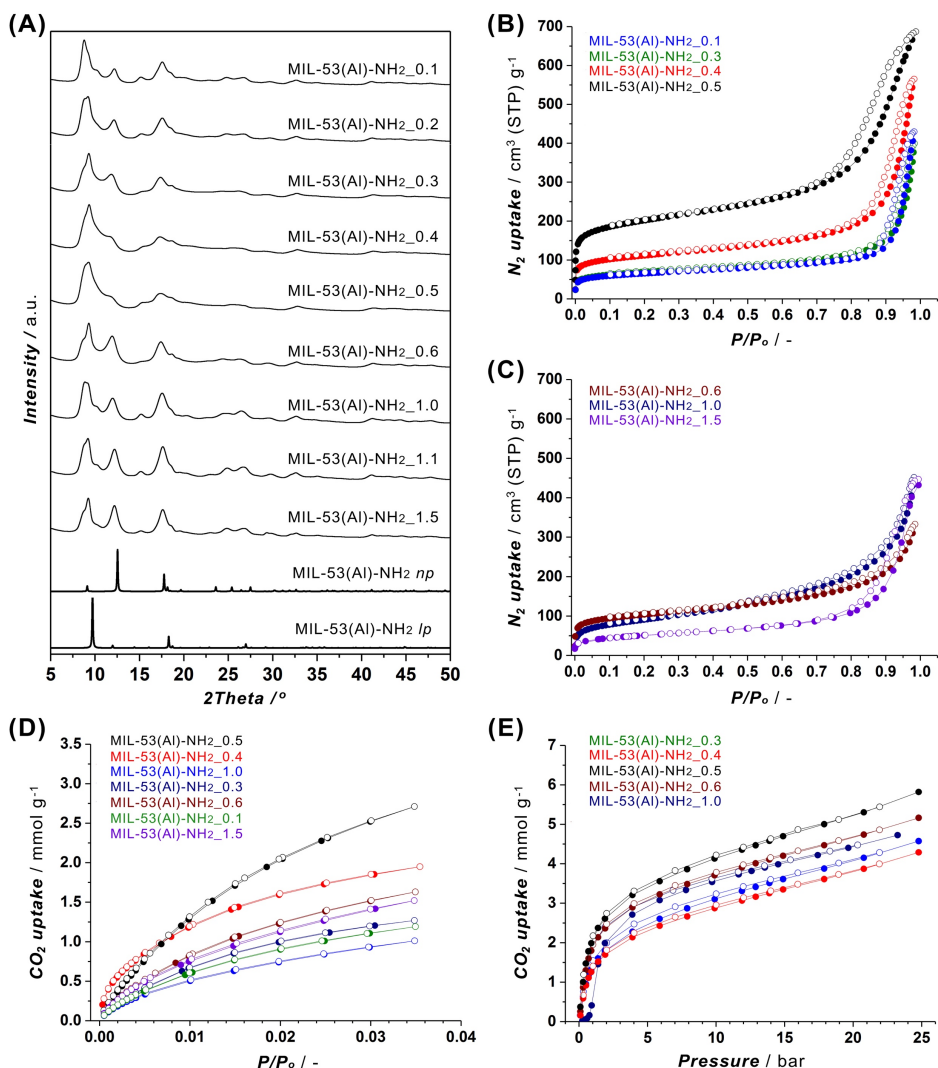


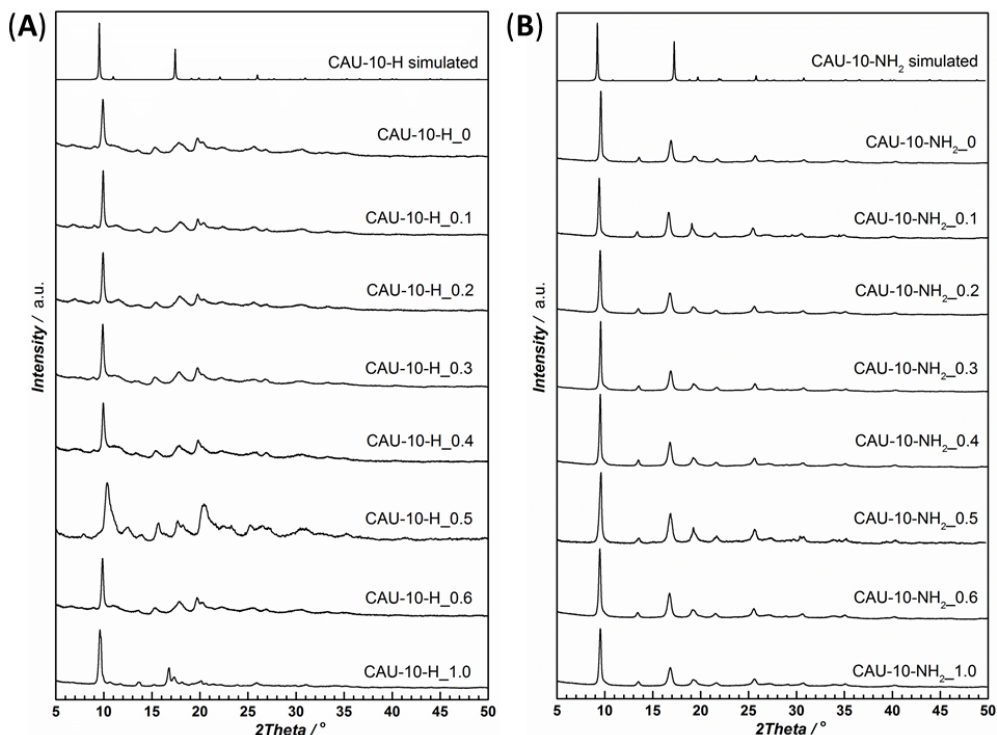
**Figure C5.** (A) PXRD patterns acquired for MIL-53(Al)-NH<sub>2</sub> synthesized at different CTAB/Al<sup>3+</sup> molar ratios. Simulated patterns for the narrow pore (*np*) and the large pore (*lp*) configurations are included for comparison *lp*: orthorhombic, space group *Imma*,  $a = 6.642$  Å,  $b = 16.387$  Å,  $c = 13.367$  Å; *np*: monoclinic, space group *Cc*,  $a = 19.756$  Å,  $b = 7.4814$  Å,  $c = 6.589$  Å,  $\beta = 105.7^\circ$ .<sup>C1</sup> (B,C) N<sub>2</sub> sorption isotherms at 77 K for the activated materials. (C,E) Low- and high-pressure CO<sub>2</sub> sorption isotherms acquired at 273 K for selected MIL-53(Al)-NH<sub>2</sub> samples after evacuation at 423 K. Solid and open symbols correspond to the adsorption and desorption branches, respectively.

**Table C2.** Summary of the structural compositions (wt.%) and the textural characteristics for MIL-53(Al)-NH<sub>2</sub> materials obtained through the screening of different CTAB/Al<sup>3+</sup> ratios.

Sample	Content (wt.%) <sup>a</sup>		S (m <sup>2</sup> ·g <sup>-1</sup> ) <sup>b</sup>		
	<i>Imma</i> ( <i>lp</i> )	<i>Cc</i> ( <i>np</i> )	Total (S <sub>BET</sub> )	Micropore	External
MIL-53(Al)-NH <sub>2</sub> _0.1	57	43	249	137	112
MIL-53(Al)-NH <sub>2</sub> _0.2	57	43	322	33	289
MIL-53(Al)-NH <sub>2</sub> _0.3	68	42	400	130	270
MIL-53(Al)-NH <sub>2</sub> _0.4	89	11	404	228	176
MIL-53(Al)-NH <sub>2</sub> _0.5	91	9	736	431	305
MIL-53(Al)-NH <sub>2</sub> _0.6	64	36	377	198	179
MIL-53(Al)-NH <sub>2</sub> _1.0	42	58	237	137	100
MIL-53(Al)-NH <sub>2</sub> _1.1	38	62	193	46	147
MIL-53(Al)-NH <sub>2</sub> _1.5	36	64	183	34	149

<sup>a</sup> Weight % compositions of orthorhombic *Imma* (*lp*) and monoclinic *Cc* (*np*) framework configurations<sup>C1</sup> in the prepared MIL-53(Al)-NH<sub>2</sub> materials were obtained from quantitative analysis performed on the experimental PXRD patterns.

<sup>b</sup> Textural properties were obtained from N<sub>2</sub> adsorption isotherms at 77 K.

**Figure C6.** PXRD patterns obtained for (A) CAU-10(Al)-H and (B) CAU-10(Al)-NH<sub>2</sub> synthesized for different CTAB/Al<sup>3+</sup> molar ratios (0.1; 0.2; 0.3; 0.4; 0.5; 0.6 and 1.0, Table S1). Simulated patterns are included for comparison (CAU-10(Al)-H: tetragonal, space group *I4*<sub>1</sub>, *a* = *b* = 21.55 Å, *c* = 10.38 Å; CAU-10(Al)-NH<sub>2</sub>: tetragonal, space group *P4n*<sub>2</sub>, *a* = *b* = 21.45 Å, *c* = 10.84 Å).<sup>C2</sup>



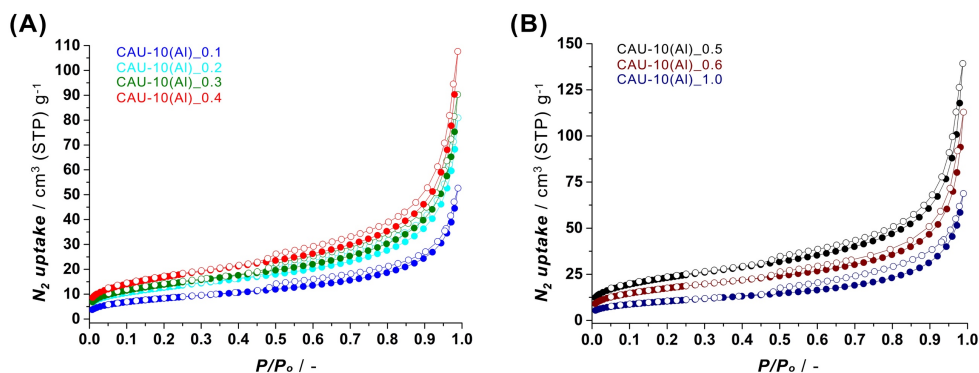


**Figure C7.**  $N_2$  sorption isotherms acquired at 77 K for CAU-10(Al)-H synthesized at (A) 0.1, 0.2, 0.3 and 0.4 and (B) 0.5, 0.6 and 1.0 CTAB/ $Al^{3+}$  molar ratios. Closed and open symbols correspond to the adsorption and desorption branches, respectively.

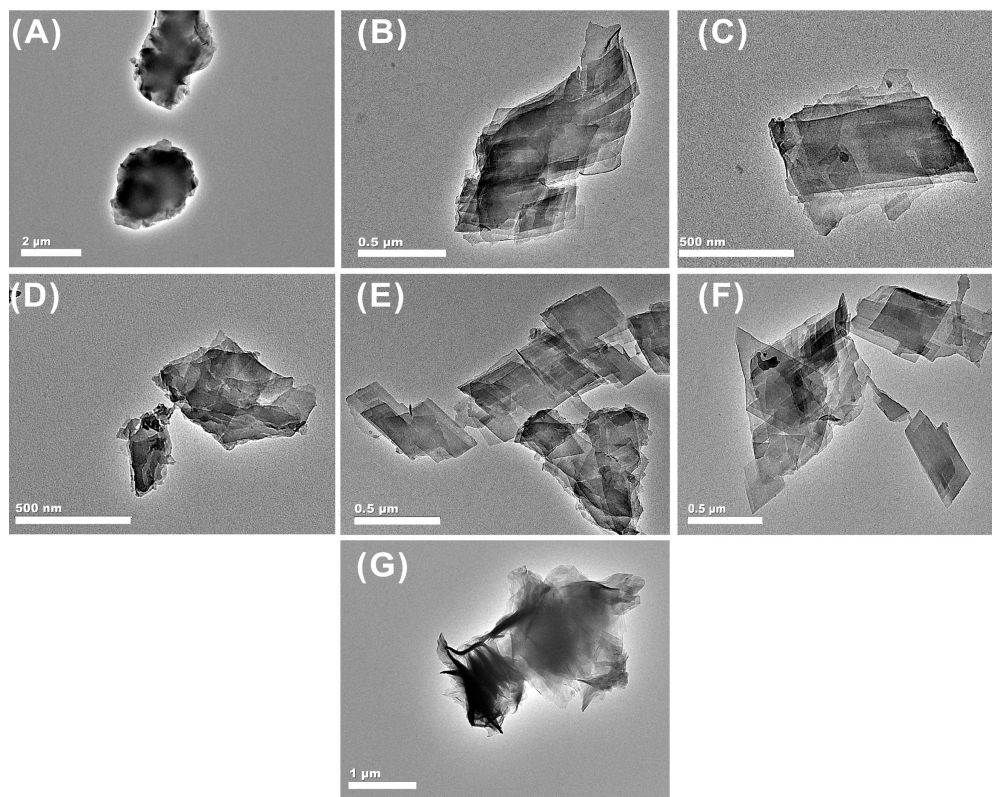


**Figure C8.** Transmission electron microscopy images for CAU-10(Al)-H synthesized at different CTAB/ $Al^{3+}$  molar ratios: 0.1 (A); 0.2 (B); 0.3 (C); 0.4 (D); 0.5 (E); 0.6 (F) and 1.0 (G).

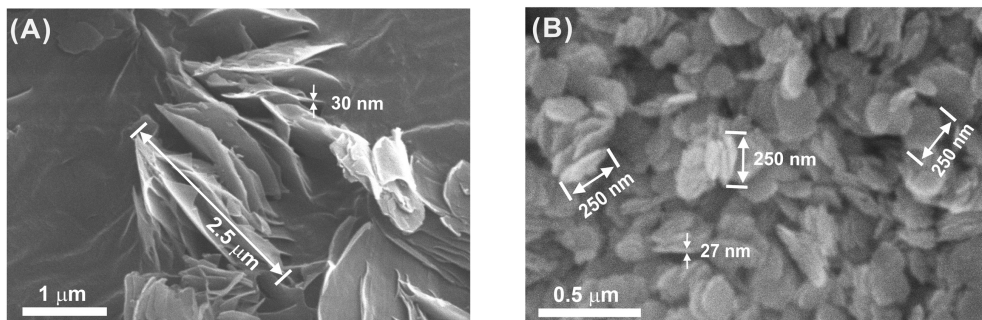


**Figure C9.** SEM micrographs of (A) CAU-10(Al)-H nanosheets and (B) CAU-10(Al)-NH<sub>2</sub> nanoslabs obtained surfactant-assisted synthesis method.

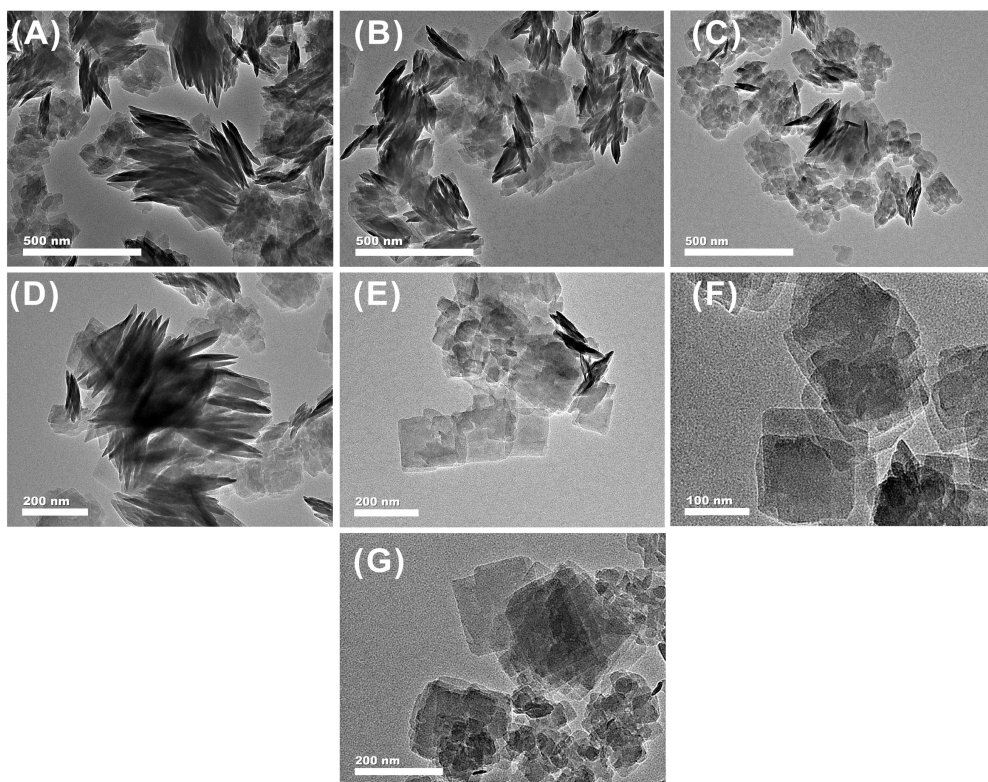


**Figure C10.** Transmission electron microscopy images for CAU-10(Al)-NH<sub>2</sub> synthesized at different CTAB/Al<sup>3+</sup> molar ratios: 0.1 (A); 0.2 (B); 0.3 (C); 0.4 (D); 0.5 (E); 0.6 (F) and 1.0 (G).

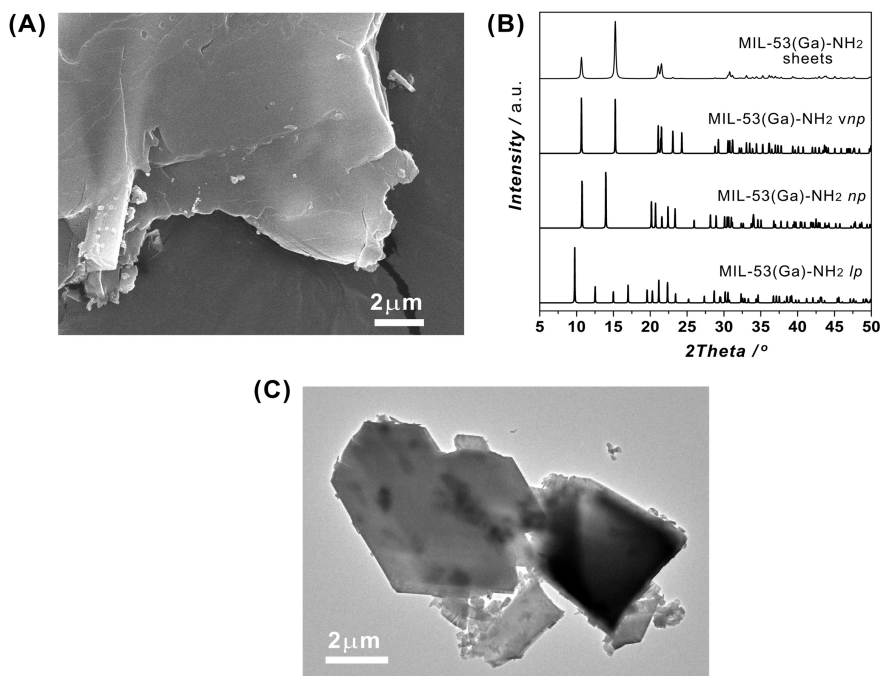


**Figure C11.** (A) SEM micrograph of MIL-53(Ga)-NH<sub>2</sub> sheets obtained with our surfactant-assisted synthesis method. (B) PXRD patterns acquired for MIL-53(Ga)-NH<sub>2</sub> sheets. Simulated patterns for the very narrow pore (*vnp*), narrow pore (*np*) and the large pore (*lp*) configurations are included for comparison (*vnp*: monoclinic, space group *Cc*,  $a = 19.903 \text{ \AA}$ ,  $b = 7.195 \text{ \AA}$ ,  $c = 6.689 \text{ \AA}$ ,  $\beta = 104.6^\circ$ ; *np*: monoclinic, space group *Cc*,  $a = 20.686 \text{ \AA}$ ,  $b = 7.966 \text{ \AA}$ ,  $c = 6.679 \text{ \AA}$ ,  $\beta = 112.5^\circ$ ; *lp*: orthorhombic, space group *Imma*,  $a = 6.748 \text{ \AA}$ ,  $b = 16.403 \text{ \AA}$ ,  $c = 13.719 \text{ \AA}$ ).<sup>C3</sup> (C) TEM micrograph of MIL-53(Ga)-NH<sub>2</sub> sheets obtained at CTAB/Al<sup>3+</sup> molar ratio of 0.5.

**Table C3.** Summary of the gas separation performance obtained with polymer and MOF-polymer composite membranes with different filler loading under several operation conditions.

MOF (wt.%)		0				
Thickness (μm)	53 ± 1					
ΔP (bar)	3		6		9	
P <sub>CO2</sub> (Barrer)	6.80 ± 0.10		6.60 ± 0.40		6.50 ± 0.50	
P <sub>CH4</sub> (Barrer)	0.22 ± 0.00		0.22 ± 0.01		0.22 ± 0.01	
Selectivity (-)	30.5 ± 0.60		30.2 ± 0.2		29.1 ± 0.3	
MOF (wt.%)		8			16	
Thickness (μm)	86 ± 1			41 ± 1		
ΔP (bar)	3	6	9	3	6	9
P <sub>CO2</sub> (Barrer)	13.32 ± 0.06	11.73 ± 0.03	10.77 ± 0.03	13.5 ± 0.04	13.29 ± 0.02	13.70 ± 0.07
P <sub>CH4</sub> (Barrer)	0.43 ± 0.00	0.37 ± 0.01	0.30 ± 0.00	0.39 ± 0.01	0.39 ± 0.00	0.41 ± 0.00
Selectivity (-)	31.06 ± 0.30	31.93 ± 0.99	35.58 ± 0.53	34.40 ± 0.53	33.81 ± 0.20	33.13 ± 0.12

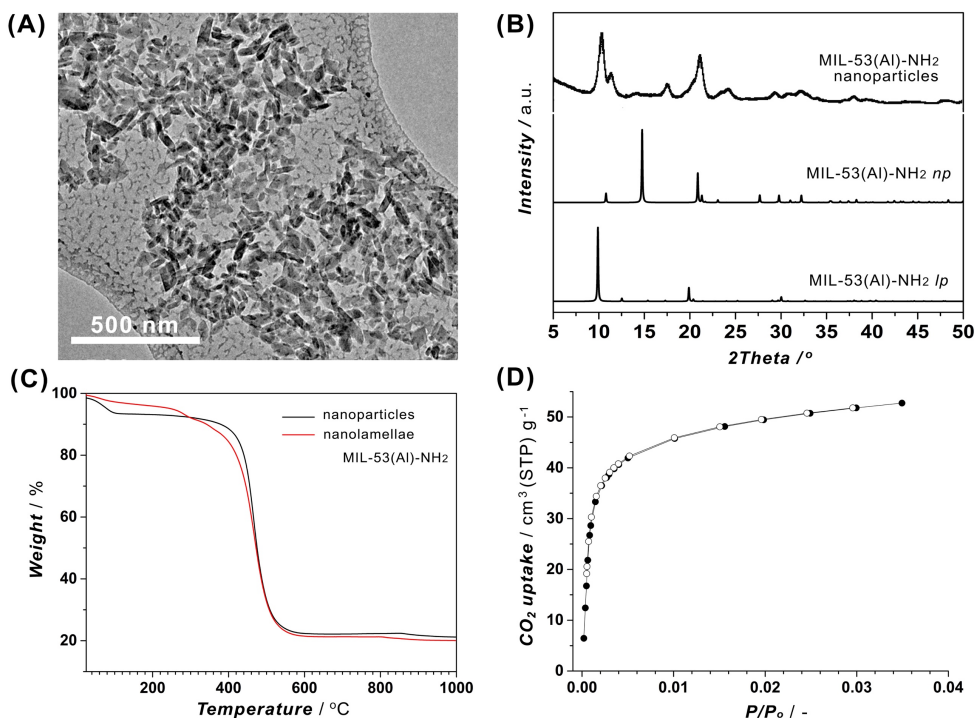


**Figure C12.** (A) TEM micrograph of MIL-53(Al)-NH<sub>2</sub> nanoparticles. (B) PXRD patterns of MIL-53(Al)-NH<sub>2</sub> nanoparticles. Simulated patterns for the narrow pore (*np*) and the large pore (*lp*) configurations are included for comparison (*lp*: orthorhombic, space group *Imma*,  $a = 6.642 \text{ \AA}$ ,  $b = 16.387 \text{ \AA}$ ,  $c = 13.367 \text{ \AA}$ ; *np*: monoclinic, space group *Cc*,  $a = 19.756 \text{ \AA}$ ,  $b = 7.4814 \text{ \AA}$ ,  $c = 6.589 \text{ \AA}$ ,  $\beta = 105.7^\circ$ ).<sup>C1</sup> (C) Thermogravimetric profiles of MIL-53(Al)-NH<sub>2</sub> nanoparticles compared to MIL-53(Al)-NH<sub>2</sub> nanosheets (0.5 CTAB/Al<sup>3+</sup> molar ratio). (D) CO<sub>2</sub> adsorption isotherms acquired at 273 K for MIL-53(Al)-NH<sub>2</sub> nanoparticles after activation at 453 K. Closed and open symbols correspond to the adsorption and desorption branches, respectively.

The thermogravimetric analysis (Fig. C12C) suggests that MIL-53(Al)-NH<sub>2</sub> nanoparticles (*black*) and nanosheets (*red*) decompose at the temperature around 500 °C and show similar weight loss. The first mass loss step for both materials was attributed to the loss of the solvent (water) and occurs at temperature below 150 °C. This temperature was chosen for materials activation.

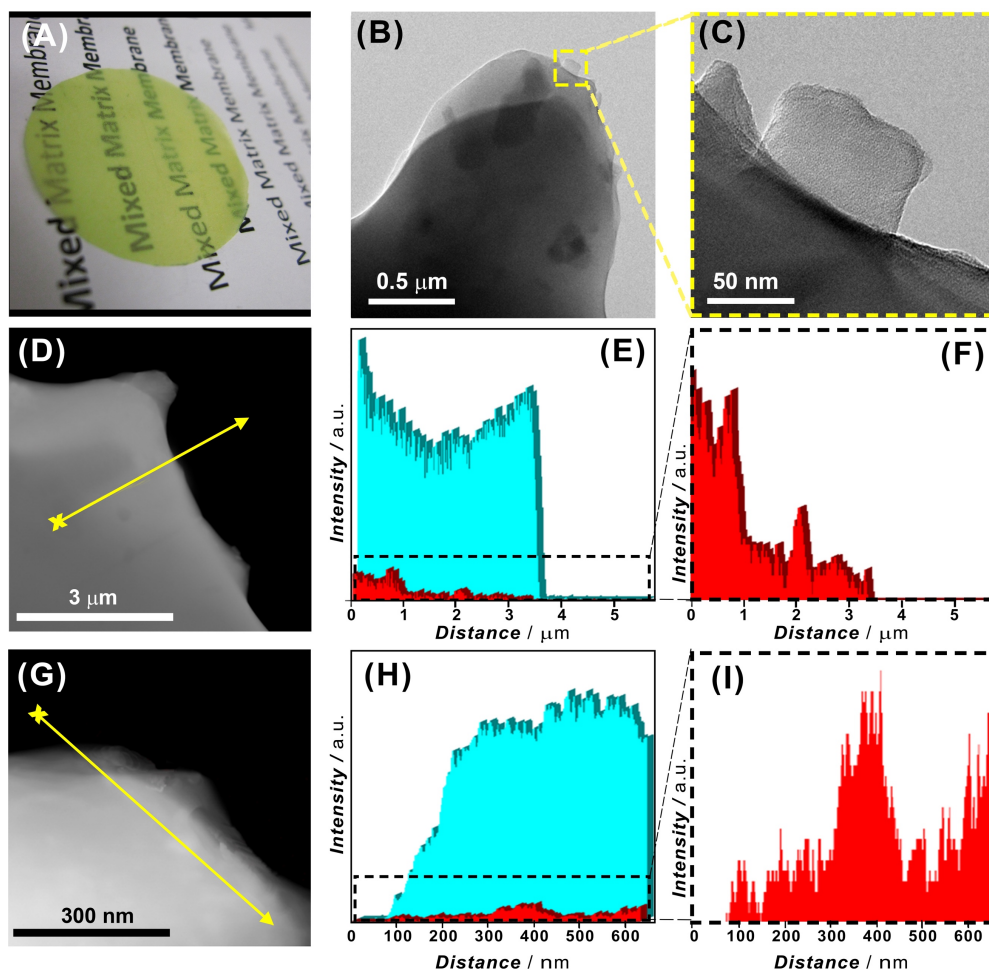


**Figure C13.** (A) Digital photo of a flexible MIL-53(Al)-NH<sub>2</sub> nanosheet@Matrimid® composite membrane with a MOF loading of 16 wt% and thickness of ca. 41 μm. (B) HRTEM image of edge area of MOF nanosheet/polymer MMM. (C) orientation of MIL-53(Al)-NH<sub>2</sub> lamellae in the polymeric matrix. (D-I) EDX line profiles at the edge of the MMM showing the evolution of carbon (blue area) and aluminium (red area) concentrations. The line profile was collected along the yellow line in the panels (D) and (G) and the direction of the profile indicated by arrows.



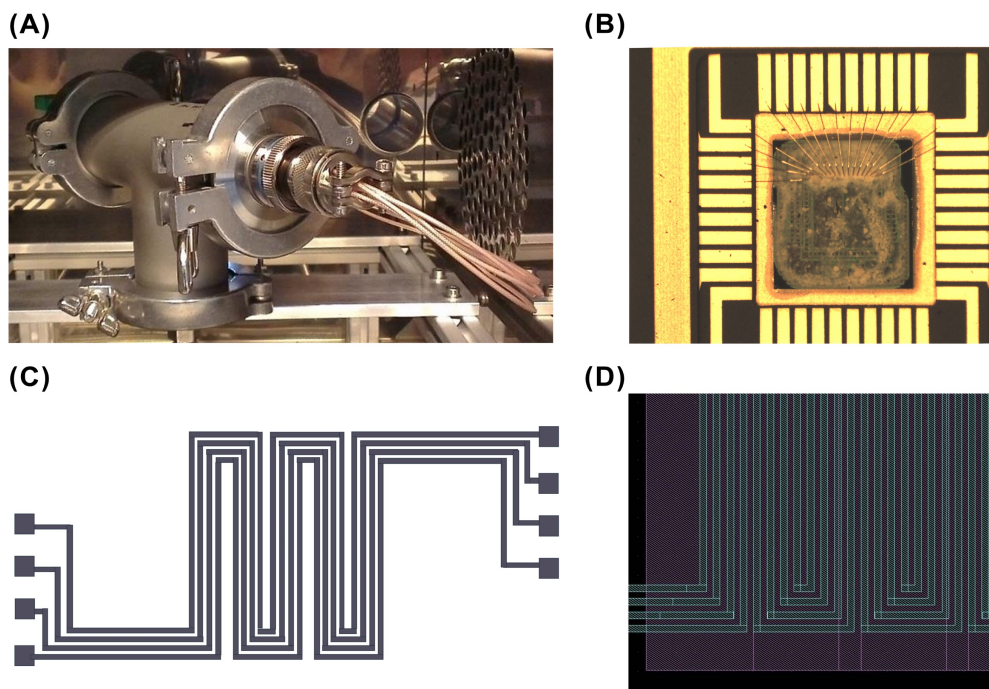


**Figure C14.** (A) Photograph of the home-built electrical measurement chamber equipped with controlled gas flow and temperature. (B) Optical image of the gas sensing device coated with MIL-53(Al)-NH<sub>2</sub> nanolamellae. (C) Schematics of the meander pattern of the electrodes. (D) Optical image of the sensor substrate illustrating the meander pattern of the electrodes.

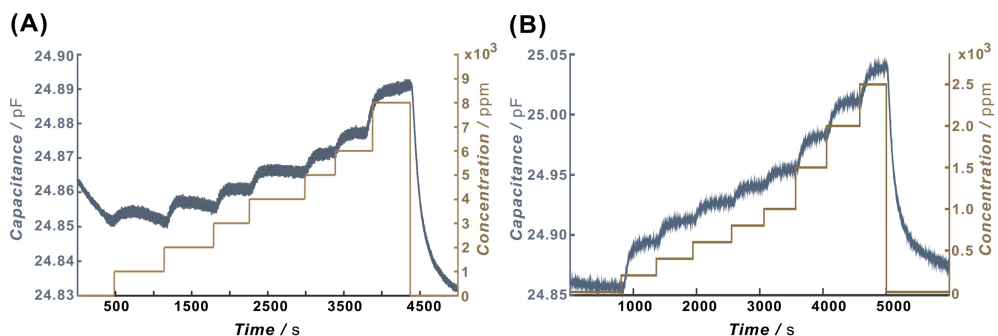


**Figure C15.** Quantitative, cumulative response towards methanol (A) and 1-butanol (B) by a sensor device coated with MIL-53(Al)-NH<sub>2</sub> lamellae.

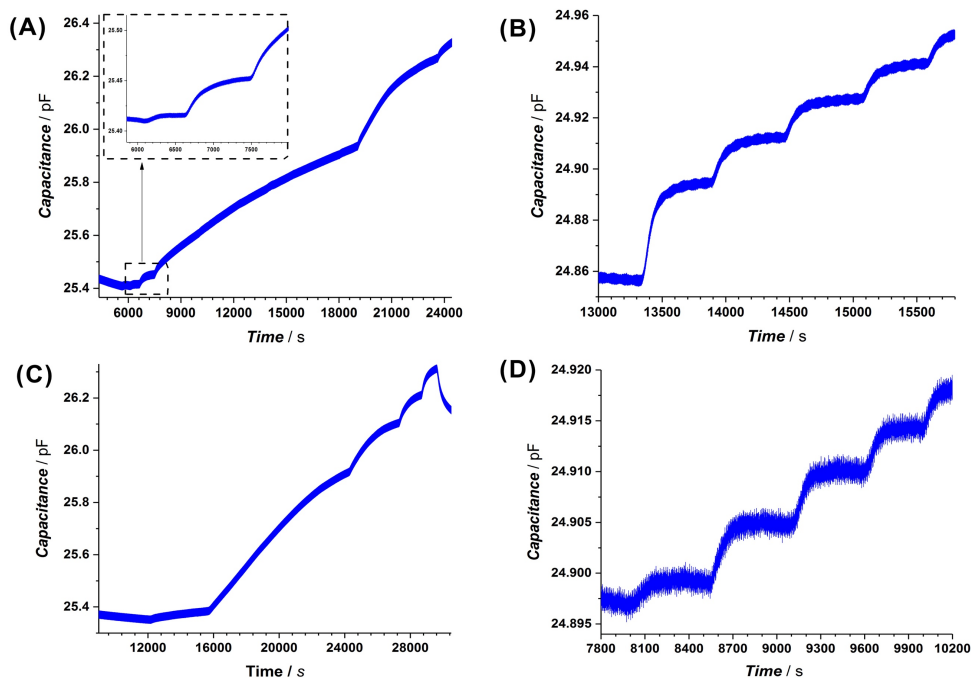


**Figure C16.** Comparison of the capacitive responses of MIL-53(Al)-NH<sub>2</sub> nanoparticles (A, C) and nanolamellae (B, D) coated sensors towards different concentrations of 1-butanol (A, B) and 2-propanol (C, D). The steps indicate response over exposure to 200, 400, 600 and 800 ppm of corresponding alcohol, respectively (from left to right).

Figure C16 shows a comparison of the capacitance responses of MIL-53(Al)-NH<sub>2</sub> nanoparticles and nanolamellae coated devices to changes of alcohol concentrations. It can be observed that MIL-53(Al)-NH<sub>2</sub> nanoparticles display bigger equilibration times (calculated as  $t_{50}$  and  $t_{90}$ ) compared to MIL-53(Al)-NH<sub>2</sub> nanolamellae (Fig. 4.5). This behaviour can be attributed to the faster diffusion in case of nanolamellae due to the shorter pathlength within the particles.

## REFERENCES

- [C1] S. Couck, E. Gobechiya, C. E. A. Kirschhock, P. Serra-Crespo, J. Juan-Alcañiz, A. Martinez Joaristi, E. Stavitski, J. Gascon, F. Kapteijn, G. V. Baron, J. F. M. Denayer, *ChemSusChem* **2012**, 5, 740-750.
- [C2] S. Couck, H. Reinsch, M. A. van der Veen, B. Gil, B. Marszalek, T. Verbiest, D. de Vos, N. Stock, *Chem. Mater.* **2013**, 25, 17.
- [C3] P. Serra-Crespo, E. Gobechiya, E. V. Ramos-Fernandez, J. Juan-Alcañiz, A. Martinez-Joaristi, E. Stavitski, C. E. A. Kirschhock, J. A. Martens, F. Kapteijn, J. Gascon, *Langmuir* **2012**, 28, 12916-12922.

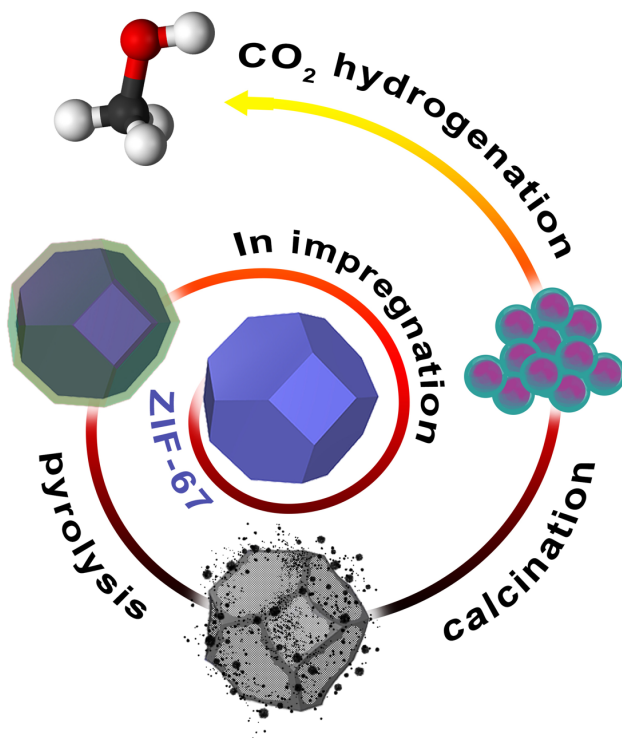




# METAL-ORGANIC FRAMEWORK DERIVED SYNTHESIS OF COBALT INDIUM CATALYSTS FOR CO<sub>2</sub> HYDROGENATION TO METHANOL

## Chapter

## 5



This chapter is based on the following publication:

A. Pustovarenko, A. Dikhtiarenko, A. Bavykina, L. Gevers,  
A. Ramírez, A. Russkikh, S. Telalovic, A. Aguilar,  
J.-L. Hazemann, S. Ould-Chikh, J. Gascon

*ACS Catalysis* **2020**, *10*, 5064-5076

---

**Abstract**

Methanol synthesis by means of direct CO<sub>2</sub> hydrogenation has the potential to contribute to climate change mitigation by turning the most important greenhouse gas into a commodity. However, for this process to become industrially relevant, catalytic systems with improved activity, selectivity and stability are required. Here we explore the potential of metal-organic frameworks (MOF) as precursors for synthesis of Co<sub>3</sub>O<sub>4</sub>-supported In<sub>2</sub>O<sub>3</sub> oxide composites for the direct CO<sub>2</sub> hydrogenation to methanol. Stepwise pyrolytic-oxidative decomposition of indium-impregnated ZIF-67(Co) MOF affords the formation of a nanostructured In<sub>2</sub>O<sub>3</sub>@Co<sub>3</sub>O<sub>4</sub> reticulated shell composite material able to reach a maximum methanol production rate of 0.65 g<sub>MeOH</sub>·g<sub>cat</sub><sup>-1</sup>·h<sup>-1</sup> with selectivity as high as 87% over 100 h on stream. Textural characteristics of the sacrificial ZIF-67(Co) matrix and In-loading were found to be important variables for optimizing the catalyst performance such as induction time, methanol productivity and selectivity. The structural investigation on the catalytic system reveals that the catalyst undergoes reorganization under reaction conditions, transforming from a Co<sub>3</sub>O<sub>4</sub> with amorphous In<sub>2</sub>O<sub>3</sub> shell into Co<sub>3</sub>InC<sub>0.75</sub> covered by a layer consisting of a mixture of amorphous CoO<sub>x</sub> and In<sub>2</sub>O<sub>3</sub> oxides. Structural reorganization is responsible for the observed induction period, while the amorphous mixed cobalt indium oxide shell is responsible for the high methanol yield and selectivity. Additionally, these results demonstrate the tunable performance of MOF-derived In<sub>2</sub>O<sub>3</sub>@Co<sub>3</sub>O<sub>4</sub> catalyst as a function of the reaction conditions which allows to establish a reasonable trade-off between high methanol yield and selectivity in a wide temperature and pressure window.

---

## 5.1 INTRODUCTION

Anthropogenic CO<sub>2</sub> emissions increase year by year, with very serious consequences for our climate. In order to solve these environmental and energy issues, intensive research is being carried out into technologies that may eventually turn our economy into a low-carbon one.<sup>1</sup> In this scenario of a circular carbon economy, carbon dioxide is viewed as an alternative resource that can be recycled to produce valuable chemicals and fuels,<sup>2-4</sup> turning, in such a way, waste to wealth. Among the potential products derived from CO<sub>2</sub>, methanol has attracted particular attention due to its relevance not only as an alternative fuel<sup>5-6</sup> but also as a convenient chemical feedstock.<sup>7-11</sup>

Indeed, methanol synthesis through direct hydrogenation of CO<sub>2</sub>, using pure H<sub>2</sub> and CO<sub>2</sub> as starting materials, is considered to be a very promising strategy to utilize CO<sub>2</sub> when green hydrogen (produced *via* electrolysis using renewable energy) is available.<sup>2,11-13</sup> At the current stage, the Cu-ZnO-Al<sub>2</sub>O<sub>3</sub> catalyst commercially used in the production of methanol from synthesis gas (CO/CO<sub>2</sub>/H<sub>2</sub>) is the benchmark.<sup>14-15</sup> In direct CO<sub>2</sub> hydrogenation, this catalyst is able to drive, to some extent, the production of methanol, however exhibiting low selectivity and fast deactivation caused by the competitive reverse water gas shift reaction (RWGS).<sup>15-17</sup> To address these selectivity and stability issues, a number of multi-metallic composite systems have been proposed, *i.e.* CuO/ZrO<sub>2</sub>, CuO/ZnO/ZrO<sub>2</sub>, CuO/ZnO/Ga<sub>2</sub>O<sub>3</sub>, Cu/ZnO/ZrO<sub>2</sub>/Al<sub>2</sub>O<sub>3</sub>/SiO<sub>2</sub>,<sup>18-21</sup> and their doped variations (*i.e.*, by Ag, Au, Pt, Pd, Rh promoters).<sup>22-27</sup> These mix-component systems are able to convert CO<sub>2</sub> to methanol with high selectivities at low conversions per pass, such as in the case of Cu@ZnO core-shell ( $S_{\text{MeOH}} \sim 100\%$ ,  $X_{\text{CO}_2}$  conversion of 2.3%)<sup>21</sup> or Au-doped ZnO-ZrO<sub>2</sub> ( $S_{\text{MeOH}} \sim 100\%$ ,  $X_{\text{CO}_2} \sim 1.5\%$ ).<sup>27</sup> Contrariwise, when higher CO<sub>2</sub> conversions are targeted, low methanol selectivities are usually achieved. This is the case, for instance, for Cu-K/Al<sub>2</sub>O<sub>3</sub> ( $S_{\text{MeOH}} = 2\%$  at  $X = 29\%$ )<sup>28</sup> and for Cu/Zn/Al/Y ( $S_{\text{MeOH}} = 52\%$  at  $X = 27\%$ ).<sup>29</sup>

Among recent studies on simpler metal oxide systems featuring higher stability, density functional theory (DFT) calculations predict that methanol synthesis *via* CO<sub>2</sub> hydrogenation is favored over In<sub>2</sub>O<sub>3</sub> surfaces.<sup>30</sup> The proposed catalytic mechanism involves cyclic generation of oxygen vacancies on In<sub>2</sub>O<sub>3</sub> by H<sub>2</sub> and their replenishment *via* CO<sub>2</sub> activation. Later, Sun *et al.*<sup>31</sup> experimentally proved the superior activity of In<sub>2</sub>O<sub>3</sub> for CO<sub>2</sub> hydrogenation to methanol. When In<sub>2</sub>O<sub>3</sub> is supported on ZrO<sub>2</sub>, further improvements in catalytic performance have been reported: at low conversion levels, almost 100% selectivity to methanol with space time yield (STY) of 0.32 g<sub>MeOH</sub>·g<sub>cat</sub><sup>-1</sup>·h<sup>-1</sup> and stable performance over 1000 h on stream can be achieved.<sup>32</sup> In light of recent advances made in In-based bimetallic formulations<sup>33</sup> with improved catalytic merits

and inspired by the drastic importance of carrier supports in such catalytic systems, Bavykina *et al.*<sup>34</sup> prepared a pre-catalyst consisting of  $\text{In}_2\text{O}_3$  supported on  $\text{Co}_3\text{O}_4$  by means of reverse co-precipitation. The resulting  $\text{In@Co}$  system catalyzes methanol formation *via*  $\text{CO}_2$  hydrogenation with selectivities above 80% and productivity of  $0.86 \text{ g}_{\text{MeOH}} \cdot \text{g}_{\text{cat}}^{-1} \cdot \text{h}^{-1}$ , at conversion levels close to thermodynamic equilibrium.

It is well known that in heterogeneous catalysis the preparation method significantly affects catalytic performance.<sup>25</sup> Over the last decade, particular interest has been paid to Metal-Organic Framework (MOF)-supported and MOF mediated synthetic approaches to prepare highly effective catalysts for a variety of catalytic transformations.<sup>35-37</sup> Being microporous crystalline materials with a tailored arrangement of metal-centers and bridging linkers,<sup>38</sup> MOFs possess a pore system that can be loaded with active components offering an optimal distribution of active sites. For instance, an encapsulation of Cu and/or ZnO nanoparticles within  $\text{UiO-66}(\text{Zr})$ <sup>39,40</sup> resulted in highly active catalyst showing an 8-fold enhanced yield and 100% selectivity towards methanol (albeit at very low conversions, where the effect of RWGS is minimized) when compared to the benchmark  $\text{Cu/ZnO/Al}_2\text{O}_3$ . Besides the promising perspectives of MOF-supported catalysts, recent investigations reveal the advantages in preparation of highly efficient heterogeneous catalytic materials from metal-organic framework supports/precursors by means of thermal decomposition.<sup>37,41-42</sup> MOF-derived nanocomposite materials, *i.e.* MOF-derived carbons and oxides, feature a range of advantages, such as high specific area, porosity and excellent distribution of the active component within the host matrix, compared to similar materials prepared by co-precipitation or impregnation methods.<sup>37,42</sup>

In light of these results, here we explore the MOF mediated route for the preparation of a highly efficient  $\text{Co}_3\text{O}_4$ -supported  $\text{In}_2\text{O}_3$  catalyst in line with our previous findings on this inorganic system.<sup>34</sup> The impregnation of  $\text{ZIF-67}(\text{Co})$  with indium, followed by thermal decomposition, results in the formation of  $\text{In@Co}$  oxide composite materials with enhanced catalytic behavior in  $\text{CO}_2$  hydrogenation to methanol, revealing higher methanol yields, selectivities and significantly shortened induction times (10 h vs. 30 h observed for  $\text{In@Co}$  prepared by co-precipitation).<sup>34</sup> The influence of the crystal size of the parent  $\text{ZIF-67}(\text{Co})$  and the amount of loaded indium on the catalytic performance has been thoroughly studied. Moreover, the importance of the two-step thermal treatment (pyrolysis followed by calcination) for  $\text{In}$ -impregnated  $\text{ZIF-67}(\text{Co})$  material in order to obtain highly performing catalysts is also discussed in detail.

## 5.2 EXPERIMENTAL SECTION

### 5.2.1 Materials

All chemicals were purchased from Sigma-Aldrich and used as received. Commercial Cu-ZnO-Al<sub>2</sub>O<sub>3</sub> methanol synthesis catalyst was obtained from Alfa Aesar™ (composition: 60-68% CuO, 22-26% ZnO, 8-12% Al<sub>2</sub>O<sub>3</sub>, 1-3% MgO).

### 5.2.2 Synthetic procedures

#### 5.2.2.1 Synthesis of 300 nm ZIF-67(Co) material

The synthesis of ZIF-67(Co) with a crystallite size of around 300 nm was performed in accordance with the previously reported method.<sup>43-44</sup> Following the typical synthetic protocol, 2.933 g (10 mmol) Co(NO<sub>3</sub>)<sub>2</sub>·6H<sub>2</sub>O and 6.489 g (79 mmol) 2-methylimidazole (Melm) were separately dissolved in 200 mL methanol. The Melm-containing clear solution was rapidly poured into the pink solution of the cobalt salt. The mixture was stirred for 12 min and then kept standing for 24 h to allow precipitation to take place. The bright purple product was collected by centrifugation, washed several times with methanol, and dried at 423 K for 10 h under vacuum.

#### 5.2.2.2 Synthesis of 22 nm ZIF-67(Co) material

ZIF-67(Co) with a crystallite size around 22 nm was obtained through modulated synthesis with triethylamine (TEA). In typical procedure, 0.582 g (2 mmol) Co(NO<sub>3</sub>)<sub>2</sub>·6H<sub>2</sub>O and 4.866 g (60 mmol) 2-methylimidazole (Melm) were dissolved in 400 mL methanol. Afterwards, 5 mL triethylamine was added to the vigorously stirred mixture and stirring continued for 15 min. When precipitation started, the mixture was kept steady for 24 h. The product was collected by centrifugation, washed several times with methanol, and dried at 423 K for 10 h under vacuum.

#### 5.2.2.3 Synthesis of MOF-derived In@Co catalysts by *IWI*

The catalysts were prepared by the incipient wetness impregnation (*IWI*) in the following manner: 1 g activated ZIF-67(Co) was impregnated with 3 mL aqueous indium nitrate solution of different indium concentrations as stated in Table D1 and then dried under vacuum at 100 °C overnight. For thermal treatment, an In-impregnated ZIF-67(Co) precursor sample was transferred into a quartz reactor ( $L = 1$  m and ID = 5 cm), vertically inserted into tubular oven equipped with temperature (Nabertherm) and mass-flow controllers (Bronkhorst® High-Tech), and followed by two thermal treatment steps in sequential order: first, pyrolysis at 600 °C (1 °C·min<sup>-1</sup>, 4 h) in nitrogen flow (25 mL·min<sup>-1</sup>), then calcination at 400 °C (1 °C·min<sup>-1</sup>, 2 h) in air

flow (25 mL·min<sup>-1</sup>). The obtained In@Co samples are denoted as *a*In:*b*Co(*x*) where *x* is the crystal size (nm) of the ZIF-67(Co) precursor, *a*:*b* indicate the desired In:Co molar ratio.

### 5.2.3 Characterization methods

*Powder X-ray diffraction* (PXRD) patterns were acquired on a Bruker D8 Advance diffractometer in Bragg-Brentano geometry fitted with a copper tube operating at 40 kV and 40 mA and a linear position sensitive detector. The data sets were acquired in continuous scanning mode over the 2 $\theta$  range 10 – 80°, using a stepsize of 0.05° and a counting time of 15 s per step. For phase analysis of reacted catalysts, the X-ray diffraction data were measured under inert atmosphere using an airtight sample holder which was loaded in a glove box under Ar atmosphere. The crystalline phase was identified with the help of the PDF-4+ (2019) crystal database. The profile matching of all PXRDs with expected crystalline phases was confirmed by Pawley fitting<sup>45</sup> and quantitative estimation of the phases was obtained by Rietveld refinement using TOPAS V5 (academic version) software.<sup>46</sup> The results of refinements are provided in Fig. D28.

*Nitrogen adsorption* experiments were carried out at 77 K using a Micromeritics ASAP 2040 instrument. Before the measurements, the ZIF-67(Co) samples were degassed at 150 °C for 10 h and the calcined products were degassed at 100 °C for 10 h.

*Thermogravimetric data* (TG) were collected in nitrogen and air atmospheres using a Mettler Toledo thermal analyzer at a heating rate of 5 °C·min<sup>-1</sup> in the 25 – 950 °C temperature range and at a dynamic gas flow rate of 20 mL·min<sup>-1</sup>.

*Scanning electron microscopy* (SEM) imaging was performed with secondary electrons on a FEI TENE0 VS microscope using 5 kV acceleration voltage and 5 mm working distance. The crystal size distribution for each sample was obtained analyzing several images recorded at different magnifications using ImageJ software.<sup>47</sup>

*The annular Dark-Field scanning transmission electron microscopy* (ADF-STEM) in conjunction with *Electron Energy Loss Spectroscopy* (EELS) study was carried out with a Cs-Probe Corrected Titan microscope (Thermo-Fisher Scientific) which was also equipped with a GIF Quantum of model 966 from Gatan Inc. (Pleasanton, CA). STEM-EELS analysis was performed by operating the microscope at the accelerating voltage of 300 kV, using a convergence angle  $\alpha$  of 17 mrad and a collection angle  $\beta$  of 38 mrad. Spectrum-imaging dataset includes the simultaneous acquisition of zero-loss and core-loss spectra (DualEELS) using a dispersion of 0.5 eV/channel and were recorded using a beam current of 0.2 nA and a dwell time of 20 ms/pixel. The Co L<sub>2,3</sub>-edge, In M<sub>4,5</sub>-edge, and O K-edge were selected to build the chemical maps. Carbon K-edge was acquired by continuously scanning a Co<sub>3</sub>InCo<sub>0.75</sub>

nanoparticle while simultaneously acquiring 10 Dual-EELS spectra (frame time = 10 s) using a dispersion of 0.1 eV/channel. The energy scale of all high loss EELS spectra was referenced to the zero-loss peak. Carbon *K*-edge spectra were normalized using ATHENA software.<sup>48</sup> Typically, the specimens were prepared by dispersing the catalyst in methanol under ultrasound irradiation during 30 min and placing several drops of the resulting dispersion on the copper grids having a carbon layer. For the particular study of carbon *K*-edge, a nickel grid with a lacey-carbon layer was used to record EELS spectra without the interference of the supporting carbon. The QSTEM software<sup>49</sup> was used to simulate high-resolution lattice images of the Co<sub>3</sub>InC<sub>0.75</sub> nanoparticle along the <101> zone axis using a slab thickness of 4.8 nm. For the microscope parameters, we used an accelerating voltage of 300 kV, a spherical aberration coefficient (*C<sub>s</sub>*) of 1.0 mm, a defocus (*df*) of -1.7 nm, a chromatic aberration coefficient (*C<sub>c</sub>*) of 1 mm, an energy spread (*dE*) of 1.0 eV, a convergence angle  $\alpha = 17$  mrad, and a detector collection angle of [63, 200] mrad. *Ab-initio* simulations of the carbon *K*-edge were performed using the FDMNES package. The FDMNES code features mono-electronic calculations, which are carried out in real space with Hedin-Lundqvist exchange-correlation potential and using clusters built around each non-equivalent absorbing atom.<sup>50-51</sup> The finite-difference method (FDM) implemented in the FDMNES code was used since the latter is a full potential method that introduces no approximation on the shape of the potential. To take into account the core-hole lifetime and other multielectronic phenomena occurring in the absorption process, a convolution procedure was applied to the calculated spectra. At the Fermi level, the Lorentzian full width at half-maximum (FWHM) width was set to 0.16 eV. The instrumental energy resolution was taken into account by further convoluting the calculated spectra with a Gaussian broadening of 1.5 eV width.

*X-ray absorption spectroscopy* (XAS) experiments were performed at CRG-FAME beamline (BM30B) at the European Synchrotron Radiation Facility (ESRF). The ring is operated at 6 GeV with a nominal current of 200 mA in 7/8+1 mode. The beamline is equipped with a liquid-nitrogen-cooled doubled crystal Si(220) monochromator surrounded by two Rh-coated mirrors for harmonic rejection. The beam size on the sample is 240 × 110 μm (*H*×*V*, FWHM). Cobalt *K*-edge spectra were collected in fluorescence mode using a CANBERRA 30-elements Ge solid state detector. Indium *K*-edge spectra were collected in transmission mode using silicon diodes to measure the incident and transmitted beam intensities. The monochromator was energy calibrated measuring the cobalt and indium *K* absorption edges using a metallic cobalt and indium foil respectively. First maximum of the 1<sup>st</sup> derivative of the absorption cobalt *K*-edge was set at 7709 eV and 27940 eV for indium *K*-edge. The data acquisitions of spent catalysts were performed *ex-situ* either in fluorescence or transmission mode with the samples



retrieved inside a glove box and loaded into a XAS cell dedicated for air-sensitive compounds. Non-air sensitive fresh catalyst and reference compounds were handled outside of glove box and measured in fluorescence mode using conventional sample holder. All samples were diluted with boron nitride and pressed into pellets to optimize the effective extended X-ray absorption fine structure (EXAFS) edge-step. On average four scans were acquired for each sample to improve the signal to noise level of the data. All XAS data were analyzed using the HORAE package, a graphical interface to the AUTOBK and IFEFFIT code.<sup>48</sup> The EXAFS spectra were obtained after performing standard procedures for pre-edge subtraction, normalization, polynomial removal, and wavevector conversion. The amplitude factors ( $S_0^2$ ) were fitted to the EXAFS spectra recorded for a Co metallic foil and an  $\text{In}_2\text{O}_3$  powder (Table D3 and Figure D18).  $S_0^2$  were determined to be  $0.73 \pm 0.04$  and  $0.99 \pm 0.03$  for Co and In, respectively.

*CHN elemental analyses* on selected samples were performed using a Thermo Flash 2000 Organic Elemental Analyzer with the detection limits of 0.2% (w/w) for carbon, 0.1% for nitrogen and 0.08% for hydrogen. For the analysis of the used catalysts, the corresponding samples were transferred unopened from the reactor to the glovebox and were kept under Ar atmosphere. To avoid undesired reaction of the used catalysts with air, all samples were sealed in tin sample crucibles in a glove box under Ar atmosphere. For each sample three individual measurements were performed and the mean was calculated as a final result.

*X-ray fluorescence measurements* (XRF) were performed on a HORIBA XGT-700 XRF analyzer. For every measurement, three different spots were analyzed for each sample with a total acquisition time of 1500 s per sample.

#### 5.2.4 Catalytic testing in $\text{CO}_2$ hydrogenation to methanol

Catalytic tests were performed using a parallel reactor system Flowrence<sup>®</sup> from Avantium consisting of 16 tubular fix-bed reactors installed in a furnace and operated at one mixed feed gas flow which is distributed over 16 channels with a relative standard deviation of 2%. Catalyst (50 mg) with particle fraction between 150  $\mu\text{m}$  and 250  $\mu\text{m}$  was loaded onto the stainless-steel tube reactor (30 cm long with 2 mm of internal diameter) preliminary filled with 9.5 cm bed of coarse SiC (particle grit 40, 300  $\mu\text{L}$ ) in order to ensure the isothermal zone for the catalytic bed. Before the catalytic test, the catalysts were pretreated in-situ under  $\text{N}_2$  at 300 °C for 1 h. Then, the reactors were pressurized with a mixed feed containing 20 vol.%  $\text{CO}_2$  and 80 vol.%  $\text{H}_2$  to 50 bar using a membrane-based pressure controller. In addition, 0.5 mL/min He was mixed with the feed and used as internal standard. The products were analyzed with an Agilent 7890B chromatograph equipped with two injection loops, where one was connected to the Column 5

HaysepQ6 Ft G3591-80013 and TCD and the second Gaspro 30M, 0.32 mm OD column followed by a flame ionization detector.

Conversion ( $X$ , %), space time yield ( $STY$ ,  $\text{g} \cdot \text{g}_{\text{cat}}^{-1} \cdot \text{h}^{-1}$ ), and selectivity ( $S$ , %) are defined as follows:

$$X_{\text{CO}_2} = \left(1 - \frac{C_{\text{He,blk}} \cdot C_{\text{CO}_2,\text{R}}}{C_{\text{He,R}} \cdot C_{\text{CO}_2,\text{blk}}}\right) \cdot 100 \quad (\text{eq. 5.1})$$

$$S_i = \frac{\left(\frac{C_{i,\text{R}}}{C_{\text{He,R}}}\right)}{\left(\frac{C_{\text{CO}_2,\text{blk}}}{C_{\text{He,blk}}} - \frac{C_{\text{CO}_2,\text{R}}}{C_{\text{He,R}}}\right)} \cdot 100 \quad (\text{eq. 5.2})$$

$$STY_i = \frac{\frac{X_{\text{CO}_2}}{100} \cdot \frac{S_i}{100} \cdot M_i \cdot GHSV}{22.4} \quad (\text{eq. 5.3})$$

where  $C_{\text{He,blk}}$ ,  $C_{\text{He,R}}$ ,  $C_{\text{CO}_2,\text{blk}}$ ,  $C_{\text{CO}_2,\text{R}}$  are the concentrations determined by GC analysis of He in the blank, He in the reactor effluent, CO<sub>2</sub> in the blank, and CO<sub>2</sub> in the reactor effluent, respectively,  $C_{i,\text{R}}$  is the concentration of the product determined by GC,  $M_i$  is the molecular mass of product  $i$  and GHSV is CO<sub>2</sub> gas hourly space velocity in  $\text{L} \cdot \text{g}_{\text{cat}}^{-1} \cdot \text{h}^{-1}$ .

Carbon balance in all experiments accounted for more than 97.8% of the total carbon input, whereas a small amount of carbon trapped in the form of mixed metal carbide was comparatively modest. Reproducibility of the catalytic experiment was carried out for representative samples and was found to fall within 1.7% of the relative experimental error.

### 5.3 RESULTS AND DISCUSSION

In our study we explored ZIF-67(Co) framework as a precursor material for the preparation of indium loaded MOF-derived cobalt oxide supported catalysts (In@Co). ZIF-67(Co) is a zeolitic imidazolate framework formed by cobalt and 2-methylimidazole (Melm) featuring a porous architecture with sodalite (**sod**) topology (Fig. 5.1A-B), and has been chosen as a sacrificial material because of its high cobalt content (26 wt.% Co). We synthesized two types of ZIF-67(Co) samples with different crystal sizes in order to evaluate the effect they may induce on the performance of the derived In@Co catalysts. Thus, applying a modulated synthesis protocol, ZIF-67(Co) with average crystal sizes of 20 nm and 300 nm were obtained. These samples are referred as ZIF-67(Co)-20 and ZIF-67(Co)-300, respectively. As it can be observed from Figures 5.1D-E (insets) and D1, both samples possess narrow size distribution profiles. To confirm matching of ZIF-67(Co)-20 and -300 with the ZIF-67 structure, powder X-ray diffraction analyses have been performed and compared in Figure 5.1C. Both materials reveal

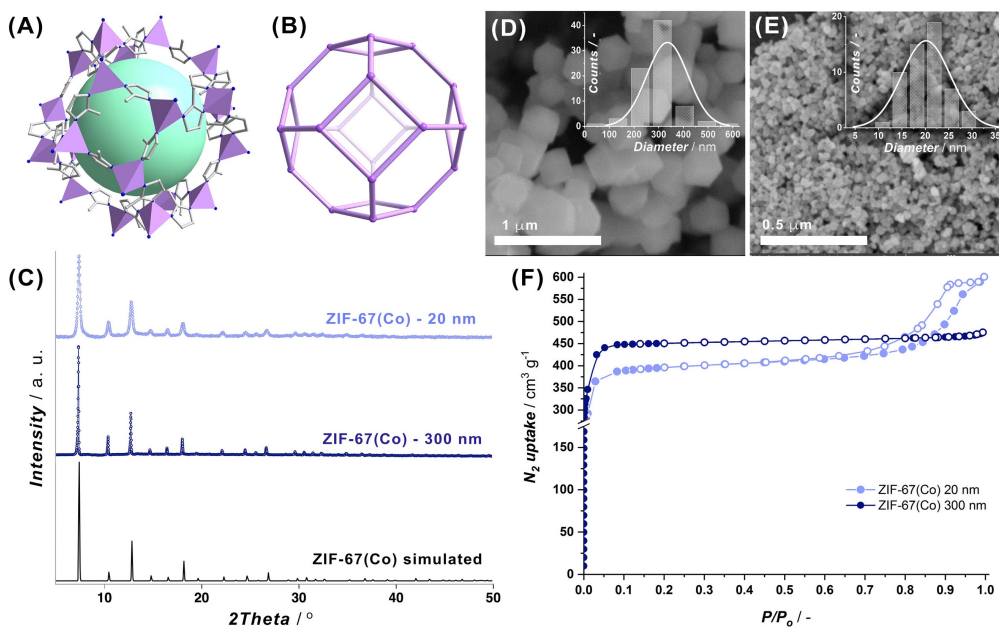


**Figure 5.1.** (A) Cage structure of ZIF-67(Co) and (B) its topological view revealing **sod** fragment. (C) Powder X-ray diffraction patterns compared to theoretically expected ZIF-67(Co) (cubic *I*-43m);<sup>53</sup> (D-E) SEM micrographs along with size distribution histograms (insets) and (F)  $N_2$  adsorption isotherms acquired at 77 K for ZIF-67(Co) precursor samples of  $300 \pm 85$  nm (blue symbols) and  $20 \pm 5$  nm (violet symbols) crystal sizes, respectively. On the isotherm graph the filled markers correspond to the adsorption curve and the hollow ones to desorption branch.

the typical reflections attributed to the cubic ZIF-67 structure.<sup>52-53</sup> However, the notable broadening of the peaks in case of ZIF-67(Co)-20 indicates that the sample has a smaller crystal size compared to the ZIF-67(Co)-300.

In order to evaluate the textural properties of the ZIF-67(Co)-20 and -300 materials with different crystal sizes, nitrogen adsorption experiments have been carried out. Figure 5.1F shows corresponding nitrogen sorption isotherms for both 20 nm and 300 nm ZIF-67(Co) precursors. The Brunauer-Emmett-Teller (BET) analyses reveal very close microporous surface areas of  $1579$  and  $1566 \text{ m}^2 \cdot \text{g}^{-1}$  for ZIF-67(Co)-300 and -20, respectively (Table D2). Notably, the  $N_2$  adsorption isotherm for ZIF-67(Co)-300 exhibits a typical type I shape, corroborating the fully microporous nature of the material, whereas ZIF-67(Co)-20 features IV-type with a hysteresis loop at high relative pressures, most likely derived from interparticle condensation of  $N_2$ .<sup>54-55</sup>

Considering that in our study the catalysts are prepared by thermal decomposition of ZIF-67(Co), thermogravimetric analysis is a necessary tool to determine optimal conditions for the treatment. ZIF-67(Co) decomposes in nitrogen atmosphere at temperatures above  $550^\circ\text{C}$  (Fig.

D2) yielding Co nanoparticles of ~ 4.7 nm size highly dispersed within a carbon matrix, which mainly consists of graphite nanotubes (Fig. D3). The PXRD data for the Co@C material derived from pristine ZIF-67(Co) show (Fig. D4) broad peaks originated from graphite (*hcp* C allotrope) and metallic Co (*fcc* form,  $\alpha$ -Co allotrope) phases. Notably, the pyrolysis of ZIF-67(Co) at 600 °C results in the formation of  $\alpha$ -Co phase,<sup>56</sup> an allotrope which is expected to be thermodynamically favored at temperatures above 417 °C and exists as a metastable phase at room temperature.<sup>56</sup> In contrast, the decomposition of ZIF-67(Co) in air flow proceeds in two steps (Fig. D2): i) oxidative destruction of the framework with a weight loss of ca. 63 wt.% yielding Co<sub>3</sub>O<sub>4</sub> as main decomposition product at 400 °C; and ii) transformation<sup>57</sup> of Co<sub>3</sub>O<sub>4</sub> to CoO occurring at 900 °C with additional 2.7 wt.% mass loss. In a similar way, Co@C decomposes during the calcination step (Fig. D5), losing 43 wt.% because of carbon oxidation resulting in Co<sub>3</sub>O<sub>4</sub> at 400 °C. The product obtained by two-step decomposition comprises uniform nanoparticles of 5.8 nm average size (Fig. D6) with the spinel Co<sub>3</sub>O<sub>4</sub> structure (Fig. D7).

Typically, we prepared In@Co catalysts in three steps: i) incipient wetness impregnation of ZIF-67(Co) with an aqueous In(NO<sub>3</sub>)<sub>3</sub> solution; ii) pyrolysis of In@ZIF-67(Co) at 600 °C in nitrogen; iii) calcination of the obtained product at 400 °C in a flow of synthetic air. Upon IWI step, ZIF-67(Co) crystals undergo agglomeration with visible sealing at the edges of the particles (Fig. D8). Thereafter, during the pyrolysis step, In@ZIF-67(Co) transforms into a mixture of freestanding spherical particles of about 12 nm size, which tend to sinter under the electron beam, and agglomerations of smaller ones with a mean size of about 10 nm (Fig. D9). Qualitative analysis performed on the XRD pattern indicates a mixture of nanosized  $\alpha$ -Co and mixed-metal carbide, Co<sub>3</sub>InCo<sub>0.75</sub> phases, where the carbide phase is dominant (Fig. D10). This observation supports the effectiveness of the IWI method and suggests high dispersion of the loaded In component. At the last step of catalyst preparation, the pyrolyzed product has been calcined in a stream of air at the temperature suitable for conversion to oxide form (*i.e.* 400 °C).

The resulting catalyst, having an In:Co molar ratio of 3:8 and referred to as **3In@8Co(300)**, consists of 5-10 nm sized oxide nanoparticles (Fig. D11) developing a considerable high surface area of 107 m<sup>2</sup>·g<sup>-1</sup>. Notably, the XRD pattern reveals broad diffraction lines attributed only to the Co<sub>3</sub>O<sub>4</sub> phase. This is also in accordance with the EXAFS spectroscopy applied at the Co *K*-edge, which reveals the characteristic fingerprint of the Co<sub>3</sub>O<sub>4</sub> crystal structure and is further supported by subsequent fitting of the EXAFS data (details in Appendix D: Table D3, Figs. D17A-B). An interesting observation is the absence of any In-derived compounds in the PXRD pattern, although the sample was calcined at 400 °C (Fig. D12). The state of indium in the **3In@8Co(300)** pre-catalyst was thus refined by EXAFS spectroscopy applied at the indium

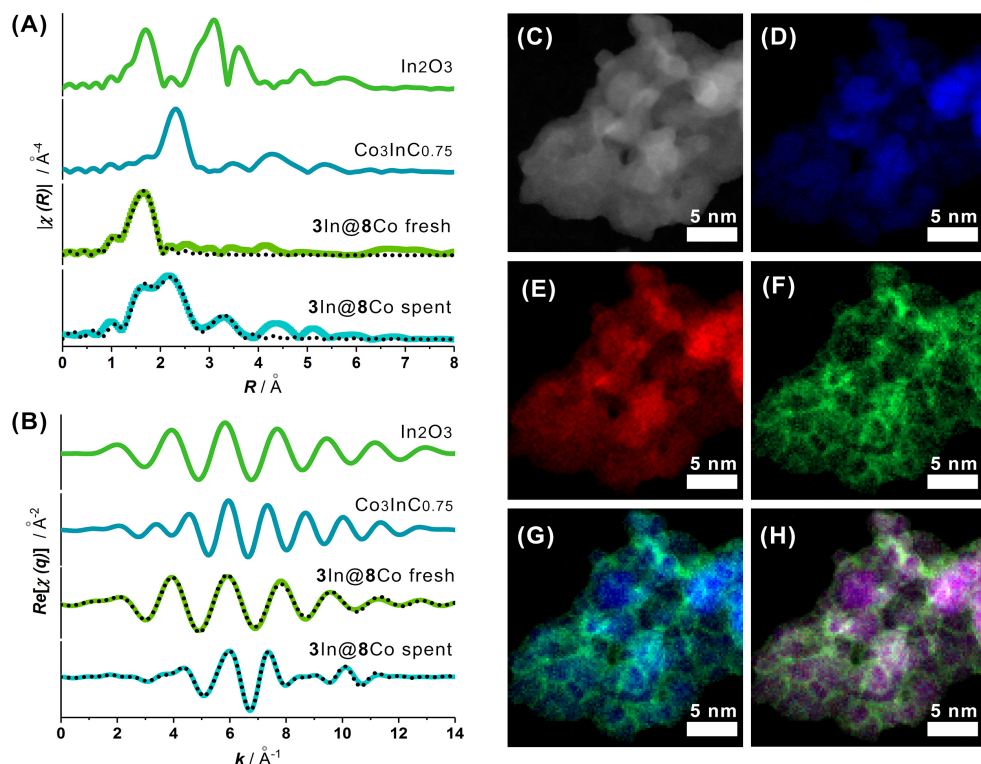


**Figure 5.2.** (A) Magnitude of the Fourier transform for the EXAFS  $k^3 \cdot \chi(k)$  functions acquired at In K-edge for  $\text{In}_2\text{O}_3$ ,  $\text{Co}_3\text{InCo}_{0.75}$ ,  $3\text{In}@8\text{Co}(300)$  catalyst before and after  $\text{CO}_2$  hydrogenation reaction and, (B) their related back Fourier transforms (real part) applied within their respective R-range for EXAFS fitting. Solid line represents experimental data whereas dotted line corresponds to fit results conducted with [1.1–2.5] Å and [1.2–3.6] Å R-range together with a [2.9–12.8] Å<sup>-1</sup> and [3.8–10.4] Å<sup>-1</sup> k-range, respectively for  $3\text{In}@8\text{Co}(300)$  catalyst before and after reaction. (C) ADF-STEM image and elemental mappings for  $3\text{In}@8\text{Co}(300)$ : (D) Co, (E) O, (F) In maps and superimposed (G) Co/In maps and (H) Co/In/O maps.

K-edge. The spectrum of  $3\text{In}@8\text{Co}(300)$  pre-catalyst is shown on Figs. 5.2A-B together with the spectrum of a crystalline  $\text{In}_2\text{O}_3$ .

Qualitative assessment of the of the Fourier transform (FT)-EXAFS spectra for the  $\text{In}_2\text{O}_3$  reference (without phase correction), indicate a main peak at 1.7 Å attributed to In-O scattering and several peaks between 2.5 and 4.3 Å assigned mainly to In-In path with some minor contributions from In-O scattering and some multiple scattering processes.<sup>58</sup> In contrast, the FT-EXAFS of the  $3\text{In}@8\text{Co}(300)$  pre-catalyst shows only one prominent peak centered around 1.6 Å which is similar to the low- $R$  peak of the  $\text{In}_2\text{O}_3$  FT-EXAFS spectrum. The lack of contribution from more distant coordination shells (e.g. In-In scattering path, Table D3) is associated with deficiency of the long-range order and proves the amorphous nature of the indium component in the  $3\text{In}@8\text{Co}(300)$  pre-catalyst. Quantitative EXAFS fitting of the first shell

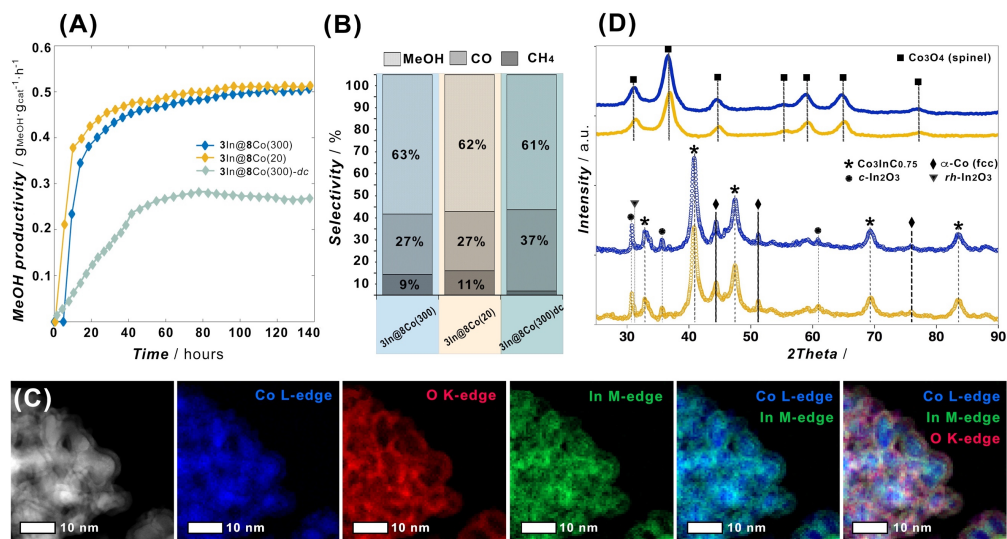


**Figure 5.3.** (A) Kinetic profile of evolution MeOH space time yield with time and (B) MeOH, CO and CH<sub>4</sub> selectivities at TOS of 100 h over **3In@8Co(300)** (orange line), **3In@8Co(20)** (navy line) and **3In@8Co(300)-dc** (turquoise line) catalysts at X<sub>CO<sub>2</sub></sub> of 18%, 19% and 13%, respectively. (B) MeOH, CO and CH<sub>4</sub> selectivities on stable plateau of the kinetic profile (100 h) on studied catalysts. Reaction conditions: 80% H<sub>2</sub>-20% CO<sub>2</sub> feed; T = 300 °C, P = 50 bar, m<sub>cat</sub> = 50 mg, GHSV = 15600 h<sup>-1</sup>. (C) ADF-STEM imaging and elemental mapping for **3In@8Co(300)** after the reaction: (from left to right) ADF-STEM image, Co, O, In maps and superimposed Co/In maps and Co/In/O maps. (D) XRD patterns for fresh (top) and spent (bottom) **3In@8Co(300)** (orange) and **3In@8Co(20)** (navy) catalysts compared to identified phases: Co<sub>3</sub>O<sub>4</sub> (■), Co<sub>3</sub>InCo<sub>0.75</sub> (\*), α-Co (fcc, ◆), c-In<sub>2</sub>O<sub>3</sub> (cubic, ●) and rh-In<sub>2</sub>O<sub>3</sub> (rhombohedral, ▼).

with a single In-O scattering path provides a coordination number of  $6.3 \pm 0.7$  at a bonding distance of  $2.14 \pm 0.01$  Å, consistent with an octahedral coordination (Table D3). The distribution of the indium oxide within the sample is further highlighted by ADF-STEM imaging and EELS elemental mapping (Figs. 5.2C-H): the amorphous indium oxide covers homogeneously the 5 nm Co<sub>3</sub>O<sub>4</sub> nanoparticles as a thin layer.

The catalytic performance of ZIF-67(Co)-derived indium containing catalysts in CO<sub>2</sub> hydrogenation has been evaluated at 300 °C and 50 bar with a constant 20% CO<sub>2</sub>/80% H<sub>2</sub> feed flow. The kinetic profile of the reaction on **3In@8Co(300)** catalyst (Fig. 5.3A) shows an induction period of 20 h until it reaches 0.4 g<sub>MeOH</sub>·g<sub>cat</sub><sup>-1</sup>·h<sup>-1</sup> methanol productivity. As the reaction proceeds, the methanol selectivity stabilizes at 63% with CO and CH<sub>4</sub> by-product selectivities of 27% and 9%, respectively (Fig. 5.3B, Fig. D29). Overall, the CO<sub>2</sub> conversion is stable over 100 h on steady state performance, yielding a STY of 0.5 g<sub>MeOH</sub>·g<sub>cat</sub><sup>-1</sup>·h<sup>-1</sup> for methanol.

As previously reported by our group<sup>34</sup> and characterized below (*vide infra*), the induction period is associated with the formation of the active phase by a solid reaction between the indium oxide layer with its supporting cobaltite phase. Having a higher external surface area in

the starting sacrificial ZIF-67(Co) is expected to enhance the contact between indium and cobalt oxides and to increase substantially the formation rate of the active phase. To this end, another ZIF-67(Co) support with smaller crystal size - ZIF-67(Co)-20nm – was used to improve the dispersion of the In-component. The impregnation at the same In:Co molar ratio (3:8) followed by a two steps thermal decomposition resulted in a material possessing  $119 \text{ m}^2\cdot\text{g}^{-1}$  of total surface area, **3In@8Co(20)** (Table D4). The kinetic profile of reaction expressed in  $\text{STY}_{\text{MeOH}}$  on **3In@8Co(20)** catalyst is shown on Figure 5.3A and compared to **3In@8Co(300)** behavior at the same reaction conditions. As anticipated, **3In@8Co(20)** catalyst obtained from MOF with smaller particle size shows considerably reduced induction period of 10 h versus 19 h ( $\text{STY}_{\text{MeOH}}$  of  $0.38 \text{ g}_{\text{MeOH}}\cdot\text{g}_{\text{cat}}^{-1}\cdot\text{h}^{-1}$ ) observed in case of **3In@8Co(300)**. However, both catalysts demonstrate similar selectivities towards MeOH (~63%) and by-products (CO, ~27% and  $\text{CH}_4$ , ~9-11%) reaching stable STY values of  $0.52 \text{ g}_{\text{MeOH}}\cdot\text{g}_{\text{cat}}^{-1}\cdot\text{h}^{-1}$  for methanol production.

To gain some insights on the structural composition of **3In@8Co** after the catalytic run, PXRD analyses were performed for spent catalysts which were protected under inert atmosphere in order to exclude any possible phase transformation caused by exposure to air. Comparison of the diffraction patterns for fresh and spent catalysts along with the  $d$ -spacing positions for identified crystalline phases is shown in Figure 5.3D. Evidently, both catalysts undergo a phase transformation – from crystalline spinel with amorphous  $\text{In}_2\text{O}_3$  to a complex mixture consisting of mixed-metal carbide  $\text{Co}_3\text{InC}_{0.75}$ ,  $\alpha$ -Co (*fcc* form), cubic allotrope of  $\text{In}_2\text{O}_3$  (*c*- $\text{In}_2\text{O}_3$ ), traces of rhombohedral  $\text{In}_2\text{O}_3$  phase (*rh*- $\text{In}_2\text{O}_3$ ) and both CoO polymorphs (Fig. D13). Besides the evidences gained from PXRD, these structural transformations were confirmed by In and Co  $K$ -edge EXAFS analyses performed *ex-situ* for the catalyst before and after catalytic process (Figs. 5.2A-B, D18A-D and D17A-B, Table D3). Interestingly, the hexagonally packed *rh*- $\text{In}_2\text{O}_3$  is a metastable polymorphic form of indium oxide which irreversibly transforms, under elevated temperatures and pressures of 0.1 MPa – 3 GPa, to the more stable cubic form.<sup>59-60</sup> Additionally, in strongly reductive atmospheres, such as CO and  $\text{H}_2$ , the allotrope transformation proceeds following the same pathway - *rh*- $\text{In}_2\text{O}_3 \rightarrow$  *c*- $\text{In}_2\text{O}_3$  meanwhile the reverse transformation happens only at high energy input.<sup>61</sup> Extrapolating the observation, one of the processes occurred during the catalytic run is recrystallization of amorphous  $\text{In}_2\text{O}_3$ : first, to *rh*- $\text{In}_2\text{O}_3$  and then to more stable *c*- $\text{In}_2\text{O}_3$ . However, a minor part of *rh*- $\text{In}_2\text{O}_3$  is still present after catalysis. Simultaneously with the formation of crystalline  $\text{In}_2\text{O}_3$ , the  $\text{Co}_3\text{O}_4$  phase undergoes reductive transformation following the sequence  $\text{Co}_3\text{O}_4 \rightarrow \text{CoO} \rightarrow \text{Co}$  which results in nanoparticles of  $\alpha$ -Co (*fcc*) polymorph and traces of CoO (*hcp/fcc*) phases (Fig. 5.3D, Fig. D13B). Finally, the third and more peculiar component found to be formed is a mixed metal

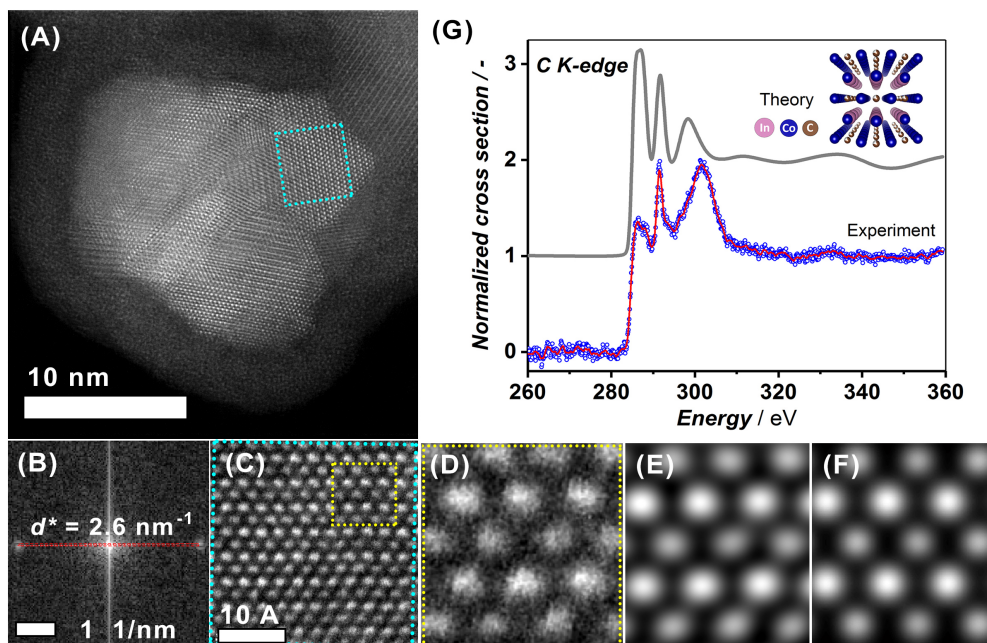


**Figure 5.4.** (A) High-resolution HAADF-STEM image of  $3\text{In}@8\text{Co}(300)$  after reaction. (B) Fourier transform ( $d^* = 2.6 \text{ nm}^{-1}$ ,  $d = 3.83 \text{ \AA}$ ) of (C) zoomed region (blue dots) of interest in (A) representing the atomic arrangement of the  $\text{Co}_3\text{InC}_{0.75}$  phase, viewed along  $\langle 110 \rangle$  zone axis. (D) Zoomed region in (C, yellow dots) processed with the Wiener and Gaussian band-pass filters (E), and (F) corresponding multi-slice STEM image simulation of a  $\text{Co}_3\text{InC}_{0.75}$  slab. (G) Comparison of experiment and theory (FDMNES calculations) for the carbon  $K$ -edge spectrum of  $\text{Co}_3\text{InC}_{0.75}$  recorded by EELS spectroscopy.

carbide,  $\text{Co}_3\text{InC}_{0.75}$  (Fig. 5.3D). Since the reductive atmosphere of reaction should drive the transformation of oxides to their corresponding metallic phases, the occurrence of this carbide is attributed to the reductive transformation under carbon-rich atmospheres better described as the carburization process.

Imaging operated by ADF-STEM microscopy and performed on the  $3\text{In}@8\text{Co}(300)$  material after the catalytic run also shows that the catalyst undergoes textural changes along with phase reorganization. The vast majority of the sample is a composite formed from aggregated nanoparticles, all displaying a core-shell morphology. The average diameter of the core-shell nanoparticle is about 10 nm with a shell thickness of 2 nm (Fig. 5.3C). Additional EELS elemental mapping reveals that elemental composition of the shell includes cobalt, indium and oxygen atoms which agrees with the formation of cobalt-indium oxides.<sup>34</sup> No lattice fringes could be observed in the shell which means that the latter cobalt-indium oxides are also amorphous. On the other hand, the core is clearly polycrystalline as evidenced from the various orientation of lattice fringes imaged by high-resolution high-angle annular dark field



(HAADF)-STEM (Fig. 5.4A-C). The high-resolution image of the lattice (Fig. 5.4C-D) is reproduced by a multi-slice STEM image simulation of a  $\text{Co}_3\text{InC}_{0.75}$  slab viewed along the  $\langle 110 \rangle$  zone axis (Figs. 5.4F and D20); the alternance of bright atom columns containing indium and cobalt atoms with fainter atom columns containing only cobalt atoms is especially well reflected.

With HAADF detection, electrons arising from Rutherford scattering are collected, meanwhile electrons deviated by coherent elastic scattering are mostly excluded (removing the phase contrast). The intensity  $I$  in the resulting images is then, in a first approximation, given by  $I \propto t \cdot Z^\alpha$  ( $\alpha = 1.5 - 2$ ) with a thickness  $t$  and an average atomic number  $Z$ .<sup>62</sup> As a direct consequence, the difference between indium and cobalt atoms is indeed observable but the carbon atoms located in-between the columns of cobalt atoms are not visualized easily. To definitely support the formation of a mixed carbide phase in the particle core, the carbon  $K$ -edge was recorded by EELS spectroscopy (Fig. 5.4G). The C  $K$ -edge originates principally from dipolar transitions from the  $1s$  state to the unoccupied  $2p$  state. Unlike X-ray Raman scattering spectroscopy, EELS spectroscopy is highly forward scattered: with a microscope tension of 300 kV, 90% of the intensity is collected within  $\approx 2.6$  mrad scattering angle corresponding to a small momentum transfer  $q$  equal to  $0.9 \text{ \AA}^{-1}$ .<sup>63</sup> With these experimental conditions, the monopole transitions ( $s \rightarrow s$ ) are thus neglected.<sup>64</sup> Self-consistent field simulations for  $\text{Co}_3\text{InC}_{0.75}$  clusters with radii of up to  $10 \text{ \AA}$  were performed to ensure the convergence of the calculation. Using the full-potential FDM approach, the three main dipolar transitions observed in the experimental spectra are relatively well reproduced. The agreement is not perfect, especially for the energy position of the third transition, but nevertheless the main features are there.

To summarize, the phase composition of the spent catalyst is dependent of several processes taking place during  $\text{CO}_2$  hydrogenation: i) the principal process is the formation of  $\text{Co}_3\text{InC}_{0.75}$  constituting the core of catalytically active nanoparticles surrounded by a Co-In oxide shell, ii) crystallization of  $\text{In}_2\text{O}_3$  from amorphous phase as separated nanoparticles, iii) reduction of  $\text{Co}_3\text{O}_4$  to metallic Co.

In order to address the question concerning the relevance of two-step thermal treatment, *i.e.* sequential pyrolysis-calcination process, the catalytic behavior of **3In@8Co(300)-dc** sample prepared through direct calcination of In-impregnated ZIF-67(Co)-300 at  $400^\circ\text{C}$  without the intermediate pyrolytic step has been evaluated. The kinetic performance profile of **3In@8Co(300)-dc** in  $\text{CO}_2$  hydrogenation towards methanol (Fig. 5.3A) reveals considerably a slower induction period that takes *approx.* 55 h to reach a plateau of  $0.28 \text{ g}_{\text{MeOH}} \cdot \text{g}_{\text{cat}}^{-1} \cdot \text{h}^{-1}$  STY for the methanol product. Additionally, the catalyst prepared by direct calcination route

concedes **3In@8Co(300)** material in methanol productivity ( $0.28 \text{ g}_{\text{MeOH}} \cdot \text{g}_{\text{cat}}^{-1} \cdot \text{h}^{-1}$  vs  $0.52 \text{ g}_{\text{MeOH}} \cdot \text{g}_{\text{cat}}^{-1} \cdot \text{h}^{-1}$ ) albeit with similar  $S_{\text{MeOH}}$  and higher  $S_{\text{CO}}$  (Fig. 5.3A-B). Given the poorer catalytic performance of **3In@8Co(300)-dc**, one may assume the significance of intermediate pyrolysis step for stabilization of indium and cobalt domains in close vicinity to each other, evidently in form of cobalt indium carbide phase,  $\text{Co}_3\text{InCo}_{0.75}$ . We presume that such mixed metal carbide redounds the homogeneity of In@Co system after calcination rendering more effective distribution of  $\text{Co}_3\text{O}_4$  and  $\text{In}_2\text{O}_3$  oxides within the composite catalyst which, consequently, diminishes the induction period for hydrogenation process.

Taking into account the above-mentioned findings and considering the higher performance of catalyst derived from the ZIF-67(Co) sacrificial support with 20 nm crystal size, a set of experiments was carried out in order to study the effect of indium loading. Thereby, ZIF-67(Co)-20 nm has been impregnated with different amounts of  $\text{In}(\text{NO}_3)_3$  in accordance with Table D1 following the same IWI procedure as before and for simplicity denoted as **xIn@yCo(20)** representing the nominal In:Co molar ratios (x:y) in each sample. As it can be observed from nitrogen absorption measurements (Fig. D22), the shape of the isotherms of In@ZIF-67(Co)-20 nm materials changes from type IV- to II- and show the total BET area descending as the indium content increases (Tables D2, D4). Although indium concentrations were increased gradually, the micropore area deviates from a linear trend; this indicates that the indium species settle not only on external surfaces of ZIF-67(Co) but also occupy the micropore area of the framework.

Afterwards, In@ZIF-67(Co)-20 nm materials with different amounts of loaded indium underwent the sequential pyrolysis-calcination treatment in order to render In@Co composite catalysts. The resulting oxide-containing materials exhibit total surface area ranging from 119 to  $87 \text{ m}^2 \cdot \text{g}^{-1}$  (Table D4) and show II-type adsorption isotherms typical for macroporous adsorbents (Fig. D23). Notably, the total BET area decreases as the indium content increases which successfully agrees with the findings, as above discussed, concerning the embedding of  $\text{Co}_3\text{O}_4$  nanoparticles possessing the large interparticle surface which is occupied by the amorphous  $\text{In}_2\text{O}_3$  phase. The targeted indium loading in MOF-derived catalysts was confirmed by XRF measurements and calculated from TG curves considering the temperature region of 870-930 °C, in which the  $\text{Co}_3\text{O}_4 \rightarrow \text{CoO}$  transition is taking place (Figs. D24, D25), in order to compare to the nominal In:Co molar ratios (Table D4). The results summarized in Table D4 show a fair agreement with the expected In:Co ratios aimed to be attained in the **xIn@yCo(20)** catalysts.

A series of MOF-derived catalysts **aIn@bCo(20)** with variable In:Co molar ratios was tested in direct CO<sub>2</sub> hydrogenation to methanol under standard conditions (80% H<sub>2</sub>-20% CO<sub>2</sub>

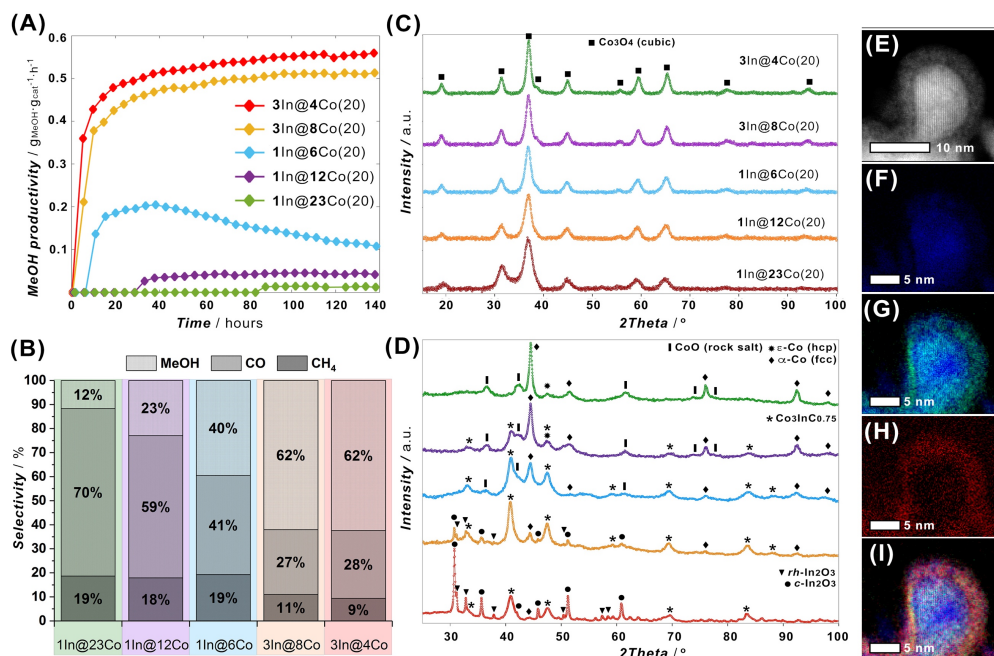


**Figure 5.5.** (A) Evolution of MeOH space time yield vs time and (B) selectivities to MeOH product, CO and CH<sub>4</sub> by-products at TOS of 100 h over catalysts with different In loadings: 3In@4Co(20) ( $X_{\text{Co}_2} = 20.5\%$ , red), 3In@8Co(20) ( $X_{\text{Co}_2} = 19.2\%$ , orange), 1In@6Co(20) ( $X_{\text{Co}_2} = 13.9\%$ , blue), 1In@12Co(20) ( $X_{\text{Co}_2} = 11.1\%$ , purple) and 1In@23Co(20) ( $X_{\text{Co}_2} = 10.1\%$ , green). Reaction conditions: 80% H<sub>2</sub>-20% CO<sub>2</sub> feed;  $T = 300^\circ\text{C}$ ,  $P = 50$  bar,  $m_{\text{cat}} = 50$  mg, GHSV = 15600 h<sup>-1</sup>. XRD patterns for (C) fresh and (D) spent catalysts and comparison with the identified phases: Co<sub>3</sub>O<sub>4</sub> (■), CoO (|), ε-Co (hcp, ★), Co<sub>3</sub>InCo<sub>0.75</sub> (\*), α-Co (fcc, ◆), c-In<sub>2</sub>O<sub>3</sub> (cubic, ●) and rh-In<sub>2</sub>O<sub>3</sub> (rhombohedral, ▼). ADF-STEM imaging (E) and elemental mappings for 3In@4Co(20) after reaction: Co map (F) and O map (H); superimposed Co/In/O maps (G) and Co/In/O maps (I).

feed;  $P = 50$  bar and GHSV = 15600 h<sup>-1</sup>, Fig. D30). Figure 5.5A shows STY evolution for the MeOH product on the catalysts with variable In:Co molar ratios. As can be observed, the aIn@bCo(20) catalysts with lower In content, that is, 1In@23Co(20) and 1In@12Co(20) exhibit the largest induction periods of 40 and 90 h and a low MeOH productivity 0.01 and 0.04  $\text{g}_{\text{MeOH}} \cdot \text{g}_{\text{cat}}^{-1} \cdot \text{h}^{-1}$ , respectively. Further increase of indium content up to 1In@6Co value reduces the induction period down to 30 h yet reaching maximum STY<sub>MeOH</sub> of 0.21  $\text{g}_{\text{MeOH}} \cdot \text{g}_{\text{cat}}^{-1} \cdot \text{h}^{-1}$  over a short period of time (5 h) after which the catalyst slowly deactivates.

In contrast, 3In@8Co(20) and 3In@4Co(20) catalysts with higher In<sub>2</sub>O<sub>3</sub> loading show a considerably reduced induction time (19 h and 7 h vs 30 h) and an outstanding stable performance over 100 h TOS with a methanol productivity of ca. 0.5 and 0.65  $\text{g}_{\text{MeOH}} \cdot \text{g}_{\text{cat}}^{-1} \cdot \text{h}^{-1}$ , respectively. Therefore, the activity towards methanol on MOF-derived mixed oxide catalysts is increasing in the order 3In@4Co > 3In@8Co > 1In@6Co > 1In@12Co > 1In@23Co. Regarding

the MeOH selectivity data compared at 100 h of time-on-stream (TOS) shown on Figure 5.5B, the methanol selectivity develops following the same trend as  $STY_{MeOH}$  whereas the selectivities toward by-products (CO and CH<sub>4</sub>) evolve in opposite manner. A higher MeOH selectivity (62%) is reached by **3In@8Co(20)** and **3In@4Co(20)** materials along with reduced selectivities toward CO (27-28%) and CH<sub>4</sub> (9-11%) by-products.

In order to understand the differences in reactivity, structural analysis was carried out on the experimental XRD data for fresh and spent catalysts with different In loadings (Fig. 5.5C, D). Although the **aIn@bCo(20)** catalysts before reaction showed identical XRD patterns with diffraction lines associated solely with the Co<sub>3</sub>O<sub>4</sub> phase (Fig. 5.5C), the composition of spent solids demonstrated a variety of phases, depending on the indium content (Fig. 5.5D, Table D5). Consequently, the difference in reactivities of the MOF-derived catalysts also relies on the compositional characteristics of the phases manifested during the reaction. As shown in Figure 5.5D, the spent **1In@23Co(20)** catalyst mainly contains *fcc*-Co phase and traces of CoO and could be associated with low MeOH selectivity (12 %) and productivity ( $0.02 \text{ g}_{MeOH} \cdot \text{g}_{cat}^{-1} \cdot \text{h}^{-1}$ ) in contrast to high CO selectivity (70 %). The appearance of Co<sub>3</sub>InC<sub>0.75</sub> phase in mixture with *fcc*-Co in **1In@12Co(20)** improves the selectivity towards MeOH twofold ( $S_{MeOH} = 23\%$ ,  $S_{CO} = 59\%$ ,  $S_{CH_4} = 18\%$ ), whereas the dominance of the mixed-metal carbide over  $\alpha$ -Co in **1In@6Co(20)** leads to maximum  $S_{MeOH}$  of 40% ( $S_{CO} = 41\%$ ,  $S_{CH_4} = 19\%$ ), after which the activity starts to decline. Finally, the mixture of Co<sub>3</sub>InC<sub>0.75</sub> and In<sub>2</sub>O<sub>3</sub> (both *rh*- and *c*-polymorphs) more likely reflects the true composition responsible for selective MeOH synthesis inasmuch as both actively performing **3In@4Co(20)** and **3In@8Co(20)** catalysts possess similar composition based on these two components ( $S_{MeOH} = 62\%$ ,  $S_{CO} = 27\text{-}28\%$ ,  $S_{CH_4} = 9\text{-}11\%$  and  $STY_{MeOH} = 0.5\text{-}0.65 \text{ g}_{MeOH} \cdot \text{g}_{cat}^{-1} \cdot \text{h}^{-1}$ ). To visualize relations between the phase contents found by PXRD studies, a correlation matrix has been added (Fig. D31). The correlation coefficients between individual phase contents and selectivities towards the catalytic products were scaled from yellow (strong positive) to navy (strong negative correlation). It demonstrates strong correlation between the carbide and indium oxides content and methanol selectivity whereas the presence of cobalt and cobalt oxide is negatively correlated with it. Although the carbide content has the strongest correlation with methanol production, its catalytic activity was excluded by performing an individual catalytic study (Table D7) and appeared to be a side product of catalysts workout and carburization (Figs. D34-D36). To support the above-mentioned results, CHN elemental analyses on the fresh and spent catalysts were carried out and compared in Table D6. As expected, the carbon content in spent catalysts increases compared to the fresh ones and can be associated with the formation of the Co<sub>3</sub>InC<sub>0.75</sub> phase; that agrees well with

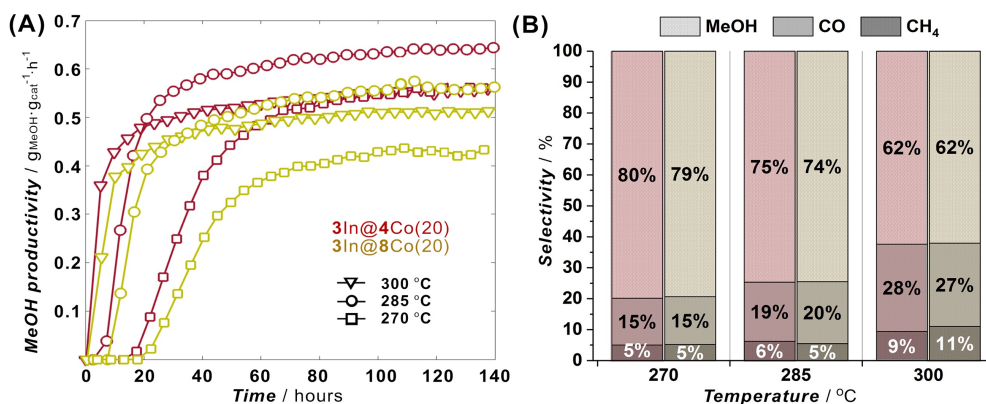


**Figure 5.6.** (A) Evolution of MeOH space time yield vs time and (B) selectivities to MeOH product, CO and CH<sub>4</sub> by-products at TOS of 100 h over catalysts 3In@4Co(20) (red) and 3In@8Co(20) (orange) at different temperatures: 270 °C ( $X_{\text{CO}_2}$  = 14.2% and 11.6%, □), 285 °C ( $X_{\text{CO}_2}$  = 17.3% and 15.5%, ○) and 300 °C ( $X_{\text{CO}_2}$  = 20.5% and 19.2%, ▽). Reaction conditions: 80% H<sub>2</sub>-20% CO<sub>2</sub> feed;  $P$  = 50 bar,  $m_{\text{cat}}$  = 50 mg, GHSV = 15600 h<sup>-1</sup>.

PXRD quantification data (Table D5). Notably, spent 3In@4Co(20) and 3In@8Co(20) catalysts differ by the relative amount of crystalline In<sub>2</sub>O<sub>3</sub> and Co<sub>3</sub>InC<sub>0.75</sub> phases (Table D5) that might have influence on the induction period considering previous finding that both components are formed along the sequentially-conjugated process. Similarly to 3In@8Co(300), the spent version of the best performing 3In@4Co(20) catalyst shows also core-shell morphological features as suggested by EELS elemental maps (Figs. 5.5E-I, Figs. D26-D27). In conclusion to all above mentioned, the optimal catalyst composition is determined by the relative molar ratio of 3In:8Co and 3In:4Co possessing enough indium to be quantitatively converted to the Co<sub>3</sub>InC<sub>0.75</sub> phase.

The most active catalysts, 3In@4Co(20) and 3In@8Co(20), were chosen to study the effect of the reaction temperature with the aim of finding optimal conditions for CO<sub>2</sub> to methanol hydrogenation process. The kinetic profiles for MeOH productivity on 3In@4Co(20) and 3In@8Co(20) catalysts at three temperatures – 270 °C, 285 °C and 300 °C, are shown in Figure 5.6A. As can be observed, the induction period for both catalysts increases from 7-19 h to 60-70 h while the reaction temperature decreases from 300 °C to 270 °C. This observation can be rationalized by the fact that both Co<sub>3</sub>InC<sub>0.75</sub> and In<sub>2</sub>O<sub>3</sub> phases formed through conjugated red-ox process become kinetically unfavorable at lower temperatures. Despite the discrepancy of initial reaction rates for both catalysts, the MeOH productivity is deviating in a range of 0.5–0.65 g<sub>MeOH</sub>·g<sub>cat</sub><sup>-1</sup>·h<sup>-1</sup> regardless the applied temperature. However, the alternate comparison of selectivities for the MeOH product and CO/CH<sub>4</sub> by-products in the steady-state region (Fig. 5.6B, Fig. D32) of the catalytic process shows that lower temperature induces high methanol

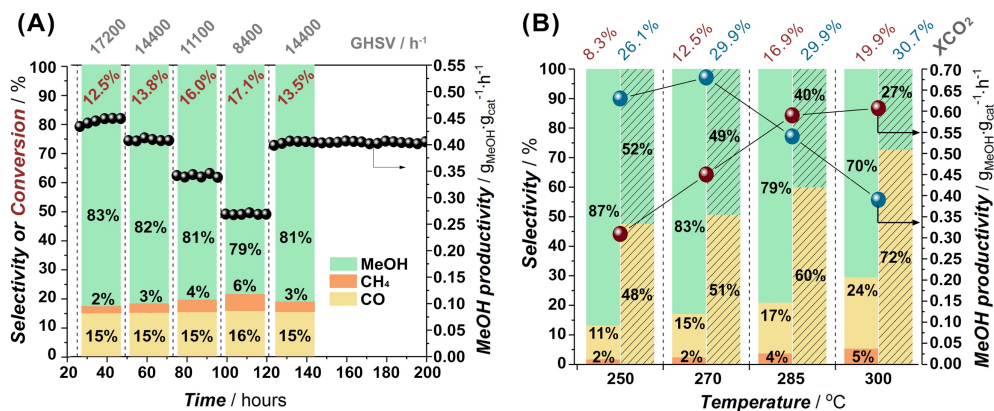


**Figure 5.7.** (A) Evolution selectivities for the MeOH product (turquoise column), CO (orange) and CH<sub>4</sub> (pumpkin) by-products, CO<sub>2</sub> conversion (wine values) and MeOH space time yield (black spheres) vs. time on catalyst 3In@4Co(20) at variable GHSV (top, grey values) and 270 °C. Catalyst was previously pretreated at 300 °C and GHSV of 15200 h<sup>-1</sup> for 20 h in the reaction mixture. (B) Comparison of methanol productivity (spheres) and MeOH, CO and CH<sub>4</sub> selectivities (columns) for 3In@4Co(20) (red markers and clear columns) and commercial Cu-ZnO-Al<sub>2</sub>O<sub>3</sub> catalyst (blue markers and striped columns) at 250 °C, 270 °C, 285 °C, 300 °C and constant GHSV of 17200 h<sup>-1</sup>, X<sub>CO<sub>2</sub></sub> levels are represented on the line above. Reaction conditions: 80% H<sub>2</sub>-20% CO<sub>2</sub> feed; P = 50 bar, m<sub>cat</sub> = 50 mg.

selectivities ( $S_{\text{MeOH}} \sim 79\text{--}80\%$  at 270 °C vs 62% at 300 °C) yet suppresses side processes ( $S_{\text{CO}} \sim 15\%$  and  $S_{\text{CH}_4} \sim 5\%$  at 270 °C vs.  $S_{\text{CO}} \sim 27\text{--}28\%$  and  $S_{\text{CH}_4} \sim 9\text{--}11\%$  at 300 °C), being methanation and RWGS reactions.

Thus, an optimal temperature needs to be considered in order to inhibit undesired side reactions and favor higher methanol selectivity and productivity yield.

Additionally, in order to tune the reaction performance, we carried out a series of experiments with gas flows variation, given the fact that RWGS and methanation processes may be suppressed to some extent this way. Figure 5.7A shows the 3In@4Co(20) catalyst performance on stream at 270 °C under different gas flow velocities (GHSV, h<sup>-1</sup>). As can be observed in Figure 5.7A, after catalyst pretreatment at 300 °C for 20 h, the increase of the contact time leads to growth in the productivity and methanol selectivity reaching MeOH productivity (0.45 g<sub>MeOH</sub>·g<sub>cat</sub><sup>-1</sup>·h<sup>-1</sup>) and selectivity (83%) at 17200 h<sup>-1</sup>. This behavior is in line with the previously observed results for In-based catalyst reported by Pérez-Ramírez *et al.*<sup>32</sup> Expectedly, this outcome runs in parallel with inhibition of side reactions showing reduction of CO and CH<sub>4</sub> selectivities down to 2% and 15%, respectively. Although the subsequent stepwise reduction of the GHSV from 17200 h<sup>-1</sup> to 8400 h<sup>-1</sup> diminishes MeOH productivity drastically (from 0.45 g<sub>MeOH</sub>·g<sub>cat</sub><sup>-1</sup>·h<sup>-1</sup> to 0.27 g<sub>MeOH</sub>·g<sub>cat</sub><sup>-1</sup>·h<sup>-1</sup>), the selectivities toward methanol lessen only slowly from 83% to 79%.

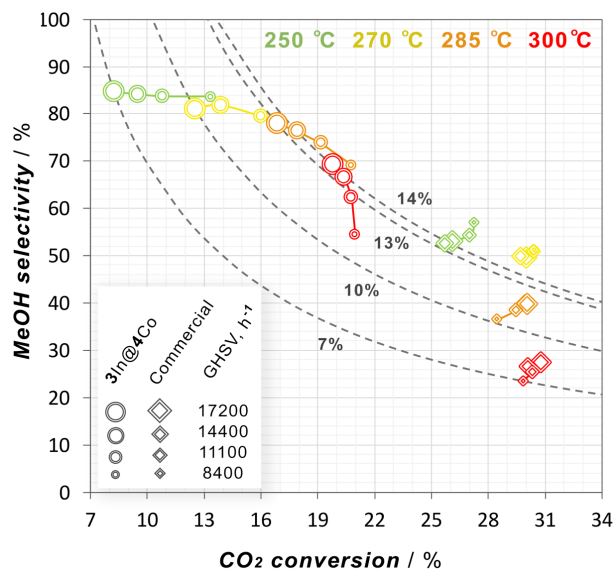


**Figure 5.8.** Methanol selectivity vs CO<sub>2</sub> conversion plots for the hydrogenation reaction, comparing behavior of **3In@4Co** (spherical symbols) and commercial Cu-ZnO-Al<sub>2</sub>O<sub>3</sub> catalysts (rhombic symbols) at different gas hourly space velocities (GHSV) and temperatures. Dashed lines indicate methanol iso-yield curves for **3In@4Co** at different temperatures.

It is worth to note that when GHSV is restored to 14400 h<sup>-1</sup>, the **3In@4Co**(20) catalyst recovers its activity reaching the same MeOH productivity (0.40 g<sub>MeOH</sub>·g<sub>cat</sub><sup>-1</sup>·h<sup>-1</sup>) and selectivities (S<sub>MeOH</sub> = 81% vs. 82%). This observation highlights the stability of the MOF-derived In@Co composite catalyst over the course of the reaction and its instant response to the changes in the reaction conditions.

To have an accurate comparison of catalytic activity for our MOF-derived composite catalyst, **3In@4Co**(20) with the commercial Cu-ZnO-Al<sub>2</sub>O<sub>3</sub>, we performed an extensive examination of both solids in CO<sub>2</sub> hydrogenation under different reaction conditions (Figs. 5.8 and D33). Because it was determined that the GHSV directly influences the methanol yield and selectivity, further comparison has been done at fixed gas velocity (17200 h<sup>-1</sup>) at which both catalysts performed the best. Accordingly, the general trends observed in both catalytic systems are summarized in Figure 5.7B. The results show two distinct regimes – above and below ca. 280 °C. In the low temperature regime (< 280 °C), the commercial Cu-ZnO-Al<sub>2</sub>O<sub>3</sub> catalyst shows a considerable high MeOH yield (0.65–0.67 g<sub>MeOH</sub>·g<sub>cat</sub><sup>-1</sup>·h<sup>-1</sup>) with moderate product selectivities (S<sub>MeOH</sub> = 49–52% and S<sub>CO</sub> = 48–51%) whereas the MOF-derived **3In@4Co**(20) composite exhibits lower MeOH productivity (0.32–0.45 g<sub>MeOH</sub>·g<sub>cat</sub><sup>-1</sup>·h<sup>-1</sup>) with remarkably higher selectivity (83–87%) towards the desired product. In contrast, the high temperature regime (> 280 °C) turns the overall catalytic performance in opposite direction

where 3In@4Co(20) catalyst reaches the maximum of  $STY_{MeOH}$  (0.60-0.63  $g_{MeOH} \cdot g_{cat}^{-1} \cdot h^{-1}$ ) with a slightly reduced methanol selectivity (70-79%), yet much higher than that of the Cu-ZnO-Al<sub>2</sub>O<sub>3</sub>.

## 5.4 CONCLUSIONS

In this work we have applied the MOF-mediated approach to prepare In<sub>2</sub>O<sub>3</sub>-Co<sub>3</sub>O<sub>4</sub> mixed-oxide catalysts for the effective and selective synthesis of methanol *via* CO<sub>2</sub> hydrogenation. The activity of the resulting In@Co catalysts reaches a maximum MeOH space time yield of 0.65  $g_{MeOH} \cdot g_{cat}^{-1} \cdot h^{-1}$  with methanol selectivities as high as 87% over 100 h on stream under industrially relevant conditions. Taking into account the relatively slow process of active phase formation in co-precipitated In@Co catalytic system previously reported, it is important to have an opportunity to tune the induction period for the hydrogenation reaction on the catalysts prepared by MOF-mediated approach. It was shown, that changing the textural properties of parent sacrificial ZIF-67(Co) support can reduce the induction time as a result of a better In-dopant distribution all over the metal-organic matrix involving both micropore and interparticle surface areas, improving in this way In utilization. Additionally, we found that the sequential pyrolysis-calcination steps in the catalysts' preparation procedure were determinant for a faster induction period because of the appearance of mixed-metal carbide, Co<sub>3</sub>InC<sub>0.75</sub>, which stabilizes high dopant distribution and prevents formation of large individual oxide domains in the final mixed oxide composite. As expected, the indium loading implies the quantitative limitation on formation of the active phase, which presumably consists of nanoparticles featuring core-shell morphologies (Co-In oxides shell over Co<sub>3</sub>InC<sub>0.75</sub> core) hereby establishing optimal composition of 3In:8Co or 3In:4Co molar ratios for more effective catalyst performance.

The screening for the optimal operational conditions shows that lower reaction temperature assists to suppress side reactions (methanation and RWGS) and improve MeOH selectivity ( $S_{MeOH} \sim 79$ -80% at 270 °C vs. 62% at 300 °C) while slightly lowering the productivity (0.55  $g_{MeOH} \cdot g_{cat}^{-1} \cdot h^{-1}$  at 270 °C vs. 0.65  $g_{MeOH} \cdot g_{cat}^{-1} \cdot h^{-1}$  at 300 °C). Additionally, further suppression of undesired side processes (methanation and RWGS) could be reached by adjusting the reaction conditions, that is, reactant gas flow, lowering  $S_{CO}$  and  $S_{CH_4}$  down to 11 and 2%, respectively.

The present study demonstrates the tunability of MOF-mediated approach in the preparation of the In<sub>2</sub>O<sub>3</sub>-Co<sub>3</sub>O<sub>4</sub> catalytic system which is able to drive effectively direct CO<sub>2</sub> hydrogenation to methanol. Our results suggest that a In@Co binary oxide system is able to reach superior performance compared to commercial Cu-ZnO-Al<sub>2</sub>O<sub>3</sub> catalyst for this reaction.



## REFERENCES

- [1] S. Fankhauser, F. Jotzo, *Wiley Interdiscip. Rev. Clim.* **2018**, 9, e495.
- [2] G. A. Olah, A. Goeppert, G. K. S. Prakash, *J. Org. Chem.* **2009**, 74, 487-498.
- [3] A. Rafiee, K. Rajab Khalilpour, D. Milani, M. Panahi, *J. Environ. Chem. Eng.* **2018**, 6, 5771-5794.
- [4] A. Dokania, A. Ramirez, A. Bavykina, J. Gascon, *ACS Energy Lett.* **2019**, 4, 167-176.
- [5] G. A. Olah, *Angew. Chem. Int. Ed.* **2005**, 44, 2636-2639.
- [6] X. Zhen, in *Methanol* (Eds: A. Basile, F. Dalena), Elsevier **2018**, 313-337.
- [7] P. Tian, Y. Wei, M. Ye, Z. Liu, *ACS Catal.* **2015**, 5, 1922-1938.
- [8] I. Yarulina, K. De Wispelaere, S. Bailleul, J. Goetze, M. Radersma, E. Abou-Hamad, I. Vollmer, M. Goesten, B. Mezari, E. J. M. Hensen, J. S. Martínez-Espín, M. Morten, S. Mitchell, J. Perez-Ramirez, U. Olsbye, B. M. Weckhuysen, V. Van Speybroeck, F. Kapteijn, J. Gascon, *Nat. Chem.* **2018**, 10, 804-812.
- [9] A. Dutta, I. A. Karimi, S. Farooq, *Ind. Eng. Chem. Res.* **2019**, 58, 963-972.
- [10] I. Yarulina, A. D. Chowdhury, F. Meirer, B. M. Weckhuysen, J. Gascon, *Nat. Catal.* **2018**, 1, 398-411.
- [11] A. Álvarez, A. Bansode, A. Urakawa, A. V. Bavykina, T. A. Wezendonk, M. Makkee, J. Gascon, F. Kapteijn, *Chem. Rev.* **2017**, 117, 9804-9838.
- [12] A. A. Kiss, J. J. Praght, H. J. Vos, G. Bargeman, M. T. de Groot, *Chem. Eng. J.* **2016**, 284, 260-269.
- [13] A. González-Garay, M. S. Frei, A. Al-Qahtani, C. Mondelli, G. Guillén-Gosálbez, J. Pérez-Ramírez, *Energy Environ. Sci.* **2019**, 12, 3425-3436.
- [14] K. A. Ali, A. Z. Abdullah, A. R. Mohamed, *Renew. Sustain. Energy Rev.* **2015**, 44, 508-518.
- [15] O. Martin, J. Pérez-Ramírez, *Catal. Sci. Technol.* **2013**, 3, 3343-3352.
- [16] J. Wu, M. Saito, M. Takeuchi, T. Watanabe, *Appl. Catal. A Gen.* **2001**, 218, 235-240.
- [17] U. Ash-Kurlander, O. Martin, L. D. Fontana, V. R. Patil, M. Bernegger, C. Mondelli, J. Pérez-Ramírez, A. Steinfeld, *Energy Technol.* **2016**, 4, 565-572.
- [18] F. Arena, K. Barbera, G. Italiano, G. Bonura, L. Spadaro, F. Frusteri, *J. Catal.* **2007**, 249, 185-194.
- [19] M. D. Porosoff, B. Yan, J. G. Chen, *Energy Environ. Sci.* **2016**, 9, 62-73.
- [20] A. Bansode, A. Urakawa, *J. Catal.* **2014**, 309, 66-70.
- [21] A. Le Valant, C. Comminges, C. Tisseraud, C. Canaff, L. Pinard, Y. Pouilloux, *J. Catal.* **2015**, 324, 41-49.
- [22] S. Tada, F. Watanabe, K. Kiyota, N. Shimoda, R. Hayashi, M. Takahashi, A. Nariyuki, A. Igarashi, S. Satokawa, *J. Catal.* **2017**, 351, 107-118.
- [23] M. M.-J. Li, Z. Zeng, F. Liao, X. Hong, S. C. E. Tsang, *J. Catal.* **2016**, 343, 157-167.
- [24] B. Hu, Y. Yin, G. Liu, S. Chen, X. Hong, S. C. E. Tsang, *J. Catal.* **2018**, 359, 17-26.
- [25] S. Dang, H. Yang, P. Gao, H. Wang, X. Li, W. Wei, Y. Sun, *Catal. Today* **2019**, 330, 61-75.
- [26] S. G. Jadhav, P. D. Vaidya, B. M. Bhanage, J. B. Joshi, *Chem. Eng. Res. Des.* **2014**, 92, 2557-2567.
- [27] J. Słoczyński, R. Grabowski, A. Kozłowska, P. Olszewski, J. Stoch, J. Skrzypek, M. Lachowska, *Appl. Catal. A Gen.* **2004**, 278, 11-23.
- [28] A. Bansode, B. Tidona, P. R. von Rohr, A. Urakawa, *Catal. Sci. Technol.* **2013**, 3, 767-778.
- [29] P. Gao, F. Li, N. Zhao, F. Xiao, W. Wei, L. Zhong, Y. Sun, *Appl. Catal. A Gen.* **2013**, 468, 442-452.
- [30] J. Ye, C. Liu, D. Mei, Q. Ge, *ACS Catal.* **2013**, 3, 1296-1306.

- [31] K. Sun, Z. Fan, J. Ye, J. Yan, Q. Ge, Y. Li, W. He, W. Yang, C.-j. Liu, *J. CO<sub>2</sub> Util.* **2015**, 12, 1-6.
- [32] M. Oliver, M. A. J., M. Cecilia, M. Sharon, S. T. F., H. Roland, D. Charlotte, C. F. Daniel, P. R. Javier, *Angew. Chem. Int. Ed.* **2016**, 55, 6261-6265.
- [33] M. S. Frei, C. Mondelli, R. García-Muelas, K. S. Kley, B. Puértolas, N. López, O. V. Safonova, J. A. Stewart, D. Curulla Ferré, J. Pérez-Ramírez, *Nat. Commun.* **2019**, 10, 3377.
- [34] A. Bavykina, I. Yarulina, A. J. Al Abdulghani, L. Gevers, M. N. Hedhili, X. H. Miao, A. R. Galilea, A. Pustovarenko, A. Dikhtiarenko, A. Cadiau, A. Aguilar-Tapia, J. L. Hazemann, S. M. Kozlov, S. Oud-Chikh, L. Cavallo, J. Gascon, *ACS Catal.* **2019**, 9, 6910-6918.
- [35] G. Li, S. Zhao, Y. Zhang, Z. Tang, *Adv. Mater.* **2018**, 30, 1800702.
- [36] T. Drake, P. Ji, W. Lin, *Acc. Chem. Res.* **2018**, 51, 2129-2138.
- [37] S.-N. Zhao, X.-Z. Song, S.-Y. Song, H.-j. Zhang, *Coord. Chem. Rev.* **2017**, 337, 80-96.
- [38] H. Furukawa, K. E. Cordova, M. O'Keeffe, O. M. Yaghi, *Science* **2013**, 341, 1230444.
- [39] B. An, J. Zhang, K. Cheng, P. Ji, C. Wang, W. Lin, *J. Am. Chem. Soc.* **2017**, 139, 3834-3840.
- [40] B. Rungtaweeworant, J. Baek, J. R. Araujo, B. S. Archanjo, K. M. Choi, O. M. Yaghi, G. A. Somorjai, *Nano Lett.* **2016**, 16, 7645-7649.
- [41] L. Oar-Arteta, T. Wezendonk, X. Sun, F. Kapteijn, J. Gascon, in *Nanotechnology in Catalysis*, John Wiley & Sons, Ltd **2017**, 225-250.
- [42] L. Oar-Arteta, T. Wezendonk, X. Sun, F. Kapteijn, J. Gascon, *Mater. Chem. Front.* **2017**, 1, 1709-1745.
- [43] W. Xia, J. Zhu, W. Guo, L. An, D. Xia, R. Zou, *J. Mater. Chem. A* **2014**, 2, 11606-11613.
- [44] X. Sun, A. I. O. Suarez, M. Meijerink, T. van Deelen, S. Ould-Chikh, J. Zečević, K. P. de Jong, F. Kapteijn, J. Gascon, *Nat. Commun.* **2017**, 8, 1680.
- [45] G. Pawley, *J. Appl. Crystallogr.* **1981**, 14, 357-361.
- [46] A. Coelho, *J. Appl. Crystallogr.* **2018**, 51, 210-218.
- [47] J. Schindelin, I. Arganda-Carreras, E. Frise, V. Kaynig, M. Longair, T. Pietzsch, S. Preibisch, C. Rueden, S. Saalfeld, B. Schmid, J.-Y. Tinevez, D. J. White, V. Hartenstein, K. Eliceiri, P. Tomancak, A. Cardona, *Nat. Methods* **2012**, 9, 676.
- [48] B. Ravel, M. Newville, *J. Synchrotron Radiat.* **2005**, 12, 537-541.
- [49] C. T. Koch, *Determination of core structure periodicity and point defect density along dislocations*, **2002**.
- [50] O. Bunău, Y. Joly, *J. Condens. Matter Phys.* **2009**, 21, 345501.
- [51] S. A. Guda, A. A. Guda, M. A. Soldatov, K. A. Lomachenko, A. L. Bugaev, C. Lamberti, W. Gawelda, C. Bressler, G. Smolentsev, A. V. Soldatov, Y. Joly, *J. Chem. Theory Comput.* **2015**, 11, 4512-4521.
- [52] R. Banerjee, A. Phan, B. Wang, C. Knobler, H. Furukawa, M. O'Keeffe, O. M. Yaghi, *Science* **2008**, 319, 939-943.
- [53] H. T. Kwon, H.-K. Jeong, A. S. Lee, H. S. An, J. S. Lee, *J. Am. Chem. Soc.* **2015**, 137, 12304-12311.
- [54] M. Thommes, *Chem. Ing. Tech.* **2010**, 82, 1059-1073.
- [55] K. S. W. Sing, D. H. Everett, R. A. W. Haul, L. Moscou, R. A. Pierotti, J. Rouquerol, T. Siemieniowska, *Pure Appl. Chem.* **1985**, 57, 603-619.
- [56] *in Thermodynamic Properties of Elements, Ca to Ge2: Datasheet from Landolt-Börnstein - Group IV Physical Chemistry*, Vol. 19A1 (Eds: I. Hurtado, D. Neuschütz), Springer-Verlag Berlin Heidelberg **1999**.

- [57] Z. P. Xu, H. C. Zeng, *J. Mater. Chem.* **1998**, 8, 2499-2506.
- [58] M. Marezio, *Acta Cryst.* **1966**, 20, 723-728.
- [59] A. Gurlo, P. Kroll, R. Riedel, *Chem. Eur. J.* **2008**, 14, 3306-3310.
- [60] M. F. Bekheet, M. R. Schwarz, P. Kroll, A. Gurlo, *J. Solid State Chem.* **2015**, 229, 278-286.
- [61] E.-M. Köck, M. Kogler, C. Zhuo, L. Schlicker, M. F. Bekheet, A. Doran, A. Gurlo, S. Penner, *Phys. Chem. Chem. Phys.* **2017**, 19, 19407-19419.
- [62] A. V. Crewe, J. Wall, J. Langmore, *Science* **1970**, 168, 1338-1340.
- [63] R. F. Egerton, *Electron Energy-Loss Spectroscopy in the Electron Microscope*, Plenum Press, **1996**.
- [64] Y. Joly, C. Cavallari, S. A. Guda, C. J. Sahle, *J. Chem. Theory Comput.* **2017**, 13, 2172-2177.

## APPENDIX D

**Table D1.** Details of preparation of In-modified ZIF-67(Co) samples by incipient wetness impregnation (IWI) before pyrolysis and calcination treatment. Sample code denoted as **aIn:bCo(x)** where **x** is crystal size of ZIF-67(Co), **a** and **b** indicate the In:Co molar ratio.

Sample code	ZIF-67(Co)		In(NO <sub>3</sub> ) <sub>3</sub>		In (wt.%) <sup>d</sup>	In : Co molar ratio
	size <sup>a</sup> (nm)	mmol <sup>b</sup>	mass (g)	mmol <sup>c</sup>		
<b>1In:23Co(20)</b>	20	4.32	0.057	0.19	5	1:23
<b>1In:12Co(20)</b>	20	4.32	0.109	0.36	10	1:12
<b>1In:6Co(20)</b>	20	4.32	0.233	0.77	20	1:6
<b>3In:8Co(20)</b>	20	4.32	0.491	1.63	34	3:8
<b>3In:4Co(20)</b>	20	4.32	0.972	3.23	50	3:4
<b>3In:8Co(300)</b>	300	4.32	0.498	1.65	34	3:8

<sup>a</sup> Average crystal size determined from SEM and TEM images.<sup>b</sup> Calculated from molecular formula [Co(C<sub>4</sub>H<sub>5</sub>N<sub>2</sub>)<sub>2</sub>]<sub>n</sub> with molecular weight of 221.12 g·mol<sup>-1</sup> for non-solvated form of the framework. The mass of ZIF-67(Co) taken for the impregnation with indium nitrate was constant in all entries, 1.0 g.<sup>c</sup> Mol calculated on the anhydrous In(NO<sub>3</sub>)<sub>3</sub> basis with molecular weight of 300.83 g·mol<sup>-1</sup>.<sup>d</sup> Indium weight percent calculated as ratio between In weight on the metal basis and weight of Co<sub>3</sub>O<sub>4</sub> considering this compound as a main product of ZIF-67(Co) calcination,  $m(In) \times 100\% / (m(Co_3O_4) + m(In))$ .**Table D2.** Summary of characteristics for ZIF-67(Co) sacrificial metal-organic frameworks prepared by modulated synthesis procedures.

Sample	ZIF-67(Co) average crystal size <sup>a</sup> (nm)	BET area (m <sup>2</sup> ·g <sup>-1</sup> )		
		Total (S <sub>BET</sub> )	Micro	Meso <sup>b</sup>
ZIF-67(Co)-300	300	1579	1521	57
ZIF-67(Co)-20	20	1566	1457	109

<sup>a</sup> Determined from SEM and TEM imaging.<sup>b</sup> Mesopore surface area obtained from the *t*-plot applied to the N<sub>2</sub> isotherm

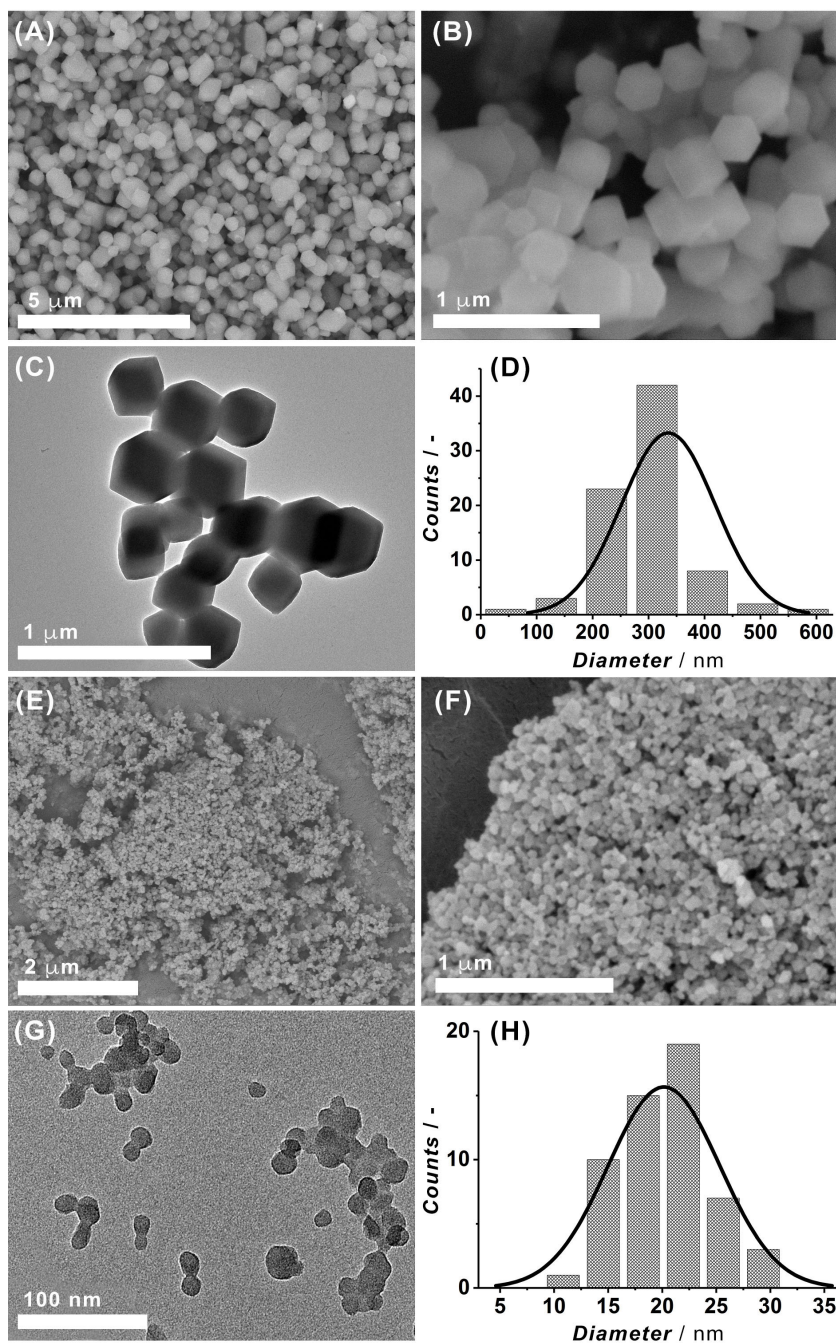


**Figure D1.** Electron microscopy images of ZIF-67(Co) precursor materials: (A,B) SEM and (C,D) TEM images for sample with  $300 \pm 85$  nm particle size and the corresponding particle size distribution histogram; (E,F) SEM and (G,H) TEM images for sample with  $20 \pm 5$  nm particle size and the corresponding particle size distribution histogram.

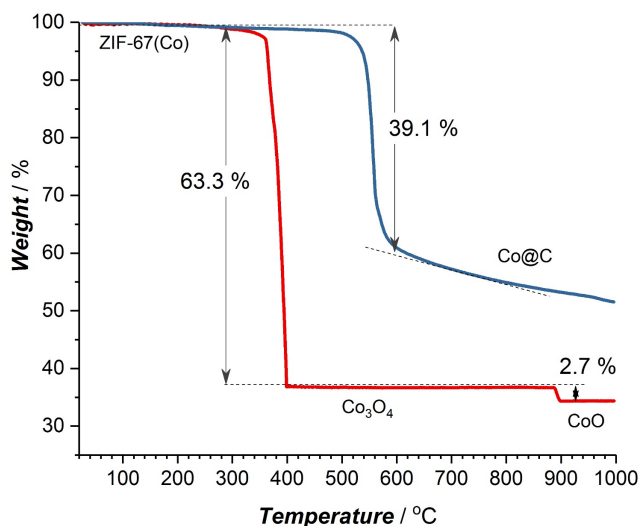


**Figure D2.** Thermogravimetric curves for ZIF-67(Co) precursor material in nitrogen (blue line) and air (red line) flows (20 mL·min<sup>-1</sup>).

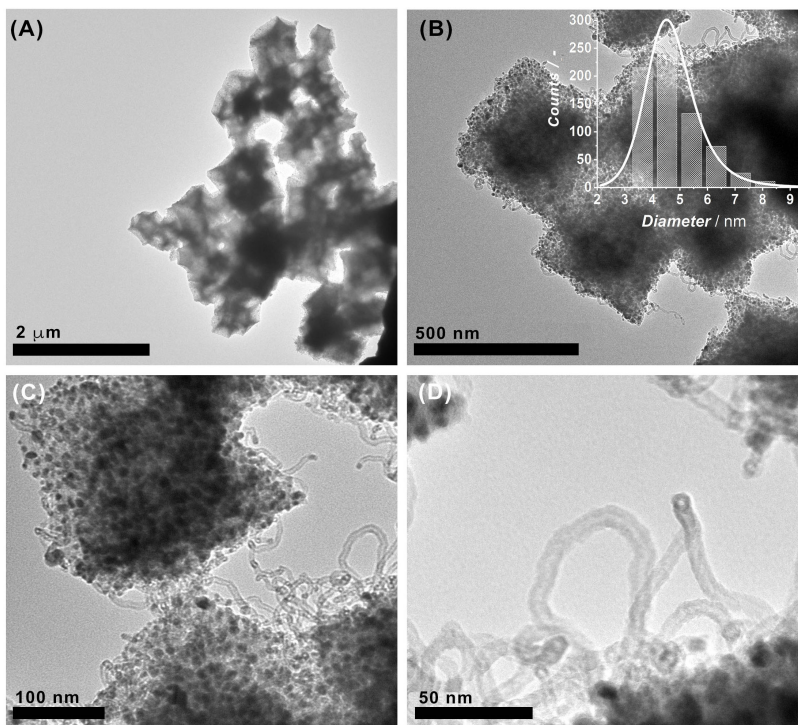


**Figure D3.** Transmission electron microscopy images at different magnifications of the pyrolyzed product of ZIF-67(Co) at 600 °C for 4 h in nitrogen flow (25 mL·min<sup>-1</sup>) showing the morphology preserved agglomerations which consist of Co nanoparticles and carbon nanotubes. Inset on graph (B) shows Co nanoparticle size distribution histogram indicating the average particle size of  $4.7 \pm 1.1$  nm.

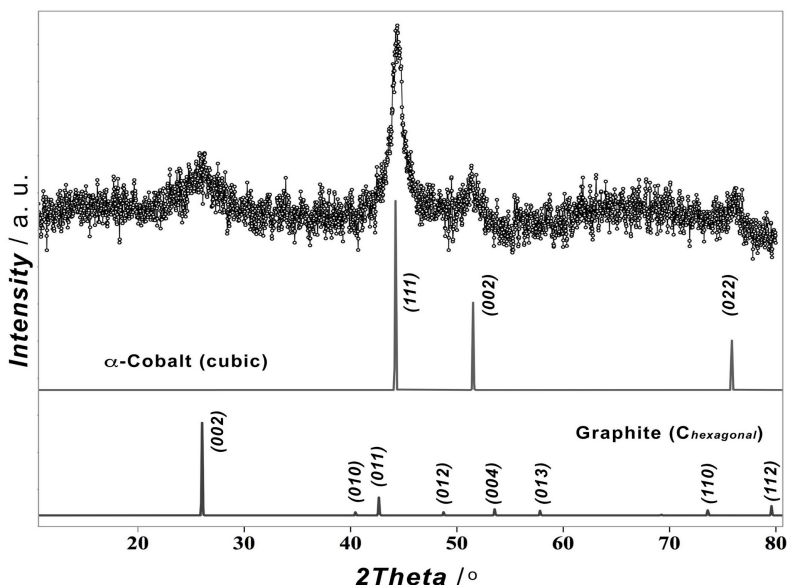


**Figure D4.** Powder X-ray diffraction pattern of pyrolyzed ZIF-67(Co) at 600 °C for 4 h in nitrogen flow (25 mL·min<sup>-1</sup>). Phase identification suggests the composition: metallic cobalt ( $\alpha$ -allotrope, *fcc*: cubic *Fm-3m*,  $a = b = c = 3.5442 \text{ \AA}$ ,  $\alpha = \beta = \gamma = 90^\circ$ , ISCD 04-007-8519)<sup>D1</sup> and carbon (graphite: hexagonal *P6<sub>3</sub>/mmc*,  $a = b = 2.5714 \text{ \AA}$ ,  $c = 6.8382 \text{ \AA}$ ,  $\alpha = \beta = 90^\circ$ ,  $\gamma = 120^\circ$ , ISCD 04-020-4354).<sup>D2</sup>

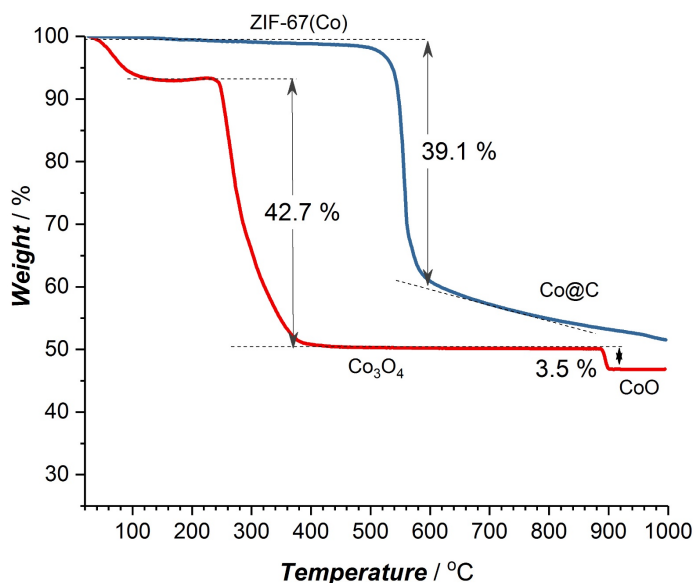


**Figure D5.** Thermogravimetric curves for ZIF-67(Co) precursor material in nitrogen (*blue line*) flow and calcination curve (*red line*) for Co@C product of ZIF-67(Co) pyrolysis at 600 °C.



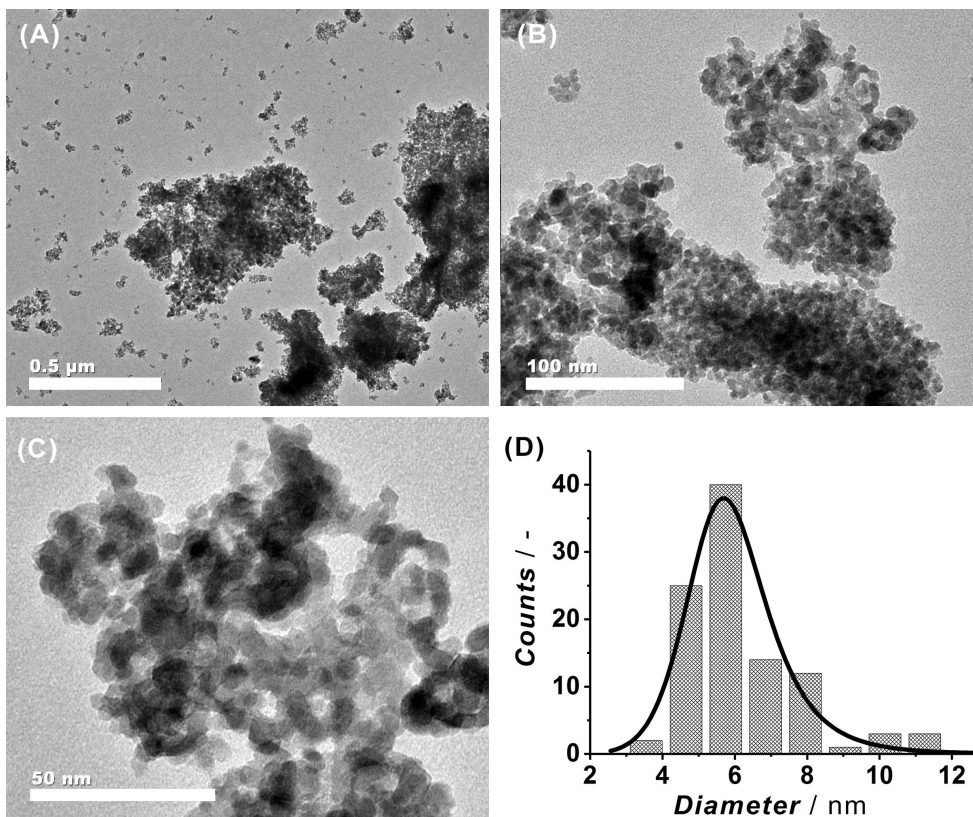


**Figure D6.** Transmission electron microscopy images at different magnifications (A-C) of the product obtained by calcination of pyrolyzed ZIF-67(Co) at 400 °C for 2 h in air flow (25 mL·min<sup>-1</sup>). (D) Particle size distribution histogram indicating the particle size of  $5.8 \pm 1.4$  nm.



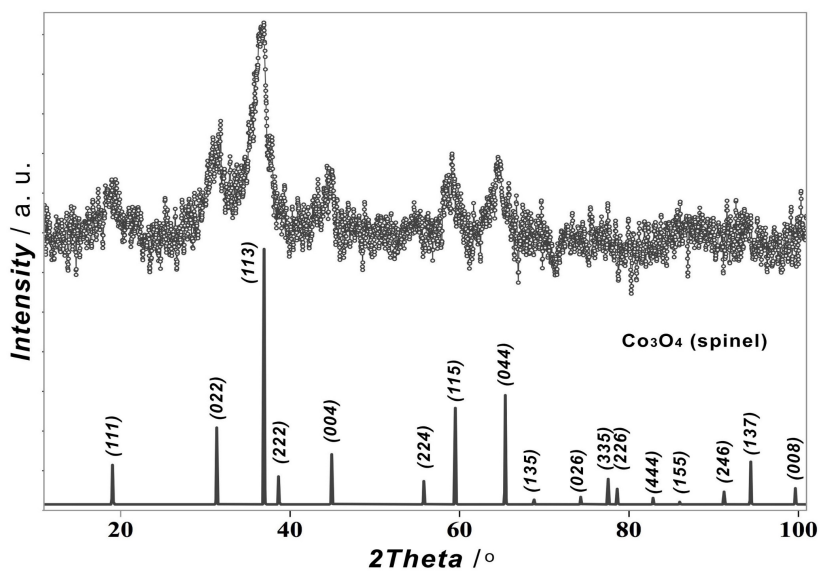


**Figure D7.** Powder X-ray diffraction pattern of the product obtained by calcination of pyrolyzed ZIF-67(Co) (600 °C for 4 h in nitrogen flow) at 400 °C for 2 h in air flow (25 mL·min<sup>-1</sup>). Phase identification reveals the composition: mixed CoO·Co<sub>2</sub>O<sub>3</sub> oxide (Co<sub>3</sub>O<sub>4</sub>) (spinel: cubic *Fd-3m*,  $a = b = c = 8.089 \text{ \AA}$ ,  $\alpha = \beta = \gamma = 90^\circ$ , ICSD 04-008-3173).<sup>D3</sup>

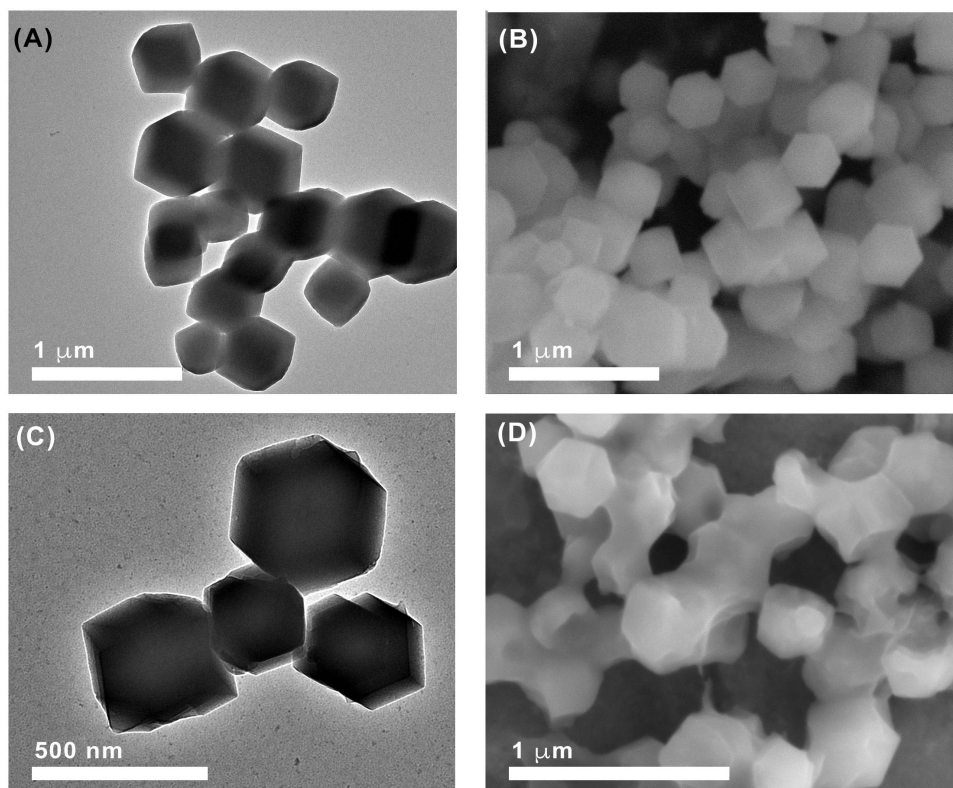


**Figure D8.** (A)-(B) Transmission and scanning electron microscopy images of parent ZIF-67(Co) metal organic framework with 300 nm crystal size (ZIF-67(Co)-300) and corresponding images for In-modified ZIF-67(Co)-300 before pyrolysis and calcination steps.

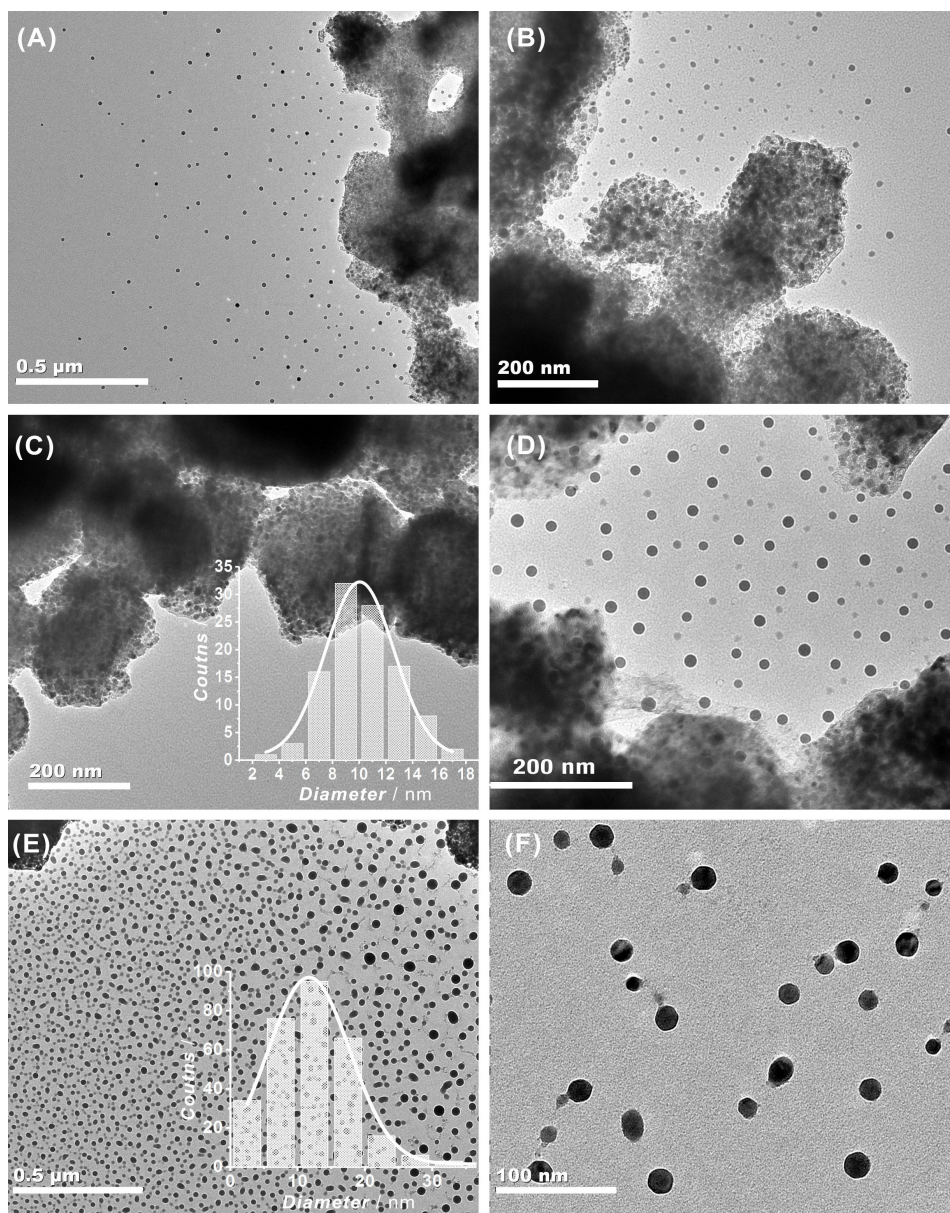


**Figure D9.** Transmission electron microscopy images at different magnifications (A-F) of pyrolyzed In-modified ZIF-67(Co)-300 (In:Co molar ratio = 3:8) at 600 °C for 4 h in nitrogen flow (25 mL·min<sup>-1</sup>) showing agglomerates composed of nanoparticles with average size of 10.0 ± 3.0 nm and free-standing spherical nanoparticles of 11.7 ± 7.2 nm size. Free-standing particles tend to sinter under electron beam exposure resulting in the particles with the sizes up to 30 – 40 nm.

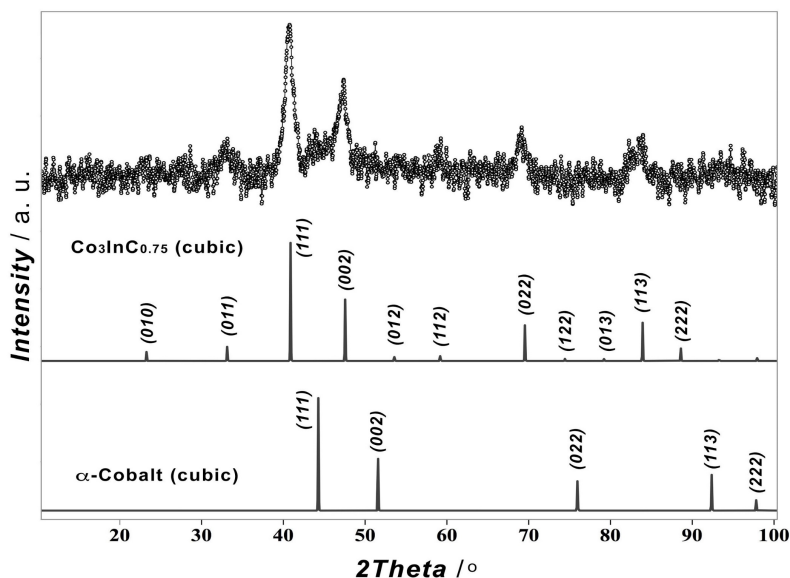


**Figure D10.** Powder X-ray diffraction pattern of the product resulted from the pyrolysis of In-modified ZIF-67(Co)-300 (In:Co molar ratio = 3:8) at 600 °C in nitrogen for 4 h flow (25 mL·min<sup>-1</sup>). Phase identification reveals the composition:  $\text{Co}_3\text{InC}_{0.75}$  (cubic  $Pm\text{-}3m$ ,  $a = b = c = 3.82 \text{ \AA}$ ,  $\alpha = \beta = \gamma = 90^\circ$ , ICSD 04-003-9712)<sup>D4</sup> and metallic cobalt ( $\alpha$ -allotrope: cubic  $Fm\text{-}3m$ ,  $a = b = c = 3.5442 \text{ \AA}$ ,  $\alpha = \beta = \gamma = 90^\circ$ , ICSD 04-007-8519).<sup>D1</sup>

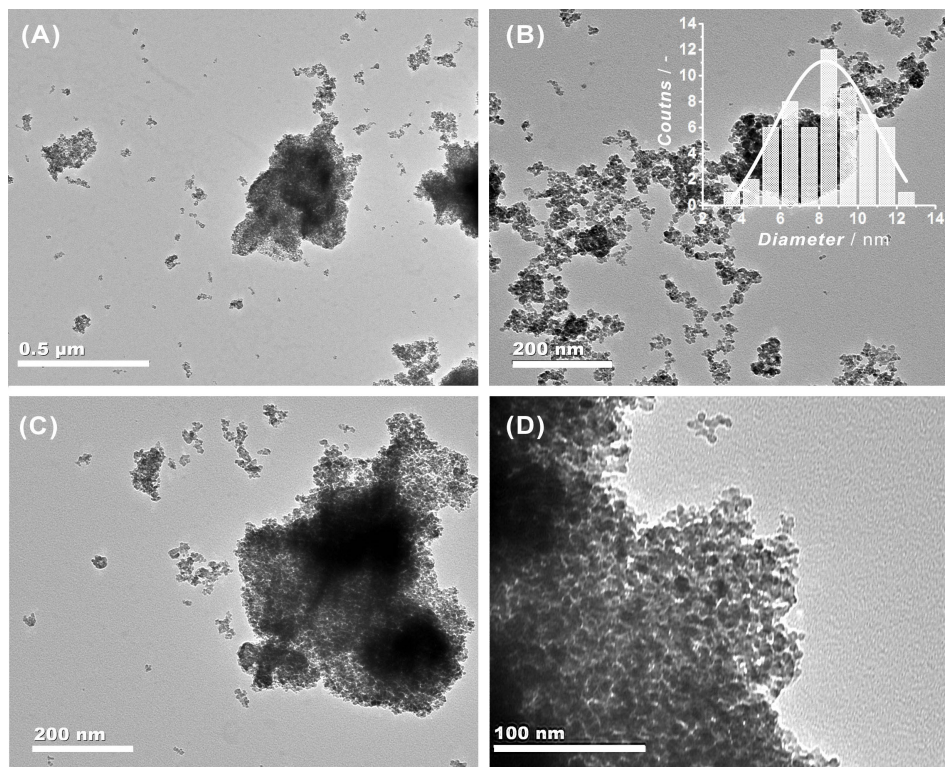


**Figure D11.** Transmission electron microscopy images at different magnifications (A-D) of calcined In-modified ZIF-67(Co)-300 (catalyst **3In:8Co(300)**) with In:Co molar ratio = 3:8 at 400 °C for 2 h in air flow (25 mL·min<sup>-1</sup>). Insert on graph (B) shows particle size distribution histogram (particle size about 8.3 ± 3.2 nm).



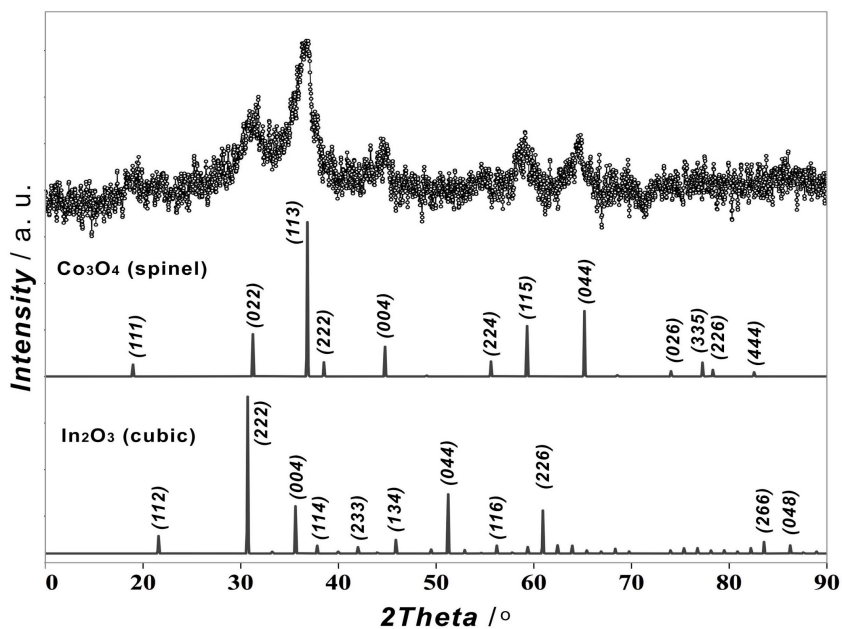


**Figure D12.** Powder X-ray diffraction pattern of 3In:8Co(300) sample obtained by calcination of pyrolyzed In-modified ZIF-67(Co)-300 (Co<sub>3</sub>InC<sub>0.75</sub>/Co@C) at 400 °C for 2 h in air flow (25 mL·min<sup>-1</sup>). Phase identification suggests the composition: mixed CoO·Co<sub>2</sub>O<sub>3</sub> oxide (Co<sub>3</sub>O<sub>4</sub>) (spinel: cubic *Fd-3m*,  $a = b = c = 8.089$  Å,  $\alpha = \beta = \gamma = 90^\circ$ , ISCD 04-008-3173)<sup>D3</sup> and In<sub>2</sub>O<sub>3</sub> oxide (cubic *Ia-3*,  $a = b = c = 10.077$  Å,  $\alpha = \beta = \gamma = 90^\circ$ , ISCD 04-004-3575).<sup>D5</sup>

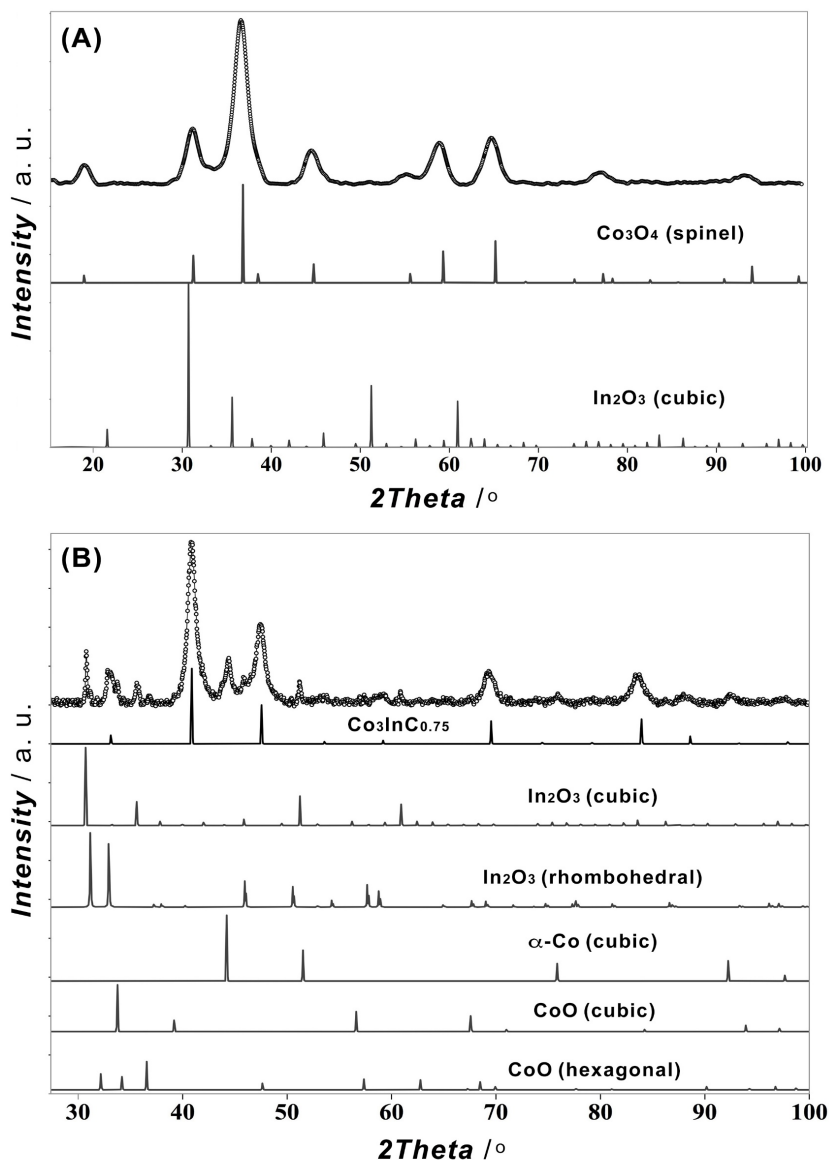


**Figure D13.** Powder X-ray diffraction pattern of 3In:8Co(300) catalyst before (A) and after (B) CO<sub>2</sub> hydrogenation. Phase identification suggests the composition: (A) Co<sub>3</sub>O<sub>4</sub> (spinel: cubic *Fd-3m*,  $a = b = c = 8.089 \text{ \AA}$ ,  $\alpha = \beta = \gamma = 90^\circ$ , ISCD 04-008-3173)<sup>D3</sup> and (B) Co<sub>3</sub>InC<sub>0.75</sub> (cubic *Pm-3m*,  $a = b = c = 3.82 \text{ \AA}$ ,  $\alpha = \beta = \gamma = 90^\circ$ , ISCD 04-003-9712),<sup>D4</sup> metallic cobalt ( $\alpha$ -allotrope: cubic *Fm-3m*,  $a = b = c = 3.5442 \text{ \AA}$ ,  $\alpha = \beta = \gamma = 90^\circ$ , ISCD 04-007-8519),<sup>D1</sup> CoO allotrope: hexagonal *P6<sub>3</sub>mc*,  $a = b = 3.21 \text{ \AA}$ ,  $c = 5.24 \text{ \AA}$ ,  $\alpha = \beta = 90^\circ$ ,  $\gamma = 120^\circ$ , ISCD 04-002-2693)<sup>D6</sup> and cubic *Fm-3m*,  $a = b = c = 4.2603 \text{ \AA}$ ,  $\alpha = \beta = \gamma = 90^\circ$ , ISCD 03-065-2902),<sup>D6-D7</sup> In<sub>2</sub>O<sub>3</sub> oxide (cubic *Ia-3*,  $a = b = c = 10.077 \text{ \AA}$ ,  $\alpha = \beta = \gamma = 90^\circ$ , ISCD 04-004-3575)<sup>D5</sup> and rhombohedral *R-3cH*,  $a = b = 5.4761 \text{ \AA}$ ,  $c = 14.4861 \text{ \AA}$ ,  $\alpha = \beta = 90^\circ$ ,  $\gamma = 120^\circ$ , ISCD 00-068-0337).<sup>D8</sup>

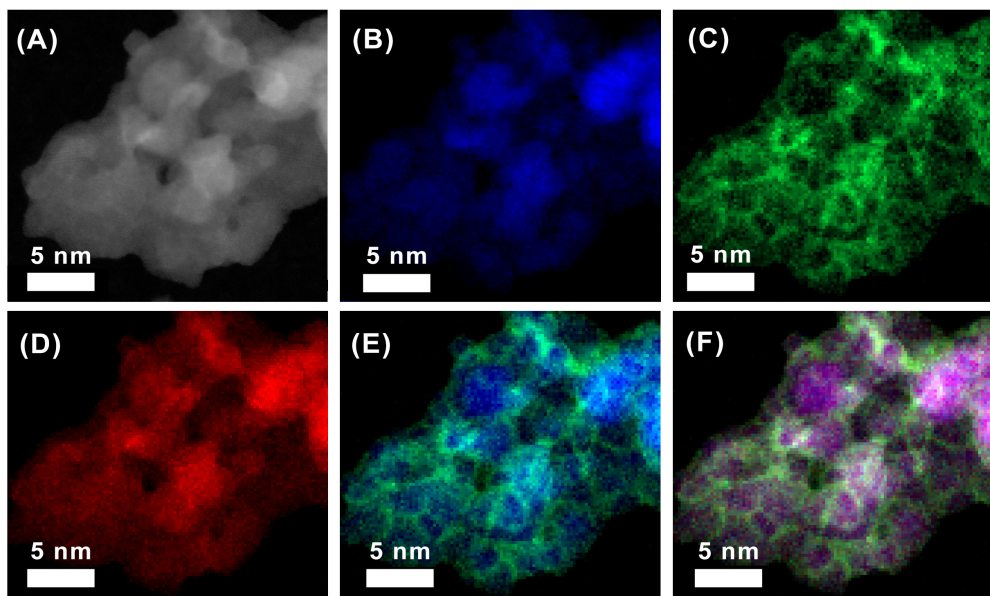


**Figure D14.** ADF-STEM imaging (A) and elemental mappings for 3In@4Co(300) before CO<sub>2</sub> hydrogenation reaction: Co *L*-edge map (B), In *M*-edge map (C) and O *K*-edge map (D); superimposed Co/In maps (E) and Co/In/O maps (F).

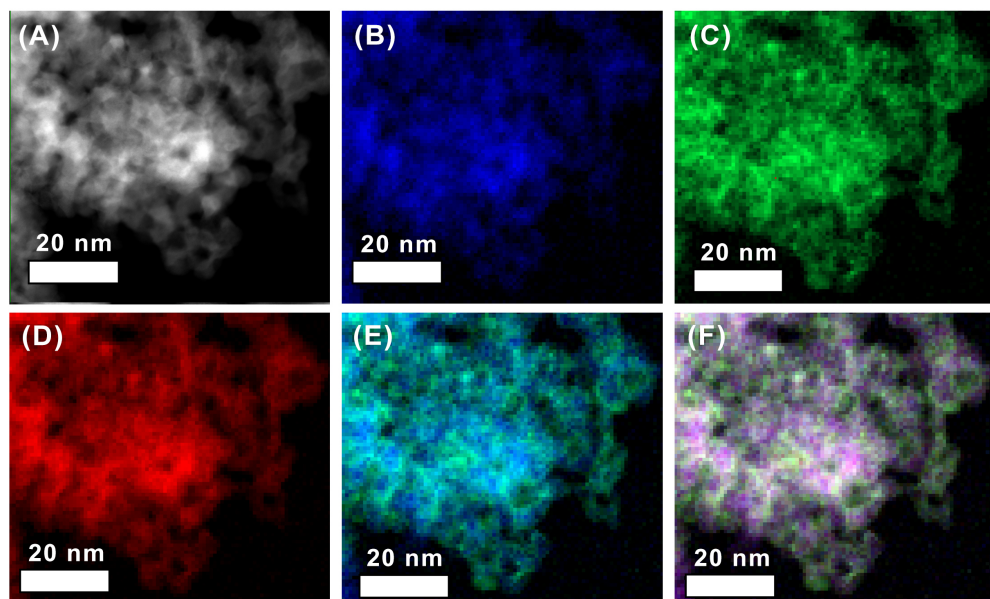


**Figure D15.** ADF-STEM imaging (A) and elemental mappings for 3In@4Co(300) before CO<sub>2</sub> hydrogenation reaction: Co *L*-edge map (B), In *M*-edge map (C) and O *K*-edge map (D); superimposed Co/In maps (E) and Co/In/O maps (F).



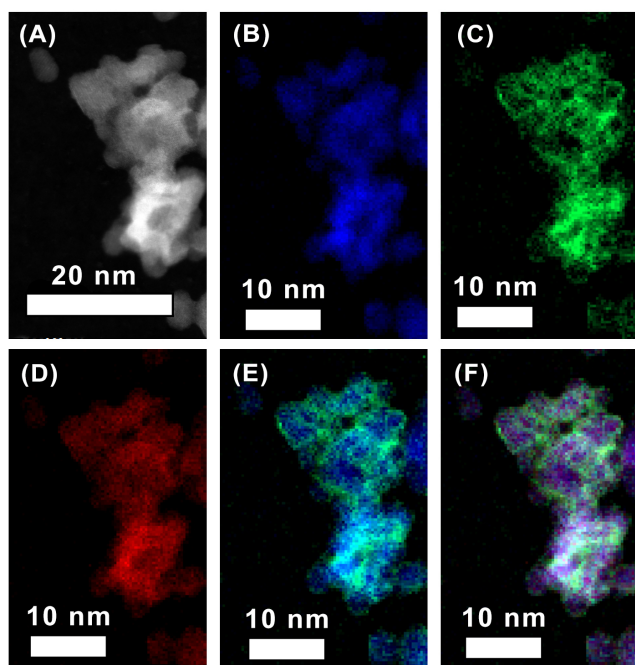


**Figure D16.** ADF-STEM imaging (A) and elemental mappings for  $3\text{In}@4\text{Co}(300)$  before  $\text{CO}_2$  hydrogenation reaction: Co  $L$ -edge map (B), In  $M$ -edge map (C) and O  $K$ -edge map (D); superimposed Co/In maps (E) and Co/In/O maps (F).

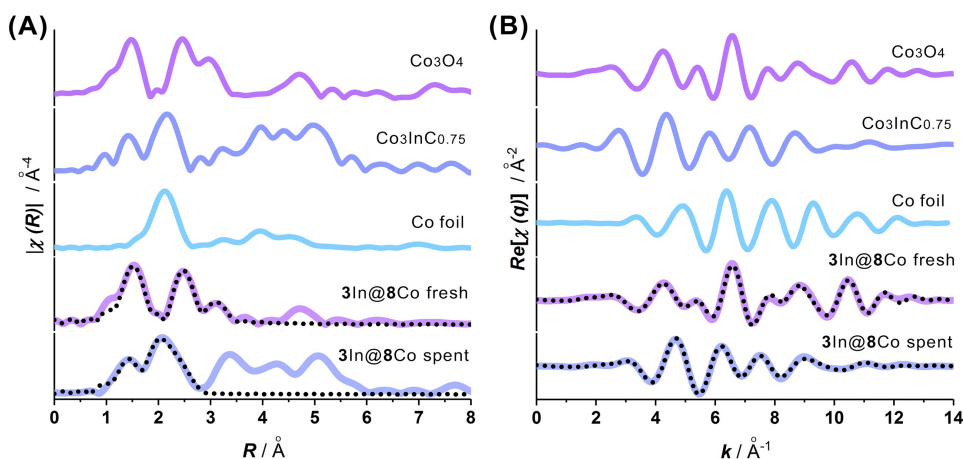


**Figure D17.** (A) Magnitude of the Fourier transform for the EXAFS  $k^3\chi(k)$  functions acquired at Co  $K$ -edge for  $\text{Co}_3\text{O}_4$ ,  $\text{Co}_3\text{InCo}_{0.75}$ , Co metal (*hcp*),  $3\text{In}@8\text{Co}(300)$  catalyst before and after  $\text{CO}_2$  hydrogenation reaction and, (B) their related back Fourier transforms (real part) applied within their respective  $R$ -range for EXAFS fitting. Solid line represents experimental data whereas dotted line corresponds to fit results conducted with  $[1.1 - 3.5] \text{ \AA}$  and  $[1.1 - 2.8] \text{ \AA}$   $R$ -range together with a  $[3.1 - 11.8] \text{ \AA}^{-1}$  and  $[3.3 - 12.1] \text{ \AA}^{-1}$   $k$ -range, respectively for  $3\text{In}@8\text{Co}(300)$  catalyst before and after reaction.

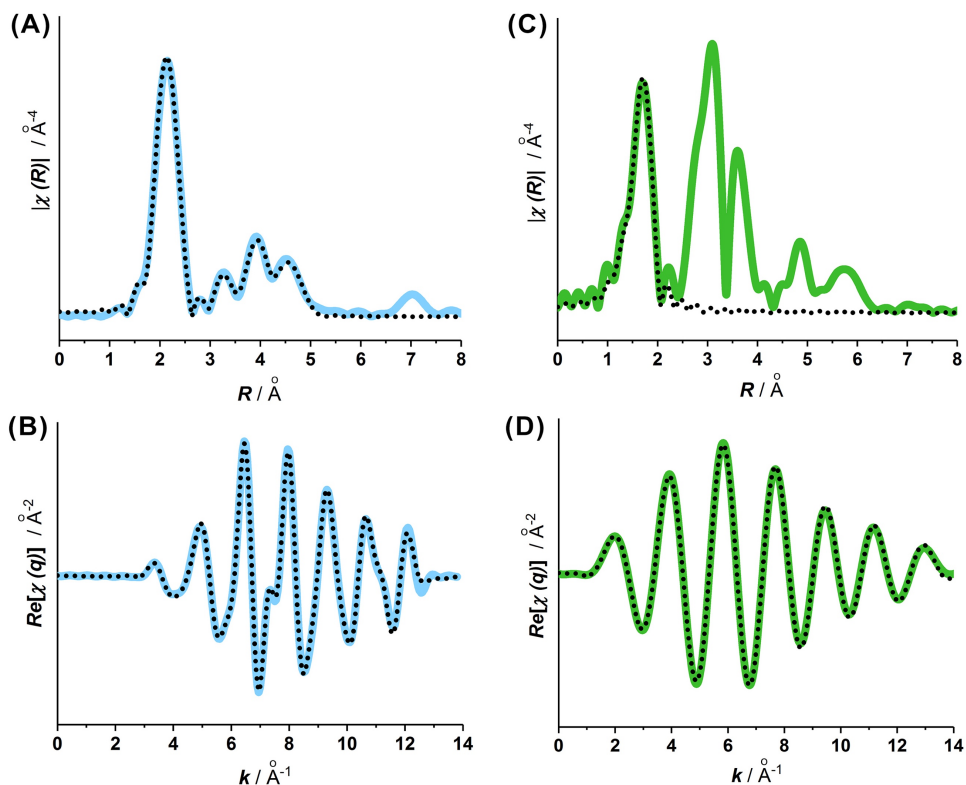


**Figure D18.** (A and C) Magnitude of the Fourier transform for the EXAFS  $k^3 \cdot \chi(k)$  functions acquired at Co and In  $K$ -edge for Co metal (*hcp*) (*blue graphs*), In<sub>2</sub>O<sub>3</sub> (*green graphs*), and (B) their related back Fourier transforms (real part) applied within their respective  $R$ -range for EXAFS fitting. Solid line represents experimental data whereas dotted line corresponds to fit results conducted with [1.1 - 5.1] Å and [1.2 - 2.1] Å  $R$ -range together with a [3.3 - 12.2] Å<sup>-1</sup> and [2.8 - 13.1] Å<sup>-1</sup>  $k$ -range, respectively for Co (*hcp*) and In<sub>2</sub>O<sub>3</sub>.

**Table D3.** Parameters extracted from the fits of EXAFS data for Co metallic foil (*hcp*),  $\text{In}_2\text{O}_3$  references,  $3\text{In}@8\text{Co}(300)$  fresh and reacted catalysts at both Co and In *K*-edges. For the fit of Co foil, multiple scattering paths are omitted for the sake of clarity.

Sample	Scale factors	Scattering path	N	R, Å	$\sigma^2$ , Å <sup>2</sup>	$\Delta E$ , eV	R-factor, %
Co foil ( <i>hcp</i> model) ( $S_0^2 = 0.73 \pm 0.04$ )		Co-Co	6	$2.49 \pm 0.01$	$0.0042 \pm 0.0003$	$0.0 \pm 0.5$	0.2
		Co-Co	6	$2.52 \pm 0.01$	$0.011 \pm 0.002$		
		Co-Co	6	$3.54 \pm 0.02$	$0.011 \pm 0.001$		
		Co-Co	2	$4.04 \pm 0.02$	$0.011 \pm 0.009$		
		Co-Co	12	$4.34 \pm 0.02$	$0.009 \pm 0.007$		
		Co-Co	6	$4.36 \pm 0.02$	$0.01 \pm 0.02$		
		Co-Co	12	$4.76 \pm 0.02$	$0.009 \pm 0.004$		
$\text{In}_2\text{O}_3$ ( $S_0^2 = 0.99 \pm 0.03$ )		In-O	6	$2.171 \pm 0.003$	$0.0055 \pm 0.0003$	$-6.6 \pm 0.3$	0.1
$3\text{In}@8\text{Co}$ fresh	$\text{Co}_{\text{Co}(\text{octahedral})}$ $S_{\text{Co}(\text{octahedral})} = 2/3^b$	Co-O	6	$1.92 \pm 0.01$	$0.0026 \pm 0.0008$	$2.3 \pm 1.1$	2.0
		Co-Co	6	$2.87 \pm 0.01$	$0.003 \pm 0.002$		
		Co-Co	6	$3.38 \pm 0.03$	$0.008^a$		
		Co-O	6	$3.59 \pm 0.03$	$0.003^a$		
	$\text{Co}_{\text{Co}(\text{tetrahedral})}$ $S_{\text{Co}(\text{tetrahedral})} = 1/3^b$	Co-O	4	$1.96 \pm 0.02$	$0.0026^a$		
		Co-Co	12	$3.37 \pm 0.01$	$0.008 \pm 0.003$		
		Co-O	12	$3.42 \pm 0.03$	$0.008^a$		
		Co-Co	4	$3.52 \pm 0.03$	$0.008^a$		
$3\text{In}@8\text{Co}$ fresh		In-O	$6.3 \pm 0.7$	$2.14 \pm 0.01$	$0.008 \pm 0.002$	$7 \pm 2$	0.7
$3\text{In}@8\text{Co}$ spent	cf. note <sup>c</sup>	Co-C	$0.8 \pm 0.2$	$1.88 \pm 0.03$	$0.002^a$	$-5 \pm 2$	0.9
		Co-Co	12	$2.56 \pm 0.05$	$0.0274 \pm 0.0007$		
$3\text{In}@8\text{Co}$ spent	$\text{In}_2\text{O}_3$ $S_{\text{In}_2\text{O}_3} = 0.64 \pm 0.06$	In-O	6	$2.172 \pm 0.009$	$0.007 \pm 0.002$	$8^e \pm 3$	0.8
		In-In	6	$3.34 \pm 0.03$	$0.011 \pm 0.002$		
	$\text{Co}_3\text{InC}_{0.75}$ $S_{\text{carbide}} = 0.36 \pm 0.06$	In-Co	12	$2.72 \pm 0.02$	$0.010 \pm 0.002$	$8^e$	
		In-C	6	$3.34 \pm 0.03$	$0.005 \pm 0.01$		

<sup>a</sup> Parameters constrained during the refinement.

<sup>b</sup> Scale factors determined from the multiplicities of the crystallographic sites in  $\text{Co}_3\text{O}_4$  structure.

<sup>c</sup> Due to a restricted number of independent parameters, it is particularly difficult to perform a satisfactory fit using a Co-Co path (2.5 Å) from the Co (*fcc*) metal augmented by two additional Co-In and Co-Co paths (2.7 Å) from the  $\text{Co}_3\text{InC}_{0.75}$  carbide. Since the coordination of the metal shells are equal to 12 in both phases, a single Co-Co path with a degeneracy of 12 was used to model the ensemble of metal-metal shells while its related mean square relative displacement was left free to adjust.

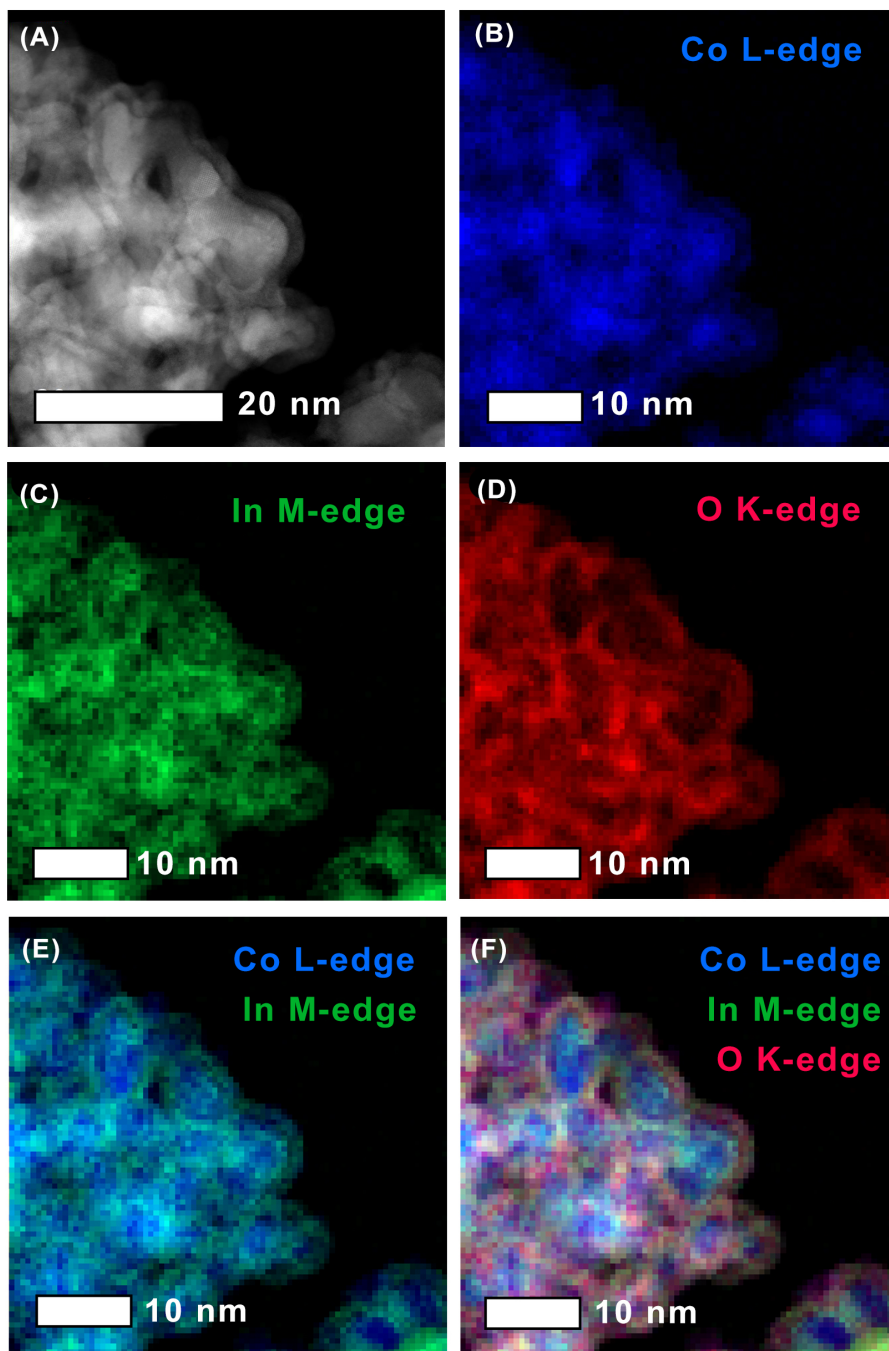


**Figure D19.** ADF-STEM imaging (A) and elemental mappings for 3In@4Co(300) after reaction: Co map (B), In map (C) and O map (D); superimposed Co/In maps (E) and Co/In/O maps (F).

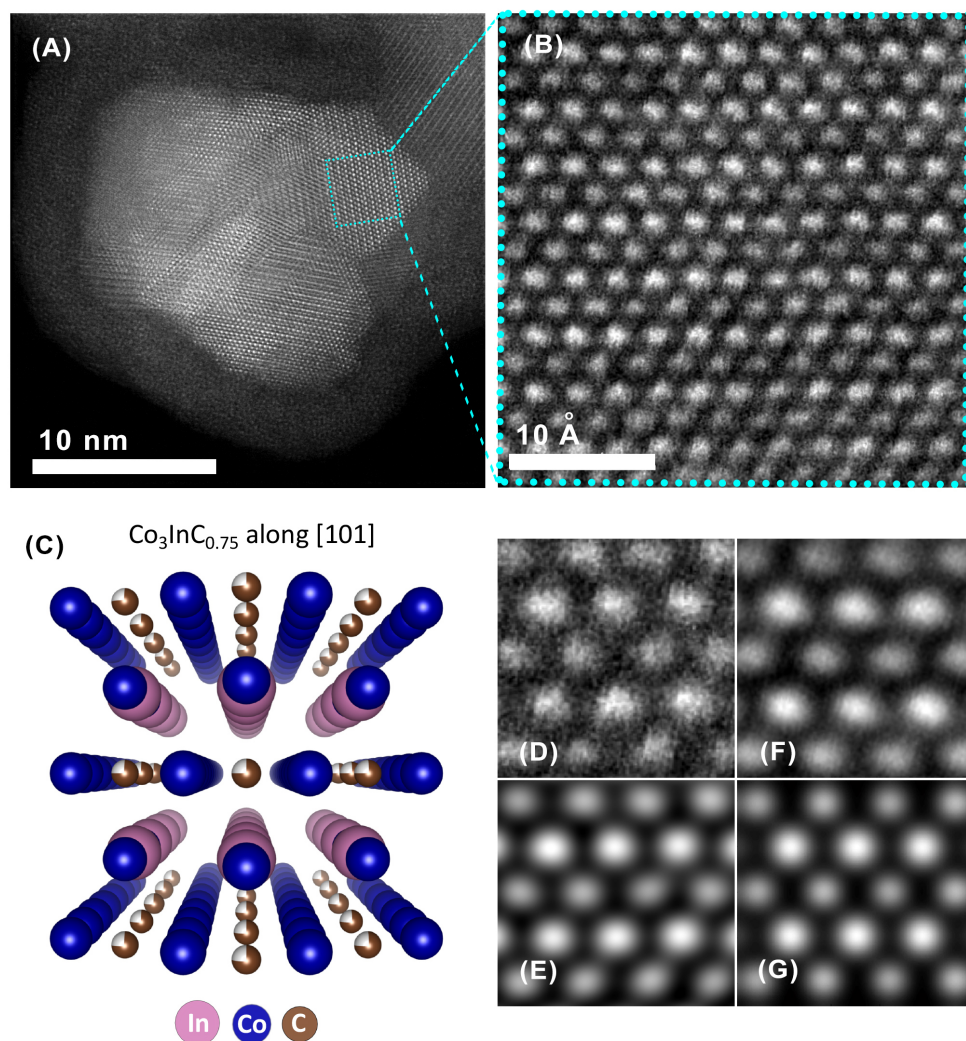


**Figure D20.** (A) High-resolution HAADF-STEM image of  $3\text{In}@4\text{Co}(300)$  after reaction. (B) Zoomed region of interest in (A) representing the atomic arrangement with interplanar distances of  $3.83 \text{ \AA}$  which corresponds to  $\text{Co}_3\text{InC}_{0.75}$  phase, viewed along  $[101]$ -zone axis. (D) Atomic arrangement of  $\text{Co}_3\text{InC}_{0.75}$  zoomed from raw (B) image, the same region of interest processed with Wiener (F) and band pass (E) filters and compared to the simulated one for  $\text{Co}_3\text{InC}_{0.75}$  packing viewed along  $[101]$ -zone axis. Simulation parameters:  $E = 300 \text{ kV}$ ,  $df = -1.7 \text{ nm}$ ,  $C_s = 1 \text{ mm}$ ,  $C_c = 1 \text{ mm}$ ,  $dE = 0.9 \text{ eV}$ ,  $\alpha = 17 \text{ mrad}$ , detector collection angle =  $[63, 200] \text{ mrad}$ , slab thickness =  $4.8 \text{ nm}$ .

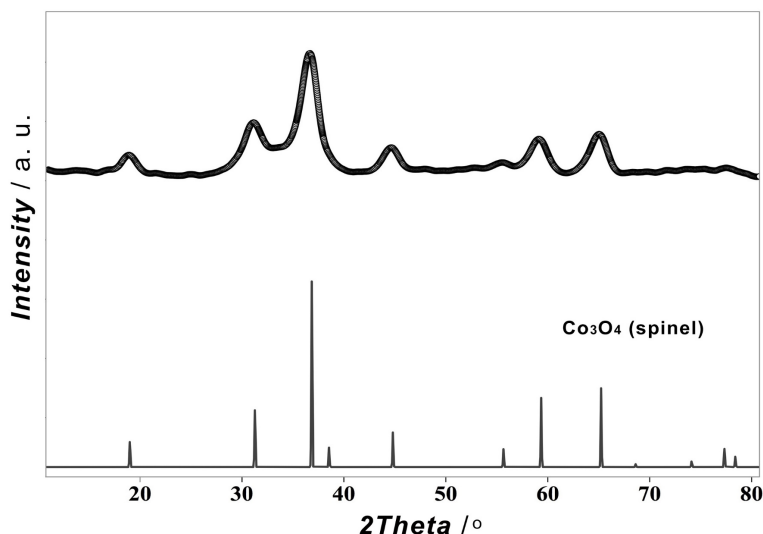


**Figure D21.** Powder X-ray diffraction pattern of **3In:8Co(300)-dc** sample obtained by direct calcination of In-modified ZIF-67(Co)-300 at 400 °C for 2 h in air flow (25 mL·min<sup>-1</sup>). Phase identification suggests the composition: mixed CoO-Co<sub>2</sub>O<sub>3</sub> oxide (Co<sub>3</sub>O<sub>4</sub>) (spinel: cubic *Fd-3m*,  $a = b = c = 8.089 \text{ \AA}$ ,  $\alpha = \beta = \gamma = 90^\circ$ , ISCD 04-008-3173).<sup>D3</sup>

**Table D4.** Selected characteristics of In@ZIF-67 sacrificial composites and derived from them **aIn:bCo(x)** catalysts (where **x** is crystal size of ZIF-67(Co), **a** and **b** indicate the In:Co molar ratio). The sacrificial In@ZIF-67 composites were prepared by incipient wetness impregnation (*IWI*) of ZIF-67(Co) with indium and corresponding catalysts were prepared by two step thermal treatment: pyrolysis at 600 °C and calcination at 400 °C.

Catalyst code	In@ZIF-67	In@Co		
	BET area (m <sup>2</sup> ·g <sup>-1</sup> )	BET area (m <sup>2</sup> ·g <sup>-1</sup> )	In : Co molar ratio	
			TGA <sup>a</sup>	XRF
<b>1In:23Co(20)</b>	1332	96	1:21	1:18
<b>1In:12Co(20)</b>	806	103	1:9	1:11
<b>1In:6Co(20)</b>	138	87	1:5	1:4
<b>3In:8Co(20)</b>	39	119	2:9	2:5
<b>3In:4Co(20)</b>	2	109	4:7	2:3
<b>3In:8Co(300)</b>	52	107	2:7	2:5

<sup>a</sup> Determined from thermogravimetric data in the range of temperatures 840–950 °C where Co<sub>3</sub>O<sub>4</sub>→CoO conversion is taking place

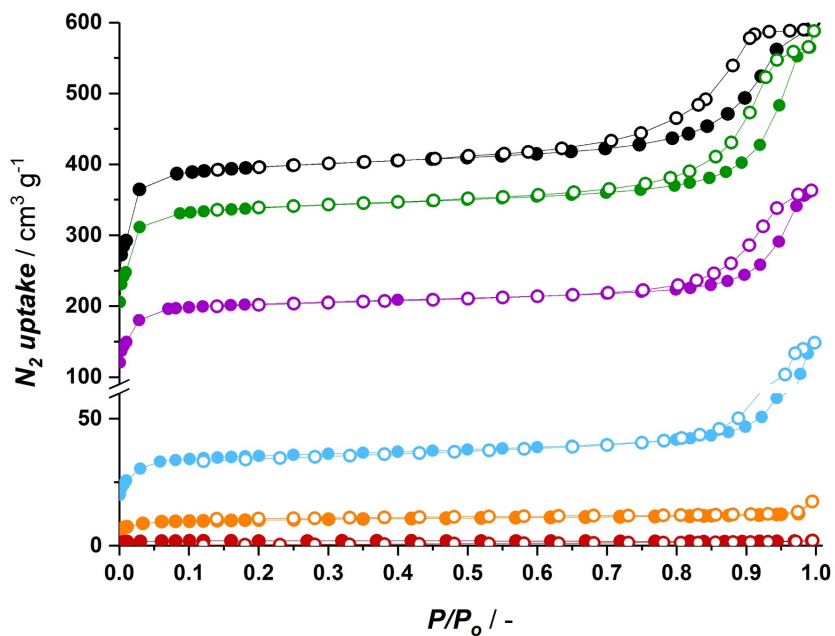


**Figure D22.** N<sub>2</sub> adsorption isotherm curves acquired at 77 K for parent (black) and In-modified ZIF-67(Co)-20 nm with following In:Co molar ratios: 1In:23Co (green), 1In:12Co (purple), 1In:6Co (blue), 3In:8Co (orange) and 3In:4Co (red). Solid markers correspond to the adsorption curve and open ones for desorption branch.

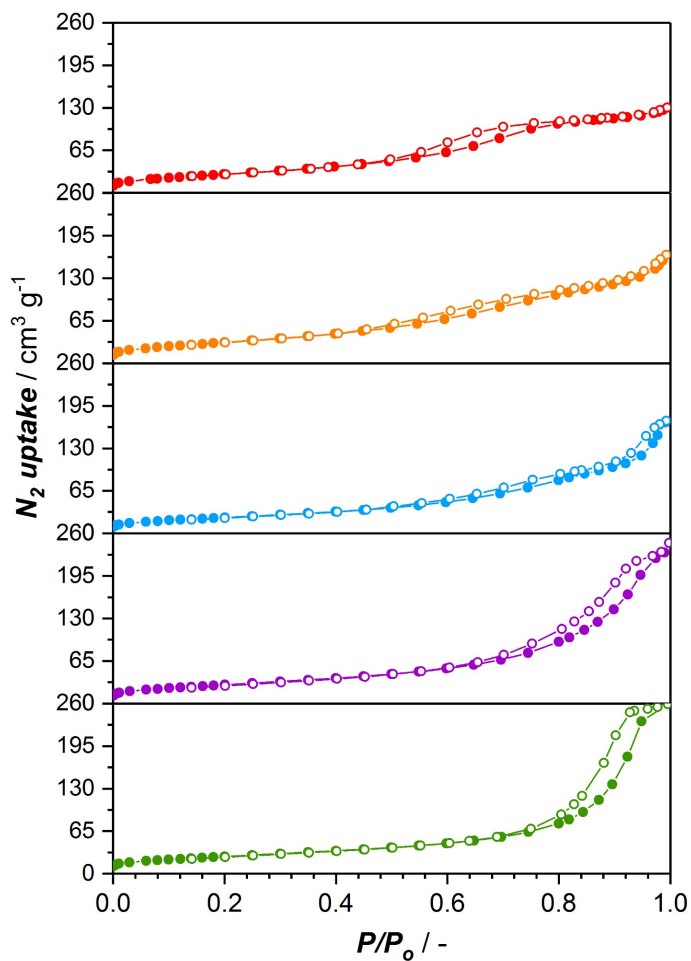


**Figure D23.** N<sub>2</sub> adsorption isotherm curves acquired at 77 K for In@Co catalysts prepared by two step thermal treatment out of ZIF-67(Co)-20 nm with certain In:Co molar ratio: **1In:23Co** (green), **1In:12Co** (purple), **1In:6Co** (blue), **3In:8Co** (orange) and **3In:4Co** (red). Solid markers correspond to the adsorption curve and open ones for desorption branch.



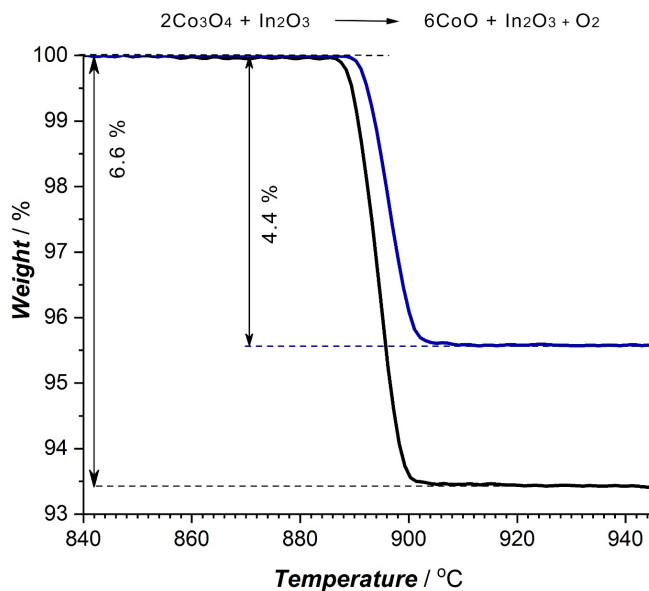


**Figure D24.** Selected region of thermogravimetric curves performed in air flow assigned to  $\text{Co}_3\text{O}_4$ – $\text{CoO}$  phase transition for different samples: **3In:8Co(300)** (blue line) and **Co@C** material derived from parent ZIF-67(Co) (black line).

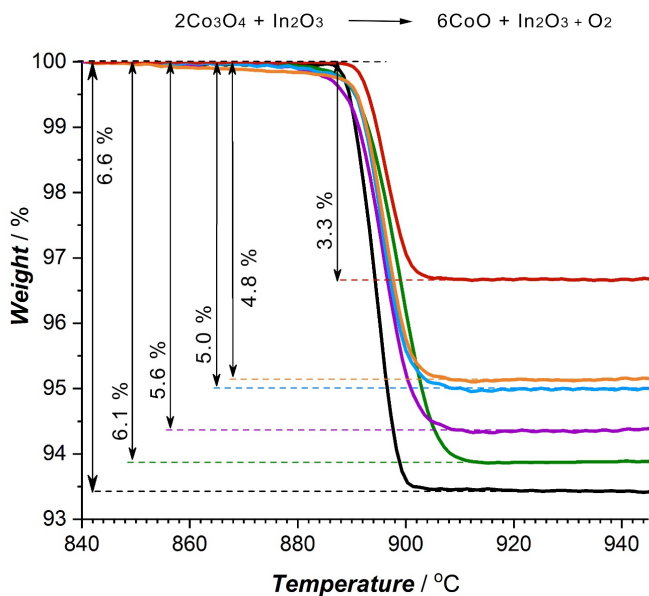


**Figure D25.** Selected region of thermogravimetric curves performed in air flow assigned to  $\text{Co}_3\text{O}_4$ – $\text{CoO}$  phase transition for different catalyst samples: **1In:23Co(20)** (red line), **1In:12Co(20)** (orange line), **1In:6Co(20)** (blue line), **3In:8Co(20)** (purple line), **3In:4Co(20)** (green line) and **Co@C** material derived from parent ZIF-67(Co) (black line).

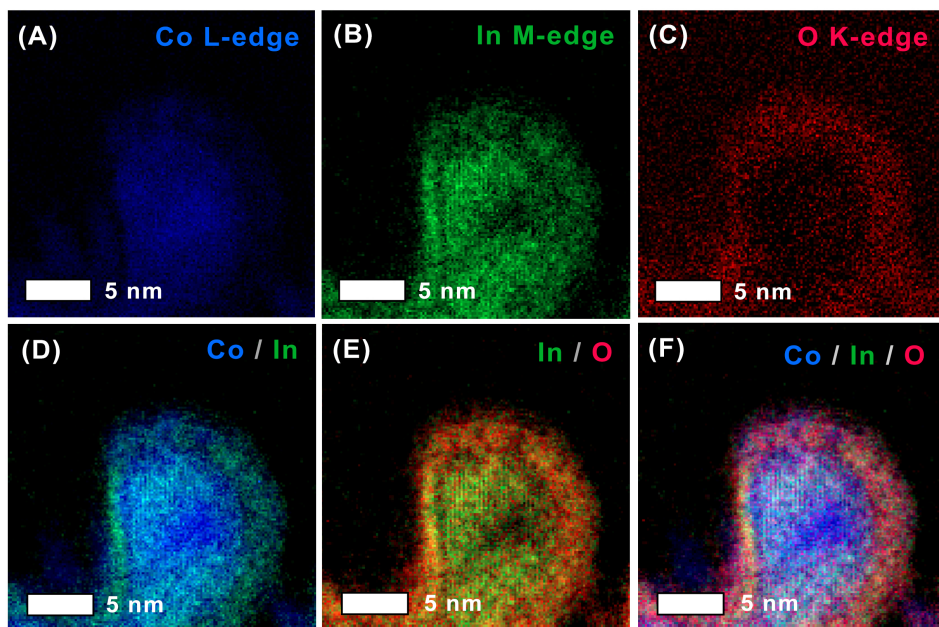


**Figure D26.** Elemental mappings for **3In@4Co(20)** after reaction: Co map (A), In map (B), O map (C); superimposed Co/In maps (D), In/O maps (E) and Co/In/O maps (F).

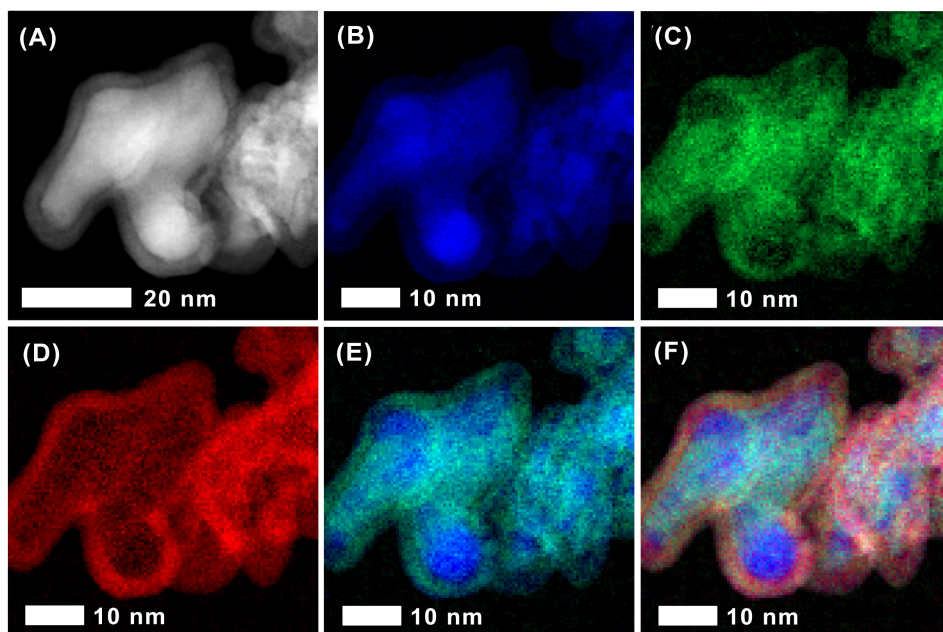


**Figure D27.** ADF-STEM imaging (A) and elemental mappings for **3In@4Co(20)** after reaction: Co L-edge map (B), In M-edge map (C) and O K-edge map (D); superimposed Co/In maps (E) and Co/In/O maps (F).

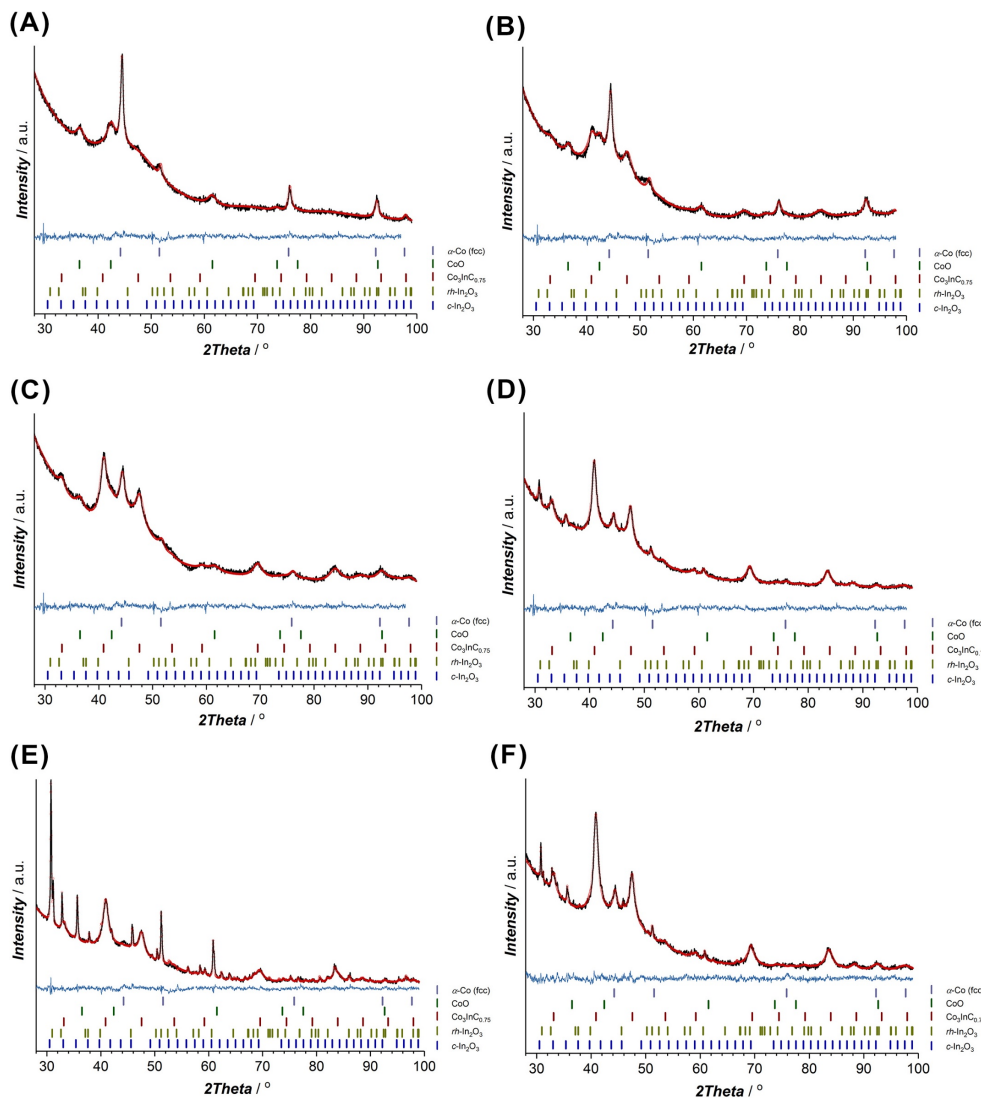


**Figure D28.** Rietveld refinement plots for crystal phase quantification of the reacted catalysts: (A) **1In:23Co(20)** ( $R_p = 1.45$ ,  $R_{wp} = 2.00$ ), (B) **1In:12Co(20)** ( $R_p = 1.59$ ,  $R_{wp} = 2.12$ ), (C) **1In:6Co(20)** ( $R_p = 1.90$ ,  $R_{wp} = 2.44$ ), (D) **3In:8Co(20)** ( $R_p = 2.33$ ,  $R_{wp} = 3.08$ ), (E) **3In:4Co(20)** ( $R_p = 2.75$ ,  $R_{wp} = 3.63$ ) and (F) **3In:8Co(300)** ( $R_p = 1.98$ ,  $R_{wp} = 2.54$ ). Black solid line corresponds to the experimental pattern, red dots – fit, blue line – the difference between experimentally obtained and fitted patterns, sticks – expected Bragg position for quantified phases. Measurements were performed using an airtight zero-background holder.

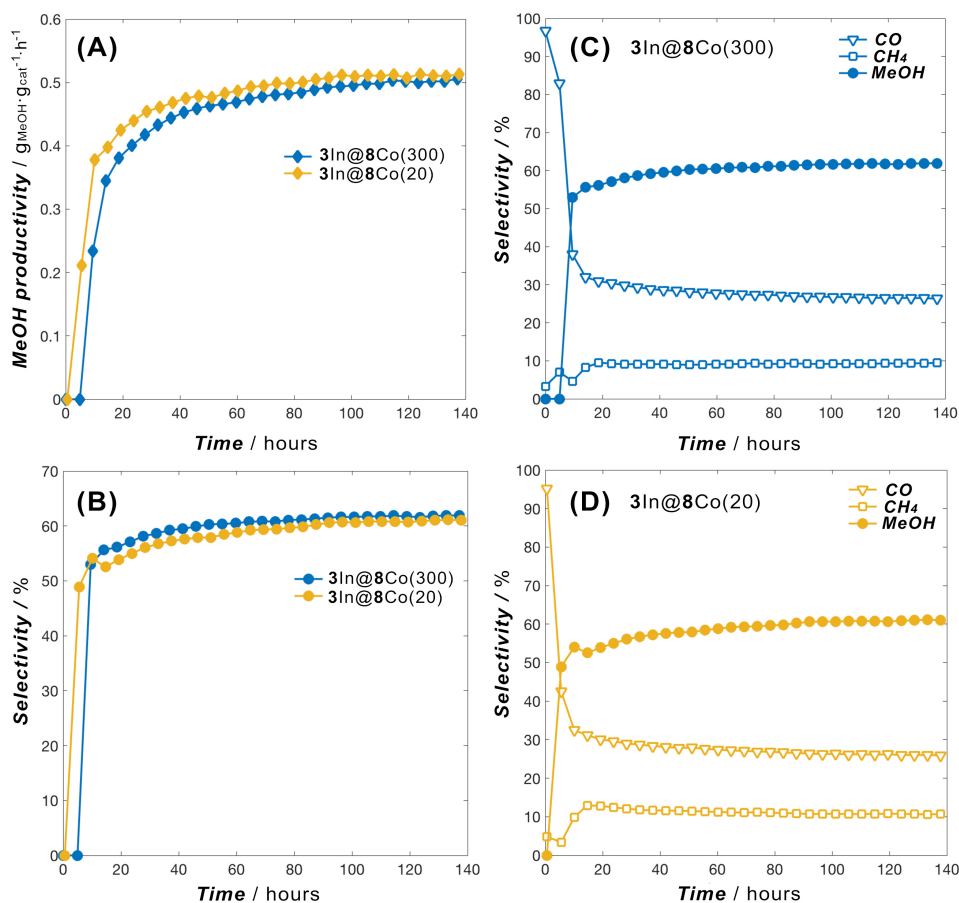


**Figure D29.** (A) Evolution of MeOH space time yield and (B) MeOH selectivity with time on In@Co catalysts derived from ZIF-67(Co) with 300 nm (navy) and 20 nm (orange) crystal sizes and with constant In:Co molar ratio (3In@8Co). Time on stream evolution of selectivities for MeOH product (filled circle) and CO (hollow triangle)/CH<sub>4</sub> (hollow square) by-products over In@Co catalysts (In:Co = 3:8 molar ratio): (C) 3In@8Co(300) and 3In@8Co(20) derived from ZIF-67(Co) with 300 nm (navy) and 20 nm (orange) crystal sizes, respectively. Reaction conditions:  $m_{\text{cat}} = 50$  mg,  $T = 300$  °C, GHSV = 15600 h<sup>-1</sup>,  $P = 50$  bar and feed of 80% H<sub>2</sub>-20% CO<sub>2</sub>.

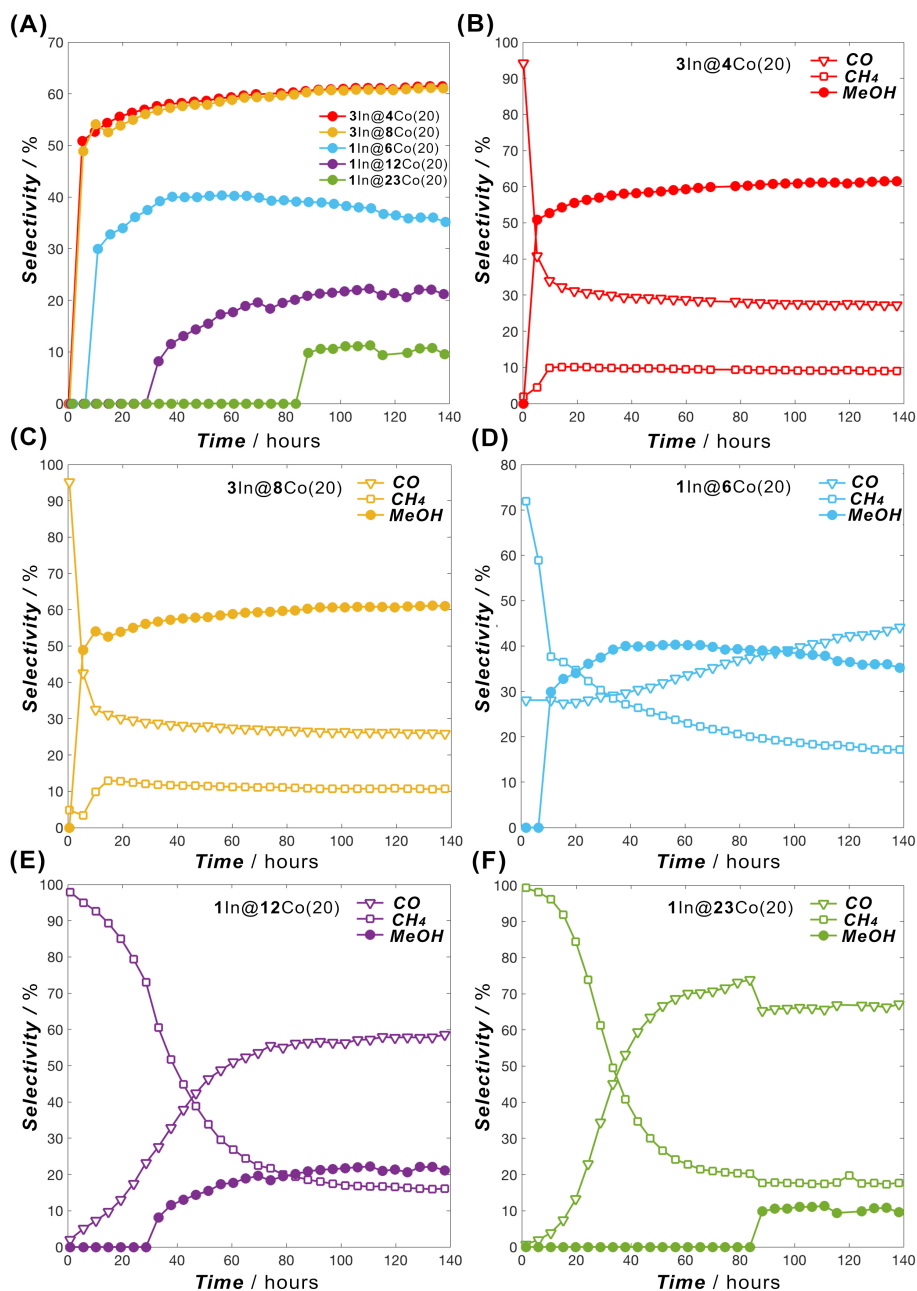


**Figure D30.** (A) MeOH selectivity evolution against time on stream over ZIF-67-20 nm derived In@Co catalysts with different In:Co molar ratios: 3In@4Co (red), 3In@8Co (orange), 1In@6Co (blue), 1In@12Co (purple) and 1In@23Co (green). Time on stream evolution of selectivities for MeOH product (filled circle) and CO (hollow triangle)/CH<sub>4</sub> (hollow square) by-products over In@Co catalysts with different In:Co molar ratios: (B) 3In@4Co, (C) 3In@8Co, (D) 1In@6Co, (E) 1In@12Co and (F) 1In@23Co. Reaction conditions:  $m_{\text{cat}} = 50 \text{ mg}$ ,  $T = 300 \text{ }^{\circ}\text{C}$ , GHSV =  $15600 \text{ h}^{-1}$ ,  $P = 50 \text{ bar}$  and feed of  $80\% \text{H}_2\text{-}20\% \text{CO}_2$ .

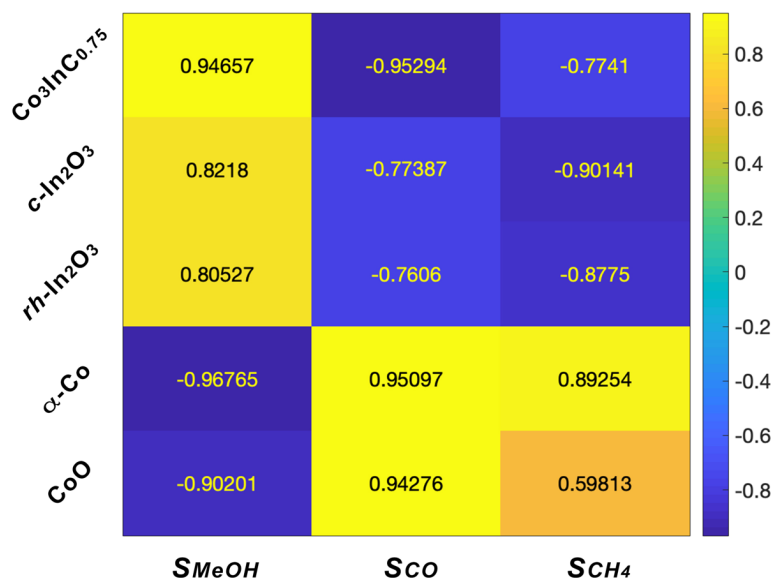


**Figure D31.** Correlation matrix showing correlation coefficients between individual phase contents (in wt.%, rows) and selectivities towards MeOH, CO and CH<sub>4</sub> (% , columns). Scaled from 1 (yellow) to -1 (navy).

**Table D5.** Results of phase analysis and compositions for In@Co reacted catalysts calculated from powder X-ray diffraction data associated with the product selectivities in CO<sub>2</sub> hydrogenation process.\* Reacted catalysts were sealed under Ar atmosphere and measured using airtight sample holder.

Catalyst code	Reacted catalyst (wt. %)						Selectivities* (%)		
	Co <sub>3</sub> InCo <sub>0.75</sub>	In <sub>2</sub> O <sub>3</sub>		α-Co	Co <sub>3</sub> O <sub>4</sub>	CoO	MeOH	CO	CH <sub>4</sub>
		c-	rh-						
1In:23Co(20)	27.53	0	0	64.27	0	8.21	12	70	18
1In:12Co(20)	57.89	0	0	37.91	0	4.20	23	59	18
1In:6Co(20)	62.14	0	0	37.86	0	0	40	41	19
3In:8Co(20)	82.11	7.25	3.62	7.62	0	0	62	27	11
3In:4Co(20)	80.09	11.51	2.57	5.83	0	0	62	28	9
3In:8Co(300)	78.91	5.06	6.60	5.42	0	0	63	27	9

\* Reaction conditions:  $m_{\text{cat}} = 50$  mg, 300 °C, 50 bar, 80% H<sub>2</sub>-20% CO<sub>2</sub>, GHSV of 15600 h<sup>-1</sup>, TOS = 100 h

**Table D6.** Summary of HCN elemental analysis for as-prepared fresh In@Co catalysts and corresponding spent catalysts after CO<sub>2</sub> hydrogenation.

Catalyst code	Fresh catalyst			Spent catalyst		
	H (wt.%)	C (wt.%)	N (wt.%)	H (wt.%)	C (wt.%)	N (wt.%)
<b>1In:23Co(20)</b>	0.35	0.44	0.0	0.22	0.83	0.0
<b>1In:12Co(20)</b>	0.32	0.35	0.0	0.0	0.98	0.0
<b>1In:6Co(20)</b>	0.42	0.39	0.0	0.35	1.14	0.0
<b>3In:8Co(20)</b>	0.47	0.40	0.0	0.0	0.57	0.0
<b>3In:4Co(20)</b>	0.39	0.49	0.0	0.23	2.39	0.0
<b>3In:8Co(300)</b>	0.45	0.52	0.0	0.40	1.55	0.0

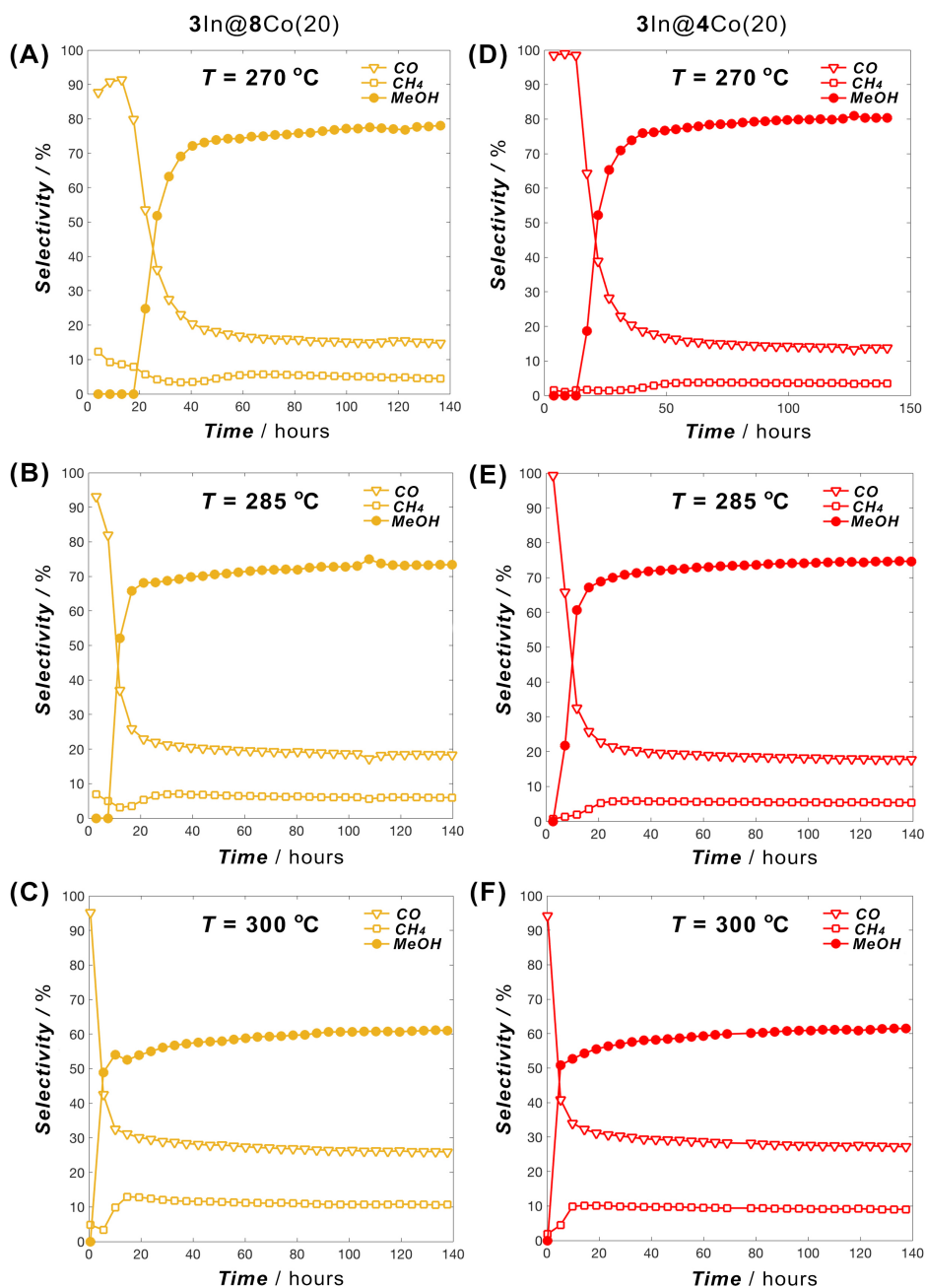


**Figure D32.** Time on stream evolution of selectivities for MeOH product (filled circle) and CO (hollow triangle)/CH<sub>4</sub> (hollow square) by-products on 3In@8Co (left column, orange) catalyst at 270 °C (A), 285 °C (B) and 300 °C (C) and on 3In@4Co (right column, red) catalyst at 270 °C (D), 285 °C (E) and 300 °C (F). Reaction conditions:  $m_{\text{cat}} = 50 \text{ mg}$ ,  $P = 50 \text{ bar}$ ,  $\text{GHSV} = 15600 \text{ h}^{-1}$  and feed of 80% H<sub>2</sub>-20% CO<sub>2</sub>.



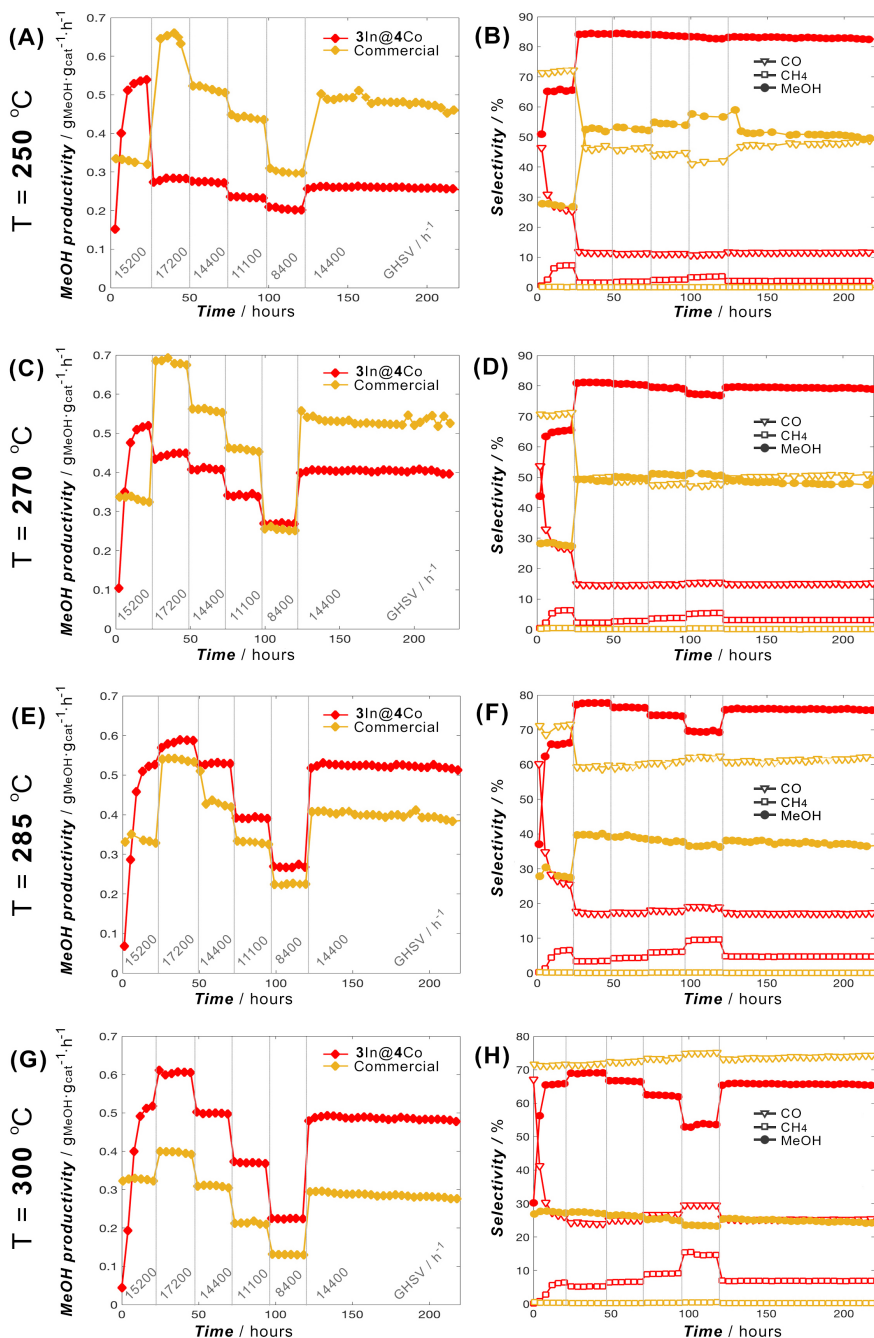


**Figure D33.** Time on stream evolution of methanol productivity, left side, and selectivities for MeOH product (filled circle) and CO (hollow triangle)/CH<sub>4</sub> (hollow square), right side, over 3In@4Co (red symbols) and commercial Cu-ZnO-Al<sub>2</sub>O<sub>3</sub> catalyst (orange symbols) at four different temperatures – 250 °C, 270 °C, 285 °C, 300 °C and variable gas flow velocities (grey marks). GHSV are identical for the left side as for the right side of the graphs.

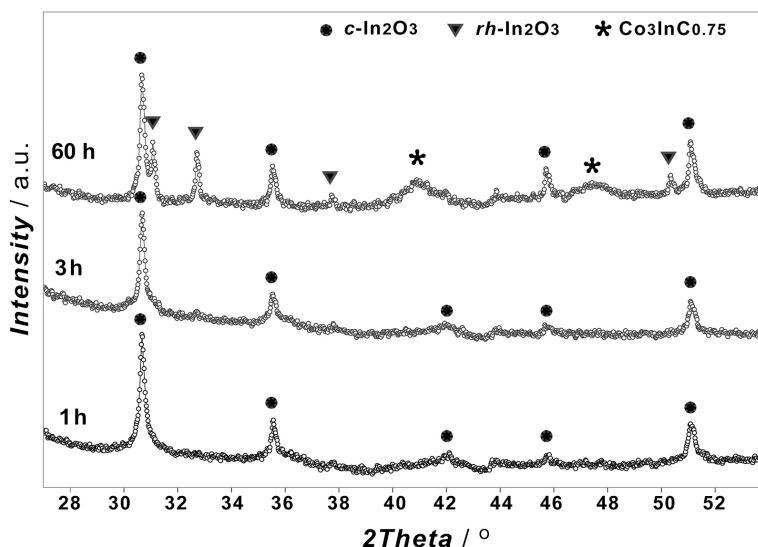


**Figure D34.** Evolution of crystalline phases in  $3\text{In}@4\text{Co}$  catalyst after 1, 3 and 60 hours of CO<sub>2</sub> hydrogenation reaction. Conditions: 80% H<sub>2</sub>-20% CO<sub>2</sub> feed,  $T = 300\text{ }^{\circ}\text{C}$ ,  $P = 50\text{ bar}$ ,  $m_{\text{cat}} = 50\text{ mg}$ , GHSV = 15600 h<sup>-1</sup>.

In order to evaluate the transformations occurring over the induction period, we examined the structural changes at different stages of the reaction applying X-ray diffraction and EDS TEM analyses. These results are summarized in Figs. D34-D35 and confirm a gradual change in structure of the catalyst. After the first hour of reaction, the cobaltite phase undergoes reduction losing crystalline features and it is no longer detected on PXRD, whereas the indium oxide appears recrystallizing from the amorphous state. It is conclusive that the formation of carbide phase proceeds through a reduction of Co-In interphases and their further carburization. In other hand, the presence of CO<sub>2</sub> as oxidizing component of the reaction mixture allows Co and In oxidized species exist on the surface of the particles throughout the catalytic process. Thus, the carbide becomes detectable in PXRD by the end of the catalytic run developing its fraction along the reaction.

**Table D7.** Catalytic data of CO<sub>2</sub> hydrogenation over some individual components and In@Co catalysts prepared by alternative routes. Reaction conditions:  $m_{\text{cat}} = 50$  mg, 300 °C, 50 bar, 80% H<sub>2</sub>-20% CO<sub>2</sub>, GHSV of 15600 h<sup>-1</sup>, TOS = 50 h.

Catalyst	S <sub>MeOH</sub> (%)	STY (g <sub>MeOH</sub> ·g <sub>cat</sub> <sup>-1</sup> ·h <sup>-1</sup> )	S <sub>CH<sub>4</sub></sub> (%)	S <sub>CO</sub> (%)	X <sub>CO<sub>2</sub></sub> (%)
3In:8Co(20)	62	0.48	11	27	19
In <sub>2</sub> O <sub>3</sub> @Co <sub>3</sub> O <sub>4</sub> <sup>W</sup>	48	0.22	19	33	16
Co <sub>3</sub> InC <sub>0.75</sub> <sup>a</sup>	0	0	6	94	3
Co <sub>3</sub> O <sub>4</sub> <sup>b</sup>	0	0	100	0	80
In <sub>2</sub> O <sub>3</sub> <sup>c</sup>	96	0.16	4	0	4

<sup>W</sup> Sample was prepared by wetness impregnation of commercially available Co<sub>3</sub>O<sub>4</sub> (< 50 nm, Sigma-Aldrich) with In(NO<sub>3</sub>)<sub>3</sub> aqueous solution to ensure a nominal In:Co molar ratio of 3:8 and followed by calcination at 400 °C for 4 h.

<sup>a</sup> Mixed metal carbide, Co<sub>3</sub>InC<sub>0.75</sub>, sample was prepared according to previously reported protocol <sup>D9</sup> with a few adaptations that consisted of a pyrolytic decomposition of CPM-16(Co/In) MOF <sup>D10</sup> at 700 °C for 2 h. The identity of CPM-16(Co/In) MOF and product of pyrolysis were confirmed by powder XRD technique.

<sup>b</sup> After the reaction mixture of CoO and Co metal is detected.

<sup>c</sup> Indium oxide sample was prepared by calcination of In<sub>4</sub>(OH)<sub>6</sub>(BDC)<sub>3</sub> MOF <sup>D11</sup> at 400 °C for 4 h.

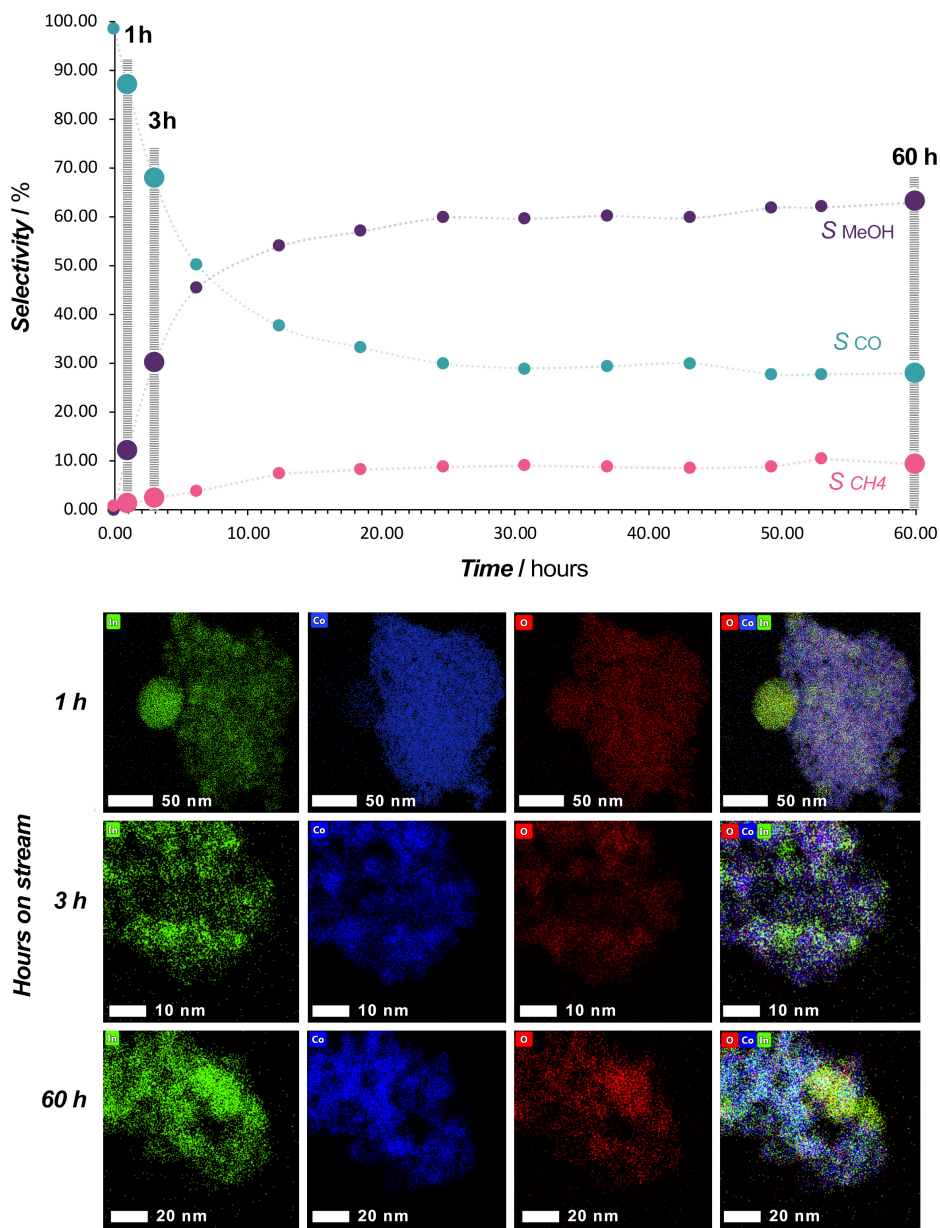


**Figure D35.** Evolution MeOH (purple), CO (cyan) and CH<sub>4</sub> (pink) selectivities over 60 h for 3In@4Co(20) analyzed after 1, 3 and 60 hours of CO<sub>2</sub> hydrogenation reaction with their corresponding EDS-TEM mappings. Conditions: 80% H<sub>2</sub>-20% CO<sub>2</sub> feed;  $T = 300\text{ }^{\circ}\text{C}$ ,  $P = 50\text{ bar}$ ,  $m_{\text{cat}} = 50\text{ mg}$ , GHSV = 15600 h<sup>-1</sup>.

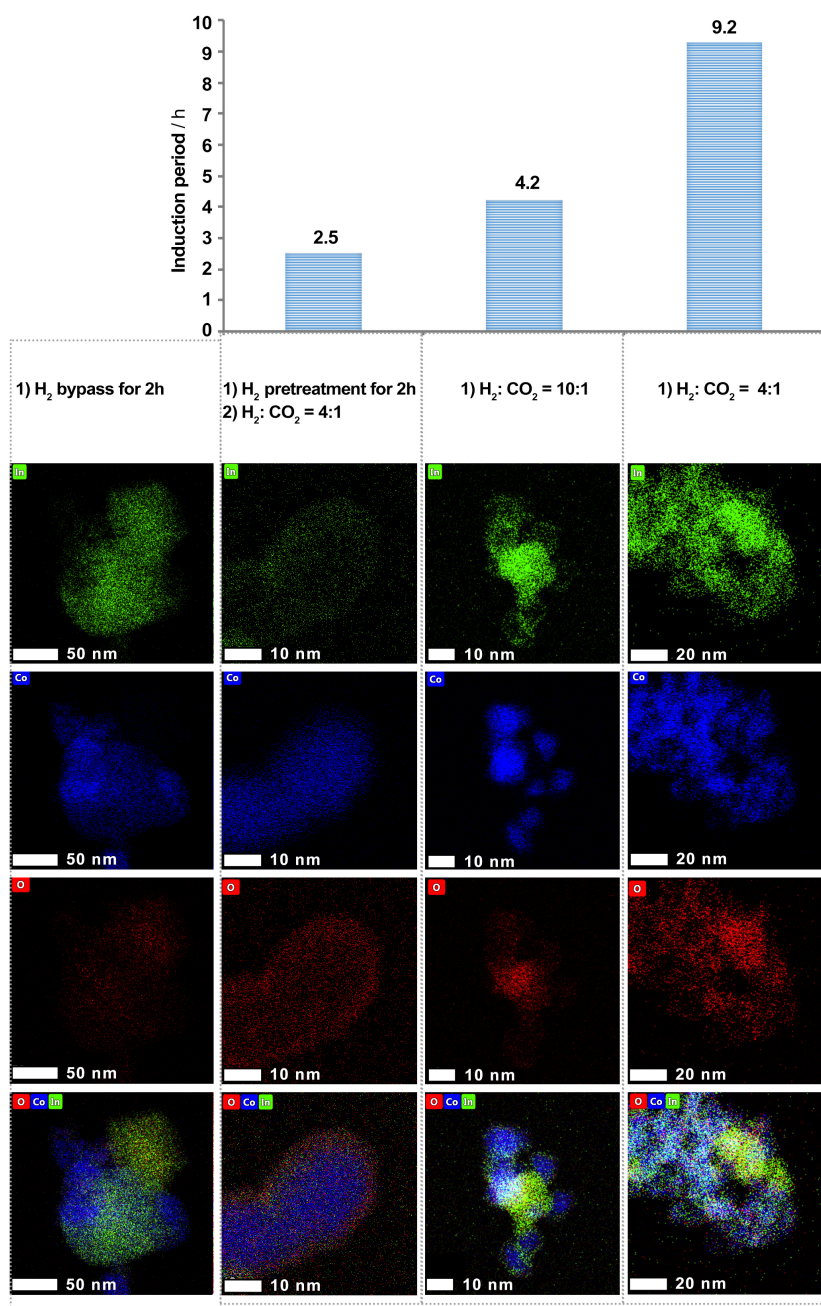


**Figure D36.** Evolution of induction period over 3In@4Co(20) catalyst under H<sub>2</sub> pretreatment for 2 h; (b) H<sub>2</sub> pretreatment for 2 h then bypassing H<sub>2</sub>:CO<sub>2</sub> (4:1) feed; (c) directly bypassing H<sub>2</sub>:CO<sub>2</sub> (10:1) feed; (d) standard reaction directly bypassing H<sub>2</sub>:CO<sub>2</sub> (4:1) feed for 30 h and their corresponding EDS-TEM mappings including for H<sub>2</sub> pretreatment only. Conditions:  $P = 50$  bar,  $m_{\text{cat}} = 50$  mg, TOS = 30 h,  $T = 300$  °C, GHSV = 15600 h<sup>-1</sup>.

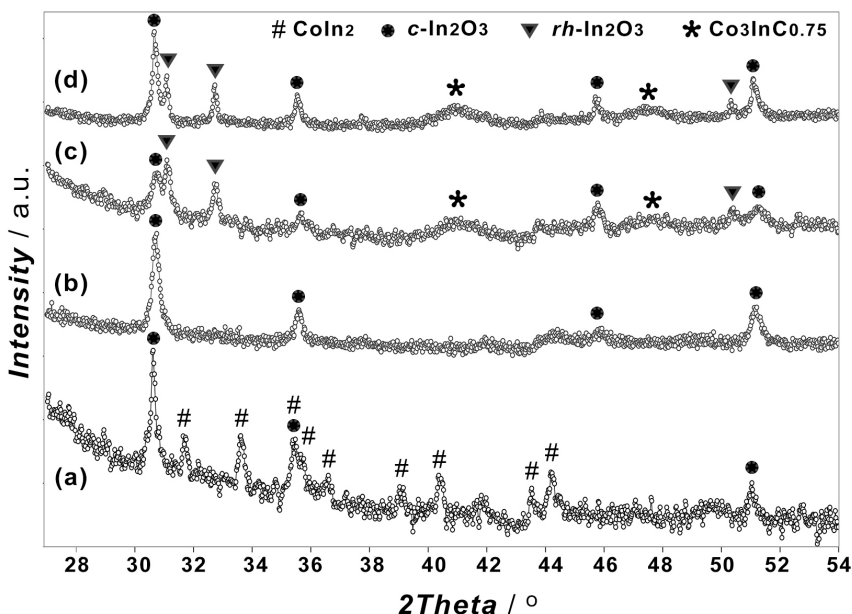


**Figure D37.** Evolution of crystalline phases in 3In@4Co catalyst after (a) H<sub>2</sub> pretreatment for 2 h; (b) H<sub>2</sub> pretreatment for 2 h then bypassing H<sub>2</sub>:CO<sub>2</sub> (4:1) feed; (c) directly bypassing H<sub>2</sub>:CO<sub>2</sub> (10:1) feed; (d) standard reaction conditions without pretreatment directly bypassing H<sub>2</sub>:CO<sub>2</sub> (4:1) feed. Reaction conditions: TOS = 30 h,  $P = 50$  bar,  $m_{\text{cat}} = 50$  mg,  $T = 300$  °C, GHSV = 15600 h<sup>-1</sup>.

In order to elucidate the role of In<sub>2</sub>O<sub>3</sub>/CoO<sub>x</sub> layer and formation mechanism of the supporting mixed cobalt indium carbide phase, we performed experiments exploring an effect of reductive pretreatment with hydrogen and its proportion in the reacting gas on the induction period and structural characteristics of the catalyst. The catalytic performance depends on the state of the surface of the catalyst, which undergoes subsequent processes of the reduction and re-oxidation of the surface. The experiments were designed in such a way that the reduction and re-oxidation processes were separated in time. The catalyst, firstly reduced in H<sub>2</sub> for 2 h (Figs. D36 and D37a), was then exposed to H<sub>2</sub>/CO<sub>2</sub> (4:1) mixture revealing shorter induction period and formation of characteristic oxidized shell (Figs. D36 and D37b). In order to reinforce the idea of importance of the preliminary reduction process, the catalyst was tested in condition of lower partial CO<sub>2</sub> pressure (H<sub>2</sub>/CO<sub>2</sub> = 10:1) also resulting in a reduced induction period. PXRD analysis (Fig. D37a) performed on the catalyst after 2 h of hydrogen pretreatment showed presence of CoIn<sub>2</sub> intermetallic phase which expectably disappeared after exposure to H<sub>2</sub>/CO<sub>2</sub> (4:1) mixture flow (Fig. D37a-b) for 30 h. The reduced induction period in the experiment with H<sub>2</sub>/CO<sub>2</sub> = 10:1 mixture, compared to the regular experiment (H<sub>2</sub>/CO<sub>2</sub> = 4:1)

suggests that the higher partial pressure of hydrogen favors a faster reduction of the catalyst surface which allows an acceleration in reaching the stable catalyst performance. It is conclusive that the formation of mixed metal carbide phase is a result of carburization occurred during the course of the reaction whereas the mixed oxide shell behaves as catalytically active phase.

## REFERENCES

- [D1] A. Taylor, R. W. Floyd, *Acta Crystallogr.* **1950**, 3, 285-289.
- [D2] L. Lei, W. Yin, X. Jiang, S. Lin, D. He, *Inorg. Chem.* **2013**, 52, 13356-13362.
- [D3] G. R. Patzke, J. Koepke, M. Binnewies, *Z. Anorg. Allg. Chem.* **2000**, 626, 1482-1487.
- [D4] L. Hütter, *Z. Metallkde* **1959**, 50, 199.
- [D5] M. Marezio, *Acta Crystallogr.* **1966**, 20, 723-728.
- [D6] R. W. Grimes, K. P. D. Lagerlof, *J. Am. Ceramic Soc.* **1991**, 74, 270-273.
- [D7] R. E. Carter, F. D. Richardson, C. Wagner, *JOM* **1955**, 7, 336-343.
- [D8] E.-M. Köck, M. Kogler, M. Grünbacher, C. Zhuo, R. Thalinger, D. Schmidmair, L. Schlicker, A. Gurlo, S. Penner, *J. Phys. Chem. C* **2016**, 120, 15272-15281.
- [D9] A. Kong, Q. Lin, C. Mao, X. Bu, P. Feng, *Chem. Comm.* **2014**, 50, 15619-15622.
- [D10] S.-T. Zheng, C. Mao, T. Wu, S. Lee, P. Feng, X. Bu, *J. Am. Chem. Soc.* **2012**, 134, 11936–11939.
- [D11] B. Gomez-Lor, E. Gutiérrez-Puebla, M. Iglesias, A. M. Monge, C. Ruiz-Valero, N.; Snejko, *Inorg. Chem.* **2002**, 41, 2429-2432.





## SUMMARY AND OUTLOOK

A world in which there is a demand for materials with various properties for different needs, requires robust tools to assist in this matter. In this regard, crystal engineering is among the most important tools in materials design and keeps developing in a sustained manner. Obviously, the application of crystal engineering principles to multifunctional microporous materials cannot cause any surprise, and Metal-Organic Frameworks (MOFs), as an example of the latter, stay in focus of scientific and industrial interests.

This thesis aims to apply crystal engineering principles to MOF design at different structural levels and to investigate the consequences of such design on the properties of the resulting solids. Chapter 1 provides a general introduction into the crystal engineering toolbox, paying particular attention to methods used to tune MOFs characteristics starting from the functionality to particle sizes and morphology. The chapter overviews some approaches meant to manipulate MOF structures at molecular level and links to Part II (Chapter 2 and Chapter 3) of the thesis. Additionally, the methods of crystal size and morphology control were outlined afterwards, establishing connection to Part III (Chapter 4 and Chapter 5).

Chapter 2 reports the electrochemical synthesis of copper-based Metal-Organic Frameworks. Two types of linkers were involved – H<sub>3</sub>BTC (1,3,5-tricarboxylic acid) and H<sub>3</sub>TATB (4,4',4''-s-triazine-2,4,6-triyl-tribenzoic acid) – significantly different in spacing length (5.6 Å vs 8.7 Å respectively). The reactions were conducted on a copper mesh grid surface acting simultaneously as an anode and metal ion source by using a pulsed current for a limited number of cycles. Both CuBTC and CuTATB can be grown either as bulk powder or as surface-supported films on the sacrificial electrode. Powder XRD analysis showed that CuTATB possess distinctive structures with different level of interpenetration for samples collected from the bulk and from the electrode, whereas CuBTC shows the same catenation-free topology independently of the location. Absence of interpenetration in CuBTC was attributed to relatively small spacing length of the organic linker. The surface-grown phase of CuTATB consists of two equivalent interpenetrated *tbo* nets isostructural to PCN-6. In contrast, the phase of CuTATB obtained in bulk demonstrates higher degree of interpenetration, where four simple *sur* nets relate to each other by operations of translation [1 0 0] and inversion with a primitive interpenetration cell of [2 0 0] [0 1 0] [0 0 1]. The level of interpenetration in the CuTATB phases affects their gas sorption behavior revealing a two-step isotherm for the PCN-6 analogue. The differences in the level of interpenetration were explained by the higher concentration of metal ions near the electrode surface and a high nucleation rate. Under these conditions the low

concentration, *i.e.* insufficient presence of the linker leads to a decrease of the interpenetration level which is not the case for a phase formed in the solution volume. The results presented in this work suggest that electrochemically-assisted surface growth allows to influence the interpenetration level and hence the structural properties of the MOFs in a controlled way.

Chapter 3 raises the question whether MOFs can be used as a filler in 3D printing inks for fast prototyping of MOF-based mixed matrix membranes. To ensure MOF integrability into an acrylic polymer matrix a post-synthetic modification (PSM) of MIL-53(Al)-NH<sub>2</sub> nanoparticles with photocrosslinkable methacrylic groups was made. A covalent character of the PSM was confirmed by liquid- and solid-state NMR experiments. In order to favor a preferential commitment of superficial NH<sub>2</sub>-groups into the PSM process and prevent pore blockage, non-activated MIL-53(Al)-NH<sub>2</sub> was used for modification and the percentage of methacrylated amino groups was estimated to be around 34%. MOF-contained acrylate-based ink photocurable formulations show different velocities of photopolymerization which depends on the chemical composition of the acrylate matrix. Overall, the presence of MIL-53(Al)-NH<sub>2</sub>/MMA material decreased the polymerization rate by a factor of 3-4 compared to the filler-free formulations, still embracing similar conversion levels of the system. Nevertheless, the heterogenous MOF-based ink formulations fulfilled the requirements to be used in DLP manufacturing technology and were applied for fast prototyping of membranes for gas separation. As was shown, the MOF filler anchored to the polymeric matrix enhances the overall permeability while retaining selectivity when applied for H<sub>2</sub>/CO<sub>2</sub> separation. The obtained results confirm the applicability of the 3D DLP technology for fast prototyping of MOF-based MMMs and provide new opportunities for further development.

Chapter 4 presents a new bottom-up surfactant-assisted synthetic approach for the fabrication of free-standing nanosheets of various non-layered MOFs that helps to avoid complex exfoliation procedures. Self-organization of CTAB surfactant (cetyltrimethylammonium bromide) in aqueous media in the presence of a metal precursor prior to the MOF synthesis enables a directed growth of nanolayered Al-containing MOF lamellae. The preorganization process was studied by SAXS elucidating the formation of stacked lamellar micelles of the surfactant with the internal spacing between layers of 4.3 nm. It was hypothesized that the formation mechanism involves entrapment of oligomeric aqua hydroxo aluminium structures in the intermicellar space. Addition of 2-aminoterephthalic linker to the reaction mixture causes degradation of the micelles that gives access to Al oligomeric structures initiating the formation of MIL-53(Al)-NH<sub>2</sub> following the stacking predefined by the CTAB micelles. Besides the controlled nanosheets growth, a further advantage of this synthetic route is the orientation of the MIL-53(Al)-NH<sub>2</sub> channels along the shortest particle dimension.

This feature substantially shortens diffusion pathways through the particle and improves a performance in both chemical sensing and gas separation compared to other crystal morphologies. Being used as a filler in mixed-matrix membranes, MIL-53(Al)-NH<sub>2</sub> nanosheets demonstrated higher permeability towards CO<sub>2</sub> in CH<sub>4</sub>/CO<sub>2</sub> equimolar mixture separation due to the more efficient utilization of the MOF porosity, superior degree of coverage by the lamellar filler and MOF channel orientation along the direction of the gas flux. As expected, no selectivity improvements were observed compared to bare polymer because the material adopts *lp* configuration and has intrinsically low sieving ability. Slight enhancement of selectivity occurred at high filler loadings and can be associated with rigidification of the polymer chains around the MOF lamellae. The capacitance sensing of alcohols (methanol, 2-propanol and 1-butanol) over a meander-patterned planar transducer device covered by a layer of drop-casted MIL-53(Al)-NH<sub>2</sub> nanosheets showed a completely reversible and sensitive response. Moreover, the observed decrease in the response time of sensors coated with MOF nanosheets compared to nanoparticles was attributed to a faster diffusion through the channels of the material and the stabilized open pore configuration. Additionally, the method was extended to other MOFs bearing another metal (Ga) and topology (CAU-10(Al), CAU-10(Al)-NH<sub>2</sub>). All the above underlines the significance of the development of synthetic routes for the fabrication of the MOFs nanosheets to reveal the true potential of these materials.

Chapter 5 discusses the use of modulated synthesis to obtain uniformly sized ZIF-67(Co) crystals and their further utilization as sacrificial carriers for preparation of a MOF-derived Co-supported indium oxide catalyst. The obtained catalysts showed themselves as potentially useful in direct CO<sub>2</sub> hydrogenation to methanol. In-impregnated ZIF-67(Co) materials underwent a stepwise pyrolytic and oxidative decomposition that led to formation of a nanostructured In<sub>2</sub>O<sub>3</sub>@Co<sub>3</sub>O<sub>4</sub> reticular shell composite exhibiting high methanol production rates and selectivities over long periods of time on stream (1000 h). It was found that the size of the parent sacrificial ZIF-67(Co) support played an important role in the performance of the resulting catalyst. Thus, ZIF-67(Co) of 20 nm in size reduces the induction period of the hydrogenation process considerably more than ZIF-67(Co) of 300 nm. It was associated with faster kinetics of active phase formation that provides a better In dopant distribution all over the metal-organic matrix including both micropores and interparticle surface areas and improving in such a way In utilization. Additionally, the sequential pyrolysis-calcination stepwise catalyst preparation procedure is paramount for a much faster induction period, since the latter is sensitive to dopant distribution. Among the variety of phases being formed during the catalytic reaction, formation of Co<sub>3</sub>InC<sub>0.75</sub> carbide is essential as it acts as a carrier, keeping Co and In in close proximity to each other and forming the active phase in the course of the

surface re-oxidation. Structural investigations implying several analysis techniques (ex-situ powder XRD, EXAFS, EELS and HAADF-STEM) applied to the catalytic system before and after reaction suggest that the catalyst undergoes reorganization under hydrogenation conditions, being transformed from crystalline  $\text{Co}_3\text{O}_4$  with an amorphous  $\text{In}_2\text{O}_3$  shell into  $\text{Co}_3\text{InC}_{0.75}$  covered by a layer of a  $\text{CoO}_x$  and  $\text{In}_2\text{O}_3$  oxides mixture. Hence, the structural reorganization is responsible for the observed induction period, while the highly defective mixed cobalt indium oxide shell determines the high methanol yield and selectivity. The catalytic results demonstrate that a reasonable trade-off between methanol yield and selectivity can be achieved by tuning both MOF-derived catalysts design and reaction conditions.

The results presented in this thesis can be considered as a small projection of the current state of the art in crystal engineering. Trying to answer the question whether we are always able to design materials with certain structural features and properties, crystal engineering keeps manipulating the matter on different levels using a set of techniques which never stops expanding. Despite the remarkable advances in the field, crystal engineering of MOFs constantly challenges researchers. Indeed, while working at molecular level, the reticular design concept tends to fail in a MOF construction for variety of reasons. Among them uncontrolled polymorphism and catenation, steric hindrance and functional incompatibility, unavoidable dominance of kinetically favored syntones and inability to carry out a reaction under certain conditions can be mentioned.

Pore architecture and their accessibility are, perhaps, the most demanding aspect of a MOF structure when it comes to applications. One of the restraints that can heavily affect the accessibility is framework catenation. Although some approaches to control interpenetration phenomena have been developed (variation of synthetic parameters, surface growth, ultrasonic assistance and SBU structural features design), understanding of the process on the fundamental level with all the chemistry and mechanisms involved is not yet accomplished. Chapter 2 of the thesis contributes to the scope of the existing approaches with electrochemical growth of MOFs on an electrode surface that enables to gain some control over the interpenetration level. However, presence and absence of interpenetration have their own advantages and the existence of interpenetration should not be always considered as a negative outcome. If the goal is to obtain a MOF structure with small pore sizes or to achieve dynamic, hysteretic or selective sorption behavior, interpenetration could be particularly desirable.

An alternative tool to manipulate MOF properties is a photosynthetic modification technique. It gives an opportunity to revitalize structures that cannot be formed with the classical self-assembly approach. Additionally, an implementation of certain functionalities

endows preformed frameworks with enhanced properties broadening their applicability. Chapter 3 gives an example of such modification by improving integrability of a MOF in photocurable ink formulations that are able to be processed into mixed matrix membranes using DLP 3D-printing technique. Covalent bonding of the matrix components to the anchored groups of the MOF leads to better adhesion between the polymer and the MOF crystals which is crucial for gas separation performance since formation of unspecific voids is less pronounced in this case.

Another perspective to unpack the full potential of MOFs is to tune the physical aspects of their crystals, growing them in different sizes and morphologies. Depending on the envisaged application, technology should not consider exclusively frameworks compositions and topologies, but a wide range of other parameters like particle size, morphology and crystal lattice orientation with respect to its surface. Chapter 4 of the thesis demonstrates how tailoring the crystal morphology relative to its structure substantially improves the MOF performance in molecular recognition when applied in gas separation and capacitive sensing. Moreover, having control over crystal sizing can be beneficial in certain tasks in which process velocity and diffusion times dictate their requirements. Chapter 5 illustrates that even when being used as a sacrificial matrix, the MOF particles of different sizes led to a distinctive catalytic performance of the MOF-derived materials.

Although, this work is specifically dedicated to crystal engineering of MOFs, the list of promising materials is not limited by them. The crystal engineering principles can be extended to other porous frameworks obtained from predesigned building units through reticular synthesis. Covalent Organic Frameworks (COFs) including the subclass – Covalent Triazine Frameworks (CTFs) materials are being synthesized as crystalline phases with an opportunity in some cases to tune the internal architectures. However, size and morphology control of COF crystals is currently in its nascent stage which opens a room for further development of crystal engineering tools. New approaches targeting ways of crystallization of commonly amorphous materials, e.g. Porous Aromatic Frameworks (PAFs), should also be included in the list of crystal engineering prospects.

In spite of everything, crystal engineering remains a relatively young field of science and, *a fortiori*, in porous materials chemistry the pool of challenges is far from being exhausted and even more are to come in the future.



## SAMENVATTING EN VOORUITZICHTEN

In een wereld waarin er behoefte is aan materialen met uiteenlopende eigenschappen voor verschillende doeleinden, zijn robuuste hulpmiddelen vereist om hierbij te helpen. In dit opzicht is kristalengineering één van de belangrijkste instrumenten bij het ontwerpen van materialen en dat voortdurend verder ontwikkeld wordt. Het is dan ook geen verrassing dat kristalengineering principes toegepast worden op multifunctionele microporeuze materialen. Metal-Organic Frameworks (MOFs), als voorbeeld van deze materialen, staan daarbij in het centrum van de wetenschappelijke én industriële belangstelling.

Dit proefschrift richt zich op het toepassen van kristalengineering principes op het ontwerp van MOFs op verschillende structuurniveaus en te onderzoeken welke gevolgen een dergelijke aanpak heeft op de eigenschappen van de gesynthetiseerde materialen. Hoofdstuk 1 geeft een algemene inleiding van technieken in de kristalengineering gereedschapskist, met extra aandacht voor methoden die worden gebruikt om de eigenschappen van MOF's aan te passen, van functionaliteit tot deeltjesgrootte en morfologie. Het hoofdstuk geeft een overzicht van enkele benaderingen bedoeld om MOF-structuren op moleculair niveau te manipuleren en vormt een brug naar deel II (hoofdstuk 2 en hoofdstuk 3) van het proefschrift. Daarnaast worden de methoden voor controle over de kristalgrootte en morfologie toegelicht, waardoor een verband wordt gelegd met Deel III (Hoofdstuk 4 en Hoofdstuk 5).

Hoofdstuk 2 beschrijft de elektrochemische synthese van op koper gebaseerde metal-organic frameworks (MOF's). Er werden twee soorten linkers gebruikt -  $H_3BTC$  (1,3,5-benzeentricarbonsuur) en  $H_3TATB$  (4,4',4''-s-triazine-2,4,6-triyl-tribenzoëzuur) - met een significant verschil in lengte (respectievelijk 5,6 Å en 8,7 Å). De reacties werden uitgevoerd op een oppervlak van een gaas van koperdraad dat tegelijkertijd als anode en metaalionenbron fungeerde door middel van een gepulseerde stroom gedurende een beperkt aantal cycli. Zowel  $CuBTC$  als  $CuTATB$  konden worden geproduceerd in poedervorm of als een film op het oppervlak van de geconsumeerde elektrode. Poeder XRD-analyse toonde aan dat voor poedermonters en monsters van de elektrode  $CuTATB$  twee onderscheidbare structuren bezit elk met een verschillend interpenetratie niveau, terwijl de  $CuBTC$  monsters een interpenetratie-vrije topologie hebben. De afwezigheid van interpenetratie in  $CuBTC$  werd toegeschreven aan de relatief kleine lengte van de organische linker. De  $CuTATB$  vorm gegroeid op het elektrodeoppervlak bestaat uit twee equivalente, vervlochten *tbo*-netwerken die isostructureel zijn met PCN-6. Daarentegen vertoont de in poedervorm verkregen fase van  $CuTATB$  een



hogere mate van interpenetratie, hier zijn vier eenvoudige **sur**-netwerken met elkaar vervlochten na translatiebewerkingen [1 0 0] en inversie met een primitieve interpenetratie cel van [2 0 0] [0 1 0] [0 0 1]. Het niveau van interpenetratie in de CuTATB-fasen beïnvloedt hun gasabsorptiegedrag en resulteert in een tweestaps-isotherm voor de PCN-6-analoog. De verschillen in interpenetratieniveau werden verklaard door de hogere concentratie van metaalionen in de buurt van het elektrode-oppervlak en een hoge nucleatiesnelheid. Onder deze omstandigheden leidt de lage concentratie, d.w.z. onvoldoende aanwezigheid van de linker, tot een verlaging van het interpenetratieniveau, wat niet het geval is voor een fase gevormd in oplossing. De resultaten die in dit werk worden gepresenteerd, suggereren dat elektrochemisch geïnduceerde oppervlaktegroei het interpenetratieniveau en daarmee de structurele eigenschappen van de MOFs op een gecontroleerde manier kan beïnvloeden.

Hoofdstuk 3 roept de vraag op of MOFs kunnen worden gebruikt als vulmiddel in 3D-printerinkt voor snelle prototyping van op MOF gebaseerde mixed matrix-membranen (MMM's). Om de MOF-integreerbaarheid in een acrylpolymeermatrix te garanderen, werd een post-synthetische modificatie (PSM) van MIL-53(Al)-NH<sub>2</sub> nanodeeltjes uitgevoerd met methacrylgroepen die met licht ge-crosslinked kunnen worden. Het covalente karakter van de PSM werd bevestigd met vloeistof- en vaste stof-NMR. Om een preferentiële participatie van NH<sub>2</sub>-groepen aan het MOF-oppervlak in het PSM-proces te bevorderen en porieblokkering te voorkomen, werd niet-geactiveerd MIL-53(Al)-NH<sub>2</sub> gebruikt voor modificatie en het percentage gemethacryleerde aminogroepen werd geschat op ongeveer 34%. Formuleringen van MOF-bevattende op acrylaat gebaseerde inkt dat uithardt door belichting vertonen verschillende snelheden van fotopolymerisatie, afhankelijk van de chemische samenstelling van de acrylaatmatrix. In het algemeen verlaagde de aanwezigheid van MIL-53(Al)-NH<sub>2</sub>/MMA-materiaal de polymerisatiesnelheid met een factor 3-4 in vergelijking met de vulstofvrije formuleringen, waarbij nog steeds vergelijkbare conversieniveaus werden behaald. Desalniettemin voldeden de heterogene op MOF gebaseerde inktformuleringen aan de vereisten voor gebruik in DLP-fabricagetechnologie en werden toegepast voor de snelle prototyping van membranen voor gasscheiding. Zoals werd gedemonstreerd, verbeterd de MOF-vulstof verankerd in de polymeermatrix de algehele permeabiliteit met behoud van de selectiviteit wanneer toegepast voor H<sub>2</sub>/CO<sub>2</sub>-scheiding. De verkregen resultaten bevestigen de toepasbaarheid van de 3D DLP-technologie voor snelle prototyping van op MOF gebaseerde MMM's en bieden nieuwe mogelijkheden voor verdere ontwikkeling.

Hoofdstuk 4 presenteert een nieuwe 'bottom-up' surfactant-geassisteerde methode voor de synthese van nanosheets van verschillende MOF's die van nature geen laag-structuur hebben en waarmee complexe exfoliatieprocedures kunnen worden vermeden. De

zelforganisatie in waterige media van de CTAB surfactant (cetyltrimethylammoniumbromide) met een metaalprecursor voorafgaand aan de MOF-synthese maakt een gerichte groei van Al-bevattende MOF-lamellen van nanodiktes mogelijk. Het pre-organisatieproces werd bestudeerd door met SAXS de vorming van gestapelde lamellaire micellen van de surfactant met een tussenlaagafstand van 4,3 nm op te helderen. Er werd verondersteld dat het vormingsmechanisme het insluiten van oligomere aqua hydroxo aluminium structuren in de intermicellaire ruimte omvat. Toevoeging van de 2-aminotereftaalzure linker aan het reactiemengsel veroorzaakt de afbraak van micellen wat toegang geeft tot de oligomere Al-structuren en de vorming van MIL-53(Al)-NH<sub>2</sub> initieert binnen de door de lamellaire CTAB-micellen gelimiteerde ruimte. Naast de gecontroleerde groei van nanosheets, is een ander voordeel van deze synthetische route de oriëntatie van de MIL-53(Al)-NH<sub>2</sub> poriën in de richting van de kortste deeltjesafmeting. Deze eigenschap verkort de diffusieweglengte door het deeltje aanzienlijk. In vergelijking met andere kristalmorfologieën worden bij toepassing in zowel detectie van chemicaliën als gasscheiding de prestaties aanzienlijk verbeterd. MIL-53(Al)-NH<sub>2</sub> nanosheets gebruikt als vulstof in mixed matrix membranen toonden een hogere permeabiliteit voor CO<sub>2</sub> bij de equimolaire CH<sub>4</sub>/CO<sub>2</sub> mengselscheiding vanwege het efficiëntere gebruik van de MOF-porositeit, de superieure dekkingsgraad door de lamellaire vulling en de MOF-porie-oriëntatie in de gastransportrichting. Zoals verwacht werden er geen selectiviteitsverbeteringen waargenomen in vergelijking met een puur polymeermembraan omdat de MOF een *lp*-configuratie aanneemt en een intrinsiek lage selectiviteit heeft. Een lichte verbetering van de selectiviteit trad op bij hoge beladingen en kan worden geassocieerd met verstijving van de polymeerketens rond de MOF-lamellen. De capacitatieve detectie van alcoholen (methanol, 2-propanol en 1-butanol) met een vlakke transducer met meanderpatroon bedekt met een laag drop-casted MIL-53(Al)-NH<sub>2</sub> nanosheets leverde een gevoelige en volledig reversibele respons. De waargenomen afname van de responstijd van sensoren bekleed met MOF-nanosheets in vergelijking met nanodeeltjes werd toegeschreven aan een snellere diffusie door de poriën van het materiaal en de gestabiliseerde *lp* configuratie met open poriën. Bovendien werd de synthesesmethode uitgebreid tot verscheidene MOF's met een ander metaal (Ga) en topologie (CAU-10(Al), CAU-10(Al)-NH<sub>2</sub>). Al het bovenstaande benadrukt het belang van de ontwikkeling van synthetische routes voor de fabricage van de MOF nanosheets om het volledige potentieel van deze materialen te onthullen.

Hoofdstuk 5 bespreekt het gebruik van gemoduleerde synthese om ZIF-67(Co)-kristallen van uniforme grootte te verkrijgen en hun verdere gebruik als uitgangsstof voor de bereiding van een van MOF afgeleide Co-oxide gedragen indiumoxidekatalysator. De verkregen katalysatoren bleken toepasbaar in de directe hydrogenering van CO<sub>2</sub> tot methanol.

Stapsgewijze pyrolytische en oxidatieve ontleding van geïmpregneerde ZIF-67(Co)-materialen leidde tot de vorming van een nanogestructureerde  $\text{In}_2\text{O}_3@\text{Co}_3\text{O}_4$  egg-shell composiet die hoge productiesnelheden en selectiviteit voor methanol vertoonde gedurende lange testperioden (1000 uur). De grootte van de ZIF-67(Co)-precursor speelt een belangrijke rol in de prestatie van de uiteindelijke katalysator. Zo vermindert ZIF-67(Co) met een deeltjesdiameter van 20 nm de inductieperiode van het hydrogeneringsproces aanzienlijk meer dan ZIF-67(Co) van 300 nm. Dit werd geassocieerd met een snellere vorming van de actieve fase wat zorgt voor een betere dispersie van de In-dotering over de metaal-organische matrix, zowel in de microporiën als over het tussendeeltjesoppervlak. Zodoende werd het gebruik van de actieve In-fase verbeterd. De stapsgewijze sequentiële pyrolyse-calcinerings katalysatorbereidingsprocedure is bovendien van cruciaal belang voor een veel snellere inductieperiode, aangezien deze laatste gevoelig is voor de verdeling van het indium. Van de verschillende fasen die tijdens de katalytische reactie worden gevormd, is de vorming van  $\text{Co}_3\text{InC}_{0.75}$ -carbide essentieel omdat het als drager fungeert, Co en In dicht bij elkaar houdt en de actieve fase vormt tijdens de oppervlakte heroxidatie. Structuuronderzoek met verschillende analysetechnieken (ex-situ poeder XRD, EXAFS, EELS en HAADF-STEM) toegepast op het katalytische systeem vòòr en ná reactie suggereert dat de katalysator onder hydrogeneringsomstandigheden een reorganisatie ondergaat en wordt getransformeerd van kristallijne  $\text{Co}_3\text{O}_4$  met een amorf  $\text{In}_2\text{O}_3$ -schil naar  $\text{Co}_3\text{InC}_{0.75}$  bedekt door een schil van een  $\text{CoO}_x$  en  $\text{In}_2\text{O}_3$  mengsel. Deze structurele reorganisatie is verantwoordelijk voor de waargenomen inductieperiode, terwijl de zeer defecte kobalt-indiumoxideschil de hoge methanolopbrengst en selectiviteit bepaalt. De katalytische resultaten tonen aan dat een redelijke balans tussen methanolopbrengst en selectiviteit kan worden bereikt door zowel het ontwerp van MOF-afgeleide katalysatoren als de reactieomstandigheden af te stemmen.

De resultaten die in dit proefschrift worden gepresenteerd, kunnen worden beschouwd als een kleine projectie van de huidige stand van de techniek in kristalengineering. In een poging de vraag te beantwoorden of we altijd in staat zijn om materialen met bepaalde structurele kenmerken en eigenschappen te ontwerpen, blijft kristalengineering de materie op verschillende niveaus manipuleren met behulp van een reeks technieken die constant wordt uitgebreid. Ondanks de opmerkelijke vooruitgang, is de kristalengineering van MOFs een constante uitdaging voor onderzoekers. En inderdaad, tijdens het werken op moleculair niveau heeft het reticulair ontwerpconcept om verschillende redenen de neiging om te mislukken bij het construeren van een MOF. Hieronder vallen onder andere ongecontroleerd polymorfisme en interpenetratie, sterische hinder en functionele onverenigbaarheid, onvermijdelijke

dominantie van kinetisch begunstigde syntonen en onmogelijkheid om een reactie uit te voeren onder bepaalde omstandigheden.

Architectuur van poriën en hun toegankelijkheid zijn misschien wel de meest veeleisende aspecten van een MOF-structuur als het gaat om applicaties. Eén van de aspecten die de toegankelijkheid sterk kan beïnvloeden, is interpenetratie. Hoewel er enkele technieken zijn ontwikkeld om interpenetratie onder controle te houden (variatie in de synthese parameters, oppervlaktegroei, ultrasone assistentie en ontwerp van SBU's met structurele kenmerken), wordt het vormingsproces met alle chemie en mechanismen nog niet volledig fundamenteel begrepen. Hoofdstuk 2 van het proefschrift verbreedt de bestaande benaderingen met de elektrochemische groei van MOFs op een elektrode-oppervlak, wat het mogelijk maakt enige controle over het interpenetratieniveau te verkrijgen. Aanwezigheid en afwezigheid van interpenetratie hebben echter hun eigen voordelen en het bestaan van interpenetratie moet niet altijd als een negatief resultaat worden beschouwd. Als het doel is om een MOF-structuur met kleine porieafmetingen te verkrijgen of om dynamisch, hysteretisch of selectief sorptiegedrag te bereiken, kan interpenetratie bijzonder wenselijk zijn.

Een alternatieve methode om MOF-eigenschappen te manipuleren, is een fotosynthetische modificatietechniek. Het biedt de mogelijkheid om structuren te realiseren die niet kunnen worden gevormd met de klassieke zelfassemblagebenadering. Bovendien zorgt een implementatie van bepaalde functionaliteiten in bestaande frameworks voor verbeterde eigenschappen die hun toepasbaarheid verbreden. Hoofdstuk 3 geeft een voorbeeld van een dergelijke modificatie door de integreerbaarheid van een MOF te verbeteren in door licht hardbare inktformuleringen die kunnen worden verwerkt tot mixed matrix membranen met behulp van DLP 3D-printtechniek. Covalente binding van de matrixcomponenten aan de functionele groepen van de MOF leidt tot een betere hechting tussen het polymeer en de MOF-kristallen, cruciaal voor gasscheiding omdat de vorming van niet-scheidingsspecifieke holtes in dit geval gereduceerd is.

Een andere benadering om het volledige potentieel van MOFs te benutten, is om de fysieke aspecten van hun kristallen af te stemmen door ze in verschillende afmetingen en morfologieën te laten groeien. Afhankelijk van de beoogde toepassing moet technologie niet uitsluitend rekening houden met MOF-samenstellingen en topologieën, maar ook met een breed scala aan andere parameters zoals deeltjesgrootte, morfologie en kristalroosteroriëntatie ten opzichte van het buitenoppervlak. Hoofdstuk 4 van dit proefschrift laat zien hoe het afstemmen van de kristalmorfologie op de MOF-structuur de prestaties van de MOF bij moleculaire herkenning aanzienlijk verbetert bij toepassing in gasscheiding en capacitieve detectie. Bovendien kan het beheersen van de kristalgrootte gunstig zijn bij bepaalde

toepassingen waar processnelheid en diffusietijden bepalend zijn. Hoofdstuk 5 illustreerde dat zelfs wanneer ze werden gebruikt als reactant, MOF-deeltjes van verschillende afmetingen resulteerden in verschillende katalytische prestaties van de afgeleide materialen.

Hoewel dit werk specifiek is gewijd aan kristalengineering van MOFs, wordt de lijst met veelbelovende materialen er niet door beperkt. De kristalengineering principes kunnen middels reticulair synthese worden toegepast op vorming van andere poreuze frameworks gebaseerd op voorontworpen bouwstenen. Covalent Organic Frameworks (COF's), inclusief de onderklasse van Covalent Triazine Frameworks (CTF's) materialen, kunnen worden gesynthetiseerd als kristallijne fasen met in sommige gevallen de mogelijkheid om de interne architectuur te manipuleren. Beheersing van de grootte en morfologie van COF-kristallen bevindt zich momenteel in de beginfase, wat mogelijkheden biedt voor verdere ontwikkeling van kristalengineering methodieken. Nieuwe benaderingen gericht op manieren van kristallisatie van veelal amorfe materialen, b.v. poreuze aromatische frameworks (PAF's) horen ook thuis op de lijst met opkomende kristalengineering technieken.

Ondanks alles blijft kristalengineering een relatief jong wetenschapsgebied en a fortiori zijn de uitdagingen op het gebied van de chemie van poreuze materialen nog lang niet uitgeput en zullen er in de nabije toekomst nog meer volgen.

## ACKNOWLEDGEMENTS

First and foremost, I would like to wish my deepest gratitude to my supervisors. Freek and Jorge, it is a great honour to work under your supervision. Freek, thank you for your patient guidance, advices you provided throughout my PhD journey, for your extensive knowledge and experience. You gave me a lot of opportunities to learn from you and to grow professionally. Jorge, thank you for your academic courage, bright ideas and for interesting but challenging projects. I highly appreciate your support in fight with an abnormally large number of reviewers in our rebuttals.

Paraphrasing the words of Vladimir Harkonnen (F. Herbert, *Dune*), “The equipment must run”. It would not be possible without the research support staff. I would like to thank Bart for his help in literally everything, Willy for adsorption measurements and keeping the texture lab in perfect order, Liliana for her assistance with GC and sharing the idea that the blue tape can fix anything, Harrie for ordering chemicals and organizing the big migration period. Also, I want to acknowledge Duco for his support in SEM measurements, Ben for the XRD training and DSC experiments, Marcel for teaching me how to use AFM, Bart (MECS) for his valuable introduction to XPS and Stephen for helping out with NMR.

I would like to express the appreciation to the secretariat team. Els, thank you for answering tons of questions and helping with administrative issues. Caroline, thanks for your kind assistance with sending samples around the world.

I wish to thank all the people I was collaborating with. Beba, thank you for your guidance in the gas separation field and your passion about science. Sumit, thank you for the sensing studies and letting me know more about the Indian culture. Maarten, thank you for the SAXS analysis, enjoyable conversations and the dark humor we both share. Nastya and Ira, thank you for the fruitful collaboration in catalysis and keeping me updated about new popular trends. Meixia, thank you for letting me use Setup 2 and taking care about us during our travel to China. Riming, thank you for your cooking skills and teaching me forty-two Chinese characters. Sonia, thank you for interesting projects and your joyful attitudes.

Additionally, I would like to thank all colleagues and members of ChemE group. Monique, thank you for giving me opportunity to improve my teaching assistance skills in the Thermodynamics course. Michiel, thank you for your critical questions at Thursday lunch meetings. Alma, thank you for your advices, support in many areas and our out-of-work activities (many thanks to Ivo). Dima, I will never forget your dance with a scythe at our

Halloween party – it was made of plastic but still deadly dangerous. I send my special thanks to the membrane division – Ana, Miren, Xinlei and Xuerui – I really appreciate working with you all. The group atmosphere wouldn't be complete without Maria Jose, Alyona, Agi, Ina, Jara, Eduardo, Robert, Lide, Adrian, Constantino, Rupali, Kevin, Francesc, Tim, Xiaohui – it was a pleasure to have known you.

Finally, I would like to thank Alla and my family for their patience and support.

And I thank you, an occasional reader, for opening my thesis (at least to this page).

Alexey

## LIST OF PUBLICATIONS

### Publications related to this thesis

- A. Pustovarenko, B. Seoane, E. Abou-Hamad, H. E. King, B. M. Weckhuysen, F. Kapteijn, J. Gascon. Rapid Fabrication of MOF-based Mixed Matrix Membranes through a 3D Printing by Digital Light Processing. (*in preparation*)
- A. Pustovarenko, A. Dikhtiarenko, A. Bavykina, L. Gevers, A. R. Galilea, A. Russkikh, S. Telalovic, A. Aguilar-Tapia, J. L. Hazemann, S. Ould-Chickh, J. Gascon. Metal-organic framework-derived synthesis of cobalt indium catalysts for the hydrogenation of CO<sub>2</sub> to methanol. *ACS Catal.*, 10 (2020) 5064–5076.  
DOI: 10.1021/acscatal.0c00449
- A. Pustovarenko, M. G. Goesten, S. Sachdeva, M. X. Shan, Z. Amghouz, Y. Belmabkhout, A. Dikhtiarenko, T. Rodenas, D. Keskin, I. K. Voets, B. M. Weckhuysen, M. Eddaoudi, L. de Smet, E. J. R. Sudholter, F. Kapteijn, B. Seoane, J. Gascon. Nanosheets of nonlayered aluminum metal-organic frameworks through a surfactant-assisted method. *Adv. Mater.*, 30 (2018) 1707234.  
DOI: 10.1002/adma.201707234
- S. Sachdeva, A. Pustovarenko, E. J. R. Sudhölter, F. Kapteijn, L. de Smet, J. Gascon. Control of interpenetration of copper-based MOFs on supported surfaces by electrochemical synthesis. *CrystEngComm*, 18 (2016) 4018–4022.  
DOI: 10.1039/C5CE02462E

### Other publications

- A. Goryachev, A. Pustovarenko, G. Shterk, N. S. Alhajri, A. Jamal, M. Albuali, L. van Koppen, I. S. Khan, A. Russkikh, A. Ramirez, T. Shoinkhorova, E. J. M. Hensen, J. Gascon. A multi-parametric catalyst screening for CO<sub>2</sub> hydrogenation to ethanol. *ChemSusChem*, (2020). (*submitted*)
- M. Çağlayan, A. Lucini Paioni, E. Abou-Hamad, G. Shterk, A. Pustovarenko, M. Baldus, A. Dutta Chowdhury, J. Gascon. Illuminating initial carbon-carbon bond formation during the early stages of methane dehydroaromatization. *Angew. Chem., Int. Ed.*, 59 (2020) 16741–16746.  
DOI: 10.1002/anie.202007283



- A. Bavykina, I. Yarulina, A. J. Al Abdulghani, L. Gevers, M. N. Hedhili, X. H. Miao, A. R. Galilea, A. Pustovarenko, A. Dikhtiarenko, A. Cadiou, A. Aguilar-Tapia, J. L. Hazemann, S. M. Kozlov, S. Ould-Chickh, L. Cavallo, J. Gascon. Turning a methanation Co catalyst into an In-Co methanol producer. *ACS Catal.*, 9 (2019) 6910-6918.  
DOI: 10.1021/acscatal.9b01638
- R. M. Wang, H. Haspel, A. Pustovarenko, A. Dikhtiarenko, A. Russkikh, G. Sterk, D. Osadchii, S. Ould-Chickh, M. Ma, W. Smith, K. Takanabe, F. Kapteijn, J. Gascon. Maximizing Ag utilization in high-rate CO<sub>2</sub> electrochemical reduction with a coordination polymer-mediated gas diffusion electrode. *ACS Energy Lett.*, 4 (2019) 2024-2031.  
DOI: 10.1021/acsenerylett.9b01509
- M. X. Shan, B. Seoane, A. Pustovarenko, X. R. Wang, X. L. Liu, I. Yarulina, E. Abou-Hamad, F. Kapteijn, J. Gascon. Benzimidazole linked polymers (BILPs) in mixed-matrix membranes: Influence of filler porosity on the CO<sub>2</sub>/N<sub>2</sub> separation performance. *J. Membrane Sci.*, 566 (2018) 213-222.  
DOI: 10.1016/j.memsci.2018.08.023
- I. Yarulina, S. Bailleul, A. Pustovarenko, J. Ruiz Martinez, K. de Wispelaere, J. Hajek, B. M. Weckhuysen, K. Houben, M. Baldus, V. van Speybroeck, F. Kapteijn, J. Gascon. Suppression of aromatic cycle in methanol-to-olefins reaction over ZSM-5 by post-synthetic modification using calcium. *ChemCatChem*, 8 (2016) 3057-3063.  
DOI: 10.1002/cctc.201600650
- A. Dikhtiarenko, P. Serra-Crespo, S. Castellanos, A. Pustovarenko, R. Mendoza-Meroño, S. García-Granda, J. Gascon. "Temperature-dependent supramolecular isomerism of lutetium-aminoterephthalate metal-organic frameworks: synthesis, crystallography and physical properties. *Cryst. Growth Des.*, 16 (2016) 5636-5645.  
DOI: 10.1021/acs.cgd.6b00274
- A. Dikhtiarenko, A. I. Olivos-Suarez, A. Pustovarenko, S. García-Granda, J. Gascon. Crystal structure of 2,2'-diamino-[1,1'-biphenyl]- 4,4'-dicarboxylic acid dihydrate, C<sub>14</sub>H<sub>16</sub>N<sub>2</sub>O<sub>6</sub>. *Z. Kristallogr.*, 231 (2016) 65-67.  
DOI: 10.1515/ncrs-2014-9143

- S. Castellanos, A. Goulet-Hanssens, F. Zhao, A. Dikhtiarenko, A. Pustovarenko, S. Hecht, J. Gascon, F. Kapteijn, D. Bléger. Structural effects in visible-light-responsive metal-organic frameworks incorporating ortho-fluoroazobenzenes. *Chem. Eur. J.*, 22 (2016) 746–752.  
DOI: 10.1002/chem.201503503
- S. Castellanos, K. Babu Sai Sankar Gupta, A. Pustovarenko, A. Dikhtiarenko, M. Nasalevich, P. Atienzar, H. García, J. Gascon, F. Kapteijn. Anchoring of diphenylphosphinyl groups to NH<sub>2</sub>-MIL-53 by post-synthetic modification. *Eur. J. Inorg. Chem.*, (2015) 4648–4652.  
DOI: 10.1002/ejic.201500678

## Presentations

- A. Pustovarenko, M. G. Goesten, S. Sachdeva, Z. Amghouz, A. Dikhtiarenko, E. J. R. Sudholter, F. Kapteijn, B. Seoane, J. Gascon. “Nanosheets of non-layered aluminium Metal-Organic Frameworks through a surfactant-assisted method.” 31<sup>st</sup> European Crystallographic Meeting, Oviedo, Spain, August 22-27, 2018 (**Poster**)
- A. Pustovarenko, F. Kapteijn, B. Seoane, J. Gascon. “Surfactant assisted synthesis of metal organic framework nanosheets. Application in gas separation and sensing.” CAHAINS 2016: Chemistry as Innovating Science, Veldhoven, The Netherlands; December 6, 2016 (**Talk**)
- A. Pustovarenko, S. Sachdeva, M. G. Goesten, A. Dikhtiarenko, Z. Amghouz, B. Seoane, F. Kapteijn, J. Gascon. “Lamellar NH<sub>2</sub>-MIL-53(Al) in polymer composites for gas separation and sensing.” 7th International Zeolite Membrane Meeting (IZMM-2016), Dalian, China; 20-23 August 2016 (**Poster**)



## **CURRICULUM VITAE**

Alexey Pustovarenko was born on November 1<sup>st</sup>, 1986 in Vinnytsia, USSR. He received his bachelor and master's degrees from Taras Shevchenko National University of Kyiv, Ukraine. Afterwards, he worked for Thermo Scientific™ Dionex™ representative office in Ukraine as an application specialist in the field of ion chromatography. In 2012 he enrolled in the master's degree program offered by Menendez Pelayo International University and University of Oviedo, Spain with specialization in crystallography and graduated in 2013. In 2015 he joined the Catalysis Engineering group of Delft University of Technology and started his PhD project related to the crystal engineering of metal-organic frameworks for molecular recognition under the supervision of Prof. dr. Jorge Gascon and Prof. dr. Freek Kapteijn.

